

International Design Study for the Neutrino Factory

IDS-NF-???

Other preprint and report numbers

Reference Design Report

The IDS-NF collaboration

Abstract

The study of the phenomenon of neutrino oscillations provides a unique window on physics beyond the Standard Model. The recent discovery that θ_{13} is non-zero admits the possibility that CP invariance may be violated through the neutrino-mixing matrix. Further, the fact that $\theta_{13} \approx 9^\circ$, a comparatively large value, implies that emphasis must be placed on the development of techniques in which statistical and systematic uncertainties can be reduced to the percent level. The Neutrino Factory, in which intense beams of high energy ν_e ($\bar{\nu}_e$) and $\bar{\nu}_\mu$ (ν_μ) are produced from the decay of muons confined within a storage ring, is capable of making measurements with the requisite precision. This Reference Design Report (RDR) presents the design for the Neutrino Factory accelerator facility and neutrino detectors developed by the International Design Study for the Neutrino Factory (the IDS-NF) collaboration which was established by the community at the ninth “International Workshop on Neutrino Factories, super-beams, and beta-beams” which was held in Okayama in August 2007.

The baseline accelerator facility provides 10^{21} muon decays per year from a 10 GeV stored muon beam. The neutrino beam illuminates a single far detector placed at a distance of between 1 500 km and 2 500 km from the source. A suite of near detectors provides a rich programme of neutrino-nucleus scattering measurements. The muon beam is derived from pions produced by the bombardment of a target with a high-power, pulsed proton beam. Site-specific proton-driver options are presented that would allow the Neutrino Factory to be implemented at CERN, Fermi National Laboratory or the Rutherford Appleton Laboratory. Designs for the pion-production target and pion/muon capture systems are presented. The design of the muon front-end is presented including bunching, phase-rotation and cooling sections. The muon front-end includes a novel “chicane” by which unwanted particles are removed from the beam before it is injected into the cooling channel. A linac followed by two recirculating linear accelerators (RLAs) are then used to accelerate the beam to the energy at which it is injected into the storage ring. A 100 kT Magnetised Iron Neutrino Detector (MIND) has been optimised for the study of the “golden” $\nu_e \rightarrow \nu_\mu$ ($\bar{\nu}_e \rightarrow \bar{\nu}_\mu$) channel; the specification, design and simulated performance of the MIND is presented. The neutrino-nucleus scattering programme that may be carried out using a suite of detectors placed close to the end of the straight sections of the storage ring is presented. Options for the near detectors are described. The performance of facility is presented and compared with that of alternative proposals. Finally, an incremental approach to constructing the facility in which each increment is capable of delivering a first class neutrino-physics programme and of supporting the R&D necessary to deliver the next increment is outlined.

Draft 1; December 24, 2013

S. Choubey, R. Gandhi, S. Goswami
Harish-Chandra Research Institute, Chhatnag Road, Jhansi, Allahabad, 211019, India

J.S. Berg, R. Fernow, J.C. Gallardo, R. Gupta, H. Kirk, N. Simos, N. Souchlas
Brookhaven National Lab, P.O. Box 5000, Upton, NY 11973-5000, USA

M. Ellis¹, P. Kyberd
Brunel University West London, Uxbridge, Middlesex UB8 3PH, UK

E. Benedetto, E. Fernandez-Martinez, I. Efthymiopoulos, R. Garoby, S. Gilardoni, M. Martini, G. Prior
European Organization for Nuclear Research, CERN CH-1211, Geneva 23, Switzerland

D. Indumathi, N. Sinha
The Institute of Mathematical Sciences, IV Cross Road, CIT Campus, Taramani, Chennai 600 113, Tamil Nadu, India

P. Ballett, S. Pascoli
Institute for Particle Physics Phenomenology, Department of Physics, University of Durham, Science Laboratories, South Rd, Durham, DH1 3LE, UK

A. Bross, S. Geer, C. Johnstone, J. Kopp, N. Mokhov, J. Morfin, D. Neuffer, S. Parke, M. Popovic, J. Strait, S. Striganov
Fermilab, P.O. Box 500, Batavia, IL 60510-5011, USA

A. Blondel, F. Dufour
University de Geneve, 24, Quai Ernest-Ansermet, 1211 Geneva 4, Suisse

A. Laing, F.J.P. Soler
School of Physics and Astronomy, Kelvin Building, University of Glasgow, Glasgow G12 8QQ, Scotland, UK

M. Lindner, T. Schwetz
Max Planck Institut für Kernphysik, PO Box 103980, 69029 Heidelberg, Germany

A. Alekou, M. Apollonio, M. Aslaninejad, C. Bontoiu, P. Dornan, R. Eccleston, A. Kurup, K. Long, J. Pasternak, J. Pozimski
Physics Department, Blackett Laboratory, Imperial College London, Exhibition Road, London, SW7 2AZ, UK

A. Bogacz, V. Morozov, Y. Roblin
Thomas Jefferson National Laboratory, 12000 Jefferson Avenue, Newport News, VA 23606, USA

S. Bhattacharya, D. Majumdar
Saha Institute of Nuclear Physics, Sector-I, Block-AF, Bidhannagar, Kolkata 700064, India

Y. Mori, T. Planche²
Kyoto University, Research Reactor Institute, 2,Asashiro-Nishi, Kumatori-cho, Sennan-gun, Osaka 590-0494 Japan

M. Zisman
Lawrence Berkeley National Laboratory, 1 Cyclotron Road, Berkeley, CA 94720, USA

D. Cline, D. Stratakis, X. Ding
Department of Physics and Astronomy, University of California, Los Angeles, CA 90095, USA

P. Coloma, A. Donini³, B. Gavela, J. Lopez Pavon, M. Maltoni
Universidad Autonoma de Madrid and Instituto de Fisica Teorica, UAM/CSIC, Cantoblanco, E-28049, Madrid, Spain;

C. Bromberg
Michigan State University, 150 Administration Building, East Lansing, Michigan 48824, USA

¹Now at Westpac Institutional Bank, Sydney, NSW, Australia

²Now at TRIUMF, 4004 Wesbrook Mall, Vancouver, B.C., V6T 2A3, Canada

³Also at Universidad de Valencia and Instituto de Fisica Corpuscular, UV/CSIC, Apart. 22085, E-46071, Valencia, Spain

M. Bonesini

Sezione INFN Milano Bicocca, Dipartimento di Fisica G. Occhialini, Piazza Scienza 3, 20126 Milano, Italy

T. Hart

The University of Mississippi, Department of Physics and Astronomy, 108 Lewis Hall, PO Box 1848, Oxford, Mississippi 38677-1848, USA

Y. Kudenko

Institute for Nuclear Research of Russian Academy of Sciences, 7a, 60th October Anniversary prospect, Moscow 117312, Russia

N. Mondal

Tata Institute of Fundamental Research, School of Natural Sciences, Homi Bhabha Rd., Mumbai 400005, India

S. Antusch, M. Blennow, T. Ota

Max Planck Institut für Physik, Werner Heisenberg Institut für Physik, Fohringer Ring 6, D-80805 Munich, Germany

R.J. Abrams, C.M. Ankenbrandt, K.B. Beard, M.A.C. Cummings, G. Flanagan, R.P. Johnson, T.J. Roberts, C.Y. Yoshikawa

Muons Inc., 552 N. Batavia Avenue, Batavia, IL 60510, USA

P. Migliozzi, V. Palladino

Universita di Napoli Federico II, Dipartimento di Scienze Fisiche, Complesso Universitario di Monte S. Angelo, via Cintia, I-80126 Napoli, Italy

A. de Gouvea

Northwestern University, Dept. of Physics and Astronomy, 2145 Sheridan Road, Evanston, Illinois 60208-3112 USA

P. Snopok

Illinois Institute of Technology, 3101 S Dearborn St, Chicago, IL 60616, USA

V.B. Graves

Oak Ridge National Laboratory, P.O. Box 2008, Oak Ridge, TN 37831, USA

Y. Kuno

Osaka University, Graduate School, School of Science, 1-1 Machikaneyama-cho, Toyonaka, Osaka 560-0043, Japan

J. Peltoniemi

Puulinnankatu 12 F 50, FI-90570 Oulu, Finland

V. Blackmore, J. Cobb, C. Tunnell, H. Witte

Particle Physics Department, The Denys Wilkinson Building, Keble Road, Oxford, OX1 3RH, UK

M. Mezzetto, S. Rigolin

Dipartimento di Fisica, Universita di Padova and INFN Padova, Via Marzolo 8, I-35131, Padova, Italy

K.T. McDonald

Princeton University, Princeton, NJ, 08544, USA

L. Coney, G. Hanson

Department of Physics and Astronomy, University of California, Riverside, CA 92521, USA

L. Tortora

Sezione INFN Roma Tre, Dipartimento di Fisica E. Amaldi, Via della Vasca Navale 84, 00146 Roma, Italy

C. Andreopoulos, J.R.J. Bennett, S. Brooks, O. Caretta, T. Davenne, C. Densham, R. Edgecock⁴, D. Kelliher, P. Loveridge, A. McFarland, S. Machida, C. Prior, G. Rees, C. Rogers, J.W.G. Thomason

STFC Rutherford Appleton Laboratory, Chilton, Didcot, Oxfordshire, OX11 0QX, UK

⁴also at University of Huddersfield, Queensgate, Huddersfield, HD1 3DH, UK

C. Booth, G. Skoro

University of Sheffield, Dept. of Physics and Astronomy, Hicks Bldg., Sheffield S3 7RH, UK

Y. Karadzhov⁵, R. Matev, R. Tsenov

Department of Atomic Physics, St. Kliment Ohridski University of Sofia, 5 James Bourchier Boulevard, BG-1164 Sofia, Bulgaria

R. Samulyak

Physics and Astronomy Department, Stony Brook University, Stony Brook, NY 11794-3800, USA

S.R. Mishra, R. Petti

Department of Physics and Astronomy, University of South Carolina, Columbia SC 29208, USA

M. Dracos

IPHC, Université de Strasbourg, CNRS/IN2P3, F-67037 Strasbourg, France

O. Yasuda

Department of Physics, Toyko Metropolitan University, 1-1 Minami-Osawa, Hachioji-shi, Toyko, Japan 192-0397

S.K. Agarwalla, A. Cervera-Villanueva, J.J. Gomez-Cadenas, P. Hernandez, T. Li, J. Martin-Albo

Instituto de Fisica Corpuscular (IFIC), Centro Mixto CSIC-UVEG, Edificio Investigacion Paterna, Apartado 22085, 46071 Valencia, Spain

P. Huber

Virginia Polytechnic Inst. and State Univ., Physics Dept., Blacksburg, VA 24061-0435

J. Back, G. Barker, P. Harrison

Department of Physics, University of Warwick, Coventry, CV4 7AL, UK

D. Meloni, J. Tang, W. Winter

Fakultät für Physik und Astronomie, Am Hubland, 97074 Würzburg, Germany

⁵Now at the University of Geneva, Geneva, Switzerland

Contents

1	Introduction	1
2	Physics at the Neutrino Factory	5
2.1	The physics case for advanced neutrino experiments	5
2.2	Global fit to neutrino oscillation data	9
2.3	The baseline configuration	15
2.4	Comparison with the physics performance of alternative experiments	17
3	The Neutrino Factory Accelerator Complex	23
3.1	Proton Driver	24
3.2	Proton driver	24
3.3	Target	26
3.4	Front End	28
3.5	Acceleration	37
3.6	Decay Ring	44
4	Detector systems for the Neutrino Factory	50
4.1	Introduction	50
4.2	Far Detectors	52
4.3	Near detectors	82
5	Conclusions	114
A	Incremental Development of a 10 GeV Neutrino Factory	133
A.1	Neutrino Factory baseline	133
A.2	Staging Schemes	133
A.3	Rate Staging	133
A.4	Physics Reach of a Staged Facility	139
B	Conclusion	139
C	PPEG appendices	141
D	The Muon Front End	142
D.1	Decay Region	142
D.2	Particle Selection System	142
D.3	Chicane Energy Deposition Studies	143
D.4	Modifications to the RF capture system	147
D.5	Ionisation Cooling Channel	150
D.6	Summary	150
E	Front End Engineering	153
E.1	Buncher and Phase Rotation	153
E.2	Cooling	156

F	Acceleration Lattice Details	158
F.1	Overall Lattice Description	158
F.2	Pre-linac	158
F.3	RLA I	163
F.4	RLA II	166
F.5	Double Arc Chicane	169
G	Acceleration Engineering	171
G.1	Pre-LINAC	172
G.2	Recirculating Linear Accelerator 1	177
H	Decay Ring Lattice Details	184
H.1	Injection	184
H.2	Dynamic aperture	186
I	FNAL Proton Driver Annex	187
J	Detector working group appendices	194
J.1	Far Detector Migration Matrices	194
J.2	Near Detector Migration Matrices	219
K	Cost estimate	224

1 Introduction

The properties of the neutrino make it a unique tool for the study of fundamental physics. Alone among the fundamental fermions, the neutrino has no electric charge and interacts solely via the weak force. In the Universe of today, the abundance of neutrinos is second only to that of photons. The weakness of its interactions with matter allows the neutrino to travel great distances through the Universe, thereby allowing it to play an important role in the evolution of the cosmos. Furthermore, the mass of the neutrino is tiny compared to the mass of all the other fundamental fermions. Without electric charge to distinguish a neutrino (ν) from an anti-neutrino ($\bar{\nu}$), the neutrino may be indistinguishable from its own anti-particle, i.e. the neutrino may be “Majorana” fermion, a completely new state of matter. The observation of the decay of a nucleus to two electrons (or two positrons) without any accompanying neutrinos (neutrino-less double-beta, $0\nu 2\beta$, decay) would imply that the neutrino is Majorana in nature.

Historically, the study of neutrino interactions has been seminal in the development of the Standard Model (SM) of particle physics. The recent discovery that the flavour of a neutrino changes as it propagates through space and time, a phenomenon known as “neutrino oscillations”, provides the germ for the development of a deeper understanding of the physics of fundamental particles and the impact of the neutrino on the evolution of the Universe. However, the fact that neutrinos interact only weakly with matter means that novel techniques must be developed to provide data sets of the quality and size required to study the details of neutrino oscillation. The Neutrino Factory described in this report employs a novel accelerator complex to generate high-energy neutrino beams of uniquely well-defined flux and flavour composition from the decay of muons confined within a storage ring.

Neutrino oscillations may be described as the “beating” of the phase of neutrino-mass eigenstates in the propagation of a neutrino produced as an eigenstate of flavour. The three flavour eigenstates, ν_e , ν_μ , and ν_τ may be written as linear super-positions of the mass eigenstates, ν_1 , ν_2 , and ν_3 . To describe neutrino oscillations, the matrix by which the neutrino mass basis is rotated into the neutrino flavour basis is usually parameterised in terms of three mixing angles (θ_{12} , θ_{23} , and θ_{13}) and one phase parameter (δ) [1–4]. The measured values of the neutrino-mixing angles are large, much larger than those observed in the quark sector [5]. If δ is non-zero, the symmetry between the properties of matter and antimatter will be broken via the neutrino-mixing matrix. Measurements of neutrino oscillations are not sensitive to the neutrino masses themselves, but may be used to determine the mass-squared differences $\Delta m_{31}^2 = m_3^2 - m_1^2$ and $\Delta m_{21}^2 = m_2^2 - m_1^2$. The sign of Δm_{31}^2 determines the neutrino mass hierarchy; the “normal hierarchy” (NH) refers to the case in which the mass eigenstate ν_3 is heavier than the other two neutrinos while the case in which ν_3 is lighter than the other two is referred to as the “inverted hierarchy” (IH). While θ_{12} , θ_{13} , $|\theta_{23} - \frac{\pi}{2}|$, the magnitude of the mass-squared differences and the sign of Δm_{21}^2 have been determined, the sign of $(\theta_{23} - \frac{\pi}{2})$ and Δm_{31}^2 are unknown and the CP-violating phase, δ , is at present essentially unconstrained (see, for example, [6]).

The introduction of neutrino mass requires the SM to be extended. As a minimum, a right-handed neutrino state must be added to accompany the left-handed state of the Standard Model. The tiny neutrino mass, so different from that of the other fundamental fermions, hints that the mechanism responsible for neutrino mass is different to the Higgs mechanism by which the quarks and charged leptons acquire mass. To explain, rather than describe, neutrino oscillations requires a theory of the physics of flavour that accommodates the patterns in the observed properties of the fundamental fermions as well as the ways in which the properties of the neutrino differ from those of the quarks and charged leptons. Theories have been constructed in which the patterns observed within a generation are explained by assigning the fermions to a representation of a large symmetry group (Grand Unified Theories, GUTs) [7–10] and the patterns observed between or across generations are explained by assuming a “family symmetry” [11–13]. Such theories admit an explanation of the tiny neutrino mass and the large neutrino-mixing angles. The “see-saw mechanism”, arguably the most attractive scheme to

explain the tiny neutrino mass, requires the introduction of extremely heavy, Majorana neutrinos [14–17]. Such heavy Majorana neutrinos would not feel the weak force—i.e. they would be “sterile neutrinos” incapable of interacting directly with ordinary matter. Through the see-saw mechanism the properties of the neutrino may be related to physics at extremely large energy scales beyond the reach of present, or realistic future, energy-frontier accelerators. Moreover, in see-saw models, if the heavy Majorana neutrinos are abundant in the early Universe and if the heavy neutrinos decay preferentially to matter fermions, then the lepton-number asymmetry generated in the heavy-neutrino decay would be converted into a baryon asymmetry during the electroweak era. Detailed and precise measurements of the properties of the neutrino are essential for the fascinating particle-physics and cosmological phenomena outline above to be elucidated.

Such a breadth of impact justifies a robust, far-reaching experimental programme. The search for sterile neutrinos, the determination of the nature of the neutrino, Majorana or Dirac, and the determination of the absolute neutrino mass are important parts of this programme. Equally important is the determination of the parameters that govern neutrino oscillations. First, the scientific imperative is to complete the Standard Neutrino Model (the $S\nu M$) by determining the sign of $(\theta_{23} - \frac{\pi}{2})$ and Δm_{31}^2 and searching for CP-invariance violation by measuring δ . Then, precise measurements of the oscillation parameters are required to over-constrain the $S\nu M$. Such measurements will either establish the $S\nu M$ as the correct description of nature, or, by establishing parameter sets inconsistent with it, point to the existence of entirely new phenomena. The ultimate theory must surely unify the description of quarks and leptons. Many such theories have been proposed. To put them to the test requires measurements of the neutrino-mixing parameters with an uncertainty that matches the precision with which the quark mixing parameters are known. The incremental implementation of the Neutrino Factory described in this report is capable of making the exquisitely sensitive searches needed to establish the $S\nu M$ and of making neutrino-oscillation measurements with the precision necessary to test relationships between the quark and lepton mixing parameters that arise in theories that purport to explain the physics of flavour (see, for example, [18? , 19]).

A schematic diagram of the IDS-NF baseline for the Neutrino Factory accelerator facility is shown in the left panel of figure 1. The process of creating the muon beam begins with the bombardment of a pion-production target with a pulsed proton beam. Pions, both positive and negative, are captured and transported in a solenoid-focusing channel in which they decay to produce the muon beam. A sequence of accelerators is then used to manipulate and reduce (cool) the muon-beam phase space and to accelerate to the muons to their final energy. These accelerators are designed to handle both positive and negative muons at the same time. The short muon lifetime has required novel techniques to be developed to carry out these steps. Ionisation cooling, the technique by which it is proposed to cool the muon beam, involves passing the beam through a material in which it loses energy through ionisation and then re-accelerating the beam in the longitudinal direction to replace the lost energy. Muon acceleration to 10 GeV will be carried out in a series of superconducting linear and re-circulating linear accelerators

The muon storage ring is arranged such that the long straight sections point at a single far detector sited at a distance of between 1 500 km and 2 500 km from the source. The source-detector distance (L) and the stored-muon energy (E_μ) have been chosen such that the neutrino-energy (E_ν) spectrum is well matched to the performance of the Magnetised Iron Neutrino Detector (MIND) [20–22] (see the right panel of figure 1). The IDS-NF baseline calls for a 100 kT MIND and a suite of near detectors to measure the unoscillated neutrino flux, to study in detail neutrino-nucleus scattering and to search for non-standard interactions. The key parameters that specify the IDS-NF baseline facility are listed in table 1.

Figure 2 shows the performance of the IDS-NF baseline facility. The ordinate shows the fraction of all possible values of δ for which a particular uncertainty on δ ($\Delta\delta$, shown on the abscissa) can be achieved after 10 years of running. The facility is able to deliver a measurement of δ with a precision comparable to that with which the CKM phase is known. The figure also shows the effect of running for 10 years with a variety of

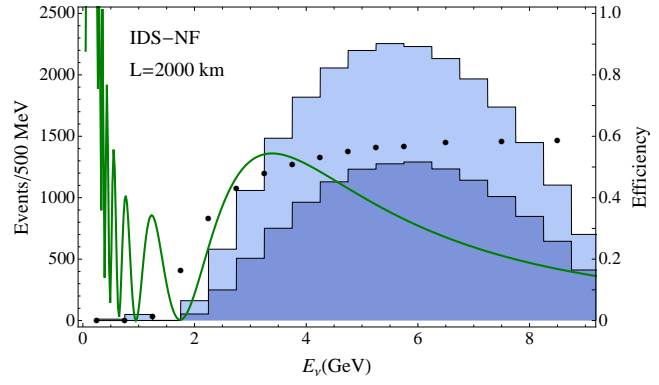
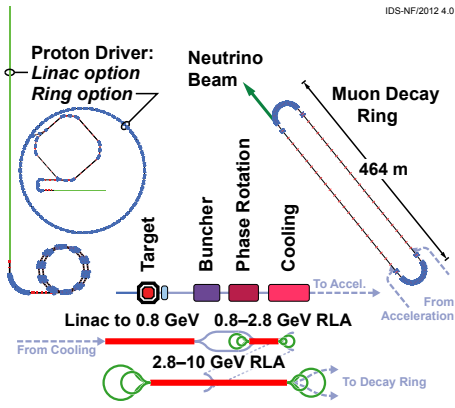


Figure 1: Left panel: Schematic diagram of the IDS-NF baseline Neutrino Factory accelerator facility. The function of the principal systems are outlined in the text and described in detail in section 3. Right panel: The green solid line shows the probability for the transition $\nu_e \rightarrow \nu_\mu$ as a function of neutrino energy (E_ν) for a baseline of 2000 km and taking $\sin^2 2\theta_{13} = 0.1$; $\theta_{23} = 45^\circ$; $\delta = 0$; and $\Delta m_{31}^2 = (2.45 \times 10^{-3}) \text{ eV}^2$. The light shaded histogram shows the event rate that would be recorded in the MIND detector described in section 4 if the efficiency were 100% for all E_ν . The dark shaded histogram shows the event rate if the simulated efficiency (shown as the solid black dots) is taken into account. spectrum:

“descope” facilities in which the product of neutrino flux and far-detector mass is decreased by factors of 10 and 40. The excellent performance of the full IDS-NF baseline can be approached in a set of incremental steps; each step having a unique and first-rate scientific programme and each step being capable of serving the R&D programme required to deliver the next.

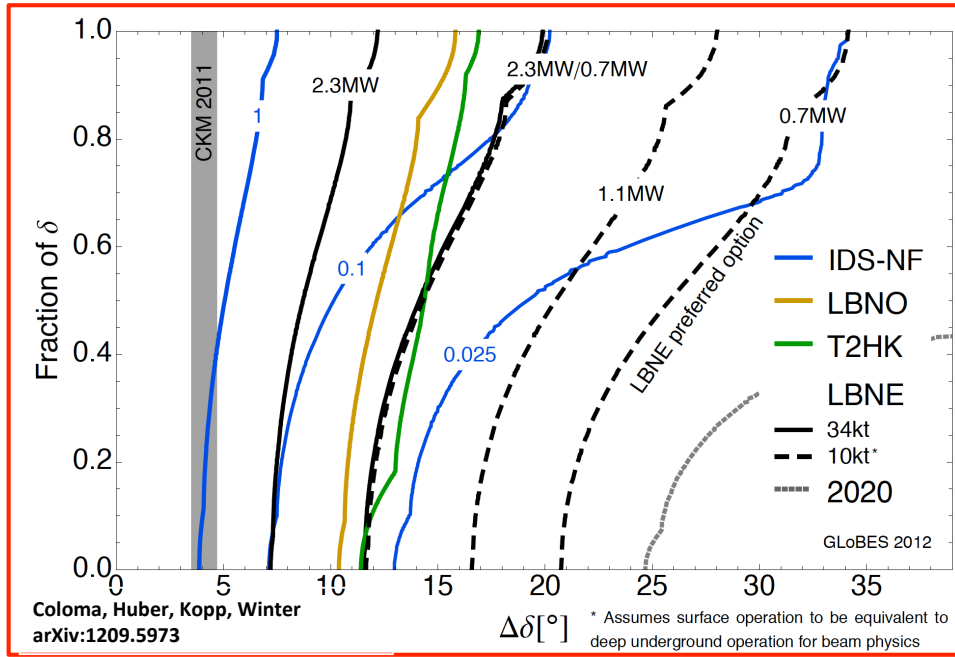


Figure 2: Precision with which δ can be measured at the Neutrino Factory. The fraction of all values of δ for which a certain precision ($\Delta\delta$) can be reached is shown for the IDS-NF baseline Neutrino Factory facility by the blue solid line. The dashed and dash dotted lines show the precision with which δ can be measured for a descoped facility in which the product of neutrino flux and detector mass has been reduced by a factor of 10 and 40 respectively.

Table 1: Parameters characterising the IDS-NF baseline Neutrino Factory facility. The number muon decays per year includes both positive- and negative-muon decays. The symbol γ is the relativistic γ of the muons confined within the storage ring.

	Value
Accelerator facility	
Muon total energy	10 GeV
Production straight muon decays in 10^7 s	10^{21}
Maximum RMS angular divergence of muons in production straight	$0.1/\gamma$
Neutrino Detectors	
Distance to long-baseline neutrino detector	1 500–2 500 km
Long-baseline Magnetised Iron Detector (MIND)	100 kT
Near detectors, magnetised, high-resolution spectrometers	2

2 Physics at the Neutrino Factory

2.1 The physics case for advanced neutrino experiments

The unambiguous observation of neutrino oscillations is arguably the most significant development in particle physics of the past two decades [23]. It revealed, beyond reasonable doubt, that neutrinos have mass and that leptons mix. Neutrino masses are not accounted for in the Standard Model of particle physics. It is not hard to modify the Standard Model Lagrangian to accommodate neutrino masses [24]. Indeed, one can write down several different “Standard Neutrino Model” ($S\nu M$) Lagrangians that render neutrinos massive that are consistent with the available data. The candidates for the $S\nu M$ introduce various new degrees of freedom at a variety of energy scales (from below the electron-Volt scale all the way to the Grand Unification scale). Part of the mission of particle-physics experiments in the next few decades will be to elucidate the mechanism by which neutrino mass is generated. The next generation of neutrino experiments will represent a moderate extension of existing techniques. This makes them technologically attractive, since the technical risks are relatively low, but also limits their physics sensitivity. To exploit to the full the discoveries made to date in neutrino physics, advanced neutrino experiments, based on novel technologies, are required. The Neutrino Factory is the ultimate advanced neutrino oscillation facility. In this section, the scientific case for advanced neutrino oscillation experiments in general and of the Neutrino Factory in particular is reviewed.

While the mechanism behind neutrino-mass generation remains unknown, a very successful phenomenological description exists. It considers the existence of three massive neutrinos ν_1, ν_2 , and ν_3 with masses m_1, m_2 , and m_3 , respectively. These mass eigenstates are linear combinations of the “active” neutrino flavours, ν_e, ν_μ , and ν_τ , labelled according to the way they interact with the W -boson and the charged-leptons, e, μ , and τ . One can pick a weak-basis in which neutrinos with a well-defined flavour are related to neutrinos with a well-defined mass via the unitary lepton mixing matrix U : $\nu_\alpha = U_{\alpha i} \nu_i$ ($\alpha = e, \mu, \tau, i = 1, 2, 3$). It is customary to define the neutrino masses as follows: $m_1 < m_2$ while m_3 is either the heaviest or the lightest neutrino. To identify m_3 , $|m_3^2 - m_1^2|$ and $|m_3^2 - m_2^2|$ are evaluated and the smaller combination is chosen such that it is larger than $m_2^2 - m_1^2$. With the masses labelled in this way, $m_3 > m_2$ if $m_3^2 - m_1^2$ is positive and $m_3 < m_1$ if $m_3^2 - m_1^2$ is negative. Note that $\Delta m_{21}^2 = m_2^2 - m_1^2$ is a positive-definite quantity, while $\Delta m_{31}^2 = m_3^2 - m_1^2$ is allowed to have either sign. It is also customary to refer to the spectrum $m_3 > m_2 > m_1$ as “normal”, in which case $\Delta m_{31}^2 > 0$, while the $m_2 > m_1 > m_3$ spectrum is referred to as “inverted,” in which case $\Delta m_{31}^2 < 0$. Once the neutrino mass eigenstates are properly defined, it is also customary to parametrise U as prescribed in the Particle Data Book [25]. The neutrino mixing angles (θ_{ij}) are related to the mixing-matrix elements by:

$$\frac{|U_{e2}|^2}{|U_{e1}|^2} \equiv \tan^2 \theta_{12}; \quad \frac{|U_{\mu 3}|^2}{|U_{\tau 3}|^2} \equiv \tan^2 \theta_{23}; \quad \text{and} \quad U_{e3} \equiv \sin \theta_{13} e^{-i\delta}; \quad (1)$$

where δ is the CP-odd, “Dirac”, phase. Two other CP-odd phases might be required to complete the parametrisation of U if the neutrinos are Majorana fermions. However, these “Majorana” phases can not be observed in neutrino oscillations and will henceforth be ignored. Neutrino-oscillation data are sensitive to the neutrino mass-squared differences, the values of the mixing angles $\theta_{12}, \theta_{13}, \theta_{23}$, and δ . The experimental results can be succinctly and accurately described by the oscillation of three active neutrinos. For the mass splitting we reach errors of a few percent; however, for all of the mixing angles and the CP phase the errors are in the 10-30% range, see *e.g.* Ref. [26]. Therefore, while three-flavor oscillation is able to describe a wide variety of experiments, it would seem premature to claim that we have entered the era of precision neutrino physics or that we have established the three-flavor paradigm at a high level of accuracy. This is also borne out by the fact that there are significant hints at short baselines for a fourth neutrino [27]. Also, more general, so-called non-standard interactions are not well constrained by neutrino data; for a recent review on the topic see Ref. [28].

Two of the three mixing angles are large, in stark contrast to the quark-mixing matrix, in which all mixing parameters are either small ($\sin \theta_c \sim 0.23$, where θ_c is the Cabibbo angle) or very small ($|V_{ub}| \sim 0.004$). In the neutrino sector, three parameters remain unknown or only poorly constrained: the sign of Δm_{31}^2 ; δ . At the time of the writing of the interim design report θ_{13} was still unknown, now it has been determined to be large and has been measured to within 10% in $\sin^2 \theta_{13}$ [29–31]. This gives existing experiments like T2K [32] and No ν a [33] a chance to determine, in combination, the mass hierarchy. Also new, dedicated experiments like PINGU [34] using atmospheric neutrinos or Daya Bay II [35] using neutrinos from a reactor have a high likelihood to measure the mass hierarchy on a 5-10 year timescale. On somewhat longer timescale LBNE [36] is certain to measure the mass hierarchy. It is also expected that the precision with which $|\Delta m_{31}^2|$ and $\sin^2 2\theta_{23}$ are known will improve significantly. Even under these conditions, it is widely anticipated that by the end of the current decade we shall have no information regarding whether CP-invariance is violated in neutrino interactions ($\delta \neq 0, \pi$).

To complete our knowledge of the parameters that describe neutrino oscillations, the goals of advanced experiments must be:

- To search for CP-invariance violation in neutrino oscillations by seeking to measure the CP-odd phase δ ;
- To establish whether the neutrino-mass spectrum is normal or inverted by determining the sign of Δm_{31}^2 ;
- To measure as precisely as possible all the oscillation parameters.

The search for CP-invariance violation in neutrino oscillations provides a unique opportunity to further our understanding of CP-invariance. Experiments have demonstrated that the CP-odd phase of the quark mixing matrix, δ_{CKM} , controls all CP-invariance violation in the quark sector. The past generation of neutrino-oscillation experiments has revealed that there is at least one more CP-violating parameter in the lepton mixing matrix, δ . In practise, δ can only be observed in neutrino oscillation experiments and an advanced neutrino experiment is required to explore this new window into CP-invariance violation.

Once one realizes that the current error bars are uncomfortably large, the next question is: how well do we want/need to determine the various mixing parameters? The answer can be given at two distinct levels. One is a purely technical one – if I want know X to a precision of x , I need to know Y with a precision of y ; an example is, where Y is given by θ_{13} and X could be the mass hierarchy. The answer, at another level, is driven by theory expectations of how large possible phenomenological deviations from the three-flavor framework could be. In order to address the technical part of the question, one first has to define the target precision from a physics point of view. Guidance from other subareas of particle physics reveal that the “target precision” evolves over time. For example, history shows that theoretical estimates of the top quark mass from electroweak precision data and other indirect observable, before its eventual discovery, seem to have been, for the most part (and with very large uncertainties), only several GeV ahead of the experimental reach – at the time, there always was a valid physics argument for why the top quark is “just around the corner.” A similar “evolution” of theoretical expectations can be observed in, for example, searches for new phenomena in quark flavor physics. Thus, any argument based on model-building-inspired target precisions is always of a preliminary nature, as our understanding of models evolves over time. With this caveat in mind, one argument for a target precision can be based on a comparison to the quark sector. Based on a theoretical guidance from Grand Unification, one would expect that the answer to the flavor question should find a concurrent answer for leptons and quarks. Therefore, a test of such a models is most sensitive if the precision in the lepton and quark sector is comparable. For instance, the CKM angle γ , which is a very close analog of δ in the neutrino sector, is determined to $(70.4_{-4.4}^{+4.3})^\circ$ [37] and thus, a precision target for δ of roughly 5° would follow.

A different argument for a similar level of precision can be made based on the concept of so-called neutrino sum-rules [38]. Neutrino sum-rules arise, for example, in models where the neutrino mixing matrix has a certain simple form or texture at a high energy scale and the actual low-energy mixing parameters are modified by a non-diagonal charged lepton mass matrix. The simplicity of the neutrino mixing matrix is typically a result of a

flavor symmetry, where the overall Lagrangian possesses an overall flavor symmetry G , which can be separated into two sub-groups G_ν and G_l for the neutrinos and charged leptons; it is the mismatch between G_ν and G_l which will yield the observed mixing pattern, see e.g. [11]. Typical candidates for G are given by discrete subgroups of $SU(3)$ which have a three dimensional representation, e.g., A_4 . In a model-building sense, these symmetries can be implemented using so-called flavon fields which undergo spontaneous symmetry breaking and it is this symmetry breaking which picks the specific realization of G , for a recent review see [13]. The idea of flavor symmetries is in stark contrast to the idea that neutrino mixing parameters are anarchic, *i.e.* random numbers with no underlying dynamics, for the most recent version of this argument, see Ref. [39]. To find out whether the patterns observed in lepton mixing correspond to an underlying symmetry is one of the prime tasks of neutrino physics. Of course, distinguishing among the many candidate underlying symmetries is also a very high priority.

In practice, flavor symmetries will lead to relations between measurable parameters, whereas anarchy will not. For example, if the neutrino mixing matrix is of tri-bi-maximal form, $|U_{e3}| = 0$ is naively expected to vanish, which is clearly in contradiction to observations. In this case, a non-diagonal charged lepton mass matrix can be used to generate the right value of $|U_{e3}|$, and, for one concrete model, the following sum-rule arises

$$\theta_{12} - \theta_{13} \cos \delta = \arcsin \frac{1}{\sqrt{3}}, \quad (2)$$

which can be tested if sufficiently precise measured values for the three parameters $\theta_{12}, \theta_{13}, \delta$ are available. Depending on the underlying symmetry of the neutrino mixing matrix different sum-rules are found. In Fig. 3 several examples are shown and for each case the values of θ_{13} and θ_{12} or θ_{23} are drawn many times from a Gaussian distribution where the mean values and ranges are taken from Ref. [26]. The resulting predictions of the value of the CP phase δ are histogrammed and shown as colored lines. The width of the distribution for each sum-rule arises from the finite experimental errors on θ_{12} or θ_{23} and θ_{13} . Two observations arise from this

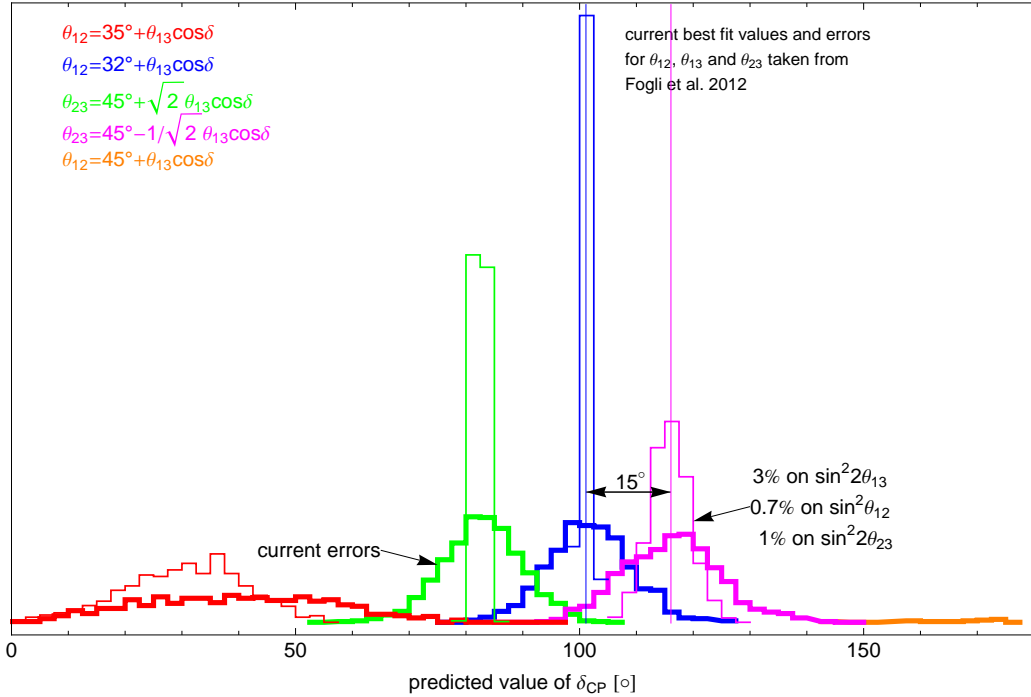


Figure 3: Shown are the distributions of predicted values from δ from various sum-rule as denoted in the legend and explained in the text.

simple comparison: first, the distance of the means of the distributions is as small as 15° , and second, the width of the distributions is significant compared to their separation and a reduction of input errors is mandated. The thin lines show the results if the errors are reduced to the value given in the plot, which would be achieved by Daya Bay for $\sin^2 2\theta_{13}$, by Daya Bay II for $\sin^2 \theta_{12}$, and by NOvA for $\sin^2 \theta_{23}$. Assuming that the errors on θ_{12} , θ_{23} and θ_{13} are reduced to this level, the limiting factor is the natural spread between models, which is about 15° . A 3σ distinction between models translates into a target precision for δ of 5° . A measurement at this precision would allow to obtain valuable information on whether indeed there is an underlying symmetry behind neutrino mixing. Moreover, it is likely to also provide hints regarding which specific class of symmetries is realized. This would constitute a major breakthrough in our understanding of flavor.

High-precision measurements of neutrino oscillations are required to test whether the origin of neutrino mass is also the origin of the baryon asymmetry of the Universe, through leptogenesis [40, 41]. Several indirect generic predictions of leptogenesis can be verified with neutrino experiments: neutrinos are expected to be Majorana fermions, and it is expected, quite generically, that neutrino oscillations violate CP-invariance, even if no model independent relation between “high-energy” and “low-energy” CP-invariance violation exists. Quantitative tests are all model dependent and will rely on very precise measurements in neutrino oscillations and elsewhere. For example, precise measurements of oscillation parameters could validate a specific flavour model, which allows one to relate “high-energy” and “low-energy” parameters. Furthermore, discoveries at collider experiments and searches for charged-lepton flavour violation may provide other hints that render leptogenesis either “very likely” or “most improbable” [42]. We are very far from testing leptogenesis conclusively, but precise measurements of all neutrino oscillation parameters – far beyond where we are now – are a *conditio sine qua non*.

Precision measurements of the oscillation parameters are also required to confirm or refute with confidence the current three-active-neutrino formalism. Ultimately, one aims not only at constraining the mixing-parameter space, but also at *over-constraining* it. Several important questions need to be addressed:

- Are there really only three light neutrinos and is U a unitary matrix?
- Are there other neutrino interactions? And,
- Is there only one source of CP-invariance violation in the neutrino sector?

While our understanding of the neutrino has increased tremendously over the past decade, we are far from providing a satisfactory answer to any of these questions. In this respect, our understanding of the lepton-flavour sector is far behind our understanding of the quark-flavour sector.

Some manifestations of new physics are best investigated with neutrino oscillation experiments. For example, the search for light sterile neutrinos which may be related to the origin of neutrino masses. Sterile neutrinos can be detected via the observation of new oscillation frequencies and mixing angles. Tests of the unitarity of the lepton-mixing matrix may also point to new “neutrino” degrees of freedom that are too heavy to be seen in oscillation experiments. Neither of these phenomena can be studied outside of neutrino oscillation experiments.

In many candidate new-physics scenarios, a combination of different experimental probes will be required in order to piece together a more fundamental description of how nature works at the smallest distance scales. In addition to studies of neutrino flavour-change, these include collider experiments (for example, the LHC and a next-generation lepton collider), searches for charged-lepton flavour violation in the muon and tau sectors, searches for the permanent electric dipole moments of fundamental particles, including the electron and the muon, searches for lepton-number violation, especially searches for neutrinoless double-beta decay, and direct and indirect searches for dark matter. In many new-physics scenarios, in particular when it comes to identifying the physics responsible for neutrino masses, advanced neutrino oscillation experiments are guaranteed to play a leading role.

Neutrino experiments have proved, over the past few decades, that our ability to predict what will be detected, and to identify what are the important questions, is limited at best. It is safe to state, however, that a Neutrino

Factory, combined with a multi-kTon detector at an underground facility, offers a unique and powerful tool for the study of fundamental physics. In order to prepare for the unexpected, it is vital that advanced set-ups be versatile and multifaceted. The Neutrino Factory fits the bill. In addition to providing the neutrino beams required for the definitive, precision neutrino-oscillation programme, the Neutrino Factory also provides an ideal environment in which to study a variety of other phenomena. The well-characterised neutrino beam from the muon storage ring allows a programme of extremely precise neutrino scattering measurements to be carried out at a near detector, including studies of neutrino flavour-change at very short baselines and precision measurements of neutrino scattering on nucleons [43] and electrons [44]. The latter allow for uniquely sensitive tests of the electroweak theory.

Activities not directly related to neutrino physics can also be addressed at a Neutrino Factory complex. The availability of a large number of muons allows one to consider new set-ups for searching for rare muon processes [45], especially $\mu \rightarrow e$ conversion in nuclei, and for measurements of the electroweak properties of the muon, including the muon electric and magnetic dipole moments. The availability of a large number of protons—used to make the muons for the storage ring—allows one to consider a suite of hadronic experiments including, for example, those required to study very rare kaon phenomena ($K \rightarrow \pi \bar{\nu} \nu$, $K \rightarrow \pi \mu^\pm e^\mp$, $K^+ \rightarrow \pi^- \ell^+ \ell'^+$, etc). At the opposite end of the neutrino beam, the very large detector complex also serves many purposes. Depending on the location and composition, very large detectors can be used to study naturally occurring neutrinos—especially the atmospheric neutrinos and, perhaps, neutrinos from Supernova explosions. Finally, the large instrumented volumes can be used for searching for proton decay. Indeed, the Kamiokande and IMB experiments were originally constructed to look for proton decay, stumbled upon atmospheric neutrino oscillations, and observed neutrinos produced in supernovæ along the way.

2.2 Global fit to neutrino oscillation data

2.2.1 Three-flavour analysis of global neutrino oscillation data

It is now an established fact that neutrinos are massive and leptonic flavors are not symmetries of Nature [46, 47]. In the last decade this picture has become fully proved thanks to the upcoming of a set of precise experiments. In particular, the results obtained with solar and atmospheric neutrinos [48, 49] have been confirmed in experiments using terrestrial beams: neutrinos produced in nuclear reactors and accelerators facilities have been detected at distances of the order of hundreds of kilometers [50, 51]. The minimum joint description of all these data requires mixing among all the three known neutrinos (ν_e , ν_μ , ν_τ), which can be expressed as quantum superpositions of three massive states ν_i ($i = 1, 2, 3$) with masses m_i . This implies the presence of a leptonic mixing matrix in the weak charged current interactions [3, 52] which can be parametrized as:

$$U = \begin{pmatrix} c_{12}c_{13} & s_{12}c_{13} & s_{13}e^{-i\delta_{\text{CP}}} \\ -s_{12}c_{23} - c_{12}s_{13}s_{23}e^{i\delta_{\text{CP}}} & c_{12}c_{23} - s_{12}s_{13}s_{23}e^{i\delta_{\text{CP}}} & c_{13}s_{23} \\ s_{12}s_{23} - c_{12}s_{13}c_{23}e^{i\delta_{\text{CP}}} & -c_{12}s_{23} - s_{12}s_{13}c_{23}e^{i\delta_{\text{CP}}} & c_{13}c_{23} \end{pmatrix}, \quad (3)$$

where $c_{ij} \equiv \cos \theta_{ij}$ and $s_{ij} \equiv \sin \theta_{ij}$. Given the observed hierarchy between the solar and atmospheric mass-squared splittings there are two possible non-equivalent orderings for the mass eigenvalues, which are conventionally chosen as $\Delta m_{21}^2 \ll (\Delta m_{32}^2 \simeq \Delta m_{31}^2 > 0)$ (normal ordering, NO) or $\Delta m_{21}^2 \ll -(\Delta m_{31}^2 \simeq \Delta m_{32}^2 < 0)$ (inverted ordering, IO), with $\Delta m_{ij}^2 \equiv m_i^2 - m_j^2$. In this form they correspond to the two possible choices of the sign of Δm_{31}^2 .⁶ In this convention the angles θ_{ij} can be taken without loss of generality to lie in the first quadrant, $\theta_{ij} \in [0, \pi/2]$, and the CP phase $\delta_{\text{CP}} \in [0, 2\pi]$.

⁶In the following we adopt the (arbitrary) convention of reporting results for Δm_{31}^2 for NO and Δm_{32}^2 for IO, *i.e.*, we always use the one which has the larger absolute value.

Table 2: Three-flavour oscillation parameters from a fit to global data [6, 56]. For “Free Fluxes + RSBL” reactor fluxes have been left free in the fit and short baseline reactor data (RSBL) with $L \lesssim 100$ m are included; for “Huber Fluxes, no RSBL” the flux prediction from [57] are adopted and RSBL data are not used in the fit.

NuFIT 1.1 (2013)				
	Free Fluxes + RSBL		Huber Fluxes, no RSBL	
	bf μ $\pm 1\sigma$	3σ range	bf μ $\pm 1\sigma$	3σ range
$\sin^2 \theta_{12}$	$0.306^{+0.012}_{-0.012}$	$0.271 \rightarrow 0.346$	$0.313^{+0.013}_{-0.012}$	$0.277 \rightarrow 0.355$
$\theta_{12}/^\circ$	$33.57^{+0.77}_{-0.75}$	$31.38 \rightarrow 36.01$	$34.03^{+0.81}_{-0.77}$	$31.78 \rightarrow 36.56$
$\sin^2 \theta_{23}$	$0.437^{+0.061}_{-0.031}$	$0.357 \rightarrow 0.654$	$0.436^{+0.047}_{-0.032}$	$0.356 \rightarrow 0.653$
$\theta_{23}/^\circ$	$41.4^{+3.5}_{-1.8}$	$36.7 \rightarrow 54.0$	$41.3^{+2.7}_{-1.8}$	$36.6 \rightarrow 53.9$
$\sin^2 \theta_{13}$	$0.0231^{+0.0023}_{-0.0022}$	$0.0161 \rightarrow 0.0299$	$0.0252^{+0.0022}_{-0.0023}$	$0.0181 \rightarrow 0.0320$
$\theta_{13}/^\circ$	$8.75^{+0.42}_{-0.44}$	$7.29 \rightarrow 9.96$	$9.13^{+0.40}_{-0.42}$	$7.73 \rightarrow 10.31$
$\delta_{CP}/^\circ$	341^{+58}_{-46}	$0 \rightarrow 360$	345^{+77}_{-46}	$0 \rightarrow 360$
$\frac{\Delta m_{21}^2}{10^{-5} \text{ eV}^2}$	$7.45^{+0.19}_{-0.16}$	$6.98 \rightarrow 8.05$	$7.50^{+0.19}_{-0.17}$	$7.03 \rightarrow 8.08$
$\frac{\Delta m_{31}^2}{10^{-3} \text{ eV}^2}$ (N)	$+2.421^{+0.022}_{-0.023}$	$+2.248 \rightarrow +2.612$	$+2.429^{+0.029}_{-0.027}$	$+2.256 \rightarrow +2.635$
$\frac{\Delta m_{32}^2}{10^{-3} \text{ eV}^2}$ (I)	$-2.410^{+0.062}_{-0.063}$	$-2.603 \rightarrow -2.226$	$-2.422^{+0.061}_{-0.063}$	$-2.618 \rightarrow -2.239$

Within this context, Δm_{21}^2 , $|\Delta m_{31}^2|$, θ_{12} , and θ_{23} are relatively well determined, whereas until recently only an upper bound was derived for the mixing angle θ_{13} . This situation has dramatically changed with the data from the reactor experiments Daya Bay [31], Reno [30], and Double Chooz [53], which together with the increased statistics of long-baseline experiments T2K [54] and MINOS [55] have provided a clear determination of the last unknown mixing angle θ_{13} . With these results at hand a first-order picture of the three-flavour lepton mixing matrix has emerged. Its precise determination, as well as that of the mass differences, can only be made by statistically combining the results of the oscillation searches.

In this section the results of such an analysis [6] are presented, based on updated results NuFIT 1.1 as of spring 2013, available at [56] where also detailed references on the used data can be found. Alternative recent global fits have been presented in Refs. [26, 58]. The one-dimensional χ^2 -projections from the global analysis are shown in Fig. 4 for two choices of how uncertainties on the predicted reactor fluxes are treated, as described in the caption. The best fit values and the derived ranges for the six parameters at the 1σ (3σ) level are given in Tab. ???. For each parameter the ranges are obtained after marginalizing with respect to the other parameters. For Δm_{31}^2 (Δm_{32}^2) the allowed ranges are formed by two disconnected intervals which correspond to the two possible mass orderings. From these results we conclude that:

1. The present global analysis disfavors $\theta_{13} = 0$ with a $\Delta\chi^2 \approx 110$. This is mostly driven by the new reactor data from Daya Bay, Reno and Double Chooz. Now θ_{13} is the most precisely measured mixing angle (smallest absolute error).
2. An uncertainty on θ_{13} at the level of 1σ remains due to a tension between predicted reactor neutrino fluxes and data from reactor experiments with baselines less than 100 m. This tension in the data may be a manifestation of additional neutrino species as discussed in section 2.2.2.

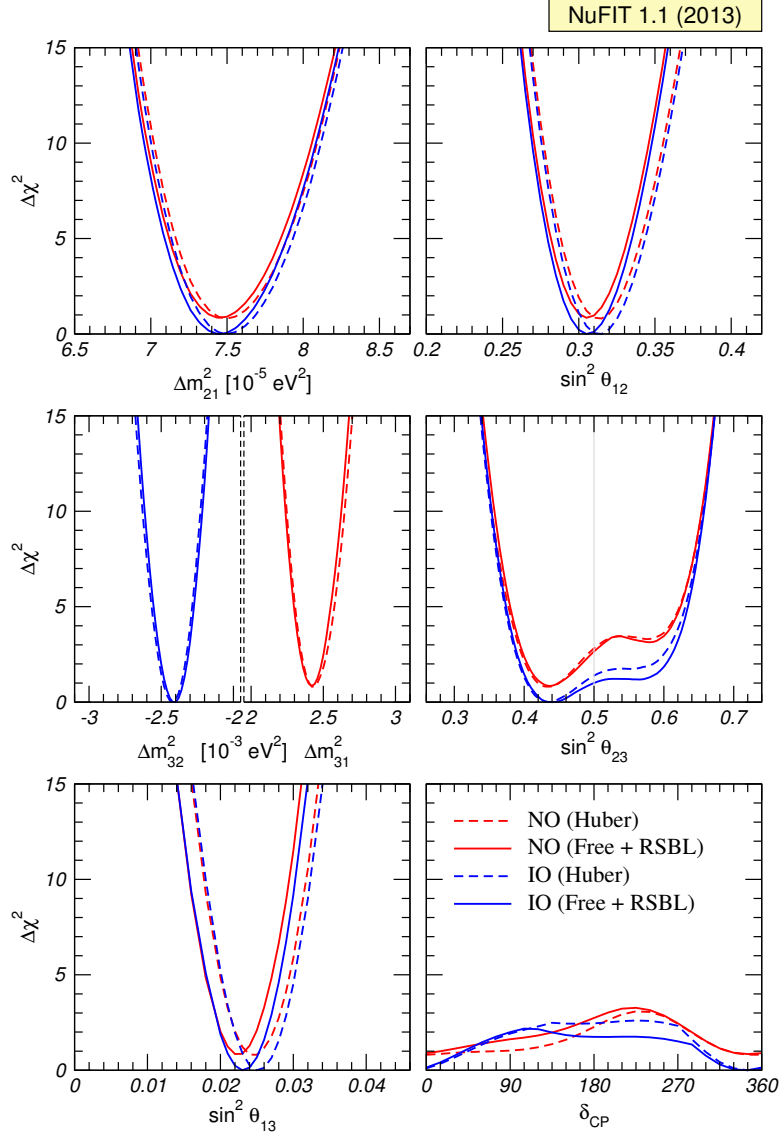


Figure 4: Global 3ν oscillation analysis [6, 56]. The red (blue) curves are for Normal (Inverted) Ordering. Results for different assumptions concerning the analysis of data from reactor experiments are shown: for solid curves the normalization of reactor fluxes is left free and data from short-baseline (less than 100 m) reactor experiments are included. For dashed curves short-baseline data are not included but reactor fluxes as predicted in [57] are assumed. Note that as atmospheric mass-squared splitting we use Δm_{31}^2 for NO and Δm_{32}^2 for IO.

3. The χ^2 shape as a function of $\sin^2 \theta_{23}$ is rather non-Gaussian. Non-maximal θ_{23} is favoured at the level of $\sim 1.5\sigma$ ($\sim 1\sigma$) for Normal (Inverted) ordering. This hint is driven by MINOS ν_μ disappearance data [59]. A minor role is played by atmospheric data, see [6] for a discussion.
4. The statistical significance of the preference of the fit for the first octant of θ_{23} is $\leq 1.5\sigma$ ($\leq 1\sigma$) for Normal (Inverted) ordering.⁷
5. Irrespective of the reactor fluxes, the absolute best-fit occurs for Inverted ordering. However, this result is not significant, since Normal ordering is consistent with the best fit point within 1σ ($\Delta\chi^2 \approx 1$).
6. The statistical significance of the effects associated with δ_{CP} is $\leq 1.4\sigma$ irrespective of the mass ordering.

2.2.2 Indications for sterile neutrinos at the eV-scale

Besides the huge success of 3-flavour oscillations described in section 2.2.1 there are some experimental “anomalies” which cannot be explained within the three-flavor framework and which might point towards the existence of additional neutrino flavors (so-called sterile neutrinos) with masses at the eV scale: (i) The LSND experiment [60] reports evidence for $\bar{\nu}_\mu \rightarrow \bar{\nu}_e$ transitions with $E/L \sim 1 \text{ eV}^2$, where E and L are the neutrino energy and the distance between source and detector, respectively. (ii) This effect is also searched for by the MiniBooNE experiment [61], which reports a yet unexplained event excess in the low-energy region of the electron neutrino and anti-neutrino event spectra. No significant excess is found at higher neutrino energies. Interpreting the data in terms of oscillations, parameter values consistent with the ones from LSND are obtained. (iii) Radioactive source experiments at the Gallium solar neutrino experiments SAGE and GALLEX have obtained an event rate which is somewhat lower than expected. This effect can be explained by the hypothesis of ν_e disappearance due to oscillations with $\Delta m^2 \gtrsim 1 \text{ eV}^2$ (“Gallium anomaly”) [62, 63]. (iv) A recent re-evaluation of the neutrino flux emitted by nuclear reactors [57, 64] has led to somewhat increased fluxes compared to previous calculations [65–68]. Based on the new flux calculation, the results of previous short-baseline ($L \lesssim 100 \text{ m}$) reactor experiments are in tension with the prediction, a result which can be explained by assuming $\bar{\nu}_e$ disappearance due to oscillations with $\Delta m^2 \sim 1 \text{ eV}^2$ (“reactor anomaly”) [69].

Here we report the results of a recent global analysis [70] of those data under the hypothesis of additional neutrino species at the eV scale. Alternative sterile neutrino fits can be found in Refs. [71, 72]. First we introduce one additional neutrino state, ν_4 , with a mass-squared difference Δm_{41}^2 much larger than $|\Delta m_{31}^2|$. This situation is called “3+1 mass scheme”. In this case the oscillation probabilities for experiments exploring the range $E/L \sim 1 \text{ eV}^2$ are rather simple:

$$P_{\alpha\alpha} = 1 - \sin^2 2\theta_{\alpha\alpha} \sin^2 \Delta, \quad P_{\mu e} = \sin^2 2\theta_{\mu e} \sin^2 \Delta, \quad (4)$$

where $\Delta \equiv \Delta m_{41}^2 L/4E$ and the effective mixing angles are defined as

$$\sin^2 2\theta_{\alpha\alpha} \equiv 4|U_{\alpha 4}|^2(1 - |U_{\alpha 4}|^2), \quad \sin^2 2\theta_{\mu e} \equiv 4|U_{\mu 4}|^2|U_{e 4}|^2, \quad (5)$$

with $\alpha = e, \mu$ and $U_{\alpha 4}$ are the elements of the lepton mixing matrix describing the mixing of the 4th neutrino mass state with the electron and muon flavour. There is no CP violation in 3+1 SBL oscillations and those relations apply for neutrinos as well as antineutrinos. Neglecting quadratic terms in the mixing matrix elements one has the following relation between the effective amplitudes relevant for appearance and disappearance probabilities:

$$4 \sin^2 2\theta_{\mu e} \approx \sin^2 2\theta_{ee} \sin^2 2\theta_{\mu\mu}. \quad (6)$$

Dividing the relevant data into ν_e disappearance, ν_μ disappearance, and $\nu_\mu \rightarrow \nu_e$ appearance searches, this relation implies that the system is over-constrained. Indeed, as will be discussed below, there is significant tension in the global data and Eq. (6) makes it difficult to obtain a good fit to all available data.

⁷Ref. [26] finds a somewhat higher significance for the preference of the first octant.

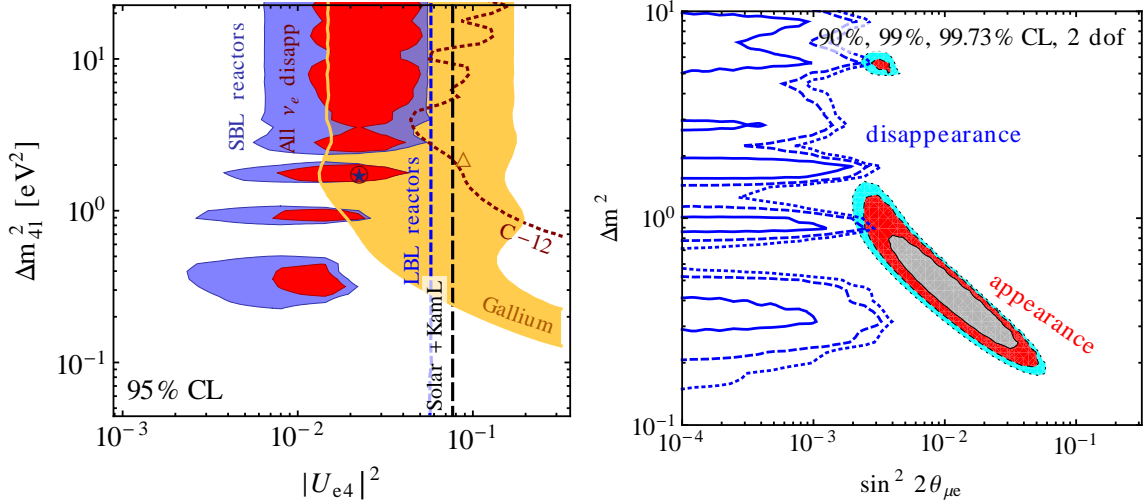


Figure 5: Left: Allowed regions at 95% CL (2 dof) for 3+1 oscillations. We show SBL reactor data (blue shaded), Gallium radioactive source data (orange shaded), ν_e disappearance constraints from ν_e - ^{12}C scattering data from LSND and KARMEN (dark red dotted), long-baseline reactor data from CHOOZ, Palo Verde, DoubleChooz, Daya Bay and RENO (blue short-dashed) and solar+KamLAND data (black long-dashed). The red shaded region is the combined region from all these ν_e and $\bar{\nu}_e$ disappearance data sets. Right: Comparison of the parameter region preferred by appearance data (LSND, MiniBooNE appearance analysis, NOMAD, KARMEN, ICARUS, E776) to the exclusion limit from disappearance data (atmospheric, solar, reactors, Gallium, CDHS, MINOS, MiniBooNE disappearance, KARMEN and LSND ν_e - ^{12}C scattering). See Ref. [70] for details and references.

Global data on ν_e and $\bar{\nu}_e$ disappearance. We consider first the global data including SBL anomalies related to $\bar{\nu}_e$ and ν_e disappearance (reactor and Gallium anomalies) but ignoring for the time being the $\nu_\mu \rightarrow \nu_e$ and $\bar{\nu}_\mu \rightarrow \bar{\nu}_e$ appearance anomalies (LSND and MiniBooNE). In this case the relevant SBL phenomenology is determined by the two parameters Δm_{41}^2 and $|U_{e4}|$. The allowed regions for them is shown in Fig. 5 (left). A consistent region emerges (shown in red), not in conflict with any other data. The best fit point occurs at $\sin^2 2\theta_{ee} = 0.09$ and $\Delta m_{41}^2 = 1.78 \text{ eV}^2$, and the no-oscillation hypothesis for the eV-scale is excluded at 3.1σ ($\Delta\chi^2 = 12.9/2 \text{ dof}$), driven by the reactor and Gallium anomalies.

Let us comment also that the θ_{13} determination is rather stable with respect to the presence of sterile neutrinos, up to an ambiguity at the level of 1σ , as mentioned in section 2.2.1. We note, however, that its interpretation becomes slightly more complicated. For instance, using a particular parametrization [70] for the 3+1 scheme, the relation between mixing matrix elements and mixing angles is $|U_{e3}| = \cos \theta_{14} \sin \theta_{13}$ and $|U_{e4}| = \sin \theta_{14}$. Hence, the one-to-one correspondence between $|U_{e3}|$ and θ_{13} as in the three-flavor case is spoiled.

Combined analysis of global data. We now address the question whether the hints for ν_e disappearance can be reconciled with the appearance hints from LSND and MiniBooNE. As mentioned above, Eq. (6) links those appearance signals to disappearance in the ν_e as well as ν_μ channels. Despite the possible signal in ν_e disappearance, so-far no positive signal has been observed in ν_μ disappearance and several experiments (CDHS, MINOS, MiniBooNE, atmospheric neutrinos) set bounds on the relevant mixing parameter $|U_{\mu 4}|$. Hence, the combined limits on ν_μ and ν_e mixing with the eV-scale mass state lead to the well-known tension between appearance signals and disappearance data in the 3+1 scheme, see e.g. [73, 74] for early references.

This tension is illustrated for the latest global data in the right panel of Fig. 5, where we show the allowed region for all appearance experiments, compared to the limit from disappearance experiments in the plane of

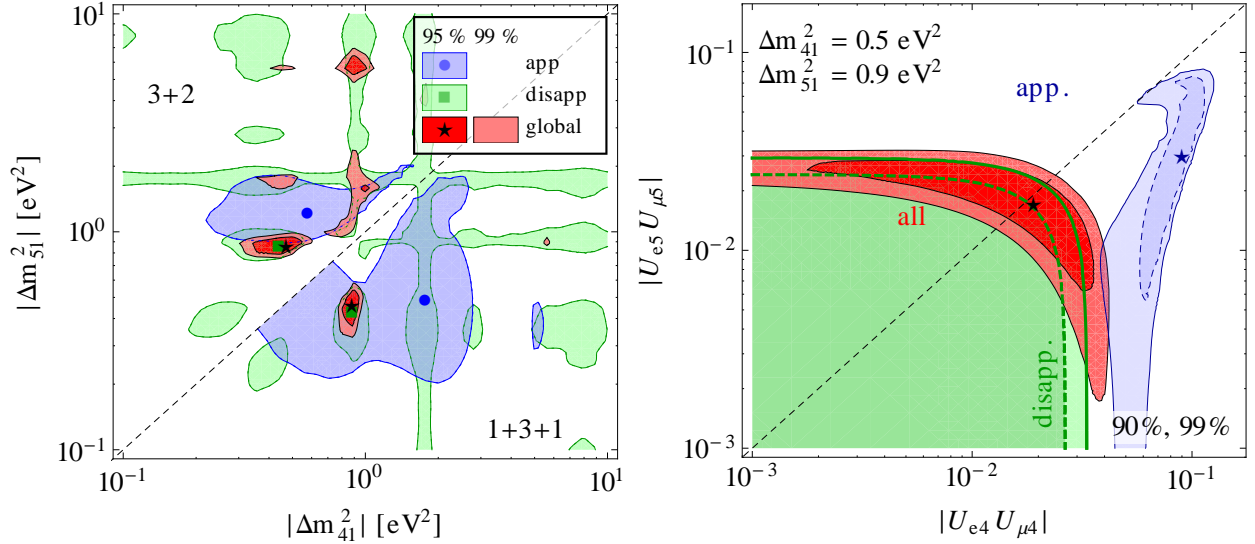


Figure 6: Global fit in 5-neutrino schemes [70]. Left: Allowed regions in the plane of $|\Delta m_{41}^2|$ and $|\Delta m_{51}^2|$ in 3+2 (upper-left part) and 1+3+1 (lower-right part) mass schemes. We minimize over all mixing angles and phases. We show the regions for appearance data (light blue) and disappearance data (light green) at 95% CL (2 dof), and global data (dark and light red) at 95% and 99% CL (2 dof). Right: Allowed regions for 3+2 in the plane of $|U_{e4}U_{\mu4}|$ vs. $|U_{e5}U_{\mu5}|$ for fixed values of Δm_{41}^2 and Δm_{51}^2 at 90% and 99% CL (2 dof). We minimize over all undisplayed mixing parameters. We show the regions for appearance data (blue), disappearance data (green), and the global data (red).

$\sin^2 2\theta_{\mu e}$ and Δm_{41}^2 . The preferred values of Δm_{41}^2 for disappearance data come from the reactor and Gallium anomalies. The regions for disappearance data, however, are not closed in this projection in the parameter space and include $\sin^2 2\theta_{\mu e} = 4|U_{e4}U_{\mu4}|^2 = 0$, which always can be achieved by letting $U_{\mu4} \rightarrow 0$ because of the non-observation of any positive signal in SBL ν_μ disappearance. The upper bound on $\sin^2 2\theta_{\mu e}$ from disappearance emerges essentially as the product of the upper bounds on $|U_{e4}|$ and $|U_{\mu4}|$ from ν_e and ν_μ disappearance according to Eq. (6). We observe from the plot the clear tension between those data sets, with only marginal overlap regions at above 99% CL around $\Delta m_{41}^2 \approx 0.9 \text{ eV}^2$ and at 3σ around $\Delta m_{41}^2 \approx 6 \text{ eV}^2$. The so-called parameter goodness of fit (PG) test [75] indicates that appearance and disappearance data are consistent with each other only with a p-value of about 10^{-4} .

A valid question to ask is whether the situation improves if more neutrino states at the eV scale are introduced. Let us consider the hypothesis of 2 states with eV scale mass splittings, ν_4 and ν_5 , which can be arranged either such that Δm_{41}^2 and Δm_{51}^2 are both positive (“3+2”) and where one of them is negative (“1+3+1”). The new qualitative feature in those 5-neutrino schemes is CP violation at the $E/L \sim \text{eV}^2$ scale [76, 77], which introduces some freedom in fitting neutrino versus anti-neutrino data from LSND and MiniBooNE together. However, the main prediction from the 4-neutrino case remains valid also for 5-neutrinos: a non-zero $\nu_\mu \rightarrow \nu_e$ appearance at SBL necessarily predicts SBL disappearance for ν_e as well as ν_μ . Indeed, the tension between appearance and disappearance data remains severe, and a PG analysis gives a consistency below 10^{-4} for 3+2, whereas for 1+3+1 consistency at the 2 per mille level can be achieved [70].

The tension in the 3+2 fit is illustrated in Fig. 6. In the left panel we show the allowed regions in the multi-dimensional parameter space projected onto the plane of the two mass-squared differences for appearance and disappearance data separately, as well as the combined region. The 3+2 global best fit point happens close to

an overlap region of appearance and disappearance data at 95% CL in that plot. However, an overlap in the projection does not imply that the multi-dimensional regions overlap. In the right panel we fix the mass-squared differences to values close to the global 3+2 best fit point and show allowed regions in the plane of $|U_{e4}U_{\mu4}|$ and $|U_{e5}U_{\mu5}|$. These are the 5-neutrino analogs to the 4-neutrino SBL amplitude $\sin 2\theta_{\mu e}$. Similar as in the 3+1 case we observe a tension between appearance and disappearance data, with no overlap at 99% CL. This explains the small PG probability at the 3+2 best fit point. A similar analysis for 1+3+1 [70] finds that regions at 99% CL overlap and the tension between appearance and disappearance appears only for the 90% CL regions (not shown), in agreement with the somewhat improved PG p-value of 2×10^{-3} .

A common feature of the 3+2 and 1+3+1 schemes is that both of them provide a rather good fit to appearance data alone, thanks to the flexibility available in 5-neutrino schemes to fit the sharp rise of the spectrum at low energies in MiniBooNE simultaneously with the LSND signal. However, none of them provides a good fit to the MiniBooNE spectra once the global data is taken into account, since this flexibility is essentially lost when constraints from disappearance are taken into account.

2.2.3 Summary

The general structure of 3-flavour mixing is known with about 10% precision. The mixing angle θ_{13} has become now the best measured angle (absolute error) but a small dependence of its value on the reactor anomaly remains. Indications of a non-maximal value of θ_{23} are below 1.5σ (driven by MINOS) and the 3σ range for $\sin^2 \theta_{23}$ is approximately symmetric. Current data are marginally sensitive to the octant of θ_{23} (below 1.5σ), and nothing can be said about the mass ordering and the phase δ_{CP} .

Several anomalies at the level of 3σ do not fit into this picture and might indicate additional neutrino states at the eV scale. While a consistent fit can be obtained for data on ν_e disappearance (reactor and Gallium anomalies) the global data suffers from severe tension between appearance and disappearance data, mostly due to the non-observation of ν_μ disappearance at the eV² scale. The existence of neutrino state at the eV is an open question to be addressed by upcoming experiments, see [27] for a compilation. Finally we mention that additional neutrino states with eV-like masses and sizeable mixings (as necessary to explain the oscillation anomalies) have severe implications for cosmology, see [27] for a discussion and references.

2.3 The baseline configuration

The optimum configuration for a neutrino factory arises from a delicate balance of accelerator capabilities, detector performance and physics goals. In particular, the size of θ_{13} plays a crucial role in defining the physics goals, and therefore, the measurement of θ_{13} in 2012 [30, 31, 53] has helped in eliminating a large degree of ambiguity. There is now, a clear cut set of measurements for which this facility is to be optimized. Also, the understanding of the performance of a MIND evolved significantly due to a more careful and detailed analysis as explained in Sec. 4.2.1. These efforts led to a large improvement in signal efficiency below 5 GeV neutrino energy.

In combination, these two factors resulted in the baseline configuration of a neutrino factory to see a considerable evolution within the IDS-NF: the first version [78] of the baseline configuration called for a stored muon energy of 25 GeV, two baselines of 4 000 km and 7 500 km, each served by a 50 kt MIND and in addition a 10 kt magnetized emulsion cloud chamber at the 4 000 km baseline. The final version, presented here, in contrast comprises one 100 kt MIND at a baseline of 2 000 km with a stored muon energy of 10 GeV. The physics rationale behind this evolution is detailed in Ref. [79] and can be roughly summarized as follows: at small $\sin^2 2\theta_{13} < 10^{-3}$ the objective is the discovery of a non-zero value of θ_{13} which is best accomplished

at the magic baseline [80]; at intermediate $10^{-3} < \sin^2 2\theta_{13} < 10^{-2}$ the eight-fold degeneracy [81], has a large impact on all measurements and therefore a combination of two baselines provides optimum sensitivity; at large $\sin^2 2\theta_{13} > 10^{-2}$ a single, relatively short baseline with a detector efficiency and beam flux closely matched to the oscillation maximum provides higher statistics and thus ultimately better sensitivities than any other configuration. This argument was already presented in the Interim Design Report and now with the measurement of θ_{13} , the third case is realized and thus a configuration with a single, relatively short, baseline is found to be optimal.

2.3.1 Simulation details

Unless otherwise stated, the true values for the oscillation parameters are the following:

$$\begin{aligned}
\delta m_{31}^2 &= 2.47 \times 10^{-3} \text{eV}^2 \\
\delta m_{21}^2 &= 7.5 \times 10^{-5} \text{eV}^2 \\
\theta_{13} &= 8.8^\circ \\
\theta_{23} &= 40^\circ \\
\theta_{12} &= 33.2^\circ
\end{aligned} \tag{7}$$

Note, that these values are slightly different from the ones in Tab. 2, however small changes in central values, as will occur over time, will have no significant impact on the sensitivities presented here.

Marginalization is performed over all the parameters not shown in the plots. This is done including a Gaussian prior in agreement with the present experimental uncertainties in the oscillation parameters from global fits. A pull-term is added for all the oscillation parameters to the χ^2 -function. In the particular case of θ_{13} and θ_{23} , the prior is implemented on the value of $\sin^2 2\theta_{ij}$ instead of the value of the angle itself. The values used for the priors are the following:

$$\begin{aligned}
\sigma(\delta m_{31}^2) &= 4\% \\
\sigma(\delta m_{21}^2) &= 3\% \\
\sigma(\sin^2 2\theta_{13}) &= 0.5\% \\
\sigma(\sin^2 2\theta_{23}) &= 4.5\% \\
\sigma(\theta_{12}) &= 3\%
\end{aligned} \tag{8}$$

The octant degeneracy is searched for, and normal hierarchy is assumed unless stated otherwise. The Earth's matter density is set to the PREM profile [82], and a 2% uncertainty is assumed unless otherwise stated. All physics sensitivities in this report are computed using the GLOBES software [83, 84].

Systematical uncertainties are included by adding a pull-term to the χ^2 -function for each nuisance parameter included in the analysis, which will then be marginalized over. The values of the systematic errors are given in Tab. 3 and have been obtained as follows:

- Normalization: adding in quadrature the systematic uncertainties associated with the construction of the MIND detector (0.5%, 0.2% and 1%), taken from Tab. 31;
- Flux: this corresponds to the source luminosity uncertainty, taken from the first row in Tab. 29;
- $\nu_{e,\mu}$ interaction rate: taken from Tab. 29. The same value, but no correlation, is assumed for neutrino and antineutrino interactions rates.
- ν_τ interaction rate: taken from Ref. [85] and [86]. Different cross section models were compared in Ref. [85], where differences as large as 50% are observed. In Ref. [86] the error is estimated to be around 25%.

Source	Uncertainty
Normalization	1.3 %
Flux	0.1%
$\nu_{e,\mu}$ interaction rate	0.5%
ν_τ interaction rate	40%
NC background	9.5%
Charge mis-ID bg.	15%

Table 3: Systematic uncertainties included in the analysis. For the flux and interaction rate errors we assume that a near detector will be able to constrain the uncertainties to the values listed in this table.

- NC background: the error is obtained by adding in quadrature the errors for the NC cross section (5%) and the hadronic model (8%) in Tab. 29;
- Charge mis-ID background is based on the numbers presented in Tabs. 29, 30 and 31 and a rough estimate yields about 10%.

Flux uncertainties are correlated between the channels where the initial neutrino flavor and polarity is the same. Interaction rate uncertainties are taken to be correlated between the different channels where the final neutrino flavor and polarity is the same. The same value for the uncertainty is assigned to neutrinos and antineutrinos, but these are kept uncorrelated during marginalization. The signal is always divided in three different interaction regimes: quasi-elastic (QE), resonance production (RES) and deep-inelastic scattering (DIS). The values of the interaction rate uncertainties assigned to each of them are numerically the same, but they are taken to be uncorrelated between the different interaction regimes.

Note, that at large θ_{13} , the background related uncertainties have only a very minor impact on the resulting physics sensitivities even if the values quoted here are varied by a factor two. On the other hand the signal uncertainties are crucial.

2.3.2 Physics sensitivities

The mass hierarchy likely will be known by the start of a neutrino factory, see e.g. Refs. [87, 88]. A neutrino factory will be able to confirm a mass hierarchy determination with a $\Delta\chi^2$ between the two hierarchies in excess of 1 600 for any value of the CP phase. The results in Fig 12 may seem at odds with large significance of the mass hierarchy determination, but for that a prior on the matter density of 2% is used. In other words, even if there is *no* constraint on the matter density at all, a neutrino factory still could achieve a $\sim 10\sigma$ determination of the mass hierarchy.

2.4 Comparison with the physics performance of alternative experiments

A Neutrino Factory is not the only facility that has been proposed for the study of neutrino oscillations with great accuracy. Given the existence of several options, each of which comes with its own advantages and disadvantages, a critical comparison of the various facilities is called for. However, this report is about the feasibility and physics reach of the Neutrino Factory and, therefore, we feel that we have neither the space, the expertise, nor a mandate to provide an in-depth critical comparison. At the same time, it would be a disservice to the reader to shun the comparison altogether and thus, we will present a comparison of the physics sensitivities only, which in turn are based on the outcome of studies of the facilities that are presently under way. The results in terms of the accuracy of a determination of the CP phase are summarized in Fig. 13.

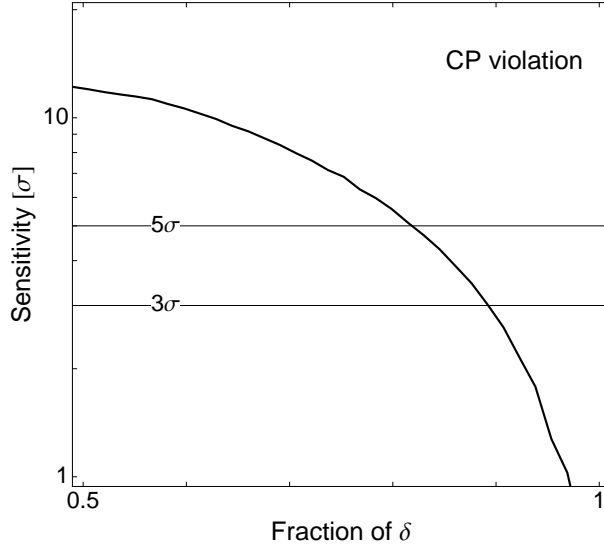


Figure 7: Left: CP violation sensitivity. The line shows the number of sigmas for which the CP-conservation hypothesis ($\delta = 0, \pi$) can be rejected for a given fraction of possible values of δ . Notice the scale on the x-axis in the plot, which has been zoomed in the region of interest.

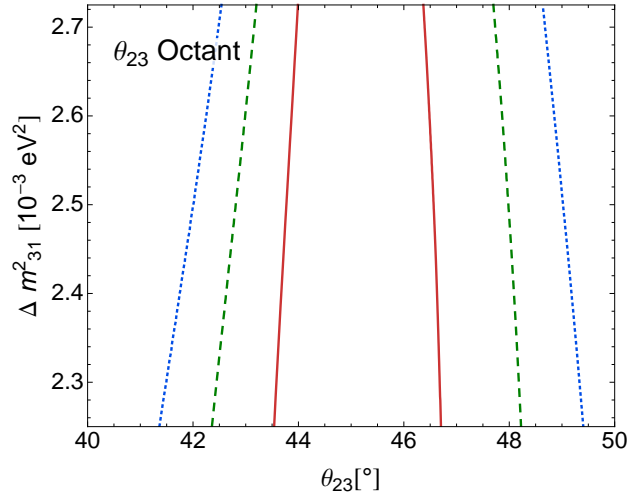


Figure 8: Octant determination for the atmospheric mixing angle θ_{23} . In the regions outside the red, green and blue lines, the wrong octant for θ_{23} can be rejected at a significance of 1,2 and 3 σ , respectively. Results are shown as a function of the true values of θ_{23} and the true value of the atmospheric mass splitting.

The alternative to a neutrino factory is to use neutrinos produced directly in pion decay. Traditionally, pion decay-in-flight is employed to obtain an actual beam, and in the context of future neutrino experiments, the term superbeam has become common to designate these; 'super' refers to the very high beam power of around 1 MW or more. This technology is considered mature in principle, however the challenges presented by high beam currents and the high energy density in the target are significant. To improve beam intensity and purity magnetic horns are used to selectively focus π^+ for a neutrino beam and π^- for an antineutrino beam. The limitations of superbeam technology are a very limited control of beam composition and systematics and in particular,

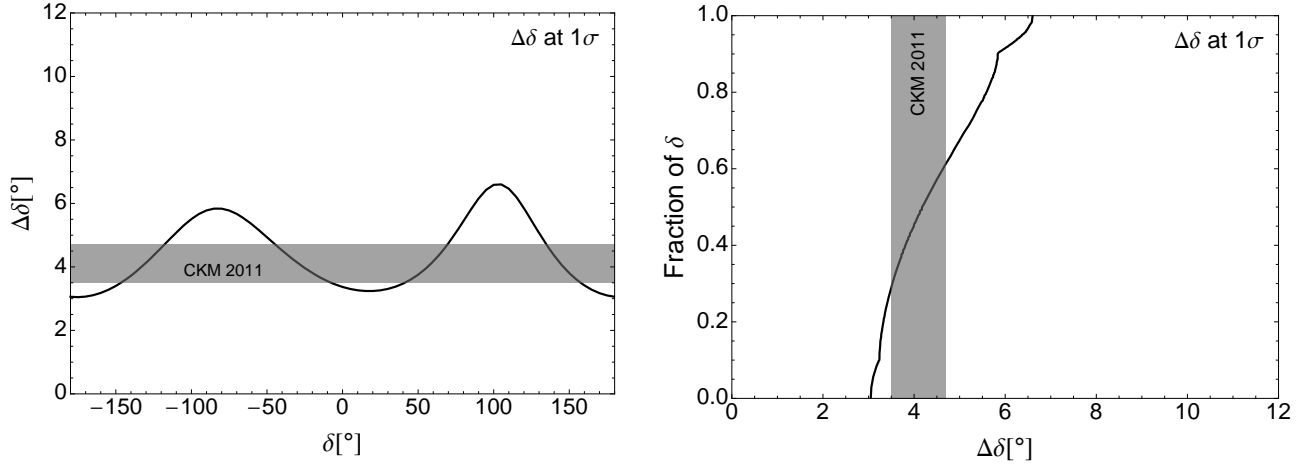


Figure 9: Expected uncertainty at 1σ (for 1 dof) for the determination of the CP-violating phase, δ . The results are shown as a function of the true value of δ in the left panel, and as a function of the fraction of values of δ in the right panel. The gray bands show the precision for the CP violating phase in the CKM matrix, as of 2011 [37].

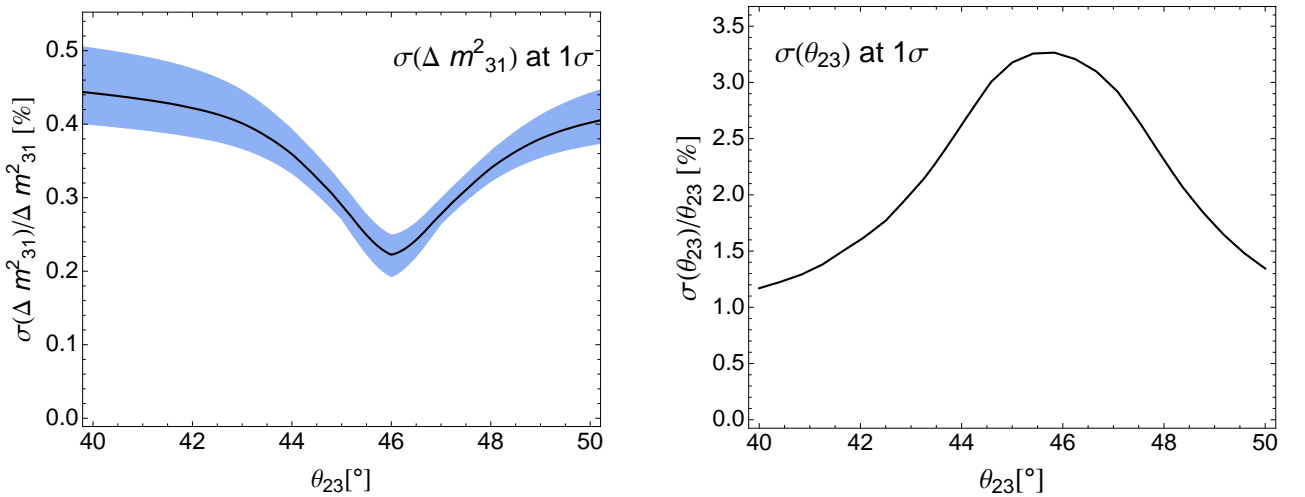


Figure 10: Expected uncertainty at 1σ (for 1 dof) for the determination of the atmospheric mass splitting (left panel) and the atmospheric mixing angle (right panel). In the left panel, the band indicates the impact on the results due to the true value of the mass splitting itself, which is varied within the currently allowed range at 3σ ($2.3 \times 10^{-3} - 2.6 \times 10^{-3} \text{ eV}^2$). In the right panel, the results have been obtained for $\delta m^2_{31} = 2.47 \times 10^{-3} \text{ eV}^2$.

neutrino and antineutrino beams have to be considered to be largely independent. This in combination with the incomplete understanding of neutrino-nucleus interactions ultimately will limit the accuracy superbeams can achieve, see e.g. [89]. For all experiments a near detector is explicitly included in the sensitivity calculation and the details of the systematics implementation as well as the input uncertainties for fluxes, cross sections asf. are taken from Ref. [90]. The running time is fixed at 10 years, however, note that the definition of a year in terms of seconds the accelerator complex is running is different among setups and we followed the original references in that.

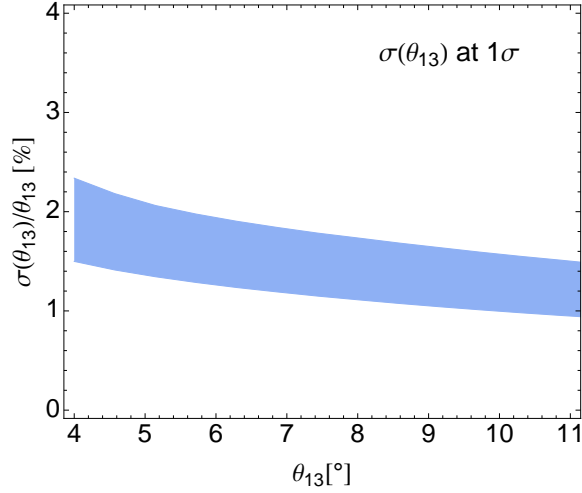


Figure 11: Expected uncertainty at 1σ (for 1 dof) for the determination of θ_{13} . Results are shown as a function of the true value of θ_{13} . The width of the band shows the variation of the result with the true value of δ .

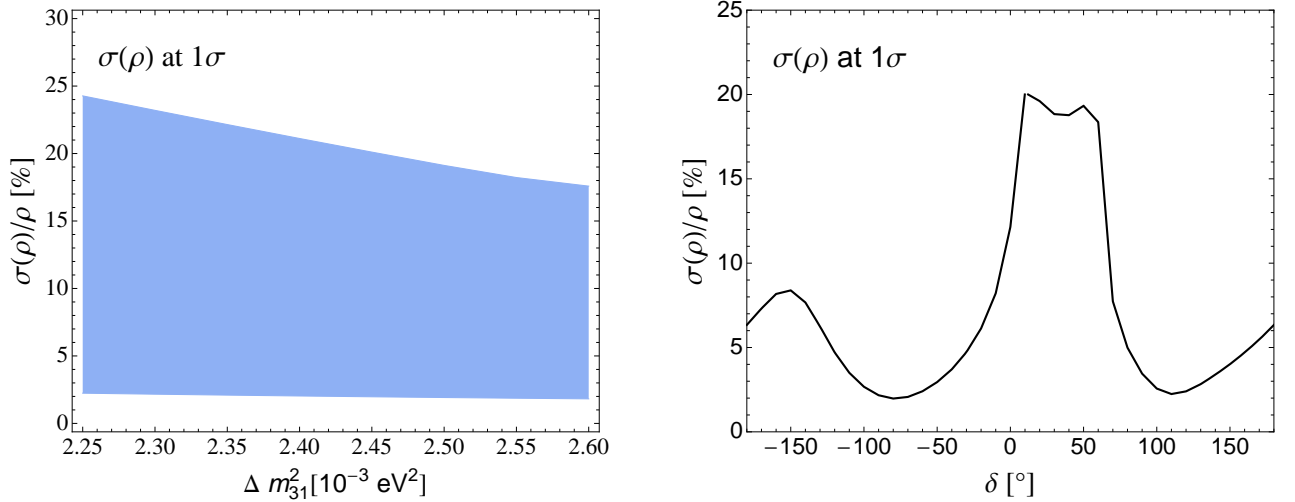


Figure 12: Expected uncertainty at 1σ (for 1 dof) for the determination of the Earth's matter density. In the left panel, results are shown as a function of the true value of the atmospheric mass splitting, and the width of the band shows the variation with the true value of δ . In the right panel, the results are shown as a function of the true value of δ , for $\delta m_{31}^2 = 2.47 \times 10^{-3} \text{ eV}^2$.

Specifically, we consider the following proposed superbeam experiments: LBNE, LBNO, T2HK and ESS ν SB. For all those experiments, the ultimate luminosity will be used, despite the fact, that practically all of them will start out with a significantly lower luminosity.

For LBNE a 34 kt liquid argon detector at a distance of 1 300 km and a 2.3 MW beam from Project X are assumed [91]. Note, that in particular, we deviate from the systematics treatment in Ref. [91] by including a near detector and by realistically propagating flux and cross section errors.

For LBNO a 100 kt liquid argon detector at a distance of 2 300 km together with a 0.8 MW beam is assumed [92].

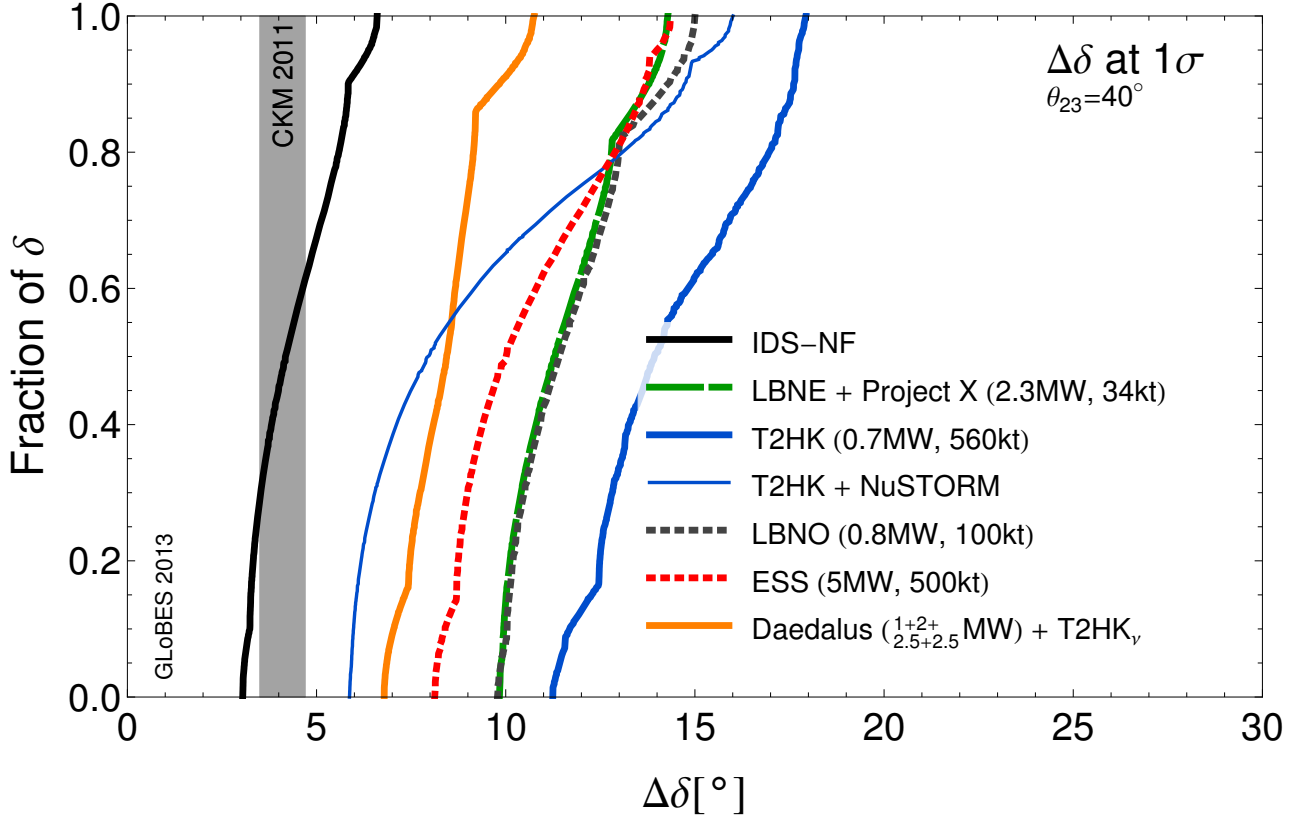


Figure 13: Expected precision for a measurement of δ . Results are shown as a function of the fraction of possible values of δ for which a given precision can be reached at 1σ . The setups are explained in the text. The gray band indicates the current precision in the quark sector for the analogous parameter [37].

For T2HK a 750 kW beam aiming from Tokai to the Hyper-Kamiokande detector (560 kt fiducial mass) is assumed, baseline and off-axis angle are the same as for T2K. Simulation details are to be found in Ref. [90].

For the ESS beam a 500 kt water Cherenkov detector at a baseline of 360 km is assumed and the beam power is 5 MW obtained from 2 GeV protons accelerated at the ESS proton linac [93]. The detector response is based on migration matrices from Refs. [94, 95].

Another possibility is to use pion decay-at-rest to produce muon antineutrinos and to use inverse beta-decay to detect the oscillated electron antineutrinos in a unambiguous way, this approach is known as DAE δ ALUS [96–99]. To effect a measurement of the CP phase the best sensitivity is reached by combining the decay-at-rest antineutrino run with a neutrino run from a superbeam [98]. Inverse beta-decay requires a detector with free protons and that leaves large water Cherenkov or liquid scintillator detectors. Specifically, we follow the setup outlined in Ref. [99], which uses a 10 year neutrino run at T2HK with the parameters described above and combines this with three clusters of cyclotrons at 1.5 km, 8 km and 20 km from the detector; the combined beam power at each site is 1 MW, 2 MW and 5 MW, respectively.

Finally we also include a line labeled T2HK+NuSTORM, which highlights the huge impact systematics from cross sections have for superbeam experiments. It has been shown [90, 100] that T2HK due its relatively low beam energy is particularly sensitive to any uncertainty in the ratio of electron to muon neutrino cross sections, which can *not* be mitigated by a near detector. Measurements of both cross sections and their ratio at NuSTORM [101] can eliminate this source of error, greatly improving the performance of T2HK. A similar consideration may apply for the ESS setup, but is not shown.

The alternative setups considered here can be grouped into high-end superbeam experiments, T2HK, LBNE,

LBNO, ESS, and augmented superbeam experiments, DAE δ ALUS and T2HK+NuSTORM, where an existing superbeam is combined with a novel, precision neutrino source. The superbeams themselves can reach a CP precision in the range of 8-17 $^\circ$ and the augmented superbeams can reach a precision in the range of 6-15 $^\circ$, where the actual value within this range depends on the true value of the CP phase. This has to be compared to a precision 3-6 $^\circ$ of the IDS-NF neutrino factory. The relative performance margin provided by a neutrino factory also depends on the true value of the CP phase and will typically be a factor of two or more. A neutrino factory is the only facility which consistently can match the CP precision in the lepton sector with the one in the quark sector.

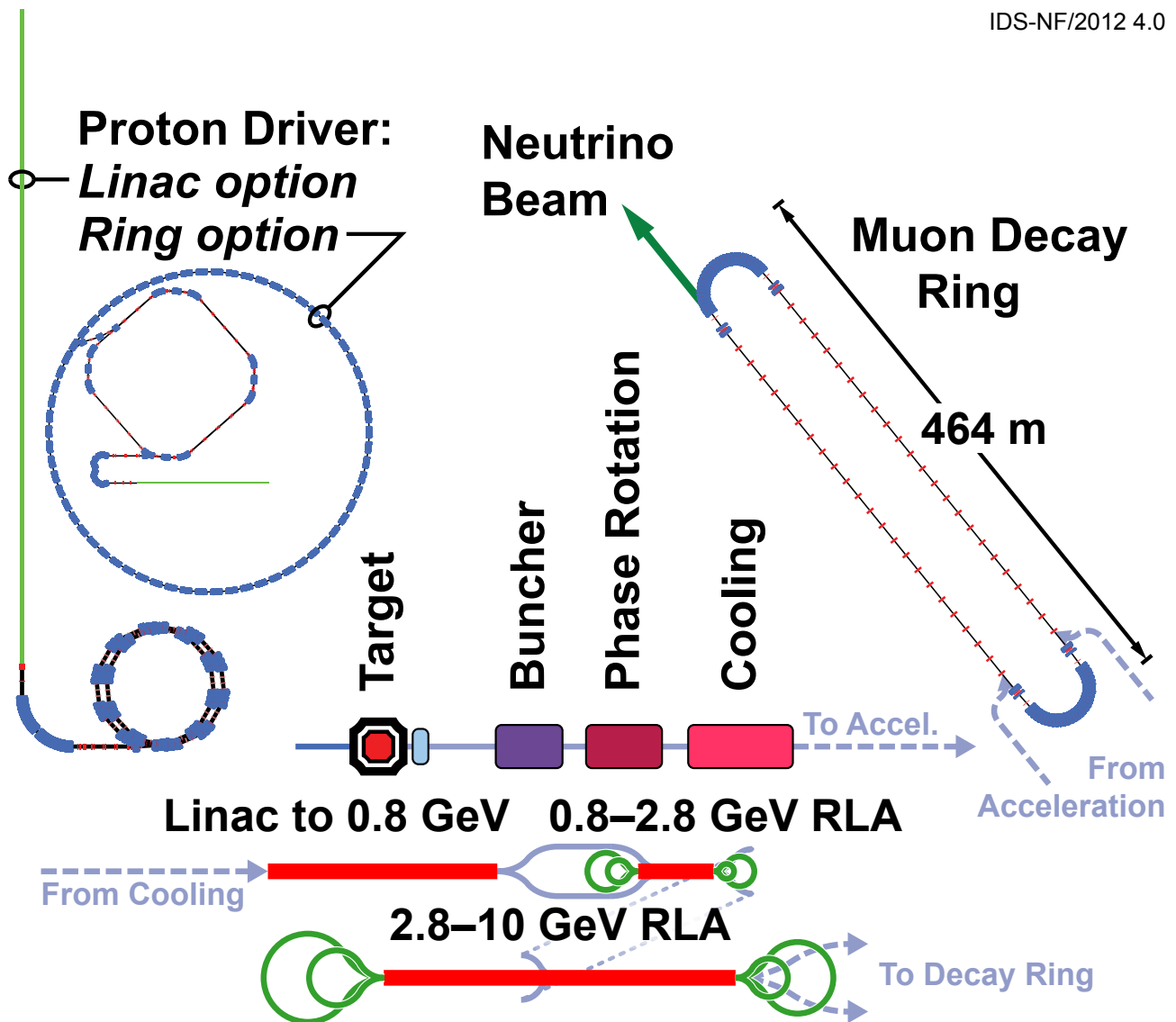


Figure 14: A diagram of the neutrino factory accelerator facility.

3 The Neutrino Factory Accelerator Complex

Lead authors: JSB, JPa

The goal of the accelerator facility is to produce 10^{21} neutrino decays per year from decays of a 10 GeV muon beam. These neutrinos are directed toward a detector at a distance of approximately 2000 km. We first give a short overview of the facility, and then individual subsections will describe the stages in more detail.

The facility begins with a high power proton driver that produces an intense pulsed proton beam. This beam hits a target that produces pions, which then decay into muons. These muons (in the “front end”) are manipulated in phase space to produce a train of muon bunches. This bunch train is then accelerated to 10 GeV and injected into a decay ring. The decay ring contains long straights wherein the muons decay into neutrinos, producing the desired neutrino beam.

The proton driver delivers a 4 MW proton beam to the target. This power is required to produce sufficient pions to give us the desired number of neutrino decays. The beam must be sufficiently small to avoid significant reduction in production in the target and capture by the front end. Each proton driver pulse can supply up to 3 bunches; these bunches must be spaced sufficiently to allow them to be accelerated individually. More bunches

from the proton driver would result in more bunch trains than would fit in the decay ring. We do not specify precisely how we would build a proton driver, since this depends strongly on the existing infrastructure at the laboratory where one would build a neutrino factory. Instead, we present descriptions of how an acceptable proton driver could be built at a couple different laboratories.

The target is a mercury jet. The large atomic number in mercury gives good pion production. Mercury is used since a solid target would likely be damaged by the high proton driver power used here. The target is within a high field solenoid, which allows the capture of both muon signs, and has a large angular acceptance. That solenoid field tapers down as the pions go downstream and begin to decay. A chicane with an absorber at the end is inserted to remove particles other than pions and muons, reducing energy deposition in the downstream systems.

Following the chicane, the remaining pions decay into muons. This is followed by a “Neuffer” buncher and phase rotation, which turns the large energy spread muon beam into a bunch train with a relatively small energy spread. The transverse emittance of this bunch train is then reduced by an ionization cooling channel. The goal of these latter two systems is to create a beam that can be readily accelerated.

The beam is accelerated in three stages in order to optimize the acceleration in each energy range. The first stage is a linac accelerating to 0.8 GeV. The subsequent two stages, accelerating to 2.8 and 10 GeV, are 4.5-pass recirculating linear accelerators (RLAs). The use of multiple linac passes in the RLAs increases the acceleration efficiency.

The 10 GeV muon beam is injected into a decay ring. The decay ring has two long straights pointed toward a detector 2000 km away. The straights are kept long compared to the arcs to ensure that a large fraction of the neutrino decays are toward the far detector. The beam in the straights has a small angular divergence (and therefore a large size) to reduce the uncertainty in the neutrino flux.

3.1 Proton Driver

3.2 Proton driver

The IDS-NF baseline for the Neutrino Factory requires a proton driver to deliver a proton-beam of 4 MW at a repetition rate of 50 Hz to the pion-production target. The proton-beam energy must be in the multi-GeV range in order to maximise the pion yield. In addition, the Neutrino Factory specifies a particular time structure consisting of three very short bunches separated by about $80 \mu s$. To allow the muon beam to be captured efficiently, short, 1–3 ns rms, bunches are required. Each bunch from the proton driver will become a separate muon bunch train. The bunch separation is constrained by beam loading in the downstream muon accelerator systems and by the time scale for disruption of the mercury-jet target. The proton beam parameters necessary to produce the desired number of muons in the storage rings of the Neutrino Factory are listed in table 5. In order to achieve such short bunches, a dedicated bunch compression system must be designed to deal with the very strong space-charge forces. Several proton-driver schemes fulfilling these requirements have been proposed (see below and appendices). Typically they consist of an H^- -ion source followed by a radio-frequency quadrupole (RFQ), a chopper, and a linear accelerator. In some cases the final energy of the proton driver is delivered by the linac. In these linac-based scenarios, the beam time structure must be obtained with the help of charge-exchange injection into an accumulator ring followed by fast phase rotation in a dedicated compressor ring.

Such a linac-based solution was adopted for the CERN Neutrino Factory scenario, which would be based on the proposed 5 GeV, high-power version of the Superconducting Proton Linac (SPL) [102], which can deliver 10^{14} protons at the bunch frequency of 352.2 MHz and the repetition rate of 50 Hz and [103, 104]. In the CERN scenario, the chopped H^- beam from the SPL would be injected into an isochronous accumulator ring in which

Table 4: Proton driver requirements. A proton kinetic energy in the range 5 GeV to 15 GeV has been shown to provide adequate performance. The number of protons, beam radius, β^* , and geometric emittance (see section ??) correspond to the values for an 8 GeV proton beam.

Parameter	Value
Kinetic energy	5–15 GeV
Average beam power	4 MW
	(3.125×10^{15} protons/s)
Repetition rate	50 Hz
Bunches per train	3
Total time for bunches	160 μ s
Bunch length (rms)	1–3 ns
Beam radius	1.2 mm (rms)
Rms geometric emittance	< 5 μ m
β^* at target	\geq 30 cm

120 ns long proton bunches are formed without the need for an RF system. The final bunch compression is performed using RF phase-rotation in the downstream compressor ring. The size of the two rings is determined by the requirement that successive bunches must arrive at the correct location in the compressor ring. The compressor ring has a large phase slip factor, which is needed for the fast phase rotation. More details of the CERN scenario can be found in Appendix ??.

A proton driver for a Neutrino Factory situated at Fermilab would be based upon a proposed Project X, which would serve for pure and applied science needs as high-intensity proton source adopting a staged approach in construction. The first and the second stage will produce 1 GeV and 3 GeV CW H^- beams respectively using superconducting linacs with RF frequencies chosen at 162.5, 325 and 650 MHz. These linacs are capable to deliver a very flexible beam time structure with average current of 1 mA upgradeable to 2 mA and even 5 mA. The third stage will use a pulsed 8 GeV superconducting linac at 1.3GHz RF frequency. Project X will serve directly several experimental areas for the intensity frontier research, but will also allow beam injection into the Booster (Stage 1 and 2) and the Main Injector (Stage 3) for further acceleration to high energy required by the long baseline neutrino program. In addition Project X is also designed such that it can be upgraded to deliver the full beam power (4 MW at 8 GeV) required for the Neutrino Factory. Just as in the CERN scheme, H^- beam will be injected by stripping using either foil or laser in the dedicated accumulator ring with circumference of 300 m. After accumulation beam will be sent to the compressor rings with identical circumference to create the time structure required by the pion production target. Project X will be located within the Tevatron ring at Fermilab. The accumulation ring will be situated near the end of the pulsed linac. More details of the FNAL scenario can be found in Appendix ??.

A Neutrino Factory sited at the Rutherford Appleton Laboratory (RAL) would be served by a proton driver based on an upgrade to the ISIS pulsed-proton source. In this scenario, a chain of circular accelerators, typically Rapid Cycling Synchrotrons (RCSs), provides an alternative to the linac-based options outlined above. Here, bunch compression is accomplished adiabatically in the RCS or, alternatively, in an FFAG ring as proposed in the ISS study [?]. Recently the attractive idea of a common proton driver for the spallation neutron source and the Neutrino Factory was proposed in the framework of the ongoing ISIS megawatt-upgrade programme. In such a scenario, the proton drivers for both facilities would share the same source, chopper, linac, accumulator, and acceleration up to 3.2 GeV. After extraction, a number of bunches would be sent directly to the neutron-spallation target while three others would be injected into a second RCS or FFAG where, after acceleration to somewhere between 6.4 and 10.3 GeV followed by bunch compression, the beam would be extracted towards

the Neutrino Factory pion-production target.

For the ISIS megawatt upgrade to be compatible with the Neutrino Factory, an 800 MeV H^- linac has been designed, candidate lattices for the 3.2 GeV booster RCS have been identified, and preliminary parameters for the final RCS ring have been proposed. More details of the Neutrino Factory proton driver option based on an upgrade of facilities at RAL are presented in Appendix ??.

3.3 Target

Lead authors: KTM

The Target System of the Neutrino Factory is considerably more than the target for the primary proton beam. It includes a high-field solenoid-magnet string for capture of low-energy pions from the target, as well as the infrastructure to house and support the target and capture magnets. Because of the high levels of activation of materials in the Target System, it includes substantial radiation shielding, and remote-handling capability.⁸

Early visions [105] of a target system for a Muon Collider considered (pulsed) toroidal collection (with a Li lens, as at a \bar{p} source), which is limited to one sign of charged particles, and has not been demonstrated for the 50-Hz repetition rate specified for a Neutrino Factory. Pion collection with DC solenoid magnets was proposed in 1995 [106] and has since been the baseline concept. An additional advantage of solenoidal capture in a high-field magnet is that longitudinal-transverse emittance exchange occurs as the field strength decreases adiabatically along the capture channel [107], which provides initial transverse cooling of the secondary pions (at the expense of longitudinal heating). Issues of survival of a solid target in a 4-MW proton beam with ≈ 2 -ns pulses led to consideration of a free-mercury-jet target [108], now the baseline. Physics feasibility of a mercury-jet target in a strong solenoid field and intense proton pulses was demonstrated in the MERIT experiment at CERN [109].⁹

Optimisation of particle production at fixed proton-beam power for maximal output of the Neutrino Factory [111] leads to various requirements on the proton driver (Table 5), and on the configuration of the Target System. Useful (low-energy) pion yield from the Hg target peaks at 8 GeV, which is taken to be the baseline value. The desired low-energy pions emerge from the side of the target, which favors a small proton-beam radius, and leads to the (demanding) requirement of geometric transverse emittance of $5 \mu\text{m}$ for the proton beam. The requirement of short proton bunches (1-3 ns) is based on the need for efficient capture of the secondary beam into rf bunches, so is not strictly a requirement by the Target System.

Pion production is maximized when the radius of the jet target is about 3 times that of the proton-beam rms radius, and the proton beam and target have a small tilt with respect to the axis of the capture-solenoid capture. The latter implies that the primary proton beam does not point into the Decay Channel, but off to the side of the Target System, where the mercury-collection pool serves as the beam dump.¹⁰ The proton beam will disrupt the liquid target over most of its effective length (≈ 2 interaction lengths = 30 cm), so the requirement to have a fresh region of the jet at the target at 50 Hz implies the jet velocity must be 20 m/s (which also implies that gravitational curvature of the jet is negligible).

Useful particle production is higher for higher peak magnetic field in the Target System, and 20 T is taken as the baseline value. This is beyond the capability of a Nb-based superconducting magnet, so a hybrid magnet with a 15-T Nb_3Sn outer coil and a 5-T Cu inner coil is specified. Such a hybrid magnet (with 45 T peak field) has been constructed at the NHMFL [112].

⁸The Final-Focus System of the primary proton beam may or may not be considered as part of the Target System. Also, the string of magnets in the Pion-Decay Channel prior to the Buncher will experience very high radiation loads, so from a technology perspective they are part Target System, although they are described in this document as part of the Front End.

⁹The MERIT experiment did not utilize a continuous-flow of mercury, which has been demonstrated at the Target System of the SNS at ORNL [110].

¹⁰Mitigation is required of splashes in this pool due to the entering mercury jet and the noninteracting part of the proton beam.

Table 5: Requirements on the Proton Driver from the Target System. Some parameters correspond to an 8 GeV beam energy.

Parameter	Value
Kinetic energy	5–15 GeV
Average beam power	4 MW (3.125×10^{15} protons/s)
Repetition rate	50 Hz
Bunches per train	3
Total time for bunches	240 μ s
Bunch length (rms)	1–3 ns
Beam radius	1.2 mm (rms)
Rms geometric emittance	< 5 μ m
β^* at target	≥ 30 cm

The magnetic field in the target system “tapers” down from the peak of 20 T to 1.5 T in the Decay Channel that begins 15 m from the target.

The requirement of dissipation of the 4-MW proton-beam power inside the Target System is a major driver of the system design. Radiation damage to magnet conductors, particularly to organic insulation, limits their useful lifetime to ≈ 10 years of 10^7 operational seconds if the energy deposition by secondary radiation is 0.1 mW/g [113] (sometimes called the ITER limit). Simulations of energy deposition by FLUKA and MARS codes indicate that the inner radius of superconducting coils near the target must be 1.2 m to satisfy the ITER limit, via internal radiation shielding by He-gas-cooled tungsten beads. This large radius implies the magnets of the Target System would have a stored energy of ≈ 3 GJ, comparable to that of the ITER Central Solenoid [114] and the CMS central solenoid [115].

The 5-T Cu coil insert would experience much larger radiation dose, such that organic insulation could not be used; rather a MgO-insulated conductor is required, as developed at KEK [116].

Some 15% of the proton-beam energy is transported into the Decay Channel, mostly via scattered beam protons (and protons from nuclear breakup in the target). This requires mitigation via a chicane in the Decay Channel, and implies that the magnets in this channel must also be designed for high radiation dose, as in the Target System.

A vertical section of the Target System is shown in Fig. 15, and the target region, with the 20-T hybrid capture solenoid is shown in more detail in Fig. 16. This magnet module weighs ≈ 200 tons, which sets the scale for the infrastructure required for the Target System.

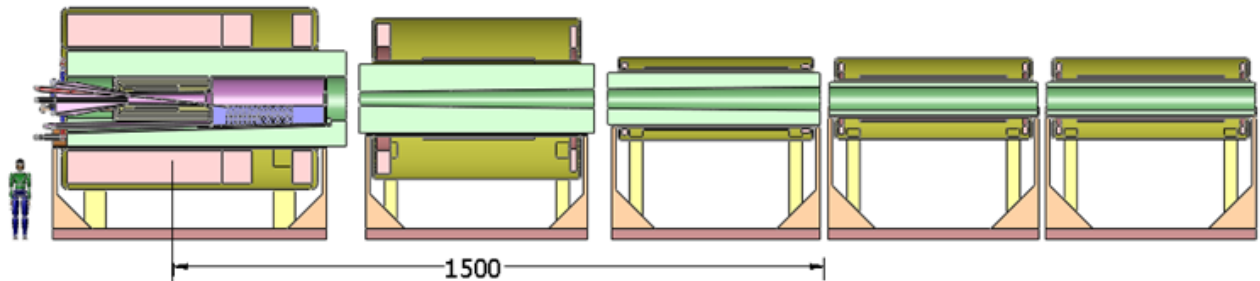


Figure 15: Vertical section of the three magnet modules of Target System (which nominally ends at $z = 1500$ cm) and the first two modules of the Decay Channel.

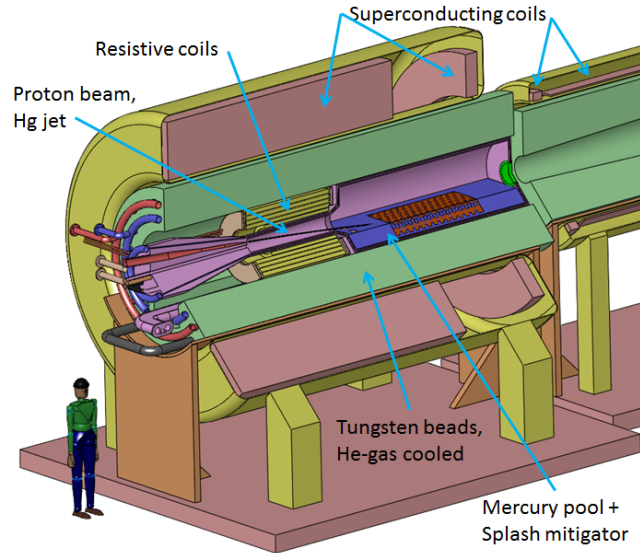


Figure 16: View of the 200-ton 20-T capture solenoid, with internal shielding by tungsten beads. The free-mercury jet target and the proton beam are tilted with respect to the magnetic axis, and impinge on the mercury-collection pool that also serves as the proton beam dump.

3.4 Front End

The Neutrino Factory muon front-end captures pions produced on the target by means of a pion decay channel and particle selection system followed by a longitudinal drift to an adiabatic buncher, energy-phase rotation system and ionisation cooling channel. Subsequently the beam enters the muon accelerator chain. A schematic of the front end is shown in fig. 17.

The present design is based on the lattice presented in the Neutrino Factory Study 2A report [117] and subsequently developed in the International Scoping Study for a Neutrino Factory (ISS) [?] and EuroNu design report [?].

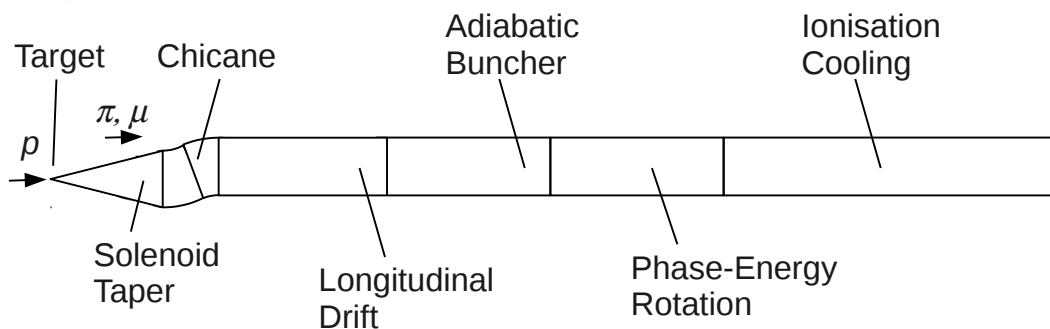


Figure 17: Schematic diagram of the muon front end.

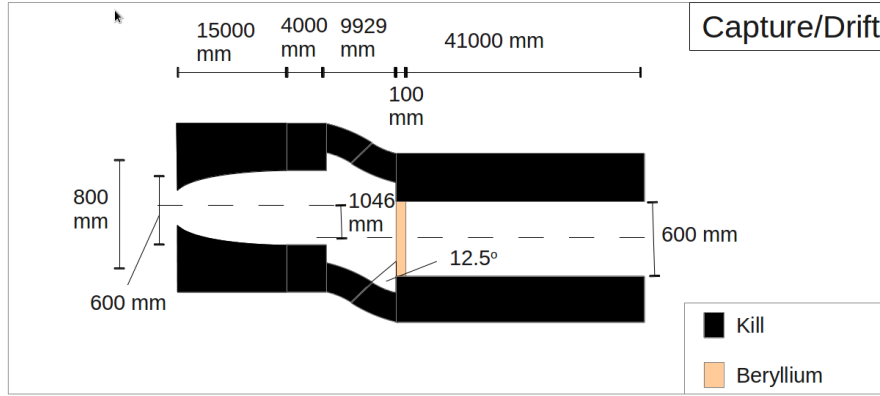


Figure 18: Schematic of the solenoid taper, chicane, proton absorber and drift system.

Table 6: Coil pack used for simulation of the solenoid taper.

Coil Number	Front Z	Inner Radius	Outer radius	Length	Current
0	-875.615	183.374	230.974	1001.77	22.0077
1	-1110.25	238.526	287.56	1236.4	20.7391
2	-1209.83	295.812	355.238	2071.54	14.1202
3	-1258.49	362.07	426.417	2120.2	12.0430
4	-1294.60	433.012	501.625	2156.32	10.5919
5	-2409.29	1200	1958.34	3523.19	19.3093
6	1113.91	1200	1843.42	777.842	21.7586
7	2764.71	1200	1958.34	451.954	26.7345
8	4702.37	1199.63	1755.92	312.275	33.4571
9	5757.48	896.518	938.067	2553.68	41.2151
10	9143.17	1182.83	1703.07	154.466	40.7164
11	10347.6	723.607	869.066	129.994	45.0315
12	10850.7	699.214	723.774	3413.12	46.6621
13	14542.8	699.438	863.938	109.612	46.4479

3.4.1 Baseline Overview

Pions are captured in a solenoidal field that tapers adiabatically from 20 T to 1.5 T while the beam pipe radius increases from 0.075 m to 0.30 m over a distance of about 15.0 m. The individual coils to generate this field are given in Table 6. A large transverse phase space of both positively and negatively charged particles with a large energy spread is captured in the solenoidal field.

The chicane follows after the solenoid taper region. A 4 m region of matching was used to match from the long coil geometry used in the solenoid taper to a short coil that could be arranged on a torus, all in a 1.5 T field on-axis. A set of match coils provide a match from the long coils used in the solenoid taper to the short coils used in the chicane. Coils in this region are identical with inner radius 430 mm, outer radius 530 mm, length 180 mm and current 16.5703 A/mm^2 . A list of current scalings used for matching is given in table 7. Coils are placed with coil centres every 250 mm.

The chicane itself starts at 19.0 m and consists of coils with the same geometry as the match coil, placed every 250 mm along a curved trajectory with radius of curvature of 22.9 m and a total bending angle of 12.5° .

Centre Z [mm]	Current Scaling [16.5703 A/mm ²]
15000	0.9
15250	0.8
15500	0.8
15750	0.9
16000	0.95
16250	0.95
16500	0.95
16750	0.95
17000	0.97
17250	0.97
17500	0.97
17750	0.97
18000	1.0
18250	1.0
18500	1.0
18750	1.0

Table 7: Current scalings for the matcher section.

Two bends were placed next to each other, one to provide a positive bending angle and the other to provide a negative bending angle, resulting in a transverse displacement of the downstream linac by 1.0468 m.

The chicane is designed to remove neutral particles and charged particles with momentum above 500 MeV/c. A 0.1 m long Beryllium plug is placed after the chicane to range out low energy protons that remain in the beam.

The beam continues in the 1.5 T field for another 40.8 m with no RF, giving rise to a time-energy correlation. The beam then passes through 44 RF cavities, each of which has frequency selected to be synchronous with particles in the beam despite the growing separation due to time of flight variation with energy. Lattice cells are 0.75 cm long, with an 0.5 m RF cavity in the center, with 200 μm beryllium windows on the ends (Fig. 19). The voltage of each cavity is higher than the previous to enable a pseudo-adiabatic formation of a bunch train. This leads to cavities with frequencies of 358.92 MHz at the start to 235.40 MHz at the end of the buncher and gradients up to 11.904 MV/m (Table 8).

Once the voltage has reached its nominal peak value and bunches have formed, the cavities are slightly dephased so that fast muons at the head of the bunch experience a decelerating phase and slow muons at the tail of the bunch experience an accelerating phase. The phase is chosen so that the head bunch and tail bunch have the same energy when the bunch frequency is 201.25 MHz, with a gradient of 13.0 MV/m used throughout the energy-phase rotation system. Cavity frequencies continue to decrease to keep the bunches at the same phase despite their different energies (Table 9). Cavities have beryllium windows with 400 μm thickness.

Subsequently the beam enters an ionisation cooling channel. The muons are passed through an absorber reducing both transverse and longitudinal momentum. They are then reaccelerated in an RF cavity, replacing momentum in only the longitudinal direction resulting in a reduction of transverse emittance. Multiple Coulomb scattering and energy straggling tend to create noise counteracting the emittance reduction. A low-Z material is chosen for the absorber to minimise these effects.

The beam is matched from the constant 1.5 T field to a field that alternates from +2.8 T to -2.8 T with a period of 0.86 m. The magnet section comprises eight 0.75 m cells similar to the cooling cells (Fig. 20). Cavities and absorbers are identical to the cooling cells. Coil currents that generate the matching section fields are given in

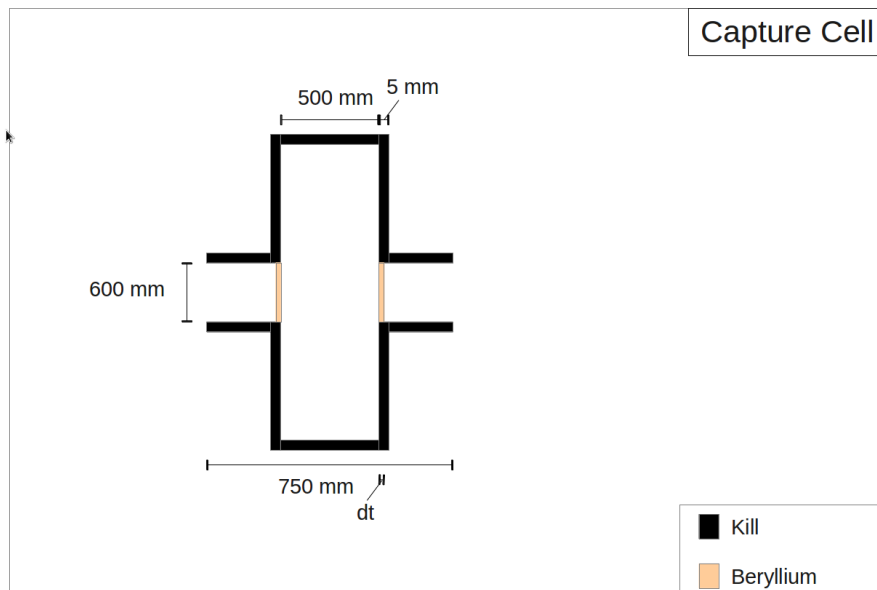


Figure 19: Schematic of a single cell in the RF capture system.

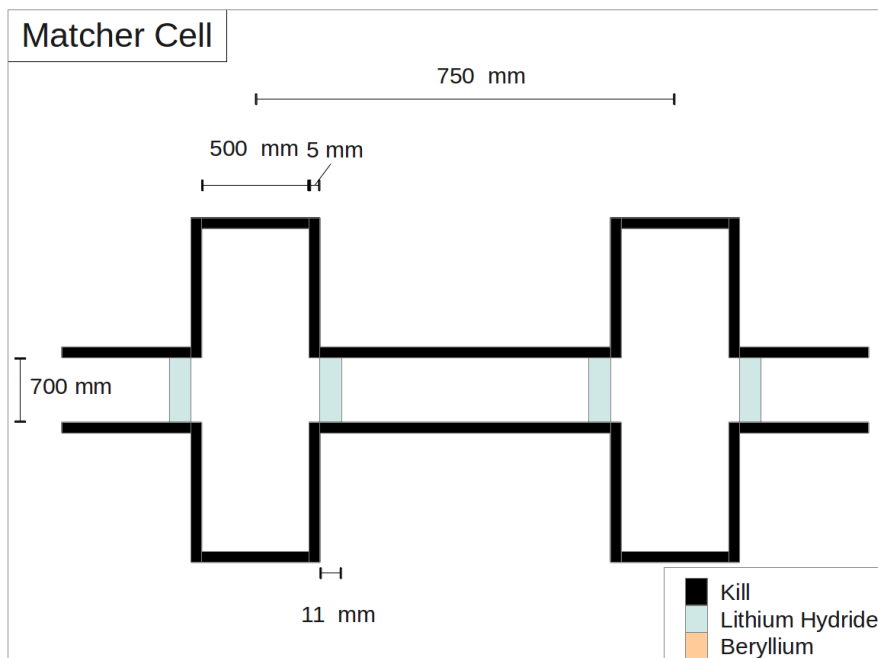


Figure 20: Schematic of a cell in the region between the phase rotation and the cooling proper.

Cell	Frequency [GHz]	Peak Voltage [MV/m]
1	0.35892	0.178
2	0.35892	0.451
3	0.35892	0.724
4	0.35892	0.996
5	0.35892	1.269
6	0.34102	1.542
7	0.34102	1.815
8	0.34102	2.087
9	0.32873	2.36
10	0.32873	2.633
11	0.32873	2.906
12	0.31727	3.178
13	0.31727	3.451
14	0.31727	3.724
15	0.30663	4.269
16	0.30663	4.269
17	0.30663	4.542
18	0.29665	4.815
19	0.29665	5.087
20	0.29665	5.36
21	0.28731	5.633
22	0.28731	5.906
23	0.28731	6.178
24	0.27853	6.451
25	0.27853	6.724
26	0.27853	6.996
27	0.27028	7.269
28	0.27028	7.542
29	0.27028	7.851
30	0.2625	8.087
31	0.2625	8.36
32	0.2625	8.633
33	0.25516	8.906
34	0.25516	9.178
35	0.25516	9.451
36	0.24821	9.724
37	0.24821	9.996
38	0.24821	10.269
39	0.24163	10.542
40	0.24163	10.851
41	0.24163	11.087
42	0.2354	11.36
43	0.2354	11.633
44	0.2354	11.905

Table 8: Design frequencies and peak voltages for the buncher system.

Cell	Frequency [GHz]	Peak Voltage [MV/m]
45	0.23155	13
46	0.23155	13
47	0.22801	13
48	0.22801	13
49	0.22487	13
50	0.22487	13
51	0.22206	13
52	0.22206	13
53	0.2195	13
54	0.2195	13
55	0.21731	13
56	0.21731	13
57	0.21482	13
58	0.21482	13
59	0.21482	13
60	0.21226	13
61	0.21226	13
62	0.21226	13
63	0.2101	13
64	0.2101	13
65	0.2101	13
66	0.20827	13
67	0.20827	13
68	0.20827	13
69	0.20675	13
70	0.20675	13
71	0.20675	13
72	0.20549	13
73	0.20549	13
74	0.20549	13
75	0.20447	13
76	0.20447	13
77	0.20447	13
78	0.20365	13
79	0.20365	13
80	0.20365	13
81	0.20303	13
82	0.20303	13
83	0.20303	13
84	0.20257	13
85	0.20257	13
86	0.20257	13
87	0.20228	13
88	0.20228	13
89	0.20228	13
90	0.20213	13
91	0.20213	13
92	0.20213	13

Table 9: Design frequencies and peak voltages for the phase rotator system.

Upstream Position (m)	Length (m)	Inside Radius (m)	Radial Thickness (m)	Current Density (A/mm ²)
-4.325	6.00	0.35	0.15	8.0413
1.675	0.30	0.35	0.15	28.7796
2.175	0.15	0.35	0.15	-104.38
2.925	0.15	0.35	0.15	88.0
3.675	0.15	0.35	0.15	-94.22
4.425	0.15	0.35	0.15	99.26
5.175	0.15	0.35	0.15	-106.66
5.925	0.15	0.35	0.15	106.66
6.675	0.15	0.35	0.15	-106.66

Table 10: Matching region coil configuration.

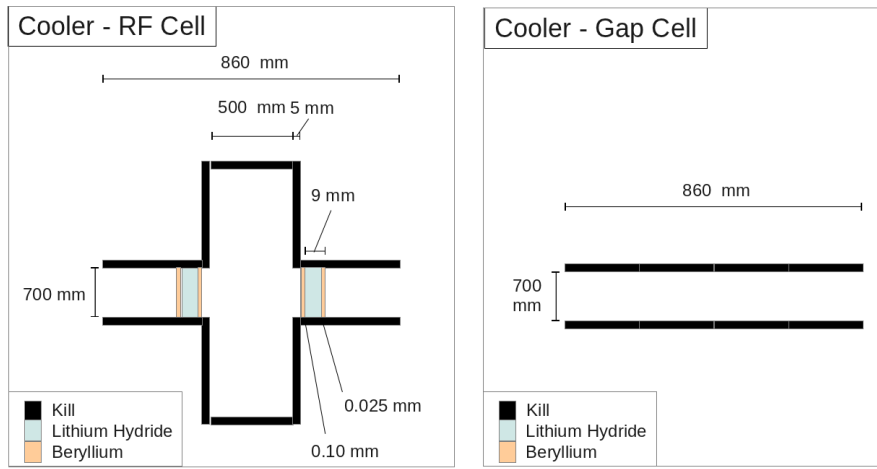


Figure 21: Schematic of a cell in the cooling channel proper.

Table 10.

The cooling section comprises 28 supercells, each of which comprises 5 cooling cells followed by an empty cell to provide space for bellows, diagnostics and other services (Fig. 21). Superconducting coils are placed between each RF cavity to provide the alternating field. The coils have inner radius 350 mm, outer radius 500 mm, length 150 mm and current density 106.66 A/mm². Coils are placed with coil centres every 860 mm, with coils swapping polarity every cell, giving a field of 2.8 T peak on-axis. RF cavities have a frequency of 201.25 MHz, operate with 16 MV/m gradient operating at a nominal 35° reference phase and are 0.5 m long. Cavity windows are made of 9 mm thick Beryllium-coated Lithium Hydride, which absorbs energy to provide ionisation cooling.

3.4.2 Capture Performance

The capture performance of the muon front end is shown in fig. 22. Overall, 0.066 good μ^+ are captured per 8 GeV proton on target. Muons are considered to be good if they fall within a momentum range of 100 to 300 MeV/c, a normalized transverse 4D amplitude of 30 mm and a longitudinal 2D amplitude of 150 mm. This is considered to be the nominal acceptance of the accelerator system.

In 2D, normalized amplitude is $a^2 mc / (\beta p)$, where a is the transverse size of the matched phase space ellipse on which the particle lies, m is the particle mass, β is the Courant-Snyder beta function, and c is the speed of light. The normalized transverse 4D amplitude is the sum of the horizontal and vertical transverse amplitudes, modulo correlations. The normalized longitudinal amplitude is the equivalent quantity for the longitudinal plane, which is approximately $(\Delta E)(\Delta t) / (mc)$, where ΔE is the energy difference from the average momentum, and δt is the time difference from the average time (where all bunches are aliased onto a single bunch). The calculation used for this study is more formally defined in [?].

A rapid loss of particles from the good region after 20 m can be attributed to the effect of the proton absorber. The number of particles within the good region increases rapidly in the phase rotator, with a more leisurely rise in the ionisation cooling section.

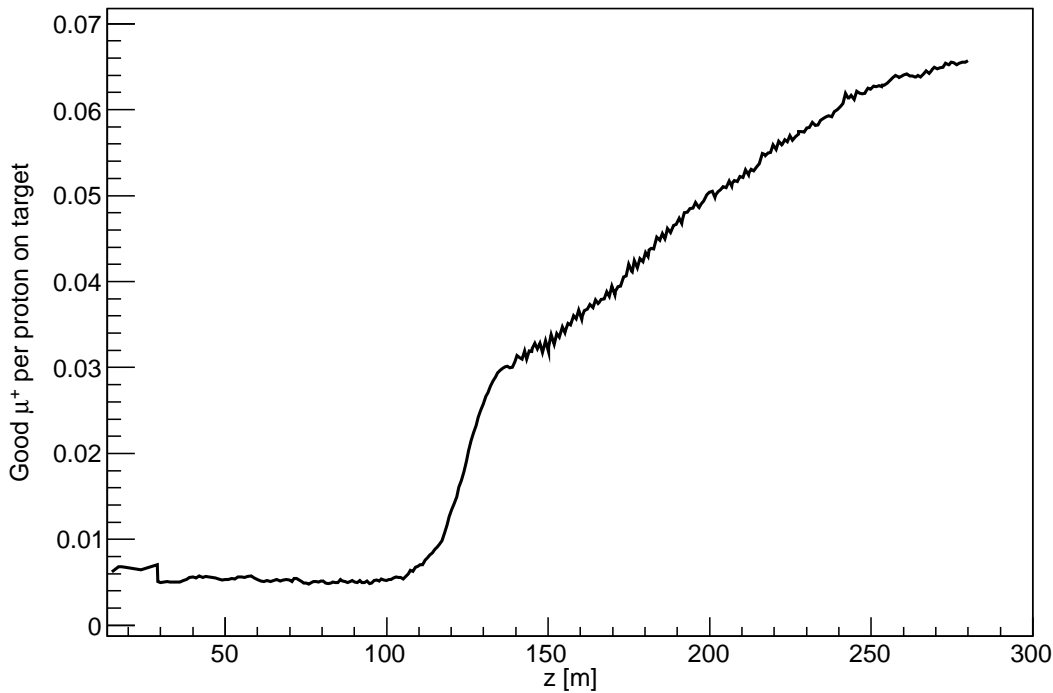


Figure 22: Number of muons captured by the front end, as simulated in ICOOL v3.20. TODO: negatives; error bars; G4BL capture, (G4BL version)

3.4.3 Activation of Components

Energy deposition has been identified as a serious issue in the muon front end, and a particle selection system has been designed to constrain the majority of hadronic losses in an active handling area near to the target region.

The efficacy of the particle selection system is demonstrated in fig. 23. The particle selection system reduces uncontrolled protonic losses by 2 orders of magnitude. Nonetheless 1.2 kW of proton beam power is lost outside of the active handling region, with roughly 0.2 kW lost at the interface between the phase rotator and cooler.

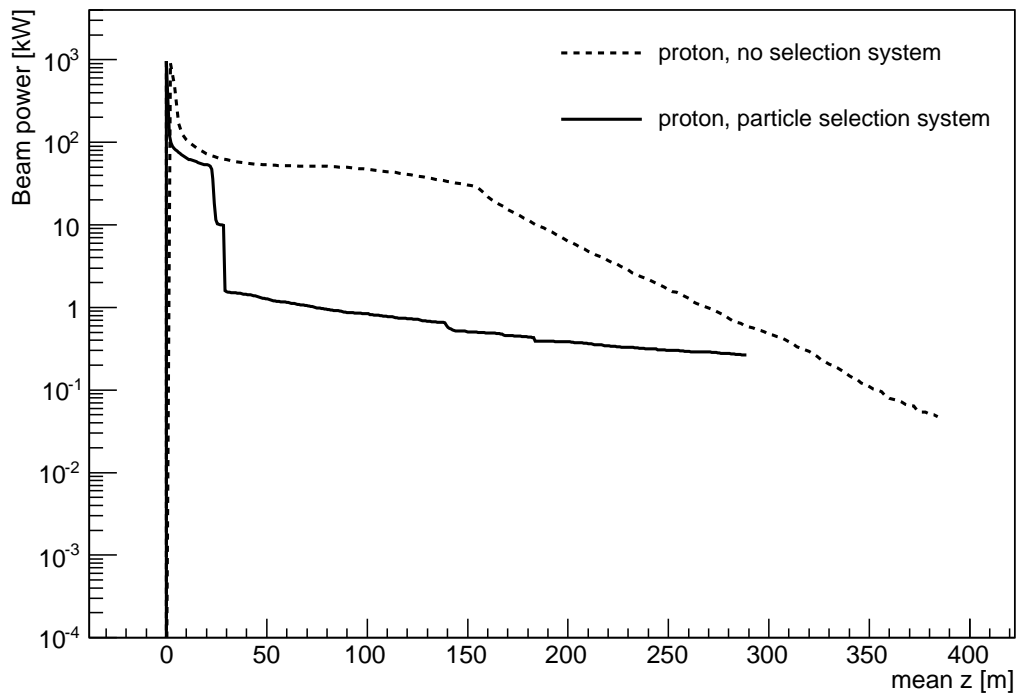
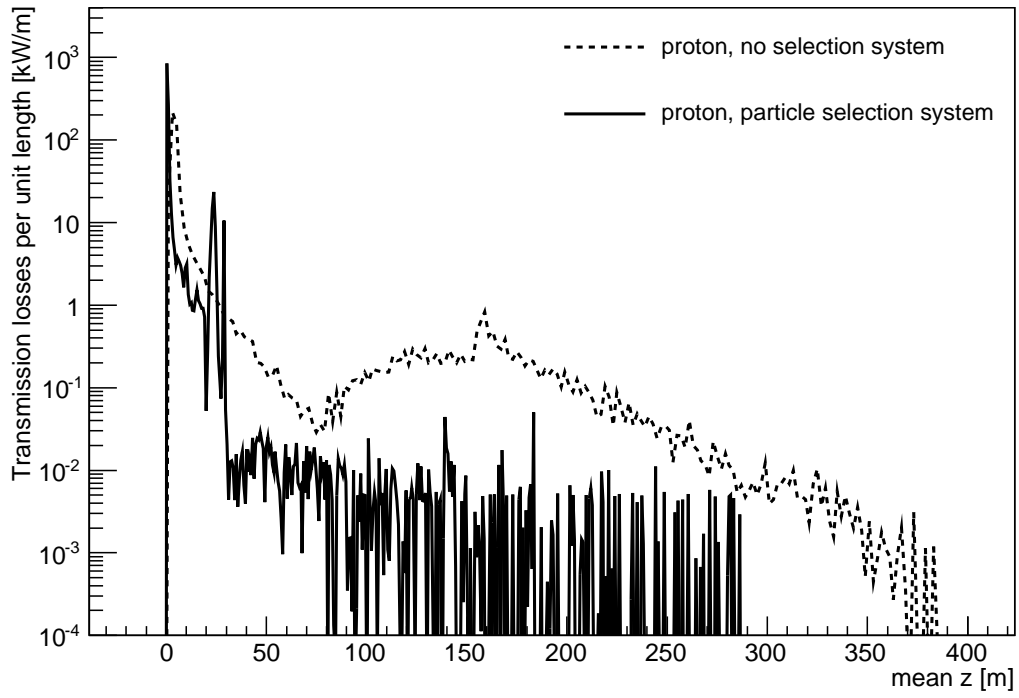


Figure 23: The (top) transmission losses of protons and (bottom) residual proton beam power in the muon front end are shown, as simulated in G4Beamline v2.06. (Dashed) without a particle selection system (Full) with the chicane and proton absorber as a particle selection system.

3.5 Acceleration

3.5.1 Introduction

Here we present a scheme to accelerate muons from the end of the cooling channel (244 MeV) to about 10 GeV - the energy required by the Neutrino Factory under study. To ensure an adequate survival rate for the short-lived muons, acceleration must occur at high average gradient. The accelerator must also accommodate the phase-space volume occupied by the beam after the cooling channel, which is still large [Ref. Cooling Channel Sec]. The need for large transverse and longitudinal acceptances drives the design of the acceleration system to low RF frequency, e.g. 201 MHz. High-gradient normal conducting RF cavities at these frequencies require very high peak power RF sources. Hence Superconducting RF (SRF) cavities are preferred. In the following we choose a SRF gradient of 15-17 MV/m, which will allow survival of about 85% of the muons as they are accelerated to 10 GeV.

3.5.2 Accelerator Complex

The proposed muon accelerator complex consists of a single-pass, 201 MHz SRF linac, that captures the large muon phase space coming from the cooling channel. The Pre-linac accelerates the muons to sufficiently relativistic energies (775 MeV kinetic energy) to facilitate efficient multi-pass acceleration in the RLA, while adiabatically decreasing the phase-space volume. The large acceptance of the linac requires large aperture (23 cm radius) and tight focusing. This combined with moderate beam energies favors solenoidal rather than quadrupole focusing for the entire linac. The Pre-linac is followed by the first Recirculating Linear Accelerator (RLA I) that further compresses and shapes the longitudinal and transverse phase-space, while increasing the energy to 2.8 GeV in in 4.5 passes. The beam is injected at the middle of 850 MeV SRF linac to minimize the effect of phase slippage for initially 0.8 GeV muon beam accelerated in a linac phased for the speed-of-light particle. In a “Dogbone” RLA the beams at the ends of the linac need to be directed into the appropriate energy-dependent “droplet” arcs (4) for recirculation. Finally, the RLA I is followed by the second, 4.5 pass RLA, based on 1.6 GeV SRF linac, that accelerates muons to 10 GeV. All linacs are based on 201 MHz SRF cavities; with the Pre-linac utilizing large aperture (23 cm radius), lower gradient (15 MV/m) cavity design, while RLA I and RLA II are configured with smaller aperture (15 cm radius), higher gradient (17 MV/m) cavities

For practical civil engineering reasons the in-plane horizontal layout of all three components is favored rather than a vertically stacked, somehow more compact configuration. All three accelerators are connected by compact transfer lines, configured as vertically separated double arcs, capable of transferring both charge species between consecutive acceleration stages.

The overall layout of the accelerator complex is shown in Fig. 24.

3.5.3 Initial Linac

Each linac cell is solenoid focused, and contains a solenoid and an RF cavity. There are two types of linac cells: a short 3 m long cell and a medium 5 m long cell. The short cell has a single-cell 201.25 MHz RF cavity with a 11.17 MV maximum energy gain for a speed of light particle, and the medium cell has a two-cell RF cavity with a 22.34 MV maximum energy gain. The solenoid fields increase down the line so as to maintain a tune per cell of 0.175, except for the solenoids in the last short cell and the first medium cell, whose fields are adjusted to match the beam between the two sections. The transition from short to medium cells occurs once the beam is small enough to fit within the 23 cm radius aperture of the RF cavities in the medium cells.

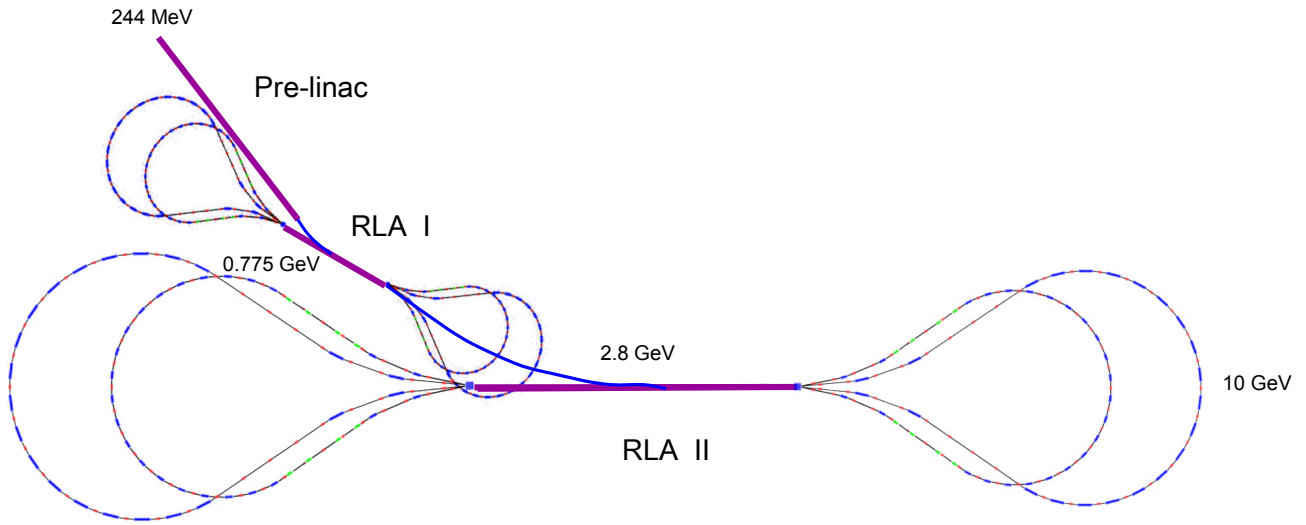


Figure 24: Layout of the accelerator complex: a single-pass Pre-linac to 0.775 GeV followed by a pair of 4.5-pass “Dogbone” RLAs: to 2.8 GeV and 10 GeV.

Table 11: Structure of cells in the initial linac. Fields and phases of individual cells are given in Table 12. Maximum energy gain for a speed of light particle in the cavities is 11.17 MV and 22.34 MV for the cavities in the short and medium cells, respectively.

	Short Length (m)	Medium Length (m)
Drift	0.455	0.710
Solenoid	1.000	0.100
Drift	0.500	0.100
Cavity	0.745	1.490
Drift	0.300	0.800
Total	3.000	5.000

Table 12: Initial linac phases and solenoid fields. Zero phase is maximum acceleration.

Short Cells		Long Cells	
RF Phase (deg.)	Solenoid Field (T)	RF Phase (deg.)	Solenoid Field (T)
73.3	-1.060	45.5	1.452
72.2	1.076	43.7	1.431
71.0	-1.093	41.9	-1.495
69.9	1.111	40.1	1.560
68.8	-1.130	38.4	-1.627
67.6	1.150	36.6	1.696
66.5	-1.171	34.9	-1.766
65.3	-1.193	33.3	1.838
64.2	-1.216	31.6	-1.911
63.0	-1.240	30.0	-1.985
61.8	-1.265	28.4	-2.061
60.7	-1.291	26.9	-2.137
59.5	-1.317	25.3	-2.215
58.4	-1.345	23.9	-2.293
57.2	-1.373	22.4	-2.373
56.1	-1.403	21.0	-2.453
55.0	-1.434	19.6	-2.535
53.8	-1.465	18.3	-2.616
52.7	-1.497	17.0	-2.699
51.5	-1.531	15.7	-2.782
50.4	-1.565	14.5	-2.865
49.3	-1.599	13.3	-2.949
48.2	-1.635	12.1	-3.034
47.1	-1.321	11.0	-3.118



Figure 25: Diagram of the RLA 1 linac layout. **F#** are the focusing quadrupoles, **D#** are the defocusing quadrupoles, and **C** are the cavities.

Table 13: Quadrupole gradients in the RLA 1 linac.

	Gradient (T/m)		Gradient (T/m)
		D1	−3.013
F2	3.013	D2	−3.082
F3	3.151	D3	−3.223
F4	3.288	D4	−3.363
F5	3.425	D5	−3.503
F6	3.562	D6	−3.644
F7	3.699	D7	−3.784

Parameters for the cells are given in Tables 11 and 12. The RF phases are chosen to initially have sufficient bucket area to capture the beam longitudinally, then to adiabatically increase the phase to improve the acceleration rate as the bucket area increases with energy. The design takes into account transit time factors in the cavities, transverse RF focusing, and a correction to the focusing at the ends of the solenoids to take into account the finite distance over which the solenoid field drops to zero. That correction is a cylindrically symmetric defocusing kick of the form

$$\Delta p_x = \frac{q^2 B^2 a}{8p} x \quad (9)$$

at each end, where p_x is the momentum in the x direction, x is the displacement in that direction, p is the total momentum, B is the solenoid field, q is the particle charge, and a is the solenoid radius. For our case, a is 23 cm.

3.5.4 Recirculating Linear Accelerators

The linac in RLA 1 is a quadrupole-focused FODO lattice, arranged as shown in Fig. 25. Quadrupoles are 50 cm long, and have a 149 cm cavity centered between them, except between the D1 and F2 quadrupoles, where that 149 cm is a drift instead. The space between each quadrupole and the adjacent cavity is 50.5 cm. There is 20.5 cm between the D7 quadrupoles and the end of the linac. The RF cavities are identical to the two-cell cavities in the initial linac. The beam goes through the cavity 20.5 deg. off crest, chosen such that the beam has an energy gain in the linac of 600 MeV. The quadrupole gradients are chosen to keep the phase advance 90° for each cell on the initial half-pass through the linac, and to be reflection-symmetric about the center. These gradients are given in Table 13.

The beam is returned to the linac by four “dogbone” arcs that bend outward, inward, then outward again. The FODO arc cells are designed to have a 90° phase advance, with cells on the ends matching between the arc and the linac. The lattice structure for these arcs is shown in Fig. 26, with Tables 14–16 containing the lattice parameters.

Table 14: Lattice parameters in the arcs. Cells are FODO lattices, with distances between quadrupole centers being half of the cell length. Horizontally bending dipoles are centered between quadrupoles and are rectangular, except for arcs 3 and 4 of RLA2, where there are two horizontally bending dipoles separated by 50 cm, with the pair centered between the quadrupoles (lengths given in the table are for each dipoles). Layouts near the spreader are given in Table 15, and in the regions with vertical bending dipoles (also rectangular) are given in Table 16.

	RLA 1				RLA 2			
	Arc 1	Arc 2	Arc 3	Arc 4	Arc 1	Arc 2	Arc 3	Arc 4
F1 (T/m)	3.462	4.331	4.553	4.963	3.004	3.955	3.352	3.906
D1 (T/m)	-3.528	-4.145	-4.779	-5.034	-2.777	-3.799	-3.930	-4.208
F2 (T/m)	3.214	4.051	4.708	4.995	2.829	3.425	4.045	4.390
D2 (T/m)	-3.237	-3.997	-4.778	-5.009	-2.814	-3.511	-3.792	-4.244
F4 (T/m)	3.300	4.015	5.062	5.302	2.890	3.572	4.337	4.804
D4 (T/m)	-3.380	-3.948	-4.748	-4.890	-2.934	-3.596	-3.785	-4.123
F5 (T/m)	3.592	4.261	5.080	5.453	3.330	3.922	3.920	4.177
D5 (T/m)	-3.380	-3.948	-4.859	-4.891	-2.924	-3.601	-3.811	-4.166
F6 (T/m)	3.324	4.079	5.000	5.407	3.019	3.751	4.142	4.524
D6 (T/m)	-3.096	-3.793	-4.675	-4.766	-2.694	-3.434	-3.704	-4.176
Fi (T/m)	3.474	4.226	4.769	5.197	3.004	3.684	4.169	4.553
Di (T/m)	-3.235	-3.971	-4.448	-4.872	-2.777	-3.453	-3.906	-4.289
Quad. lengths (m)	0.50	0.50	0.50	0.50	1.00	1.00	1.00	1.00
BS (T)	-0.7046	-0.6804	-0.6514	-0.6518	-1.2186	-1.1692	-1.2231	-1.0056
Bo (T)	-0.7082	-0.6840	-0.8068	-0.7465	-1.2248	-1.1751	-1.3870	-1.3728
Bi (T)	0.7648	0.7308	0.7843	0.7690	1.3243	1.2694	1.3742	1.3567
Bo/Bi length (m)	1.00	1.50	2.00	2.50	2.00	3.00	2.00	2.50
V+ (T)	-0.8722	0.8357	—	—	-1.2772	1.2582	—	—
V- (T)	0.8722	-0.8357	—	—	1.2772	-1.2582	—	—
Cell length (m)	6.00	7.00	8.00	9.00	12.00	14.00	16.00	18.00

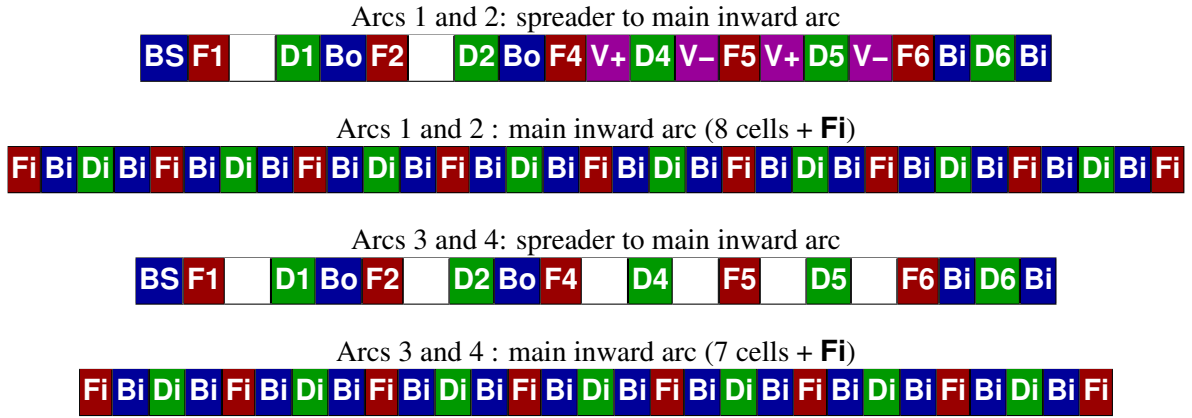


Figure 26: Lattice layout for the RLA arcs. **F_x** are the focusing quadrupoles, **D_x** are the defocusing quadrupoles, **Bo** are outward bending dipoles, **Bi** are inward bending dipoles, **BS** are the separation dipoles, and **V_x** are vertically bending dipoles. Starting at the separation dipole, “spreader to the main inward arc” connects to the “main inward arc,” then “spreader to the main inward arc” is reversed to get back to the separation dipole. Arcs 1 and 3 share a common **BS**, as do arcs 2 and 4. Layouts for RLA 1 and 2 are identical, except that in arcs 3 and 4 of RLA 2, **Bi** and **Bo** consist of two dipoles separated by 0.5 m.

Table 15: Layout near the spreader for the RLA arcs. The length given for Bo in arcs 3 and 4 of RLA 2 consists of two equal length dipoles separated by 0.50 m.

	Length (m)							
	RLA 1				RLA 2			
	Arc 1	Arc 2	Arc 3	Arc 4	Arc 1	Arc 2	Arc 3	Arc 4
BS	1.00	1.50	1.00	1.50	2.00	3.00	2.00	3.00
Drift	1.50	1.50	2.50	2.50	3.00	3.00	3.75	4.25
F1	0.50	0.50	0.50	0.50	1.00	1.00	1.00	1.00
Drift	2.50	2.50	3.50	4.00	5.00	6.00	7.00	8.00
D1	0.50	0.50	0.50	0.50	1.00	1.00	1.00	1.00
Drift	0.75	0.75	0.75	0.75	1.50	1.50	1.25	1.25
Bo	1.00	1.50	2.00	2.50	2.00	3.00	4.50	5.50
Drift	0.75	0.75	0.75	0.75	1.50	1.50	1.25	1.25
F2	0.50	0.50	0.50	0.50	1.00	1.00	1.00	1.00
Drift	2.50	2.50	3.50	4.00	5.00	6.00	7.00	8.00
D2	0.50	0.50	0.50	0.50	1.00	1.00	1.00	1.00

Table 16: Layout for RLA 1 in the regions with vertical bends.

	Lengths (m)			
	RLA 1		RLA 2	
	Arc 1	Arc 2	Arc 1	Arc 2
F4	0.500	0.500	1.000	1.000
Drift	0.192	0.120	0.413	0.1446
V+	0.750	0.900	0.750	0.900
Drift	1.558	1.980	3.837	4.9554
D4	0.500	0.500	1.000	1.000
Drift	0.130	0.120	0.900	1.289
V-	0.750	0.900	0.750	0.900
Drift	1.620	1.980	3.350	3.811
F5	0.500	0.500	1.000	1.000
Drift	1.620	1.980	3.350	3.811
V+	0.750	0.900	0.750	0.900
Drift	0.130	0.120	0.900	1.289
D5	0.500	0.500	1.000	1.000
Drift	1.558	1.980	3.837	4.9554
V-	0.750	0.900	0.750	0.900
Drift	0.192	0.120	0.413	0.1446
F6	0.500	0.500	1.000	1.000

3.6 Decay Ring

In the Neutrino Factory neutrinos are generated from muon decays according to:

$$\mu^- \rightarrow e^- \bar{\nu}_e \nu_\mu; \text{ and } \mu^+ \rightarrow e^+ \nu_e \bar{\nu}_\mu. \quad (10)$$

Neutrinos are aimed at near and far detectors by collecting muons in a storage ring with long straight sections pointing at a distant experimental facility. The storage ring dips into the ground with an angle of 9° for a 2000 km baseline.

Since the decay ring needs to serve a single baseline, a racetrack geometry, which can direct neutrinos resulting from the decays of both muon charges to the same far detector, is the logical option (triangular and bow-tie rings were considered in the IDR to serve two baselines). The racetrack ring is designed to store counter-rotating muon bunches with each long straight serving as production sections for either μ^+ or μ^- . The neutrino production efficiency η_p is defined as the length of the production straight divided by the ring circumference. In this design η_p is 35.56% which is a reasonable tradeoff between physics, geology considerations and cost.

There will be at most three μ^+ and three μ^- bunch trains in the ring. The bunch trains, 250 ns long at injection, will debunch due to their finite momentum spread and the non-zero phase-slip in the ring. Until the muon bunches have decayed in sufficient numbers, a 100 ns gap between the neutrino bursts arising from the μ^+ and the μ^- bunches should be maintained. In addition, the circumference must be large enough to allow sufficient rise/fall time for the injection kickers. Finally, there should be a rational relation between the orbit periods of the proton driver and the decay ring to ensure equal spacing of the injected bunches.

The optical properties of the ring are challenging. In order to keep the neutrino flux uncertainty sufficiently small, the rms divergence of the muon beam in the production straight section must not exceed 10% of the natural angular divergence of $1/\gamma$ that arises from the kinematics of muon decay. This requirement translates into high values for the β -functions in the production straights (~ 70 m) which need to be matched into the low values of ~ 14 m in the arcs. At the ends of each straight, small bending magnets are included to ensure that neutrinos created in the matching section (where the muon beam still has a large divergence angle) cannot be seen by the detector.

In order to allow a realistic injection scenario, a dedicated injection insertion is included. Injection into the production section is challenging owing to the low phase advance per cell and large transverse β , leading to high kicker peak fields and aperture requirements. Injecting into the arc is precluded since the elements there are tightly packed. A dedicated dispersion-free injection section is therefore located between the matching to the production straight and the arc.

From the center of the upper (closest to the surface) to the center of the lower arc, the ring structure is:

- Upper arc using FODO cells (Table 18)
- Dispersion suppression section, like the arc cells but with different dipoles (Table 18)
- Matching section (Table 19)
- Injection section with a triplet structure (Table 20)
- Matching section with a small amount of bend (Table 21)
- Production straight using FODO cells (Table 22)
- Matching section with a small amount of bend (Table 23)
- Lower arc (Table 24)

The lattice is reflection-symmetric about the centers of the arcs. Figure 27 gives a diagram of the ring. The principal ring parameters are listed in Table 17. Figure 28 shows the lattice functions for the ring. Assuming the total momentum spread is given by $\delta = 0.05$, the beam can circulate for ten mean decay times (400 turns) before the neutrino signal gap drops below 100 ns.



Figure 27: Decay ring geometry. The injection point is indicated.

Table 17: Ring Parameters

Production straight	562.0×2	m
Upper arc (incl. disp supp)	121.155	m
Lower arc	112.729	m
Insertion	46.4×2	m
Matching sections (total)	104.987	m
Circumference	1555.672	m
Width of ring	74.565	m
Length of ring	737.228	m
Angle of inclination	10	deg
Maximum depth of ring	128.02	m
Production efficiency η_p	$36.1\% \times 2$	
Total tune (H,V)	14.77, 13.73	
Chromaticity (H,V)	-17.11, -20.23	
Phase slip η	2.8×10^{-3}	
Turns per mean lifetime	40.07	

The lattice, subdivided into its main parts (straights, arcs, insertion and matching sections), is described in tables 18–24. Assuming a 30% aperture beyond the beam envelope, the production straight quadrupoles have an inner radius of 20 cm and pole tips of 0.1 T; for the arc quadrupoles, 8 cm and 1.4 T; and for the insertion quadrupoles 22.5 cm and 2.9 T (taking into account the injected beam excursion).

Table 18: Lattice for the upper arc. There are 11 repeating cells and 3 dispersion suppressor cells (at either end) with one missing and three modified dipoles. The magnet aperture (inner radius) is given by the beam envelope plus 30%. The magnet type (superconducting, SC, or normal, NC) is given in the column headed “Type”.

Element	Length (m)	Field/Gradient (T/Tm ⁻¹)	Aperture (m)	Type
Repeating cell × 11				
QD	0.8	-16.26	0.079	SC
Drift	0.3			
Dipole	2.139	-1.6	0.071	SC
Drift	0.3			
QF	0.8	16.26	0.079	SC
Drift	0.3			
Dipole	2.139	-1.6	0.071	SC
Drift	0.3			
Cell length	7.08			
Dipoles in 3 dispersion suppressor cells				
Dipole	2.139	-1.597	0.071	SC
Dipole	2.139	-1.6	0.071	SC
Dipole	2.139	-0.971	0.071	SC
Dipole	2.139	-1.6	0.071	SC
Dipole	2.139	-0.632	0.071	SC
Arc length	121.16			

Table 19: Lattice for matching section between end of upper arc and insertion. There are two such matching sections at either end of upper arc. Note the final quadrupole is identical to an insertion QF. The magnet aperture (inner radius) is given by the beam envelope plus 30%. The magnet type (superconducting, SC, or normal, NC) is given in the column headed “Type”.

Element	Length (m)	Field/Gradient (T/Tm ⁻¹)	Aperture (m)	Type
Drift	0.51			
QF	0.8	7.55	0.067	SC
Drift	1.92			
QF	0.8	23.903	0.075	SC
Drift	0.568			
QD	0.8	-20.721	0.108	SC
Drift	0.5			
QD	1.6	-1.691	0.101	SC
Drift	0.5			
QF	0.8	12.84	0.064	SC
Matching section length	8.793			

Table 20: Lattice for one of the 4 FDF insertion cells. The septum or kicker magnets (defined in Table 44) are located in the long drifts as shown in (Fig. 150). The minimum and maximum aperture for each magnet type is shown. The magnet aperture (inner radius) takes into account both the injected beam trajectory and the beam envelope (plus 30%). The magnet type (superconducting, SC, or normal, NC) is given in the column headed “Type”.

Element	Length (m)	Field/Gradient (T/Tm ⁻¹)	Aperture (m)	Type
QF	0.8	12.84	0.079 - 0.225	SC
Drift	0.5			
QD	1.6	-11.61	0.093 - 0.169	SC
Drift	0.5			
QF	0.8	12.84	0.079 - 0.225	SC
Drift	3.7			
Cell length	11.6			
Insertion length	46.4			

Table 21: Lattice for matching section between the insertion and the production straight. There are two such matching sections on either side of the racetrack. The magnet aperture (inner radius) is given by the beam envelope plus 30%. The magnet type (superconducting, SC, or normal, NC) is given in the column headed “Type”.

Element	Length (m)	Field/Gradient (T/Tm ⁻¹)	Aperture (m)	Type
Drift	0.5			
Dipole	2.0	-1.063	0.067	SC
Drift	1.5			
QF	0.4	20.935	0.073	SC
Drift	2.1			
Dipole	2.0	0.860	0.171	SC
Drift	3.5			
QD	0.4	-8.524	0.258	SC
Drift	1.2			
QD	0.8	-6.391	0.256	SC
Drift	1.2			
QF	0.4	16.895	0.19	SC
Drift	1.2			
Dipole	2.0	-0.320	0.189	SC
Drift	1.2			
Matching section length	20.4			

Table 22: Lattice for a production cell. There are 28 such cells in each of the two straights. The magnet aperture (inner radius) is given by the beam envelope plus 30%. The magnet type (superconducting, SC, or normal, NC) is given in the column headed “Type”.

Element	Length (m)	Field/Gradient (T/Tm⁻¹)	Aperture (m)	Type
QF	2.0	0.596	0.195	NC
Drift	8.0			
QD	2.0	-0.596	0.195	NC
Drift	8.0			
Cell length	20.0			
Straight length	562.0			

Table 23: Lattice for matching section between lower arc and the production straight. There are two such matching sections on either side of the racetrack. The magnet aperture (inner radius) is given by the beam envelope plus 30%. The magnet type (superconducting, SC, or normal, NC) is given in the column headed “Type”.

Element	Length (m)	Field/Gradient (T/Tm⁻¹)	Aperture (m)	Type
Drift	0.9			
Dipole	2.0	0.591	0.077	SC
Drift	1.5			
QF	0.4	14.231	0.106	SC
Drift	5.0			
Dipole	2.0	-0.645	0.159	SC
Drift	3.5			
QD	0.4	-6.555	0.230	SC
Drift	1.1			
QD	0.8	-5.729	0.231	SC
Drift	1.1			
QF	0.4	12.186	0.187	SC
Drift	1.1			
Dipole	2.0	-0.468	0.189	SC
Drift	1.1			
Matching section length	23.3			

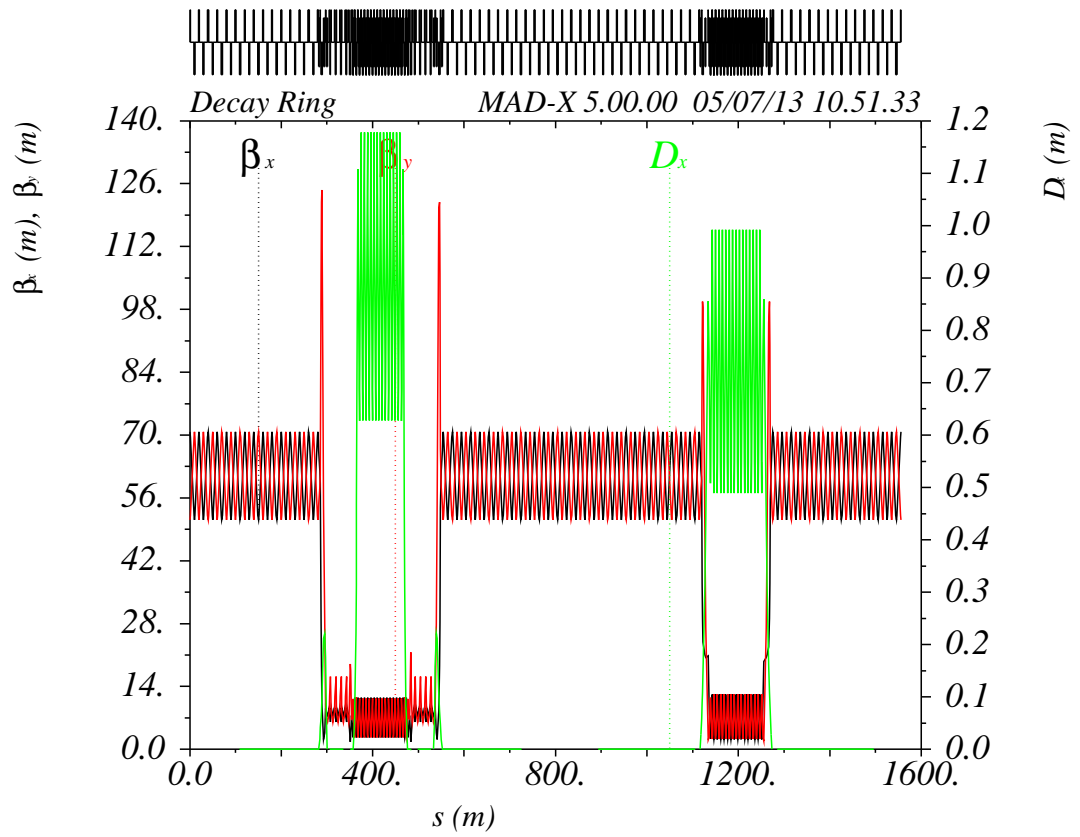


Figure 28: Decay ring optics. The origin corresponds to the middle of a production straight and the optics of the upper part of the ring are shown on the left.

Table 24: Lattice for one of the fifteen lower arc cells. The magnet aperture (inner radius) is given by the beam envelope plus 30%. The magnet type (superconducting, SC, or normal, NC) is given in the column headed “Type”.

Element	Length (m)	Field/Gradient (T/Tm ⁻¹)	Aperture (m)	Type
QD	0.8	-16.76	0.081	SC
Drift	0.395			
Dipole	2.139	-1.6	0.072	SC
Drift	0.395			
QF	0.8	17.25	0.081	SC
Drift	0.395			
Dipole	2.139	-1.6	0.072	SC
Drift	0.395			
Cell length	7.456			
Arc length	112.729			

Table 25: Baseline parameters for the Magnetised Iron Neutrino Detectors at a Neutrino Factory.

Distance (km)	2000
Fiducial mass (kT)	100
Size iron plates (cm ³)	$1400 \times 1400 \times 3 \times (2\sqrt{2} - 2)$
Length detector (m)	140
Number iron plates	2800
Maximum dimensions scintillator bars (cm ³)	$1400 \times 3.5 \times 1$
Number scintillator bars per plane	400
Total number of scintillator bars	2.24×10^6
Total number of readout channels	4.48×10^6
Photon detector	SiPMT
Magnetic field (T)	$1 < \mathbf{B} < 2.2$

4 Detector systems for the Neutrino Factory

4.1 Introduction

4.1.1 Baseline description for the far detectors

The IDS-NF baseline for the Neutrino Factory has been optimised as described in section 2. The optimum strategy to measure δ and the mass hierarchy, given a large θ_{13} , requires a single detector, with a 100 kTon fiducial mass, at 2000 km. The detector is optimised to carry out the detection of the “golden channel” ($\nu_e \rightarrow \nu_\mu$) through the wrong-sign muon signature. This strategy is more efficient for resolving degeneracies in the neutrino-oscillation formulae and provides better sensitivity than, for example, measuring the golden and the “silver” channel ($\nu_e \rightarrow \nu_\tau$) simultaneously.

The original “golden channel at a Neutrino Factory” analysis [118] assumed a cylindrical geometry with a cross-sectional radius of 10 m, with iron plates 6 cm thick, scintillator planes 2 cm thick and a 1 T solenoidal field operating at a 50 GeV Neutrino Factory. The International Scoping Study (ISS) [119, 120] assumed a cuboidal geometry of $14 \times 14 \text{ m}^2$ with 4 cm thick iron and 1 cm thick scintillator and a 1 T dipole field, while operating at a 25 GeV Neutrino Factory.

For the most recent studies we have adopted a baseline octagonal geometry with a cross-sectional height and width of 14 m, as shown in figure 29, and length of 140 m (with a total iron mass of 107.4 kTon). The thickness of each plane of iron is 3 cm, followed by two planes of scintillator, each with 1 cm thickness. The three planes form a module of thickness 5 cm. The lateral resolution requirement is 1 cm, which is provided by having co-extruded scintillator bars 3.5 cm wide, read out using optical fibres and silicon photo-multipliers (SiPMT). Table 25 lists the key parameters of the detector.

In section 4.2.2 we have studied the engineering aspects of this realistic octagonal geometry, with a toroidal field between 1 T and 2.2 T over the whole fiducial area. These parameters can be achieved with a 100 kA/turn current traversing the centre of the MIND plates and are shown to be feasible to manufacture. This geometry has been simulated, using the magnetic field map generated from the finite element simulations, as described in section 4.2.1.

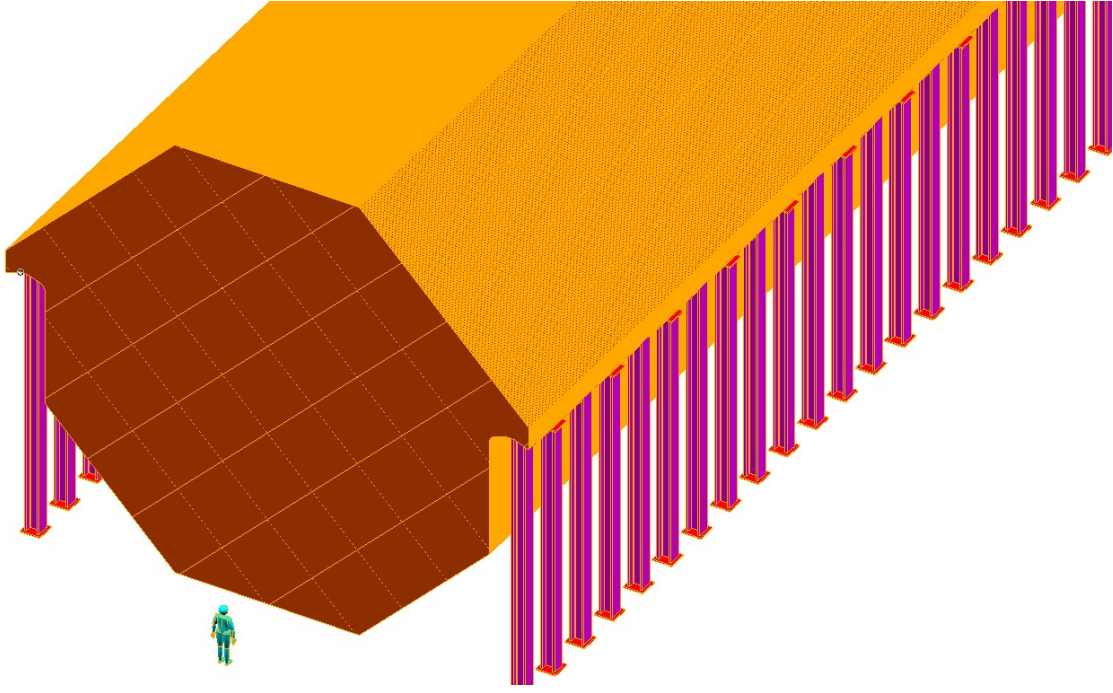


Figure 29: Schematic drawing of the Magnetised Iron Neutrino Detector (MIND).

4.1.2 Baseline description for the near detectors

The baseline for the Neutrino Factory includes the need for at least two near detectors, designed to carry out measurements essential to the sensitivity of the oscillation-physics programme. It is necessary to have one near detector for each of the straight sections of the storage ring at each of the two polarities. The near-detector measurements that are essential for the neutrino oscillation analysis are:

- Determination of the neutrino flux through the measurement of neutrino-electron scattering;
- Measurement of the neutrino-beam properties that are required for the flux to be extrapolated with accuracy to the far detectors;
- Measurement of the charm production cross sections (charm production in far detectors is one of the principal backgrounds to the oscillation signal); and
- Measurement of the neutrino-nucleon deep inelastic, quasi-elastic, and resonant-scattering cross sections.

The intense neutrino beam delivered by the Neutrino Factory makes it possible to carry out a unique neutrino-physics programme at the near detectors. This programme includes fundamental electroweak and QCD physics, such as measurements of parton distribution functions as a function of Q^2 and Bjorken x , QCD sum rules, nuclear re-interaction effects, strange particle production and a precise measurement of $\sin^2 \theta_W$. The near detector must also be capable of searching for new physics, for example by detecting tau-leptons which are particularly sensitive probes of non-standard interactions at source and at detection. Tau neutrino detection is also important in the search for sterile neutrinos.

Here we itemise the general design features of the near detector:

- A detector with micron-scale resolution for charm and tau identification (either a silicon vertex or an emulsion-based detector);
- A low- Z , high-resolution target for flux and ν_μ - and ν_e -leptonic cross-section measurements (i.e., a scintillating-fibre tracker or a straw-tube tracker);
- A magnetic field for charged particle momentum measurement (with $\delta p/p \sim 1\%$ (for $p \sim 2 - 3$ GeV);

- A muon catcher for muon identification;
- Electron identification capabilities;
- Excellent energy resolution for flux extrapolation: this needs to be better than for the far detector, so the goal is to achieve $\delta E/E \sim 1\%$; and
- A variety of nuclear targets to measure cross-sections in iron and as a function of the nuclear target mass number A .

There are two options currently being considered: one which includes a high resolution scintillating fibre tracker and the other includes a transition-radiation straw-tube tracker. Both of these options are studied to determine their capabilities and a summary of their performance is included in this report.

4.2 Far Detectors

4.2.1 Magnetised Iron Neutrino Detector Performance

4.2.1.1 Introduction

The understanding of the momentum reconstruction and charge selection characteristics of a MIND (Magnetized Iron Neutrino Detector) is underpinned by a detailed simulation and reconstruction. A sophisticated analysis has also been developed to select signal events from background. Each of these elements were developed in a modular architecture so that development could be completed in parallel.

4.2.1.2 Simulation and reconstruction

Simulations of neutrino events in MIND are generated using GENIE [121] with the transport of interaction daughter particles through the detector done in GEANT4 (v9.4 patch 1) [122]. A description of this simulation has been previously presented [21]. The simulated MIND consists of repeating modules consisting of a 3 cm steel plate, and a 2 cm scintillating plane. An air gap of 1 mm is placed between each element of the detector. Hadron interactions are provided using the QGSP_BERT library in GEANT4 [122]. The magnetic field map generated by the finite element simulation of the MIND steel plate assuming a current of $100 \text{ kA} \times \text{turn}$ is used by the GEANT simulation to provide the magnetic field in the steel as shown in figure 30. Electromagnetic fields outside the steel are assumed to be zero.

The segmentation of the detector is not explicitly simulated. Instead the segmentation, signal attenuation, and smearing is implemented in a digitization algorithm. The sites of energy deposition are clustered into voxel units, $3 \times 3 \text{ cm}^2$ corresponding to the scintillator bar width. Gaussian smearing with a resolution width set by the segmentation; that is $\sigma \approx 3 \text{ cm}/\sqrt{12} \approx 1 \text{ cm}$ is applied to the hit positions prior to clustering. A 5 m attenuation length for light is assumed along the wavelength shifting fibre within each scintillator bar. To account for quantum efficiencies in the SiPMs, a hit cluster must contain the equivalent energy deposition of 4.5 photon electrons.

Muons and hadronization are identified from the digitized events through use of a reconstruction algorithm. The reconstruction is described in detail [21] but some changes have been made to the pattern recognition and fitting procedure to reduce the track muon mis-identification rate by fitting for multiple tracks in an event. Both the pattern recognition and trajectory fits rely on Kalman algorithms provided by the RecPack toolkit [123].

Pattern recognition is an iterative process which starts by identifying the largest set of single hits in a plane. An estimate of the momentum is taken from the geometric length of the track to seed a Kalman filter algorithm. The Kalman filter then sorts the remaining hits in the event into the track. Those hits that are not sorted into

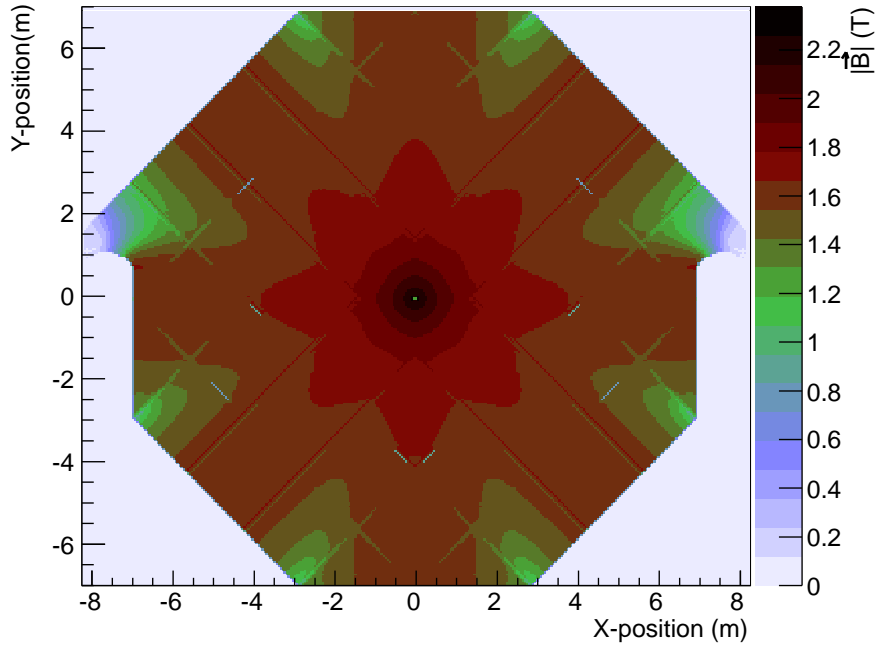


Figure 30: Magnetic field map used for the tracking of particles through the steel plates in the simulation and reconstruction.

this first track are subject to additional passes of this track sorting algorithm until 5 hits or fewer remain. The number of tracks identified per event in a sample of 10^6 ν_μ CC interactions is shown in Fig. 31.

All of the tracks identified by the pattern recognition are passed to a Kalman fitting algorithm to determine the momentum and charge of the track from a fit to a helix with a momentum dependent energy loss. The Kalman algorithm is seeded using momentum from the range of the track [124] assuming that it is a muon. Each track is fit with multiple passes of the Kalman fitting algorithm forward and backward along the track. All of the fits assume that particles are travelling in the positive z direction. After the fit of all tracks is complete, the longest track is assumed to be the muon, and all other tracks and hits constitute the hadronization. For the set of potential tracks passed to the reconstruction the algorithm is 99% efficient while the charge identification of those events is correct in 82% of cases for a ν_μ CC sample or 92% of cases for a $\bar{\nu}_\mu$ CC sample, assuming that the detector focuses positive charges. These efficiencies are slightly different for a negative-charge focusing detector as shown in Fig. 32. The charge identification is stable for muon momenta greater than 2 GeV/c as shown in Fig. 32(b) with complementary changes for the μ^- focusing efficiencies. Similar trends appear in the reconstruction efficiencies represented in Fig. 32(a).

The reconstruction includes a number of important new features that make improvements in this analysis over previous publications. The foremost of these improvements allows for the use of a magnetic field map for tracking a trajectory through the detector. Similarly, a momentum dependent energy loss has been implemented. These improvements produce visible changes in the pulls in the fitting variables used in the helical description of the trajectory. Distributions of the five variables used to describe the helix, the initial positions X and Y , the initial slopes of the helix dx/dz and dy/dz , and the charge over the momentum q/p , are shown in figure 33. The pulls in the helix position X and Y indicate no bias in the measurement, although an underestimate of the error in the position is evident as the widths of the distributions are larger than expected. The same can be said for the pulls in the initial slope of the tracks. The momentum pull, however, has a width close to

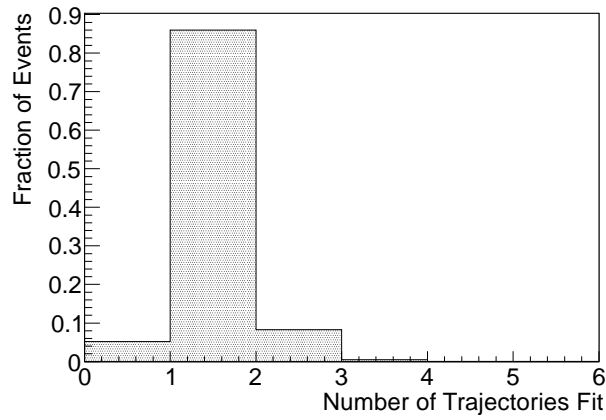


Figure 31: Track multiplicity for a ν_μ CC sample of 10^6 interactions.

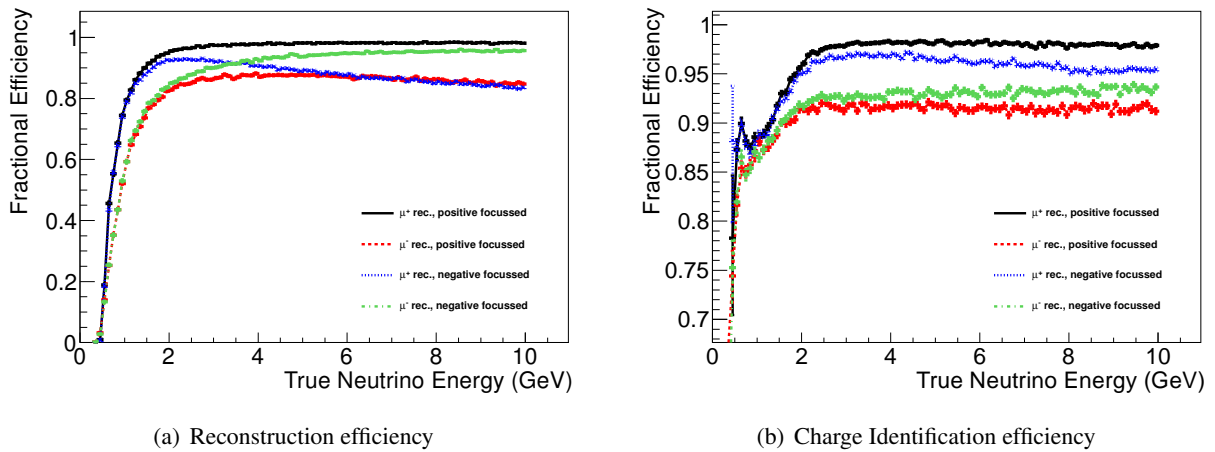


Figure 32: Reconstruction efficiency (a) and rate of correct charge identification (b) among reconstructed tracks for muon neutrino and anti-neutrino CC interactions with both detector magnetic field polarities.

one indicating that the uncertainty has been appropriately estimated. The bias in the momentum indicates that there is a systematic underestimate of the momentum, possibly because the energy loss correction is too large. However this is acceptable given the parametrization of the helix. The momentum resolution strongly depends on the momentum of the muon fit. The mean resolution was fit to the polynomial

$$\left\langle \frac{\sigma_{1/p}}{1/p} \right\rangle = q_0 + \frac{q_1}{p^2} + \frac{q_2}{p} + q_3 p + q_4 p^2 \quad (11)$$

over the muon momentum range between 1 GeV/c and 10 GeV/c as shown in figure 34.

Hadron hits from non-muon tracks and unassigned hits are grouped into a rudimentary reconstruction of the hadron direction and energy. A centroid for the non-muon hits is calculated from the hit positions. The direction of hadronization is determined from the vector between the event vertex and the centroid of hadron hits. The angle between the true hadron direction and the reconstructed hadron direction shows a high degree of consistency as presented in figure 35.

The hadron energy is the smeared true hadron energy determined from the difference of the neutrino and primary lepton energy defined by GENIE. In the physical detector the hadron energy is to be reconstructed from the sum of the energy deposited by the hadron hits in the scintillator. This underestimates the true hadron energy in this simulation. Thus, the hadron reconstruction is considered a work in progress. When there are hadron hits present the reconstructed neutrino energy is

$$E_\nu^{rec} = E_\mu^{rec} + E_{had}^{rec} \quad (12)$$

where E_{had}^{rec} is the reconstructed hadron energy and is derived from the true hadron energy, E_{had} , smeared by δE_{had} using the results of the MINOS CalDet testbeam [125];

$$\frac{\delta E_{had}}{E_{had}} = \frac{0.55}{\sqrt{E_{had}}} \oplus 0.03. \quad (13)$$

This result is expected to be reproduced and refined at the proposed AIDA testbeam facility at CERN [126].

In the case when there are no hadron hits visible, the neutrino energy is reconstructed using the quasi-elastic approximation

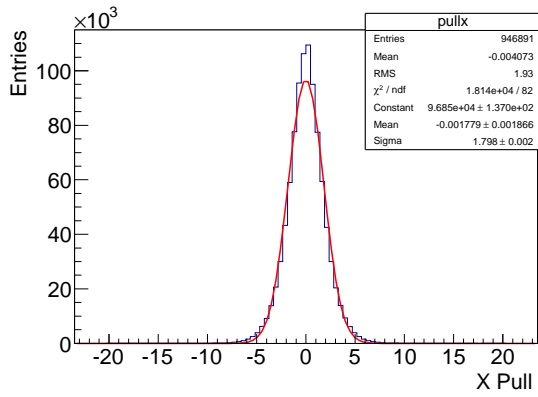
$$E_\nu = \frac{m_N E_\mu + \frac{1}{2}(m_{N_X}^2 - m_\mu^2 - m_N^2)}{m_N - E_\mu + |p_\mu| \cos \theta} \quad (14)$$

where θ is the angle between the muon direction and the beam direction, m_N is the mass of the initial state nucleon, and m_{N_X} is the mass of the outgoing nucleon. This equation only assumes energy and momentum conservation, and so it is applicable to a large subset of events appearing in the detector. When there are tracks present in a $\bar{\nu}_\mu$ CC event, there are no hadron hits present in 25% of events.

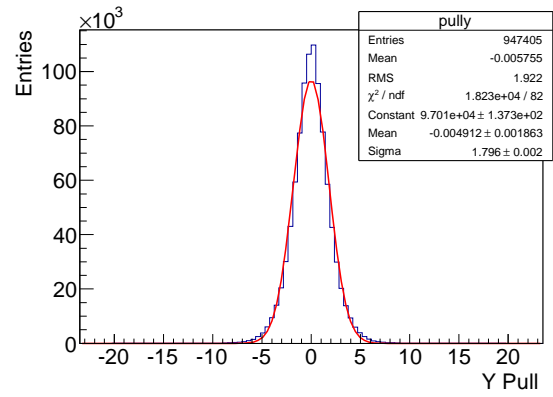
4.2.1.3 Golden channel analysis

A set of selection criteria have been established to reduce backgrounds from neutral current channels and mis-reconstructed muons. Initial criteria are applied to remove events with poorly reconstructed or no muon tracks. A candidate event must have one or more successfully fitted tracks that use a significant fraction of the clusters assigned to the track in pattern recognition, and the momentum must be reasonable given the maximum energy of the neutrino source. A full list of these criteria are summarized in Table 26. A multi-variate analysis has been developed to separate signal from background in the remaining event sample.

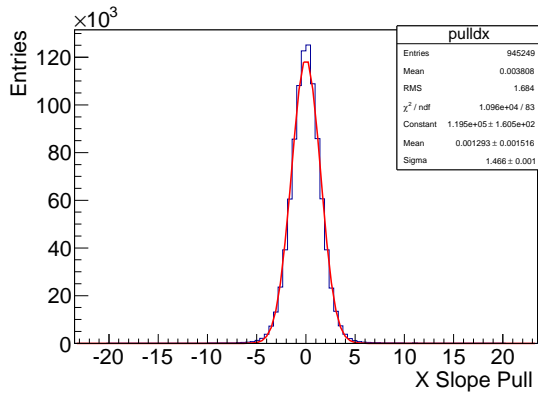
The multi-variate analysis uses the methods provided by the ROOT based TMVA package [127]. These methods allow for the use of multiple potentially correlated parameters for event selection. A likelihood method has been used in the past [21], but the use of correlated variables in this framework only acts to reduce the



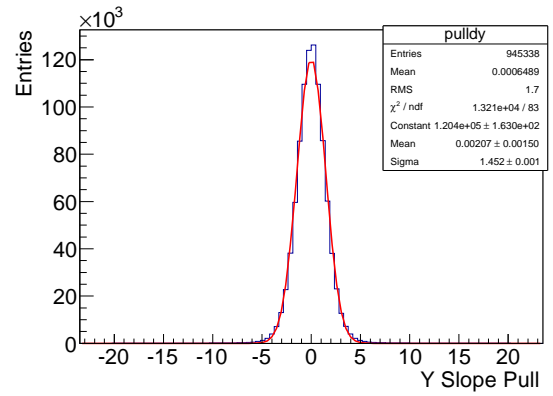
(a) Pull in initial X position



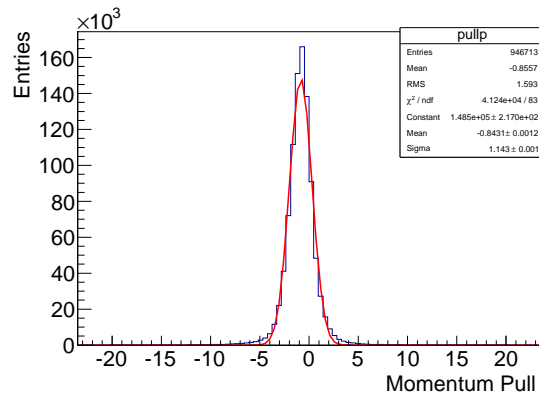
(b) Pull in initial Y position



(c) Pull in initial slope dx/dz



(d) Pull in initial slope dy/dz



(e) Pull in trajectory momentum

Figure 33: Pulls for the variables used to describe the particle trajectories in the magnetic field in MIND.

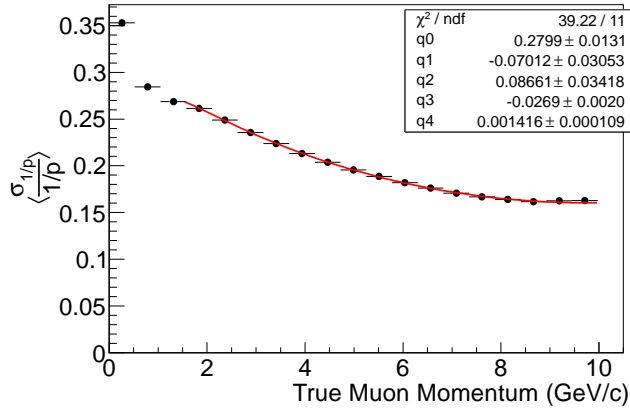


Figure 34: The mean of the momentum resolution as a function of the true muon momentum.

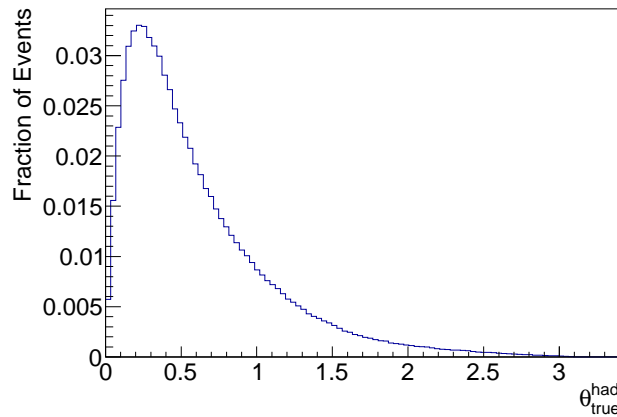


Figure 35: The angle between the reconstructed hadron shower direction and the true hadron shower direction;
 $\theta_{true}^{had} = \arccos \hat{u}_{rec} \cdot \hat{u}_{true}$.

Table 26: Pre-selection criteria for a well reconstructed track applied prior to the training and application of the multi-variate analysis.

Variable	Description
Trajectory Identified	There must be at least one trajectory identified in the event.
Successful Fit	The longest identified trajectory must be successfully fit.
Maximum Momentum	The momentum of the longest trajectory is less than 16 GeV/c
Fiducial	Longest trajectory must start prior to the last 1 m of the detector.
Minimum Nodes	Fit to longest trajectory must include more than 60% of hits assigned to trajectory by filter.
Track Quality	$\sigma_{q/p}/(q/p) < 10.0$.
Curvature Ratio	$(q_{init}/p_{range}) \times (p_{fit}/q_{fit}) > 0$.

Table 27: Variables used in multivariate analysis. The separation is a measure of the difference between the distributions of the indicated variable for signal and background events.

Variable	Description	Separation
Track Quality	$\sigma_{q/p}/(q/p)$, the error in the trajectory curvature scaled by the curvature.	0.71
Hits in Trajectory	The number of hits in the trajectory.	0.56
Mean Energy Deposition	Mean of energy deposition of hits in the fit of the trajectory.	0.30
Variation in Energy	$\sum_{i=0}^{N/2} \Delta E_i / \sum_{j=N/2}^N \Delta E_j$, where the energy deposited per hit $\Delta E_i < \Delta E_{i+1}$.	0.26
Energy Transfer	The transverse energy of the muon $Q_t = p_\mu \sin^2 \theta_\mu$	0.21

efficiency of the analysis with no gain in the ratio of signal to background. A multivariate analysis uses the input variables to develop a selection criteria that makes optimal use of the available information to discriminate between signal and background.

The set of variables used in the selection of events was based on those used in MINOS [128] for a similar multi-variate analysis. The analysis was trained to optimize for a $\nu_\mu(\bar{\nu}_\mu)$ CC signal in the presence of a $\bar{\nu}_\mu(\nu_\mu)$ NC background. Ten different quantities derived from the hits identified as part of a track and the fits to the track were considered. Five of those variables were found to make an impact on the results of the analysis without introducing unnecessarily large correlations to the analysis. These variables are listed in Table 27.

The most important of these variables is the number of hits in the candidate trajectory. This variable was used as part of the MIND Golden channel likelihood analysis [21]. Because muons are minimum ionizing particles they will pass through many detector layers before stopping. This is in contrast to tracks fit from hadronization or electromagnetic showers, which will present a large number of hits in a few planes near the neutrino interaction vertex. A neutral current neutrino interaction will have a final state composed of hadrons so the number of hits is a very good variable for the identification of muon (anti) neutrino charge current interactions against a background of neutral current interactions. The number of trajectory hits for all of the expected backgrounds for the Golden Channel before and after the application of the analysis appears in Figure 36. Neutral current (and similar) events leave fewer than 40 hits in MIND, while the number of hits left by a muon track is proportional to the initial muon momentum.

The track quality was also used in the golden channel likelihood analysis [21]. The track quality is defined to be the scaled uncertainty in the fitted charge over the momentum, $\sigma_{q/p}/(q/p)$. Tracks fit from hadronization or an electron shower produce a broad track quality distribution with a long tail as shown in figure 37 because the track does not follow a distinct path with a well defined curvature. In contrast, the track quality distribution from muon tracks is very well defined with a sharp peak below 0.5. The stark qualitative difference between these distributions allows for an easy discrimination between CC and NC events. Because trajectories fit with the wrong charge are often either due to the incorrect selection of a hadron (i.e. a pion) or significant multiple scattering, events identified with the incorrect muon charge can also be identified using this discriminating variable.

With the difference in the particle content of muon neutrino CC interaction final states (muons and hadrons) and NC final states (hadronization only) quantitative differences in the energy loss are expected. The mean

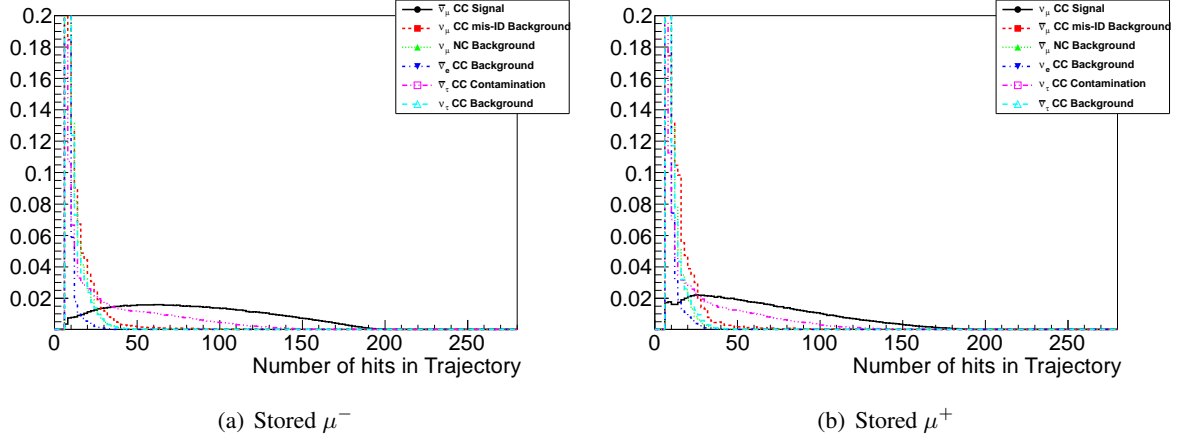


Figure 36: Number of hits for signal ($\bar{\nu}_\mu$ CC) samples and backgrounds used in an experiment involving stored μ^- (36(a)) and stored μ^+ (36(b)).

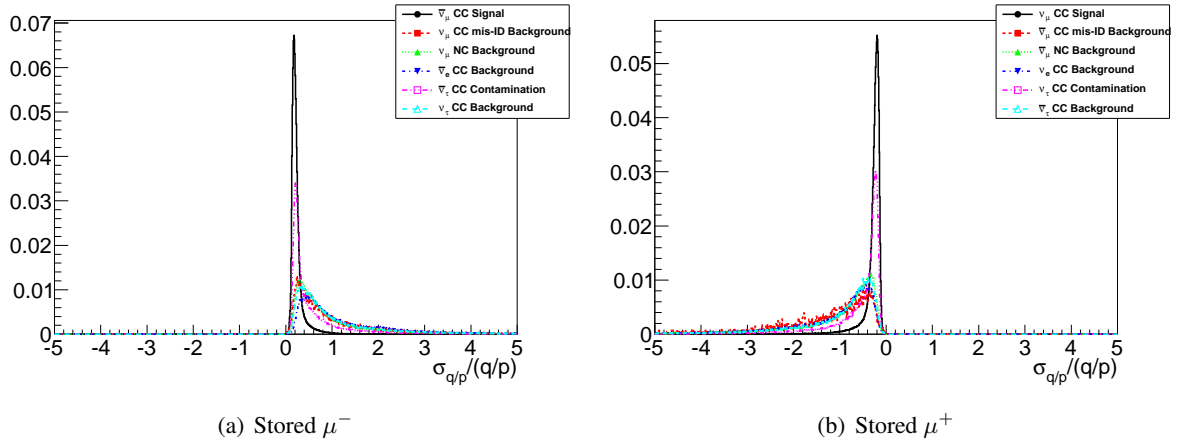


Figure 37: Distribution in the error in the helix variable q/p normalized by q/p for charge current and neutral current neutrino interaction samples used for the training of an experiment using stored μ^- .

energy loss over the trajectory is one such variable. The distributions for signal and background samples are shown in figure 38.

A stronger discriminating variable is the variation of the energy loss along the length of a trajectory [55]. The variable is defined as the ratio of the sum of low energy deposition hits over the sum of high energy deposition hits when the set of hits ordered by the energy deposited in a given voxel, alternatively expressed as;

$$R_{\Delta E} = \frac{\sum_{i=0}^{N/2} \Delta E_i}{\sum_{j=N/2+1}^N \Delta E_j} \text{ where } \Delta E_i < \Delta E_{i+1}. \quad (15)$$

A trajectory for which the energy deposition is uniform over the majority of its length, as is the case for the trajectory of a minimum ionizing particle, will have a $R_{\Delta E}$ near unity. A trajectory reconstructed from other sources will have, on average, a much lower value for $R_{\Delta E}$. The distributions of $R_{\Delta E}$ for signal and background are qualitatively different as shown in figure 39.

The last variable contributing to the multivariate analysis is the hadron energy transfer of the neutrino interaction. This is defined to be $Q_t = |\mathbf{p}_\mu| \sin^2 \theta_{\mu, had}$ where $\theta_{\mu, had}$ is the angle between the muon vector at the interaction vertex and the vector of the hadron shower based on the observed non-muon tracks and remaining unassigned hits in the event. When there are no observed hadron tracks or hits, the angle is assumed to go to

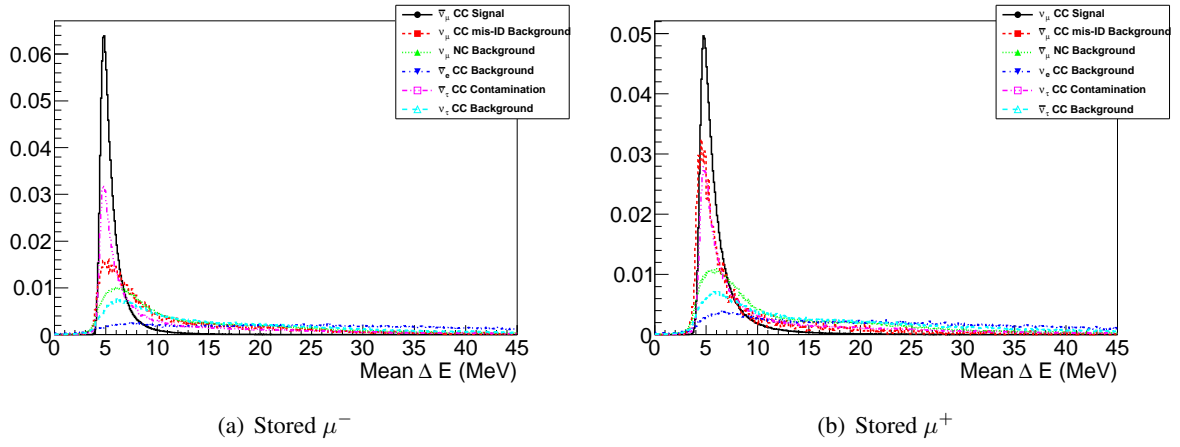


Figure 38: Distribution of the mean energy deposition for charge and neutral current neutrino interaction samples used for the training of an experiment using stored μ^-

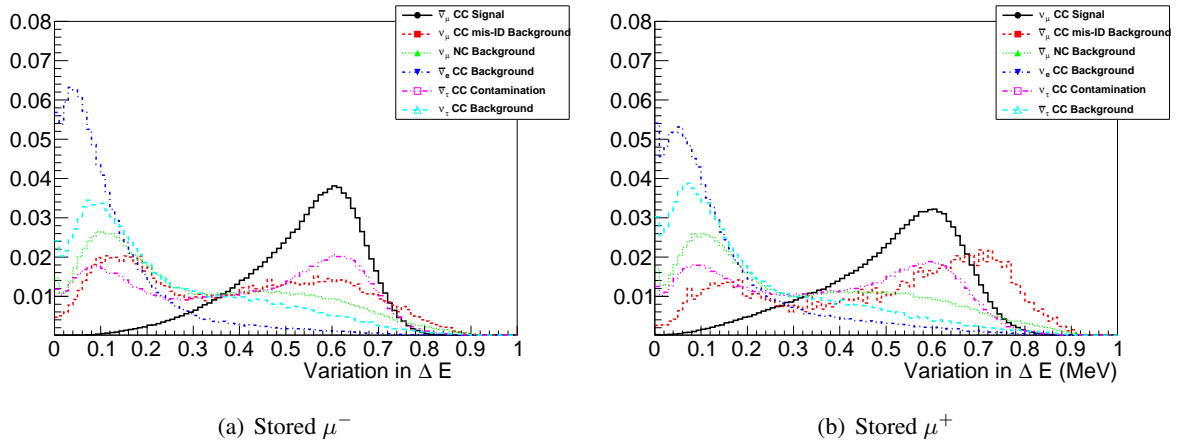


Figure 39: Distribution of the energy variation for signal and background samples for an experiment involving stored μ^- .

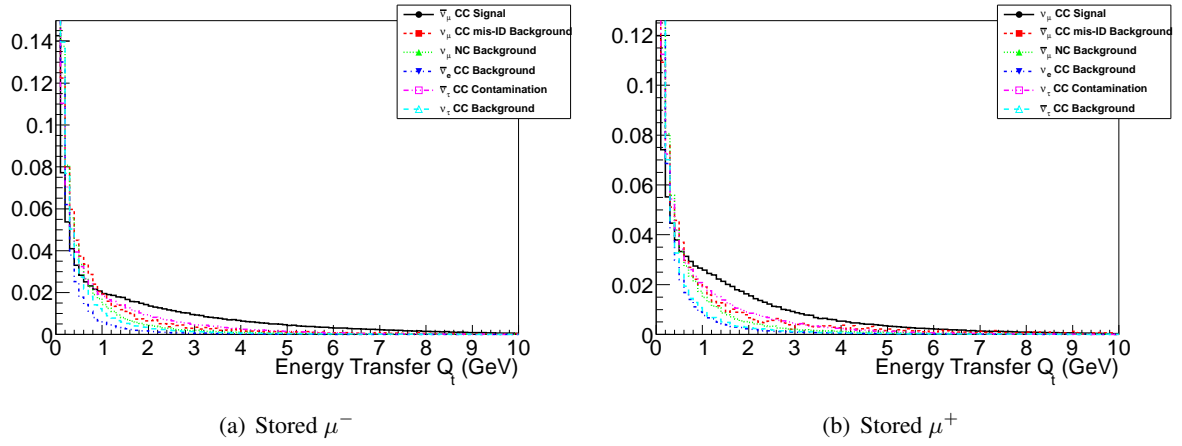


Figure 40: Distribution of the interaction energy transfer Q_t for signal and background samples in an experiment using stored μ^-

90° . If the muon track is in the same direction as the hadronization it is likely that the trajectory is in fact the result of the hadronization either from a pion decay, or a false track selected from hadronization. As such, it is expected that NC events will have a lower Q_t than CC events, as shown in figure 40. In practice this variable does not have a large impact on the results because of the relatively small sample of events in which non-muon tracks and other evidence of hadronization is visible in MIND.

Multiple methods were trained using the same set of variables. All methods underwent an optimization which maximizes the quantity $S/\sqrt{S+B}$. A list of the tested methods and the results of optimization is given in Table 28. This optimization was achieved assuming a number of neutrino interactions expected over one year as calculated by the NuTS package [129–131] using the oscillation parameters $\theta_{12} = 39^\circ$, $\theta_{13} = 8^\circ$, $\theta_{23} = 45^\circ$, $\delta_{CP} = 60^\circ$, $\Delta m_{12}^2 = 7.65 \times 10^{-5}$ and $\Delta m_{13}^2 = 2.4 \times 10^{-3}$. The best physics performance is achieved using the boosted decision tree method, which uses the characteristics of the training sample to sort events into a tree structure consisting of top level “leaves” that are deemed as “signal-like” or “background-like”. In principle, this is similar to a cuts based analysis in that it assigns a subset of the training parameter space as signal or background. Unlike a cuts based analysis, the signal can be taken from a disjoint subset of the parameter space. A second method under consideration is the k-nearest neighbour approach, which uses a point-to-point exploration of the parameter space to generate the classifier. The kNN method has a better signal efficiency, with a lower energy threshold, but poorer background rejection. Other methods tested either rendered much poorer results (as is the case of the neural networks tested) or identical results (as is the case of gradient boosted decision trees).

The optimized classification is applied to the simulated samples to determine the detector response to the appearance of signal events within the detector. The signal efficiency of the analysis for ν_μ CC and $\bar{\nu}_\mu$ CC interactions appears in figure 41. Backgrounds corresponding to these signals are shown in figure 42. Only efficiencies assuming a detector magnetic field that focuses positive charges are shown.

4.2.1.4 Study of systematic uncertainties

Studies of the systematic uncertainties pertinent to the analysis of the MIND detector have been conducted. Of primary interest are uncertainties in the neutrino flux and cross sections at MIND, uncertainties pertaining to the analysis, and uncertainties in the construction of the detector. Backgrounds from external sources such as cosmic rays were also considered.

Table 28: Multivariate analysis methods tested for the neutrino factory MIND analysis.

(a) Stored μ^- experiment, with a μ^+ focusing detector field, optimized assuming 643 signal and 79708 background events.

Classifier	Optimal-cut	$S/\sqrt{S+B}$	N_{Sig}	N_{Bkg}	Eff. Sig.	Eff. Bkg.
KNN	0.9876	17.22	606.87	635.0	0.8757	0.00797
BDT	0.4793	21.72	521.20	54.42	0.7521	0.00068

(b) Stored μ^+ experiment, with a μ^+ focusing detector field, optimized assuming 4852 signal and 100618 background events.

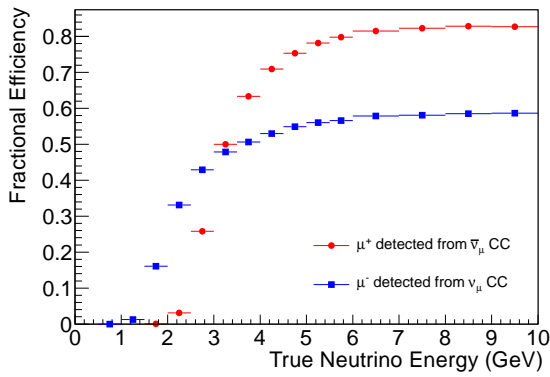
Classifier	Optimal-cut	$S/\sqrt{S+B}$	N_{Sig}	N_{Bkg}	Eff. Sig.	Eff. Bkg.
KNN	0.9876	56.91	3919.7	824.6	0.8079	0.00820
BDT	0.3675	58.37	3775.9	408.9	0.7782	0.00406

(c) Stored μ^- experiment, with a μ^- focusing detector field, optimized assuming 643 signal and 79708 background events.

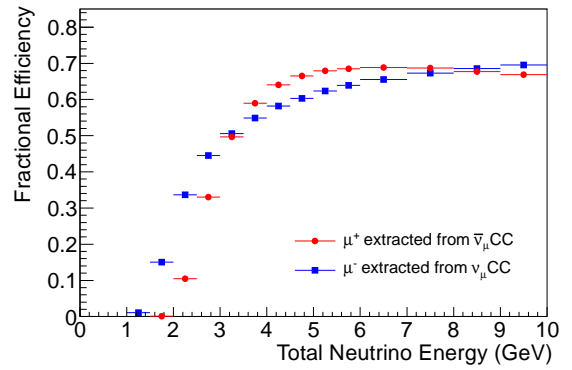
Classifier	Optimal-cut	$S/\sqrt{S+B}$	N_{Sig}	N_{Bkg}	Eff. Sig.	Eff. Bkg.
KNN	0.9876	17.08	581.00	576.0	0.8519	0.00722
BDT	0.4555	21.06	507.43	73.06	0.744	0.00092

(d) Stored μ^+ experiment, with a μ^- focusing detector field, optimized assuming 4852 signal and 100618 background events.

Classifier	Optimal-cut	$S/\sqrt{S+B}$	N_{Sig}	N_{Bkg}	Eff. Sig.	Eff. Bkg.
KNN	0.9876	57.79	4011.7	806.9	0.8268	0.00802
BDT	0.3906	59.21	3861.6	391.0	0.7959	0.0039

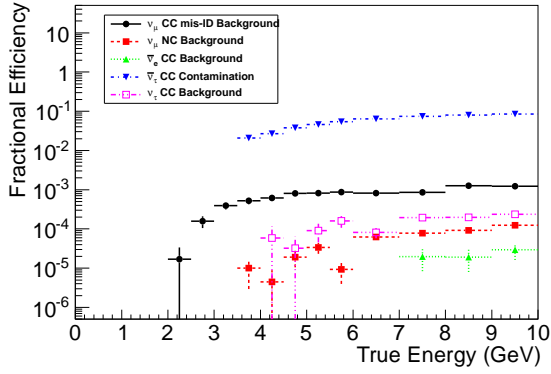


(a) Focussing μ^+ in detector field

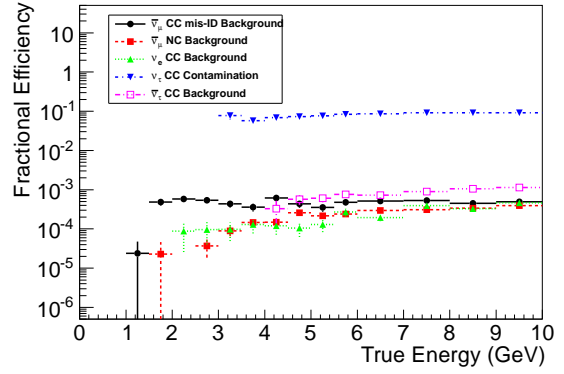


(b) Focussing μ^- in detector field

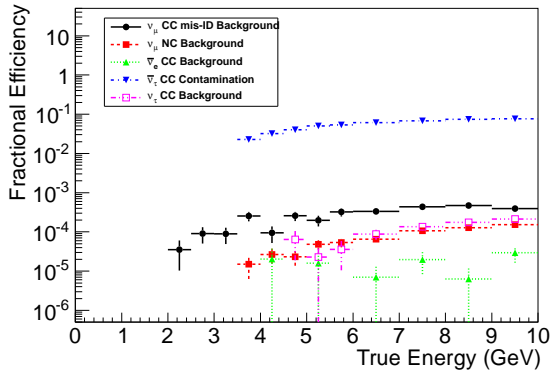
Figure 41: Efficiency of signals for neutrino samples corresponding to stored μ^+ and μ^- experiments assuming a detector magnetic field that focusses positive charges (a) and focusses negative charges (b). A boosted decision tree algorithm was used for this analysis.



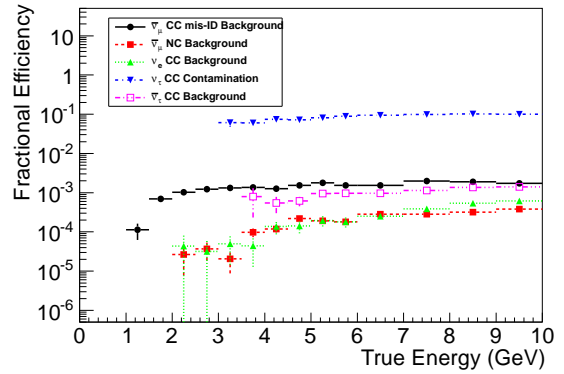
(a) Stored μ^- , focusing μ^+



(b) Stored μ^+ , focusing μ^+



(c) Stored μ^- , focusing μ^-



(d) Stored μ^+ , focusing μ^-

Figure 42: Efficiency of backgrounds for neutrino samples corresponding to stored μ^+ and μ^- experiments assuming a detector magnetic field that focusses positive charges and negative charges. A boosted decision tree algorithm was used for this analysis.

Table 29: Systematic uncertainties expected for a long baseline neutrino experiment based at a neutrino factory facility compared to the uncertainties evaluated for existing experiments.

Uncertainty	Known Measures			Expected Contribution	
	Signal	Background	Reference	Signal	Background
Source luminosity	0.1%	0.1%	[132]	0.1%	0.1%
Cross section	4%	40%	[134]	0.5%	5%
Hadronic Model	0	15%	[125]	0	8%

For past and future oscillation experiments the neutrino cross-sections and flux represent a leading concern. Estimates, first made for the 25 GeV neutrino factory [132], suggest that the characteristics of the muon beam in the muon decay ring will be known well enough to infer the neutrino rate to 0.1%, using the known spectrum of muon decay at rest. A system of instrumentation devices in the decay ring, including beam current transformers, beam position monitors, polarimeters, and wire scanners, will be used to make the beam characterization. Additionally, the specifications of the near detectors require that they make a direct measurement of the convolution of the flux and cross-section at the sub percent level.

The current state of cross-section measurements places an upper bound on its contribution to the anticipated precision of the measured neutrino rates. In current experiments the leading contribution is the relative strength of quasi-elastic cross-sections with respect to other interactions, the relative cross sections of neutrinos and anti-neutrinos, and effects pertaining to the differences between the effective cross-sections of ν_e and ν_μ . For example, the MINOS experiment sets an uncertainty on the flux convoluted with the cross-section at 4% for their signal and 40% for their background [133]. The precision in the background rate is due to the difficulty of reproducing false background signals in neutral current events in data with any significance. Specifically cited in the MINOS context are the uncertainties in the neutral current production mechanisms, such as the resonant pion production and a 15% uncertainty in the hadron model. A neutrino factory has a somewhat different set of backgrounds. The mis-identified charge current events are expected to be a leading contribution to the background of a wrong sign muon measurement, but the processes responsible for this background channel should be analogous.

These cross-sections are expected to be measured during the operation of the neutrino factory and similar facilities, leading to reduced systematic uncertainties. Measurements at the near detectors will provide information that has not been previously available, such as the direct measure of ν_e cross-sections, to refine the assumptions used in software and reduce the systematic uncertainties. For these reasons, a 1% systematic is assessed for the total convoluted flux by cross-section uncertainty, with a 15% uncertainty assigned to the background.

An uncertainty is assigned for the analysis to treat the cases where the optimization does not select the ideal classification variable for a given multivariate method, or a non-optimal method is chosen. To evaluate the effect of a non-ideal optimization, an analysis of all species was completed using a BDT analysis with a classifier selection applied that reduced $S/\sqrt{S+B}$ by 1. This is consistent with reducing the expected significance by one standard deviation. The selection of the reduced value is not perfect so the final uncertainty is normalized by the quadrature difference between the optimized significance and the reduced significance. A further normalization by a factor of 2 is added to take into account that the difference at 45° is an extreme case that is in fact averaged over the oscillation. The normalized difference was calculated from the sum of signal and background both in stored μ^- and stored μ^+ experiments. The results assuming $\delta_{CP} = 45^\circ$ are shown in Table 30. A similar calculation was done for the difference between a BDT analysis and a KNN analysis, with a similar re-normalization using the quadrature difference of the significance. The variation is very small so the variation has not been explicitly added in the fits — rather they have been added in quadrature to the flux

	Store μ^+		Store μ^-		Sum	
	Signal	Bkgd	Signal	Bkgd	Signal	Bkgd
Opt. BDT	18119.4	297.7	3658.16	243.429	21777.56	541.129
Shift BDT	17636.4	226	3531	186	21167.4	412
% Difference	1.3	13.7	1.8	13.3	1.4	13.5
Scale Factor					3.35	3.35
Uncertainty					0.4%	4%
Opt. KNN	18684.6	932.8	386.294	166.29	19070.894	1099.09
Scale Factor					22.98	22.98
Uncertainty					0.3%	1.4%

Table 30: Uncertainties in the rates associated with the analysis of signal and background in a neutrino factory oscillation experiment.

Uncertainty	Known Measures			Expected Contribution	
	Signal	Background	Reference	Signal	Background
Electromagnetic Model	2%	0	[125]	0.5%	0
Magnetic Field	<1%	<1%	[135]	0.2%	3%
Steel	0.2%	0.2%	[135]	0.2%	0.2%

uncertainty described above.

The construction of MIND can add some potential uncertainties in the measured neutrino rates. Variations in the steel from the anticipated thickness manifests as changes in the magnetic field strength and energy loss that could affect the reconstruction. These variations may be correlated — all of the modules are thicker than anticipated — or uncorrelated — there are random variations within tolerances. Based on the measurements conducted using ultrasound techniques at MINOS the variation in steel thickness should be less than 0.3%. Random variations on this will produce a negligible effect on the reconstruction of tracks. Introducing a 0.3% change as a systematic bias in the plate thickness, with no change in the overall module thickness, results in no significant difference in the reconstruction rate. If the magnetic field alone is reduced by 0.3%, a 0.7% change in the rate of signal events, and an 8% change in the rate of background events after event selection is observed. This again assumes a correlated bias in the magnetic field magnitude, which presents an upper limit, so the uncertainty presented in Table 31 is scaled by a factor of $1/\sqrt{12}$.

Cosmic rays represent a major background for the measurement of CP violation. The default assumption is that the MIND is to be placed underground to remove this background, but a surface option would improve the flexibility of the detector siting. A simulation of cosmic rays has been done using the CRY software package as a generator with the existing GEANT4 detector model to determine whether the detector can reject cosmic rays at a sufficient level for a surface detector, or how much shielding is otherwise needed.

To remove a cosmic ray (or any external event) from the data sample a simple fiducial cut has been applied that removes events with the first hits in 30 cm from the exterior edge of the detector. Investigations varying this cut has shown that this veto depth does the optimum job of removing external events while reducing the signal events by a small degree. Prior to the implementation of these simulations the timing information was not used in the reconstruction or analysis. The reconstruction is done assuming that the beam direction is parallel to the z axis of the detector and all particles are moving the \hat{z} direction. This is not always true in the case of cosmic ray events, so there is always the possibility that a track from a cosmic ray muon that stops in the detector is reconstructed backwards with respect to its direction of travel.

Table 32: Rates determined from the simulation of cosmic rays in the MIND detector for the surfaces exposed to downward going cosmic rays over a 10 year period.

	Stored μ^+	Stored μ^-
Signal	17802	3166
Background	298	244
Cosmic Rays	261370	73169

The expected rates of cosmic ray events that pass the multivariate analysis occurring in the MIND over a ten year period is shown in Table 32. To produce a viable measurement in the presence cosmic rays, the rates must be lower than the expected beam background rate. From these results it is clear that some over-burden is necessary for the successful measurement of CP violation at a neutrino factory.

The overburden required to reduce the cosmic ray background to 10% of the rate expected for the beam backgrounds can be estimated from the expression

$$\frac{dN_\mu(X)}{dE_\mu} = \frac{dN_\mu}{dE_{\mu,0}} \frac{dE_{\mu,0}}{dE_\mu} = \frac{dN_\mu}{dE_{\mu,0}} e^{bX}. \quad (16)$$

In this expression X is the “slant depth” of the cosmic ray approaching the detector, E_μ is the energy of the cosmic ray, and b is the mean energy loss of muons in the material composing the overburden. The cosmic ray spectrum at the surface, $\frac{dN_\mu}{dE_{\mu,0}}$ is determined using the CRY generator, and the energy loss can be simulated directly with a GEANT simulation of the overburden. However, a worst case scenario can be considered using the mean energy loss of minimum ionizing muons in a rock like material (aluminum) to estimate the maximum required overburden. To reduce the number of μ^- reconstructed from cosmic rays from 261370 events to 29, 5.4 m of rock is required. A simulation was run with 5 m of shielding material to confirm that this is the case.

4.2.1.5 MIND sensitivity to the golden channel

The golden channel response is summarized in terms of a set of migration matrices that encapsulate the efficiency and response of the MIND detector by recording the probability that a neutrino event with a given true energy, E_{true} , will be reconstructed with an energy E_{rec} . For each contributing neutrino species, a separate matrix is defined, reflecting the response to the charge current analysis described. A single matrix is defined for the neutral current interactions using the muon flavoured neutrino appropriate to the source beam. This produces a set of six matrices for each golden channel oscillation experiment considered. The polarity of the muon beam in the storage ring (μ^+ or μ^-) as well as the detector magnetic field (μ^+ focusing of μ^- focusing) can be considered for a total of 4 different oscillation experiments or 24 migration matrices in total. The migration matrices are recorded in Appendix J.1.

The migration matrices are used to determine the sensitivity of the neutrino factory to the presence of CP violation. The figure of merit for the evaluation of the facility is the uncertainty in the measurement of the CP violating phase, δ_{CP} . The calculation of the potential sensitivity to CP violation is done using the GLoBeS long baseline simulation package to calculate the number of neutrino interactions detected given the detector response. The uncertainty of the CP violating phase, assuming a total exposure from 5×10^{21} muon decays of both species collected over 10 years with a 100 kt detector, is shown in Fig. 43. This figure shows the uncertainty assuming detector fields of both polarities as well as the effect on the uncertainty. The effect of statistics on this figure of merit is shown in Fig. 44, as a function of the exposure to the neutrino factory beam, quoted as a product of the detector mass and the number of years. For the ultimate exposure of 1000 kt · years an uncertainty of 4° to 5° is expected. However a reasonable measurement can be made well in advance of this, with meaningful results appearing at 100 kt · years exposure.

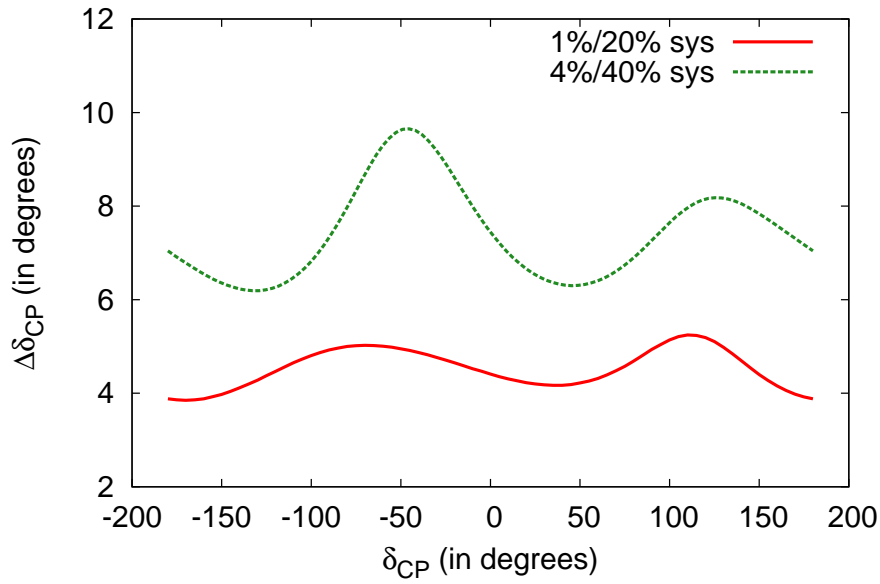


Figure 43: Uncertainty in the CP violating phase for a 100 kt MIND detector exposed to a neutrino beam resulting from 5×10^{21} muon decays of both charges. Both μ^+ and μ^- focusing detector fields are considered assuming the anticipated systematic uncertainty of 1% in the signal and 20% in the background. For contrast the effect of assuming an inflated systematic of 4% signal uncertainty and 40% background uncertainty with a μ^+ focusing detector field is also shown.

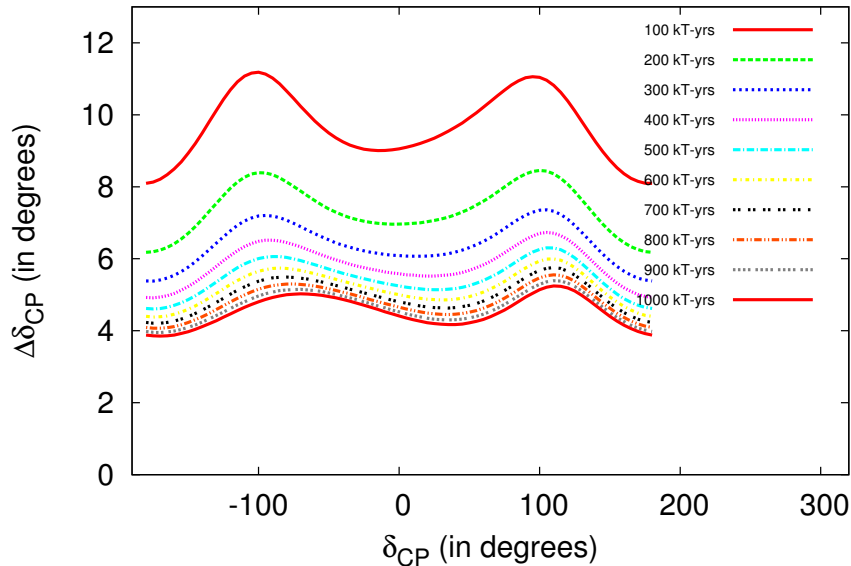


Figure 44: The uncertainty in the CP violating phase measured in the MIND at a neutrino factory for various exposures to a neutrino beam generated from 5×10^{20} muon decays per year of both species.

4.2.2 MIND conceptual design

The Magnetised Iron Neutrino Detector (MIND) is an iron and scintillator sampling calorimeter which is essentially a larger version of the MINOS detector [136]. We have chosen an octagonal cross-section of $14\text{ m} \times 14\text{ m}$ in order to maximise the ratio of the fiducial mass to the total mass. The magnetic field will be toroidal as in MINOS and MIND will also use extruded scintillator for the readout material. Details on the iron plates, magnetisation, scintillator, photo-detector and electronics are given below.

4.2.2.1 Iron plate engineering

For the iron plates in MIND, we are following the design strategy that was used for MINOS. The plates are octagons with overall dimension of $14\text{ m} \times 14\text{ m}$ and 3.0 cm thick. They are fabricated from strips that are 1.5 cm thick, 2 m (or 3 m) wide and up to 14 m long. Two layers of crossed strips are plug welded together to form the full plate. MINOS used 2 m wide strips and we know that fabrication of iron components of this width and with lengths of up to 14 m is possible. Depending on the final plate fabricator, strip widths greater than 2 m are likely to be possible, so both 2 m and 3 m strip-width models were investigated. Initially it was thought that the much larger weight of the MIND plates (40 T versus 10 T for MINOS) would preclude the concept of hanging the plates on a rail system due to excessive stress in the ears. However, our analysis of the expected stress (see section 4.2.2.2 below) has shown that this is not the case. Essentially, no R&D on the MIND iron plates is needed. Final specification of the plate mosaic structure will be determined once a plate fabricator is chosen.

For the 2 m strip model, seven 2 m strips will be required to make up a whole layer. The layout of the top layer will be perpendicular to the bottom layer in each plane. For the 3 m strip model, the 14 m long strips will be both 3 m wide and 2 m wide. Four 3 m strips and one 2 m strip will be required to make up a whole layer. The layout of the top layer and the bottom layer remains perpendicular to each other in each plane. The individual plates will be held together by plug welding the top layer to the bottom layer. Each ear of the plane is supported by a structural-steel rail which is in turn supported by structural-steel columns. The section of the MIND detector plane and the support structures are shown in figure 45 and figure 46.

A book-end will be used to provide lateral support for the planes as the MIND detector is constructed. The plane will be attached to the bookend at the minimum of each vertex point in the octagon and each midpoint between the vertexes. This bookend will consist of a framework of structural-steel members and will be vertically supported by the floor slab and horizontally supported by the wall of the enclosure.

4.2.2.2 The finite-element model

Two finite-element models of the detector plane were created using higher order solid elements. The 2 m strip model is shown in figure 47 and the 3 m strip model is shown in figure 48. Loading was simulated by the gravity load of the plane. The plane was fixed at the bottom of the ears and the two top vertexes are fixed in the z direction to resist plane buckling. The linear buckling of the plane was also investigated. The total deformed shape of the 2 m strip plane is shown in figure 49. The directional deformations are shown in figures 50, 51 and 52 respectively. The maximum deflections occur at the ear and the bottom of the plane.

The stresses in the 2 m strip plane are shown in figure 53. The maximum von Mises stress is 6.8 ksi at the ear. In the regions away from that, all stresses are below the 12 ksi limit for AISI 1006 low carbon steel. The welded connections were examined by extracting nodal forces and moments from the 2 m strip plane model at 45 locations. The maximum load in the plane is in the ear area and is approximately 15,000 pounds per inch.

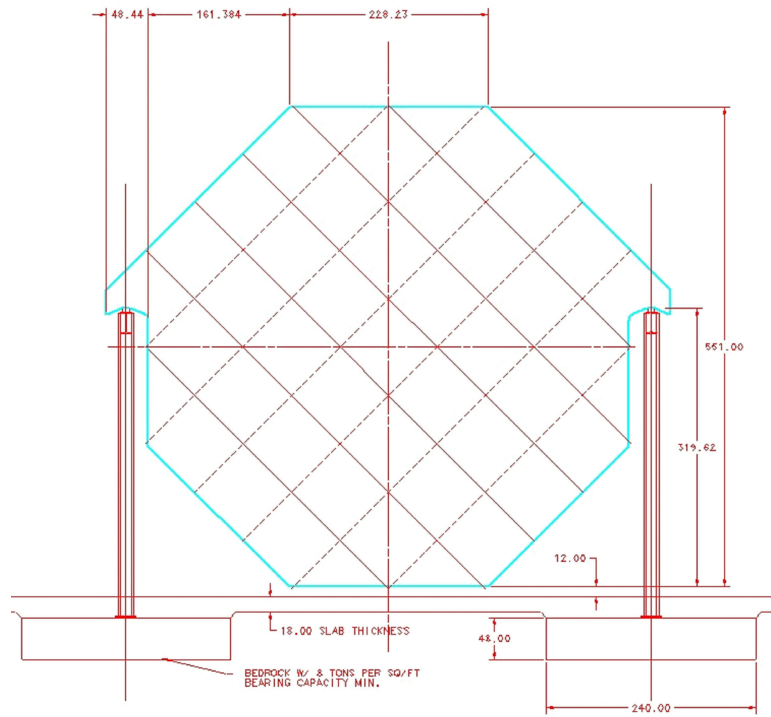


Figure 45: 2D diagram of MIND plate.

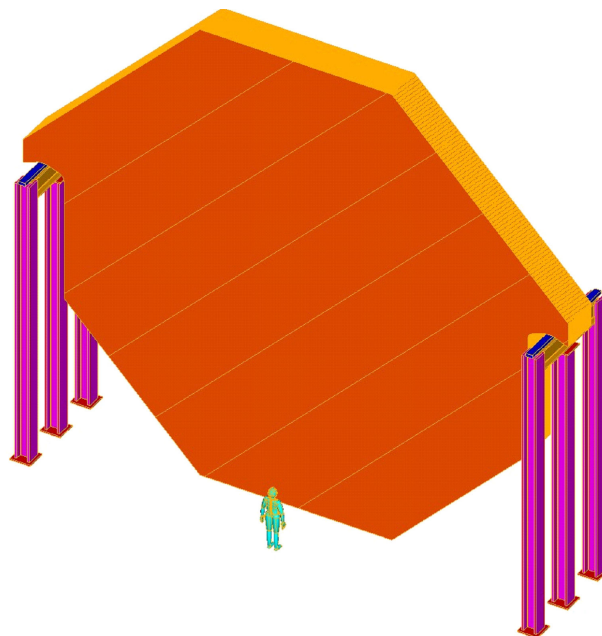


Figure 46: 3D diagram of MIND plate.

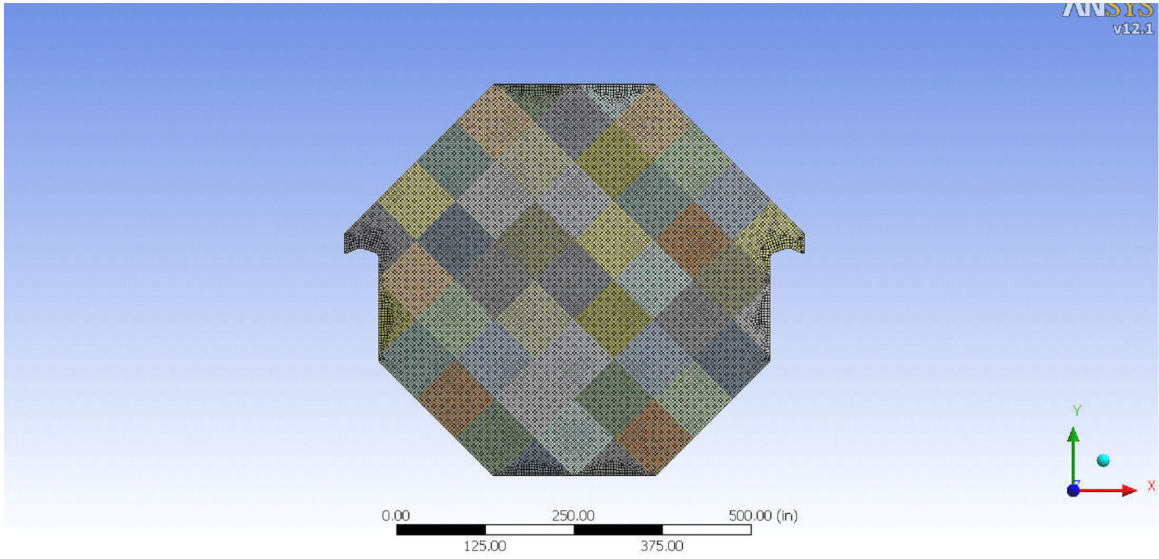


Figure 47: Finite-element model of plate with 2 m strips.

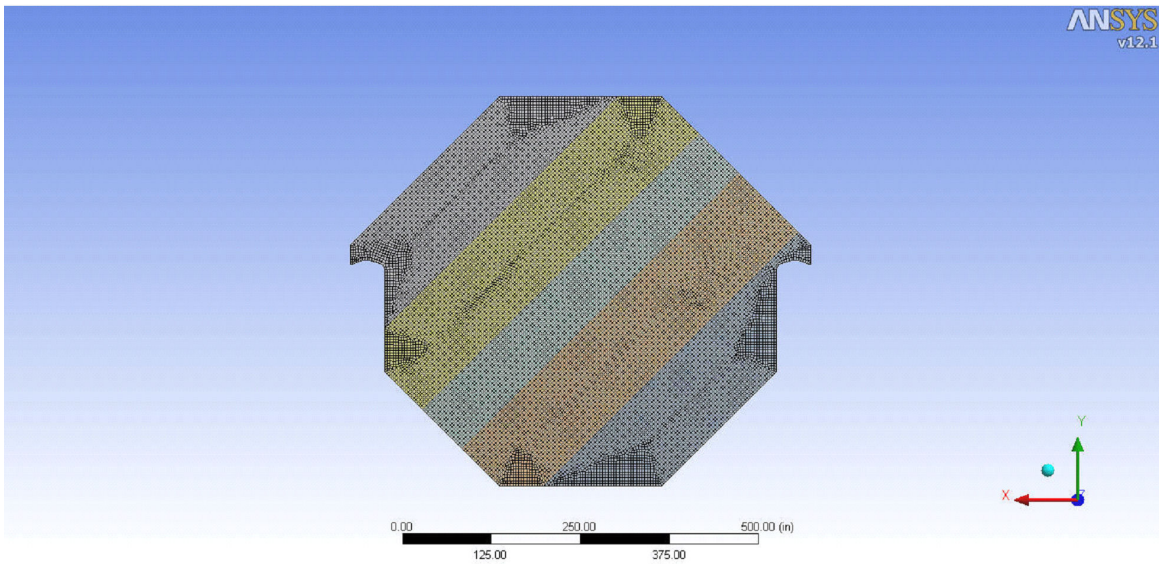


Figure 48: Finite-element model of plate that utilises both 3 m and 2 m strips.

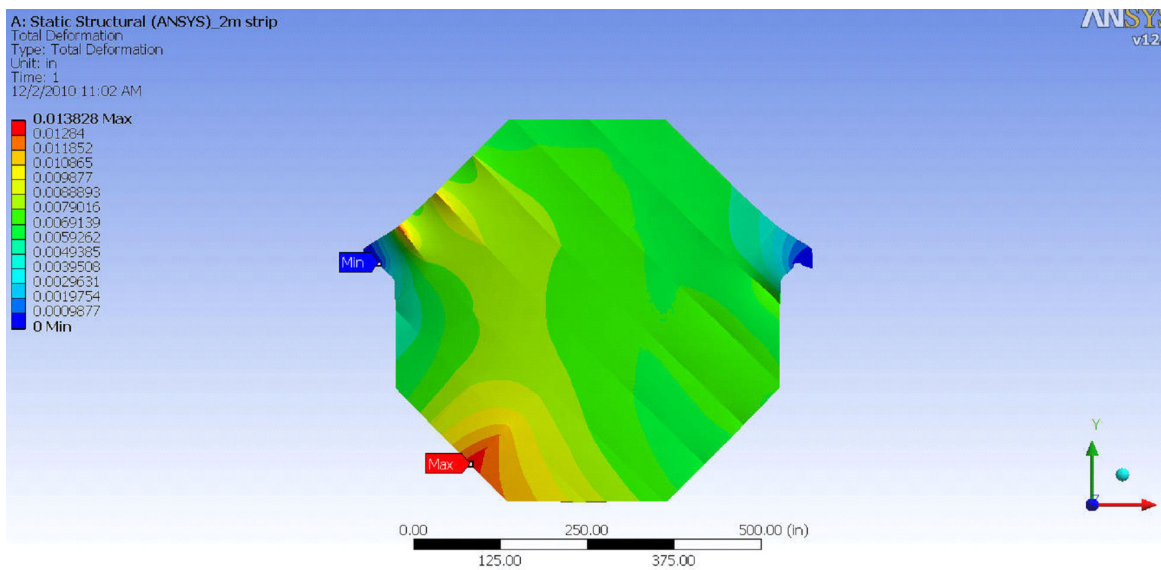


Figure 49: Total deformed shape of plate fabricated with 2 m strips

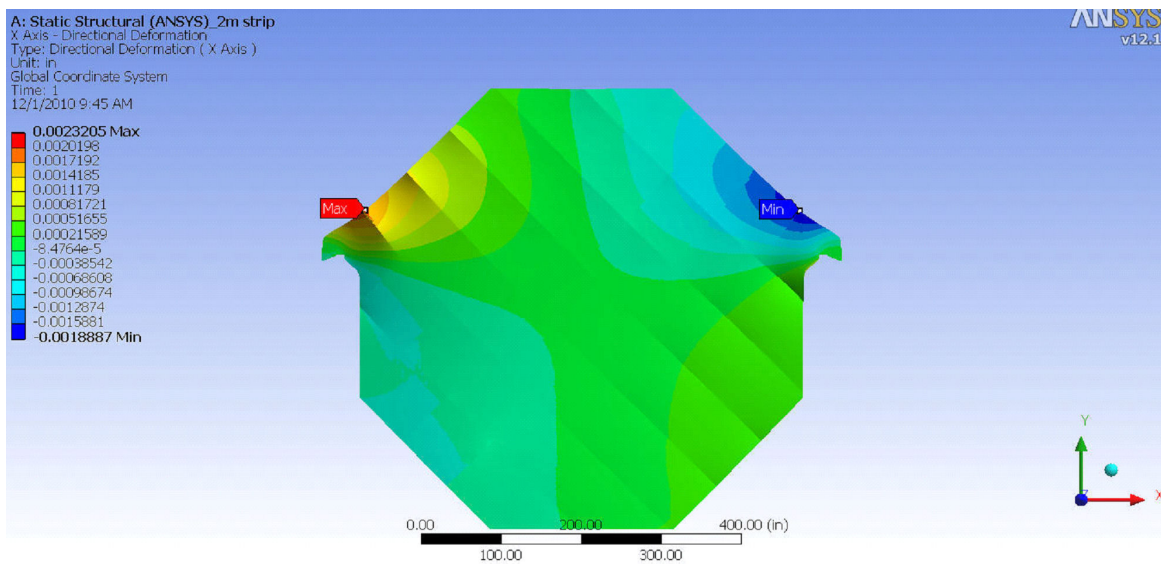


Figure 50: Deformation in x for plate using 2 m strips

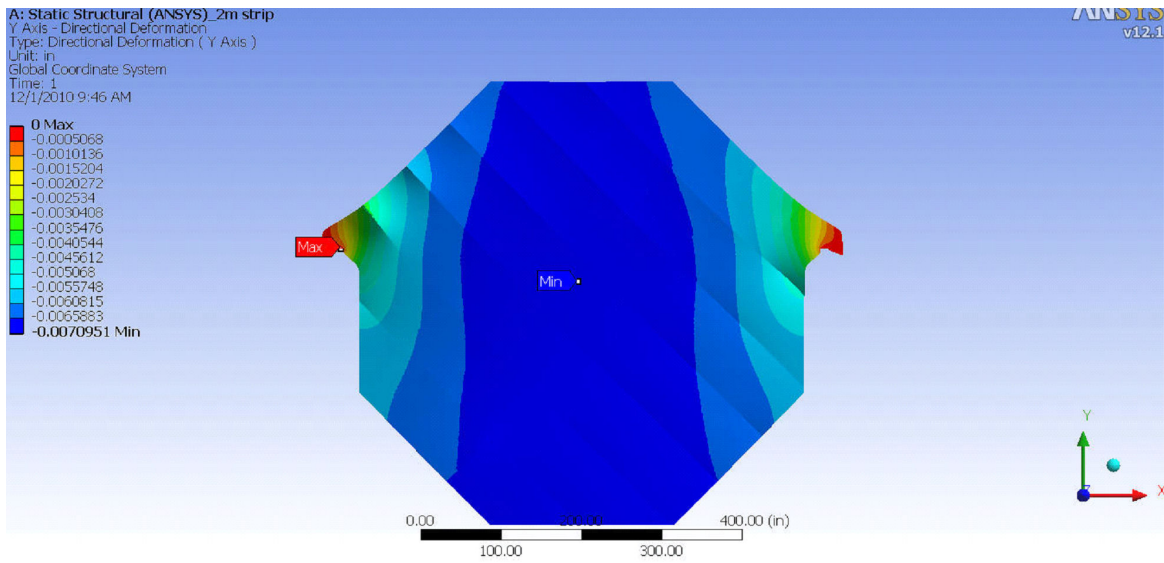


Figure 51: Deformation in y for plate using 2 m strips

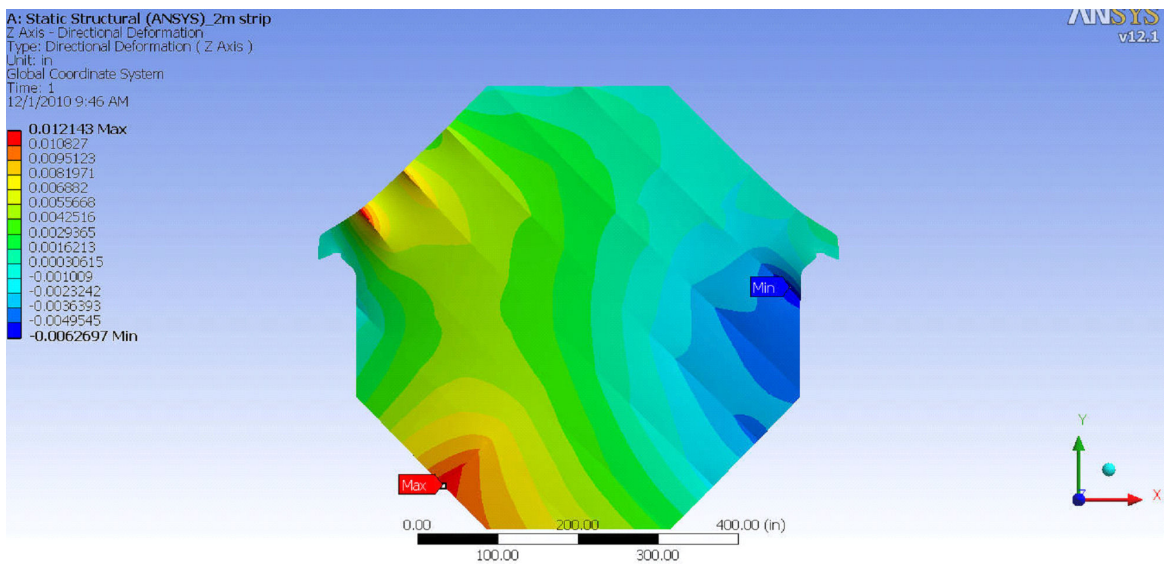


Figure 52: Deformation in z for plate using 2 m strips

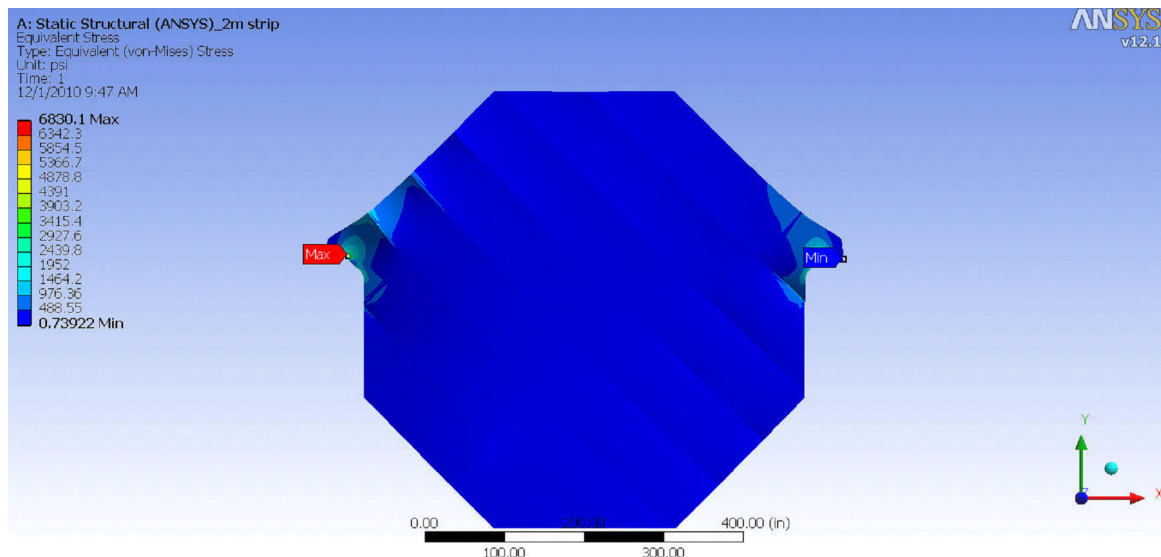


Figure 53: von Mises stress in plate using 2 m strips

In the linear buckling analysis of the 2 m strip plane, the results show the first buckling mode has a load safety factor of 4.7.

For comparison, the total deformed shape of the 3 m strip plane is shown in figure 54. Again, the maximum deflections occur at the ear and the bottom of the plane. The stresses in the 3 m strip plane are shown in figure 55. The maximum von Mises stress is 22 ksi at the ear. In the regions away from the concentration, all stresses are below the 12 ksi limit for AISI 1006 low carbon steel. In the linear buckling analysis of the 3 m strip plane, the results show the first buckling mode has a load safety factor of 4.5, somewhat worse than in the case of the 2 m wide strip case.

4.2.2.3 Magnetisation and modelling

As was mentioned above, MIND will have a toroidal magnetic field like that of MINOS. For excitation, however, we plan to use the concept of the Superconducting Transmission Line (STL) developed for the Design Study for a Staged Very Large Hadron Collider [137]. In order to obtain good field uniformity in a 14 m × 14 m plate, MIND requires a much larger excitation current-turn than the 15 kA-turn that is used in the room-temperature Cu coils of MINOS. 100kA per turn is possible utilizing the STL. The STL consists of a cylindrical superconducting braid inside a pipe cooled by supercritical helium. The superconductor and cryo-pipe are coaxial to a cylindrical cryostat/vacuum vessel. Fig. 56 shows the constructions details for the STL that was prototyped and tested for the VLHC study and consisted of: 1. a perforated Invar flow liner and support; 2. a copper stabilizer braid; 3. superconductor cable braid; 4. an Invar pipe that contains the helium; 5. the cold-pipe support; 6. Cryoshield; 7. superinsulation and 8. the vacuum jacket/pipe.

We can obtain 100 kA-turn in a single turn with the STL, but a 100 kA power supply (and current lead) does bring up some technical issues. Therefore, we have developed a scheme to use eight circuits (each operating at about 13 kA). A schematic of the central cryostat is given if Fig. 57. In this case, the central hole would have to be enlarged to 20 cm from the 10 cm. This scheme would also allow us to use “cable-in-conduit” superconductor that has been developed for the ITER project [138] and is now available from a number of manufacturers world wide. A rendering of the central cryostat and returns is shown in Fig. 58.

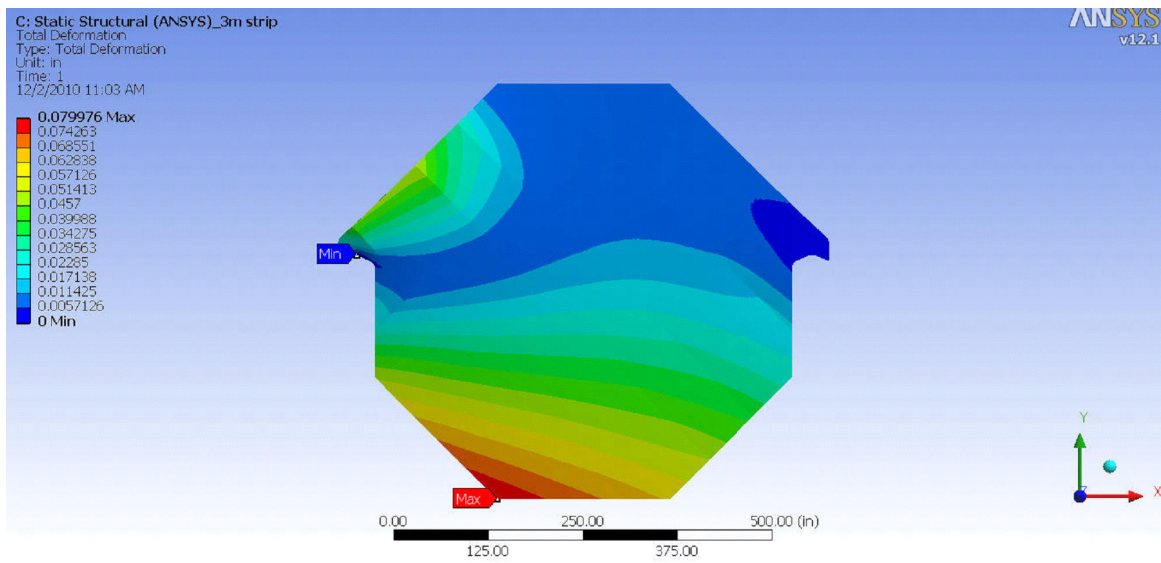


Figure 54: Total deformation for plate using 3 m and 2 m strips

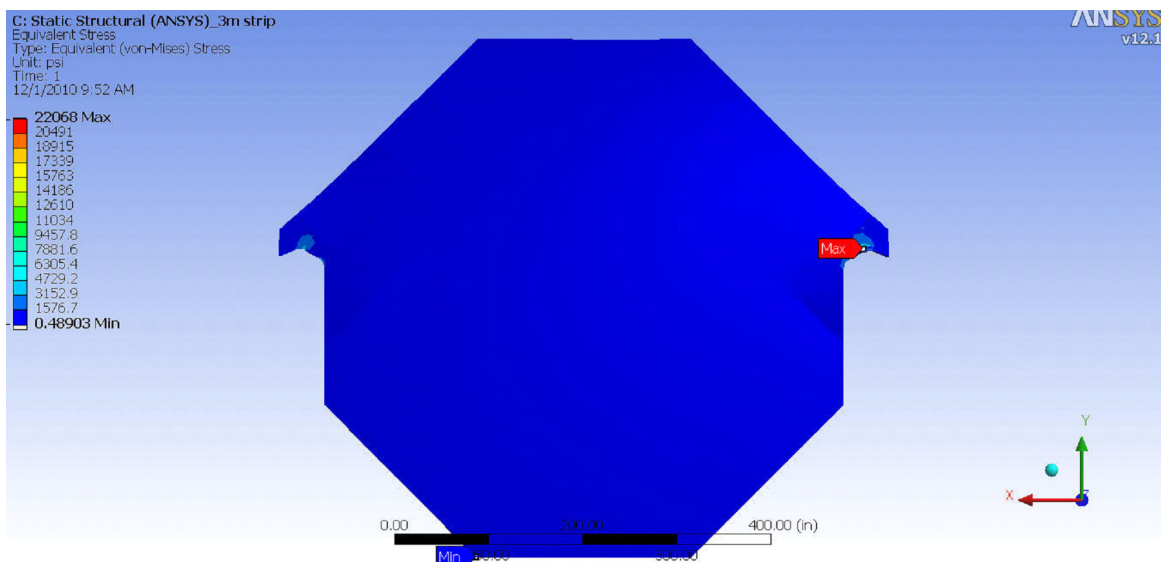


Figure 55: von Mises stress in plate using 3 m and 2 m strips

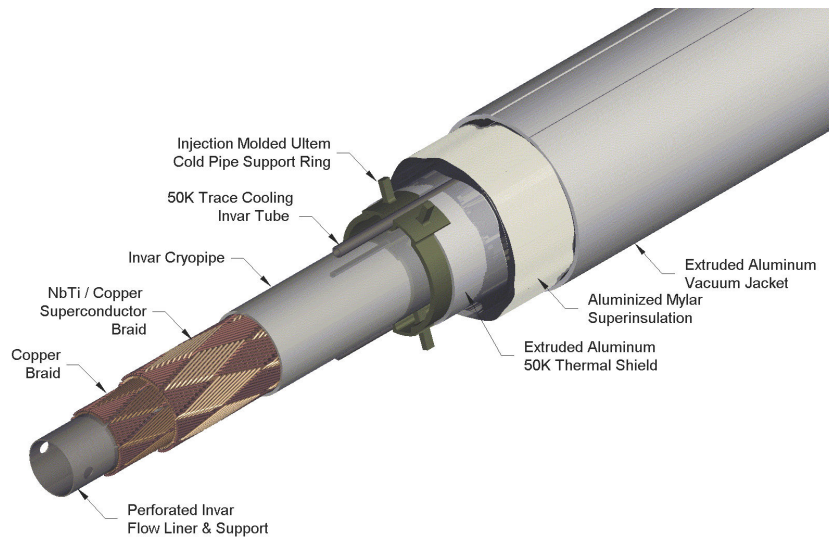


Figure 56: Schematic of superconducting transmission line showing construction details.

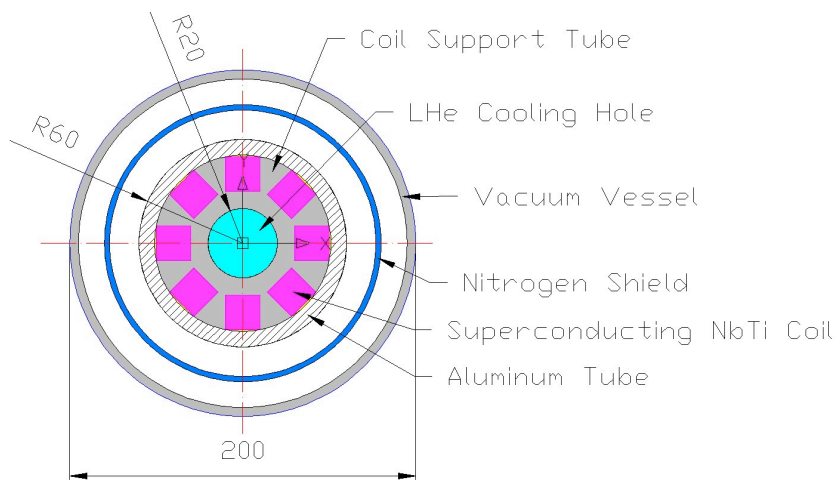


Figure 57: Schematic of the central cryostat for a superconducting transmission line system with eight turns.

Field Map

Using the MIND plate geometry shown in figure 45, a 2D magnetic analysis of the plate was performed. Figure 59 shows the model (1/8th) that was used in the analysis. A 100 cm diameter hole for the STL was assumed and the MINOS steel [139] BH curve was assumed. For this analysis, an excitation current of 100 kA was used. This was the critical current achieved at 6.5 K in the STL test stand assembled for the VLHC proof-of-principle. In figure 60 we give the azimuthal B field along the two lines (A-B and A-C) shown in figure 59. Figure 61 gives the 2D contour lines of constant B.

R&D Requirements

The STL described above was optimised for the 37 km radius of the VLHC. The loop length needed for MIND is quite a bit shorter than the 233 km needed for the VLHC. The optimised design of a STL for MIND is therefore likely to be different. The 2.5 cm He-flow region can most likely be reduced, for example. In addition, we

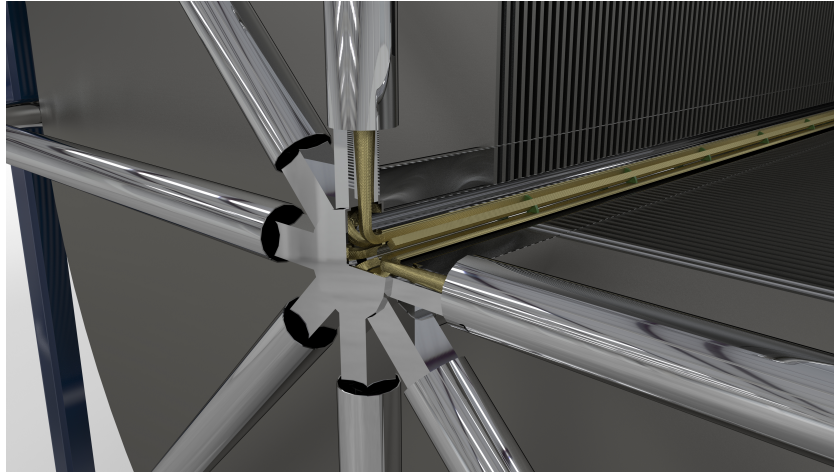


Figure 58: Rendering of the central section of MIND showing the central cryostat and the eight current return loops.

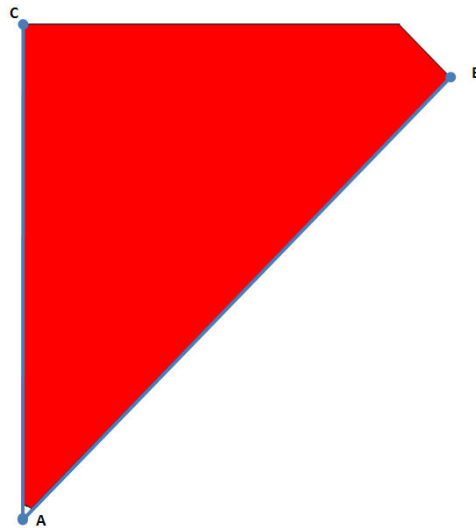


Figure 59: 1/8th model used for magnetic analysis.

would like to consider an STL with multiple internal current loops so that a 100 kA room temperature driving source is not needed. The total amount of superconductor would be roughly the same; 5-10 turns with a current of 20-10 kA each would be more manageable from the viewpoint of the power source.

4.2.2.4 Scintillator extrusions

Particle detection using extruded scintillator and optical fibres is a mature technology. MINOS has shown that co-extruded solid scintillator with embedded wavelength shifting (WLS) fibres and PMT readout produces adequate light for MIP tracking and that it can be manufactured with excellent quality control and uniformity in an industrial setting. Many experiments use this same technology for the active elements of their detectors, such as the K2K Scibar [140], the T2K INGRID, the T2K P0D, the T2K ECAL [141] and the Double-Chooz detectors [142].

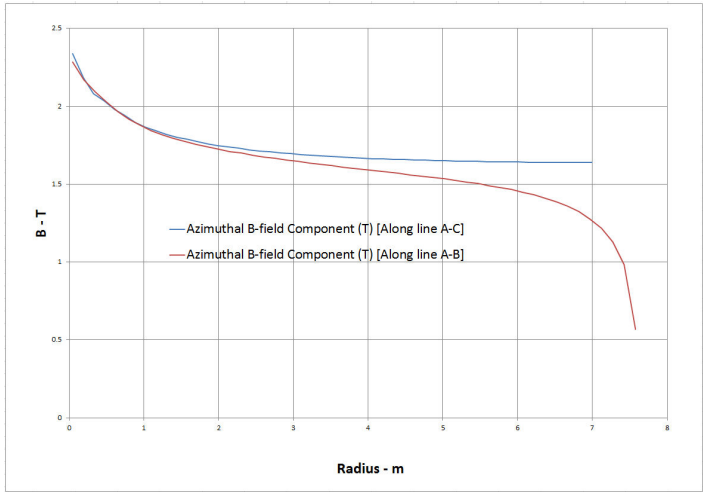
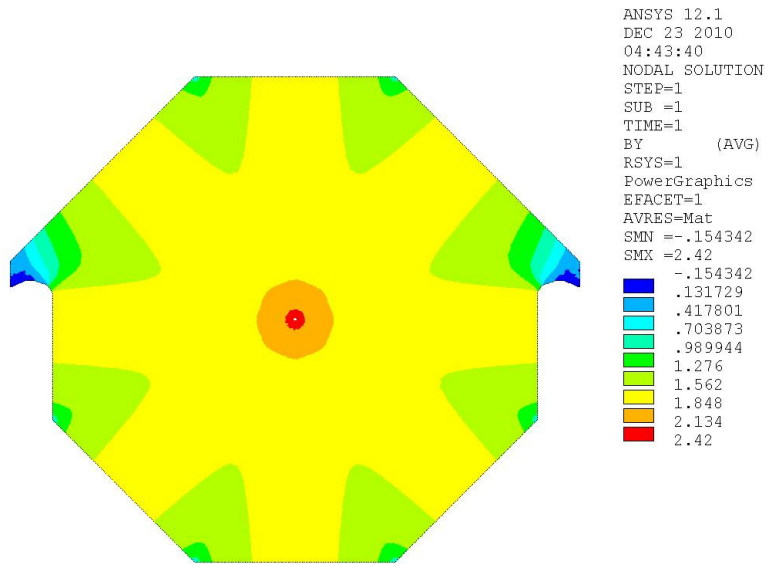


Figure 60: Magnetic field along the lines A-B and A-C in Fig 59.



Azimuthal B-field

Figure 61: Contours of constant magnetic B-field.

Our initial concept for the readout planes for MIND is to have both an x and a y view between each plate. The simulations performed to date have assumed a scintillator extrusion profile that is $3.5 \times 1.0 \text{ cm}^2$. This gives both the required point resolution and light yield. We are also considering an option where we use triangular extrusions similar to those used in Minerva [143].

The existing MIND simulations have assumed that the readout planes will use a rectangular extrusion that is $3.5 \times 1.0 \text{ cm}^2$, see figure 62 (left). A 1 mm hole down the centre of the extrusion is provided for insertion of the wavelength shifting fibre. This is a relatively simple part to manufacture and has already been fabricated in a similar form for a number of small-scale applications. The scintillator strips will consist of an extruded polystyrene core doped with blue-emitting fluorescent compounds, a co-extruded TiO_2 outer layer for reflectivity, and a hole in the middle for a WLS fibre. Dow Styron 665 W polystyrene pellets are doped with PPO (1% by weight) and POPOP (0.03% by weight). The strips have a white, co-extruded, 0.25 mm thick TiO_2 reflective coating. This layer is introduced in a single step as part of a co-extrusion process. The composition of this capstocking is 15% TiO_2 (rutile) in polystyrene. In addition to its reflectivity properties, the layer facilitates the assembly of the scintillator strips into modules. The ruggedness of this coating enables the direct gluing of the strips to each other and to the module skins which results in labour and time savings for the experiment. This process has now been used in a number of experiments.

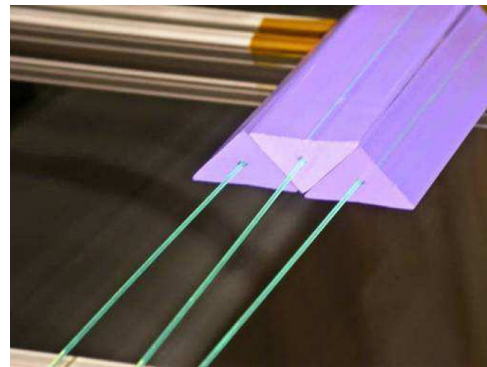
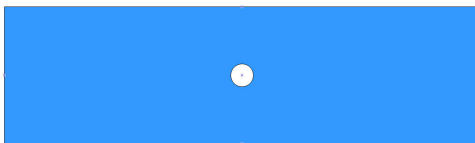


Figure 62: Left: Schematic of rectangular scintillator extrusion. Right: Minerva extrusions showing partial readout plane and wavelength shifting fibres.

We are also considering using the Minerva extrusion (see figure 62, right) for MIND. The triangle has a 3.3-cm base and a 1.7-cm height, and a 2.6 mm hole for a WLS fibre (see figure 63).

4.2.2.5 Photon detectors

Given the rapid development in recent years of solid-state photodetectors based on Geiger mode operation of silicon avalanche photodiodes, we have chosen this technology for MIND. Although various names are used for this technology, we will use silicon photomultiplier or SiPM.

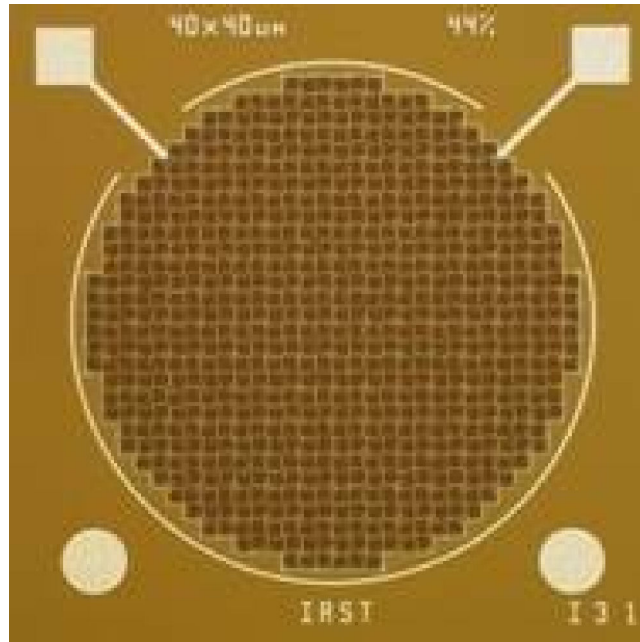


Figure 64: Photograph of SiPM

of SiPMs spreads, so will the use of custom SiPMs with integrated electronics, just as ASICs have superseded standard logic in electronics.

The photon detection efficiency (PDE) of a SiPM is the product of three factors:

$$\text{PDE} = QE \cdot \varepsilon_{\text{Geiger}} \cdot \varepsilon_{\text{pixel}} ; \quad (17)$$

where QE is the wavelength-dependent quantum efficiency, $\varepsilon_{\text{Geiger}}$ is the probability to initiate the Geiger discharge by a photoelectron, and $\varepsilon_{\text{pixel}}$ is the fraction of the total photodiode area occupied by sensitive pixels. The bias voltage affects one parameter in the equation 17, $\varepsilon_{\text{Geiger}}$. The geometrical factor $\varepsilon_{\text{pixel}}$ is completely determined by the photodiode topology, and is in the range 50-70%. The PDE of a device manufactured by Hamamatsu [149] (Hamamatsu uses the name multi-pixel photon counter, MPPC) as function of wavelength of detected light is shown in figure 65.

Implementation for a very large system

Although SiPMs with integrated electronics are in their infancy, we can say quite a bit about what such a device might look like in the case of instrumenting a very large system of extruded scintillator with wavelength shifting fibre readout, with a channel count of many million channels. In a system of that size, there is no question that an application specific approach, which can reduce the unit costs by factors of five to ten, will easily justify the additional non-refundable expense inherent in a custom development. In this application, the SiPM would have an area of about one square mm, with about 100 pixels and electronics around the periphery of the device. Each cell would have a few transistors along one of the sides to provide active quenching—this differs from first-generation SiPMs, which use a passive resistor as the quenching element. In the case of active quenching, each pixel has essentially a digital latch associated with it. When a pixel fires, the latch is set, until an external reset signal arms the latch once again. This mechanism should not be confused with devices such as vertex pixel detectors. In this case, because the pixel capacitance is very small, the signal voltage is typically between

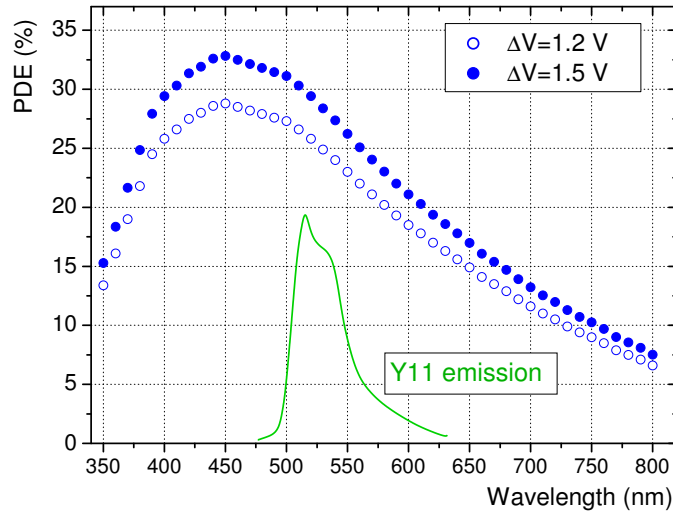


Figure 65: Photon detection efficiency of a Hamamatsu MPPC as a function of wavelength of the detected light at ΔV of 1.2 and 1.5 V at 25°C. The Y11(150 ppm) Kuraray fibre emission spectrum (in a. u.) for fibre length of 150 cm (from Kuraray specification) is also shown.

1 V and 2 V. Unlike vertex detectors, there is no amplification needed, and therefore, there is almost no standing current required in the transistors and the power dissipation is very small. It is only slightly larger than in the case of passive SiPMs and, in any case, much smaller than in vertex detectors. Active quenching has many advantages over passive quenching. For the application we are considering here, one of the main advantages is being able to control precisely when the pixels of the SiPM are rearmed. This greatly improves the dynamic range available for a given number of pixels because each pixel can fire only once during the signal collection period and therefore it is simple to correct for the probability that some pixels were hit more than once. In the passive quenching case, the pixels will start recharging while there are still signal photons arriving, allowing some pixels to fire when the pixel is not fully charged, violating the rule that every pixel gives the same signal. This makes saturation correction complicated and unreliable, as it depends on many details of the signal and the SiPM. For the application we are considering here, an active quenching SiPM with 100 pixels gives about the same resolution as a passively quenched SiPM with 250 pixels. The smaller number of pixels reduces the ratio of the active area to the area lost to routing, resistors, and optical isolation trenches between the pixels and makes up for the added dead area associated with the active-quench circuitry.

4.2.2.6 Readout Electronics

On the periphery of the chip there is circuitry that latches the number of fired pixels in a FIFO, adds a time stamp and issues periodic latch resets to the quenching circuits. The communication with the chip is serial, with an input, an output and a clock, all of which are differential signals. SiPM bias and ground complete the connections for a total of eight. The power for the digital circuitry on the chip is extracted from the clock lines. A number of chips would be connected with flex cables, in a ring topology, to a data concentrator module which would service a large number of SiPMs. A reasonable bandwidth available on differential lines over a flex cable for distances up to a few meters is between 10 Mbps and 100 Mbps. Depending on the rate of signals in the detector, and including things such as protocol overhead and data redundancy, a reasonable estimate of

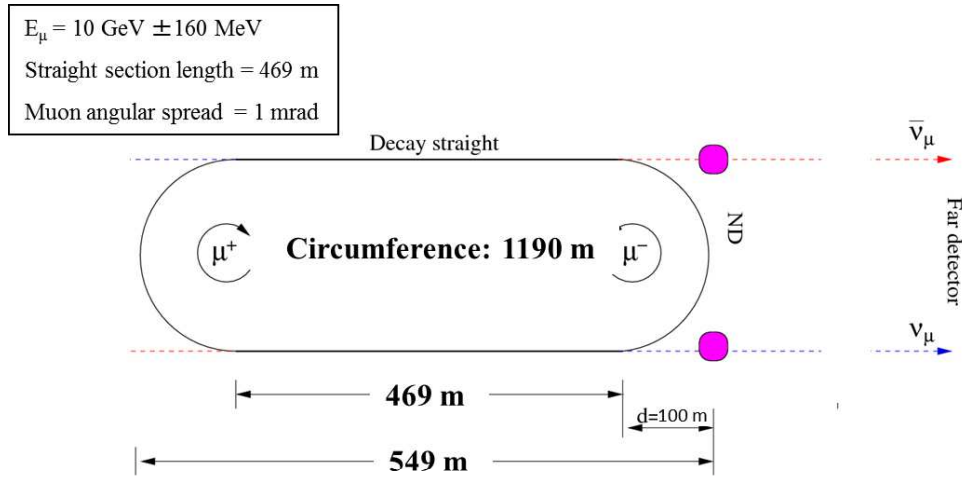


Figure 66: Baseline locations of the near detectors. The decay ring parameters are given for a 10 GeV Neutrino Factory

the number of SiPM chips that can be serviced by a single data concentrator is a few thousand. We expect that in this application, the number of SiPMs in a module associated with a single data concentrator would be limited by mechanical and operational considerations to something like 250 to 500. From the data concentrator, the data travel over optical links to higher-level data collectors.

4.3 Near detectors

4.3.1 Introduction

The Neutrino Factory will need near detectors to reach the aimed precision for a neutrino oscillation analysis. The main task of the near detector is to measure the flux of the neutrino beam. A high intensity neutrino source like a Neutrino Factory provides the opportunity for precision studies of various neutrino interaction processes in the near detector. It is necessary to have one near detector at each of the straight sections of the storage ring, thus at each of the two polarities (Figure 66). The near detector tasks include measurement of the neutrino flux through measurement of neutrino-electron scattering, measurement of neutrino beam properties needed for the flux to be extrapolated to the far detector and measurement of the charm production cross sections (charm production in the far detector is one of the main backgrounds to the oscillation signal). In addition, the high intensity Neutrino Factory beam allows for unique neutrino physics non-oscillation studies, such as the measurement of cross sections, structure functions, nuclear effects, $\sin^2 \theta_W$ etc. The near detector must also be capable of searching for new physics, for example by detecting τ -leptons, which are particularly sensitive probes of non-standard interactions at source and at detection, and since ν_τ detection is also important in the search for sterile neutrinos.

The design requirements for the near detector(s) can be formulated as follows: a low Z high resolution tracker for flux and cross section measurement (ν_μ and ν_e); a magnetic field for charge identification and momentum measurement; a muon catcher for muon identification; capability for e^+/e^- identification; a vertex detector for

charmed hadron and τ -lepton detection and good neutrino energy resolution.

4.3.2 Neutrino flux measurement using neutrino-electron scattering

Neutrino-electron interaction cross sections are straightforward to calculate in the Standard Model [150]. Any small uncertainties arise only from (well measured) Standard Model parameters. Therefore, such processes are suitable to measure the neutrino beam fluxes, provided that the beams are intense enough.

There are two pure leptonic neutrino interactions that produce an energetic muon in the final state:

$$\nu_\mu + e^- \rightarrow \mu^- + \nu_e \quad \text{and} \quad \bar{\nu}_e + e^- \rightarrow \mu^- + \bar{\nu}_\mu \quad (IMD). \quad (18)$$

The first one is known as inverse muon decay (*IMD*), while the second one produces a muon in the final state through annihilation. The neutrino energy threshold (for electrons at rest) for both processes is 10.9 GeV. Thus, these processes are not suitable for a 10 GeV Neutrino Factory, considered in this report. At an earlier stage, studies of a 25 GeV Neutrino Factory were considered. In that scenario, the above processes could have provided a very clean way of measuring the neutrino flux, as was shown in [151].

For a muon beam of 10 GeV there are four pure leptonic neutrino reactions (with very low threshold) that produce an energetic electron in the final state:

$$\nu_\mu + e^- \rightarrow \nu_\mu + e^- \quad \text{and} \quad \bar{\nu}_e + e^- \rightarrow \bar{\nu}_e + e^- \quad (ES^-) \quad (19)$$

$$\nu_e + e^- \rightarrow \nu_e + e^- \quad \text{and} \quad \bar{\nu}_\mu + e^- \rightarrow \bar{\nu}_\mu + e^- \quad (ES^+). \quad (20)$$

The processes in (19) will appear in a μ^- decay mode beam, while the processes shown in (20) are relevant for a μ^+ decay mode beam. Their cross-sections are given by [152]:

$$\sigma(\nu_l e \rightarrow \nu_l e) = \frac{G_\mu^2 m_e E_\nu}{2\pi} \left[1 - 4 \sin^2 \theta_W + \frac{16}{3} \sin^4 \theta_W \right] \quad (21)$$

$$\sigma(\bar{\nu}_l e \rightarrow \bar{\nu}_l e) = \frac{G_\mu^2 m_e E_\nu}{2\pi} \left[\frac{1}{3} - \frac{4}{3} \sin^2 \theta_W + \frac{16}{3} \sin^4 \theta_W \right] \quad (22)$$

and depend solely on θ_W , the weak mixing angle. In what follows we shall often refer to the processes (18)-(20) as *leptonic processes* or *leptonic events*.

The total cross sections for the above processes as a function of the neutrino energy are shown in Figure 67. Despite their smallness, a massive detector placed close to the straight section of the Neutrino Factory storage ring can provide sufficient interaction rate, see Figure 68.

However, inclusive CC and NC neutrino interactions with nuclei

$$\nu_\ell + N \rightarrow \ell + X \quad \text{and} \quad \nu_\ell + N \rightarrow \nu_\ell + X \quad (23)$$

have cross sections a few orders of magnitude larger. An obvious distinction between purely leptonic processes and the processes shown in (23) is the lack of a hadronic system in the former. Thus, the measured recoil energy of the hadronic system X can be used as a good criterion for background suppression. A composite variable $\theta_\ell^2 E_\ell$, proportional to the Bjorken variable $y = 1 - E_\ell/E_\nu$ in elastic scattering, provides good separation between signal and background for neutrino-electron scattering processes, provided the lepton angle and energy are measured with sufficient precision. The discrimination power of the $\theta_\ell^2 E_\ell$ and recoil energy of the hadronic system is demonstrated in Figure 69.

Figure 67: Total cross section divided by neutrino energy for the leptonic interactions in a Neutrino Factory beam. Hexagon markers show CC interactions, triangle markers show NC interactions and rhomboid markers show mixed CC+NC interactions. The threshold for IMD and muon production through annihilation (the processes in equation 18) (blue) are evident at ~ 11 GeV.

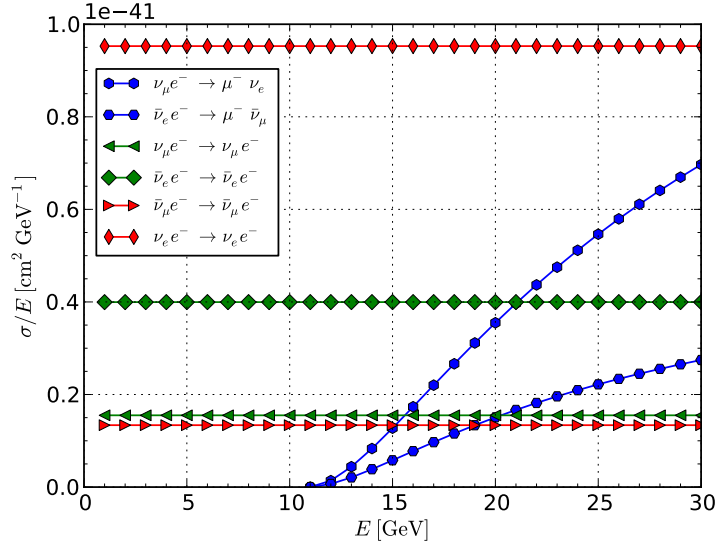
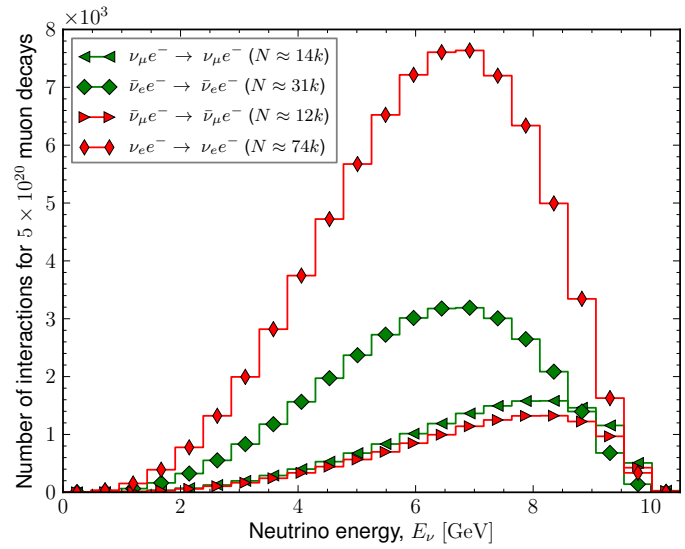


Figure 68: Number of neutrino-electron interactions for a nominal year of Neutrino Factory operation (5×10^{20} muon decays per muon charge per straight section). Rates are calculated for a 2.7 t detector with 1.5×1.5 m² frontal cross section and average $Z/A \approx 0.54$. The detector is placed 100 m after the straight section of the Neutrino Factory.



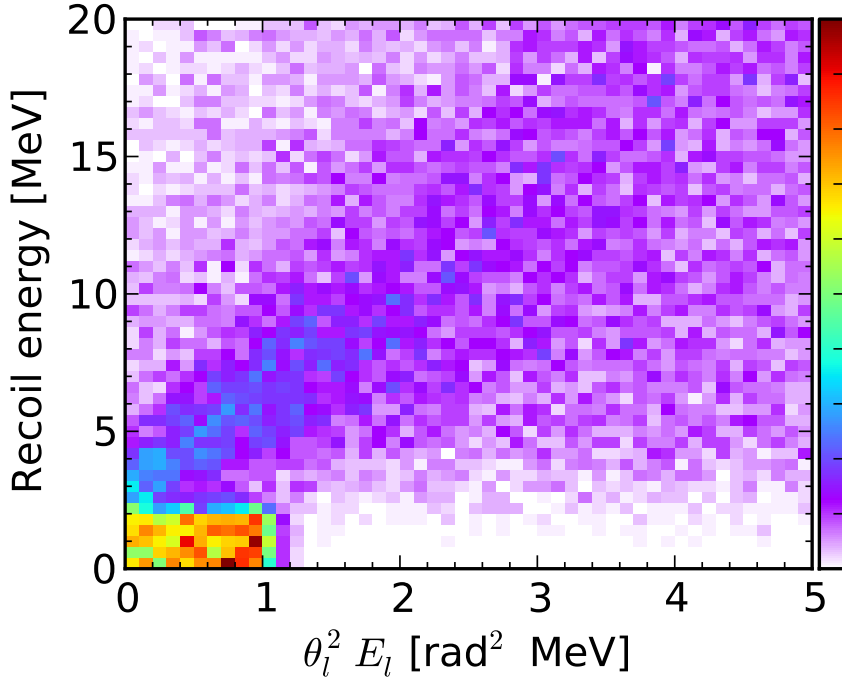


Figure 69: True $\theta_l^2 E_l$ vs. true recoil energy plus deposited energy in 1 cm of polystyrene by the scattered lepton for μ^+ decay mode. The peak below $\theta_l^2 E_l \sim 1$ $\text{rad}^2 \text{MeV}$ corresponds to the ES^+ events.

4.3.3 Near detector flux influence on far detector sensitivities

A robust method for predicting the far detector flux, based on the near detector flux, for neutrino oscillation searches was developed in [132]. The solid angle subtended by the near detector at the end of the decay straight of the Neutrino Factory is much larger than the solid angle observed by the far detector. This results in a different energy spectrum for a near detector compared to a far detector.

The technique essentially involves the use of three response matrices: the near detector response, the flux projection and the far detector response. Furthermore, matrices that describe the relevant cross-sections and a parameterisation of the oscillation probability are used in the determination of the sensitivity to oscillation parameters. The observed far detector spectrum is compared to the projection of the observed near detector spectrum [153] at each possible value of (θ_{13}, δ) :

$$N_{FD} = M_{FD} P_{osc}(\theta_{13}, \delta) M_{nOsc} M_{ND}^{-1} N_{ND}; \quad (24)$$

where N_{FD} and N_{ND} are the observed far and near detector spectra respectively, M_{FD} and M_{ND} are matrices representing the combination of cross-section and response for ν_μ ($\bar{\nu}_\mu$) at the far detector and ν_e ($\bar{\nu}_e$) at the near detector respectively, P_{osc} is the oscillation probability and M_{nOsc} relates the expected far detector ν_e ($\bar{\nu}_e$) flux without oscillations to the expected ν_e ($\bar{\nu}_e$) flux at the near detector. The extracted functions are then fit to the oscillation probability formulae to find the best fit values of the θ_{13} and δ simultaneously.

Using the near detector to measure both the ν_μ ($\bar{\nu}_\mu$) and $\bar{\nu}_e$ (ν_e) rates, the interaction spectra at the far detector can then be predicted. The only background to the ν_μ ($\bar{\nu}_\mu$) measurement is likely to be from neutral current interactions. Using a combination of missing p_T and vertex reconstruction, both of which can be measured with high resolution at a near detector, this could be suppressed to at least the level in the far detector. The $\bar{\nu}_e$ (ν_e) measurement can be carried out with electron scattering events, as shown in equations 19 and 20. The near detector resolution is used to construct a probability matrix relating directly near detector interactions to unoscillated far detector interactions, as in MINOS [154].

A feasibility study of the method was carried out assuming a 100 kg cylindrical detector of 1 m radius placed 100 m from the end of a 600 m straight decay section at a 25 GeV Neutrino Factory. The muons were assumed

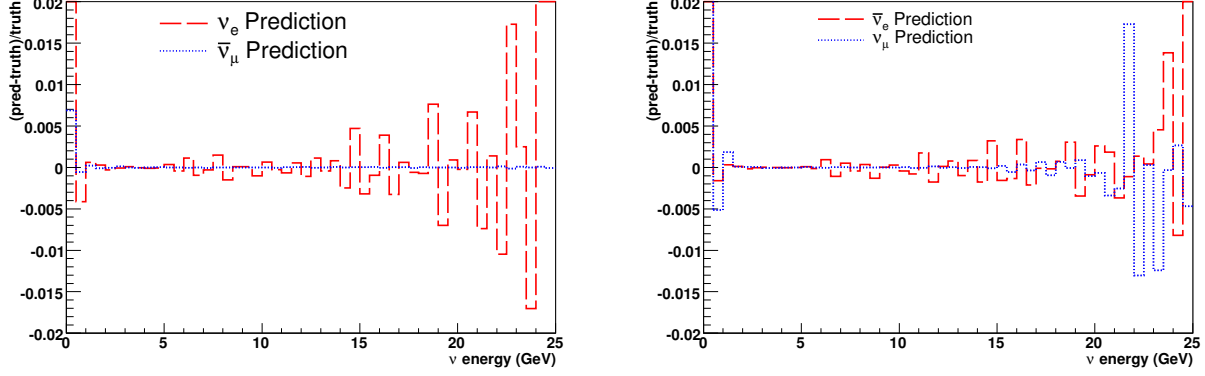


Figure 70: Comparison of predicted to true flux through the ND for stored μ^+ (left) and stored μ^- (right).

to decay randomly along a straight line with an appropriate beam divergence and calculating the expected spectrum from the near detector acceptance. The detector was modelled using a $\bar{\nu}_e$ (ν_e) energy resolution of $35\%/\sqrt{E}(\text{GeV})$. The selection efficiency was assumed to rise linearly from 0% at 0 GeV up to 70% above 4 GeV. The ν_μ ($\bar{\nu}_\mu$) resolution was set at $20\%/\sqrt{E}(\text{GeV})$, with efficiency of 80% for $\bar{\nu}_\mu$ and 60% for ν_μ above 4 GeV (similar to the far detector).

The calculated energy of the interactions at the near detector were smeared accordingly and the flux and correlation matrices for each channel were then projected to the appropriate far detector in bins of width 0.5 GeV. A comparison of the near and far detector fluxes is shown in figure 70). Differences of more than 1% with respect to the predicted fluxes are only visible at energies above 20 GeV. Below 10 GeV, the differences are seen to be $\sim 0.2\%$.

The far detector spectra are calculated with the non-oscillation predictions from the near detector. The far detector spectra obtained are then used to perform a fit using the χ^2 function:

$$\chi^2 = \sum_i (N_i - n_i) V_i^{-1} (N_i - n_i)^T ; \quad (25)$$

where N_i is the predicted spectrum, n_i is the data spectrum and V_i the correlation matrix, composed of the projected matrix of the prediction and the expected errors on the far detector measurement, for muon beam polarity i (positive or negative). Figure 71 shows the results of fits to a range of θ_{13} and δ values using this technique. The resolution of θ_{13} and δ is generally better at large θ_{13} .

The χ^2 fits obtained by performing the near-far extrapolation method generally constrain the true values of θ_{13} and δ better than when the near detector is not included in the fit. Figure 72 shows a comparison of the near-far method to a fit unconstrained by the near detector for the values $\theta_{13} = 1^\circ$ and $\delta = 45^\circ$. At the 1σ level ($\chi^2 - \chi_{min}^2 = 1$) the fits to θ_{13} and δ are very similar, but the near-far projection method shows smaller projected errors in both θ_{13} and δ at the 3σ level ($\chi^2 - \chi_{min}^2 = 9$).

Figure 73 shows the trend for the measurement of the oscillation parameters for the near-far projection method. The typical 1σ error expected for θ_{13} is $\Delta\theta_{13} \sim 0.05^\circ$. The error in δ depends on the value of δ and at larger values of θ_{13} is $\Delta\delta \sim 5^\circ$. Both θ_{13} and δ are predicted by the fit without any significant bias.

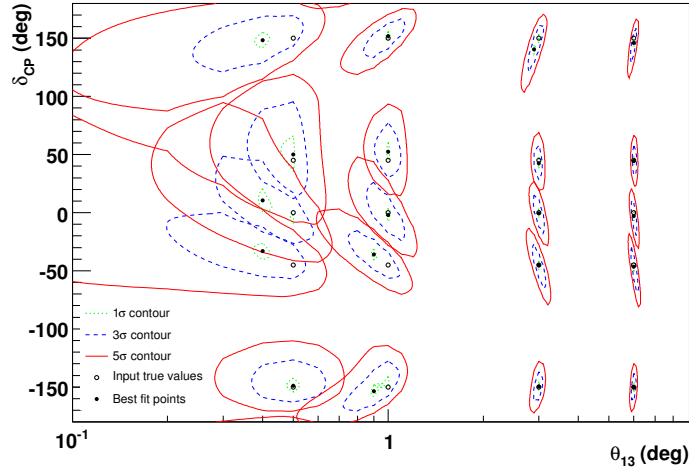


Figure 71: Fits to simulated data using the near-far prediction assuming a normal mass hierarchy.

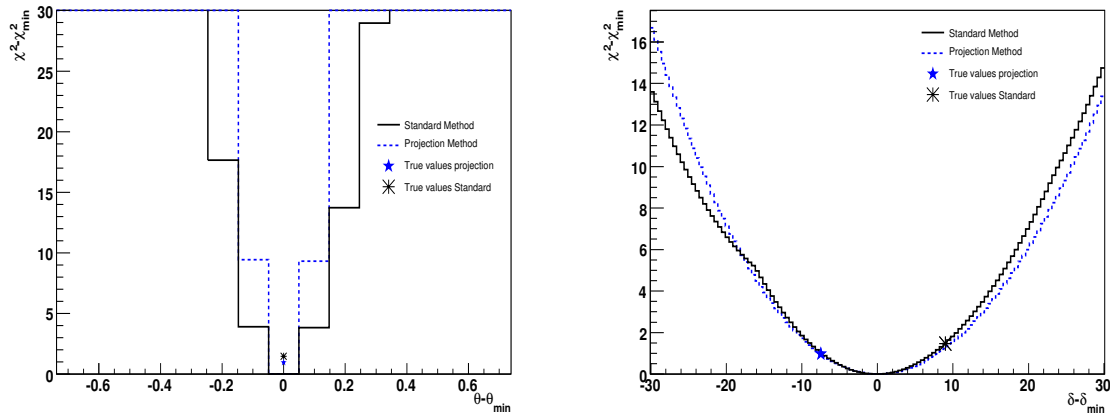


Figure 72: Projection of the minimum χ^2 onto the θ_{13} axis (left) and the δ axis (right) for $\theta_{13} = 1^\circ$ and $\delta = 45^\circ$.

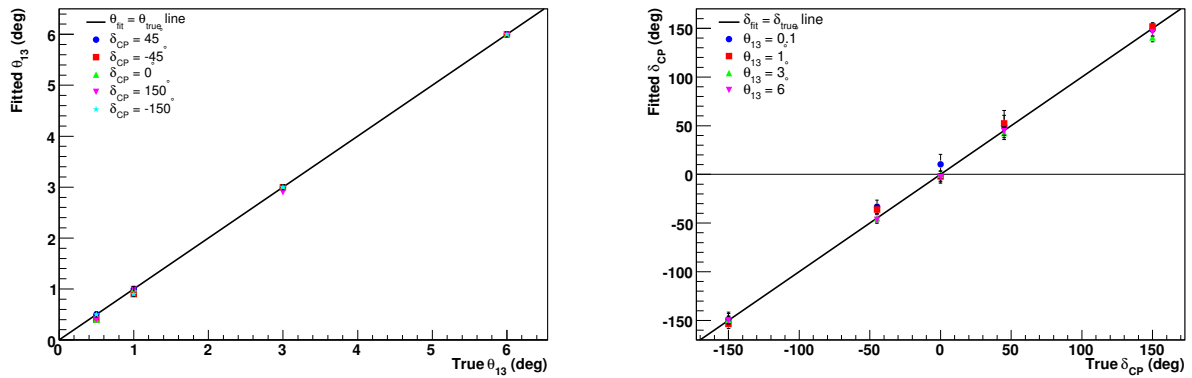


Figure 73: Quality of fit to θ_{13} (left) and δ (right) for a range of values, using the near-far projection method.

4.3.4 Neutrino-nucleus scattering

4.3.4.1 Introduction

Recent interest in neutrino interactions in the few GeV energy region arises from neutrino oscillation experiments and their need to reduce systematic errors. Cross section measurements are being performed by neutrino experiments, with T2K [155], MINERvA [156, 157], MiniBooNE [158, 159], SciBooNE [160] and NOMAD [161] as recent examples. A new effort to determine cross-sections using liquid argon (LAr) detectors (MicroBooNE) [162] is currently being planned for the near future at Fermilab.

Even with this degree of activity, the precision with which the basic neutrino-*nucleon* cross sections are known is still not better than 20 – 30%. There are two main reasons for this: the poor knowledge of neutrino fluxes and the fact that all the recent cross section measurements have been performed on nuclear targets. It is important to recall that current neutrino experiments measure events that are generated from a convolution of energy-dependent neutrino flux \otimes energy-dependent cross section \otimes energy-dependent nuclear effects. The experiments therefore measure an effective neutrino-nucleus cross section (for example, on carbon). To extract a neutrino-*nucleon* cross section from these measurements requires separation of nuclear physics effects, which can only be done with limited precision. For many oscillation experiments, using the same nuclear targets for their near and far detectors is a good start. However, even with the same near and far nuclear target, the neutrino energy spectra differ, due to beam geometry and oscillations, so a different convolution of cross section \otimes nuclear effects is observed, so there is no automatic cancellation between the near and far detectors. For a thorough comparison of measured neutrino-nucleon cross sections with theoretical models, these convoluted effects have to be understood. For further details please see [163]. This section will summarize the current status of both theoretical and experimental studies of neutrino nucleus scattering and how a neutrino factory, with its superior knowledge of the neutrino flux and its high-intensity source of electron-neutrinos, can contribute.

For neutrino-*nucleon* interactions one can distinguish: Charged Current quasi-elastic (CCQE), Neutral Current elastic (NCEI), Resonance production (RES) and more inelastic reactions involving pion production from the Δ through the transition region up to the deep-inelastic (a rather misleading "DIS" term is often used to describe all the interactions which are neither CCQE/NCEI nor RES) domain. Quite different theoretical tools are used to model each of them. **The expected event fractions at a near detector 30 m from the end of a 10 GeV neutrino factory are XX% resonant, YY% quasi-elastic and ZZ% DIS. For anti-neutrinos the breakdown is XX% resonant, YY% quasi-elastic and ZZ% DIS.**

From the experimental point of view it is most natural to speak about events in terms of the visible final state topology; that is, events with no pions in the final state or with only one or more pions above a given momentum threshold. In fact, in several recent experimental measurements that investigated quantities defined in this way, the dependence on assumptions of Monte Carlo event generators was minimal. To compare with the experimental data given in this format, one must add contributions from various dynamical mechanisms and also model Final State Interactions (FSI) effects. Several ingredients of the theoretical models are verified simultaneously. It is clear that in order to validate a model one needs many samples of precise neutrino-nucleus scattering measurements on a variety of nuclear targets with various neutrino fluxes.

4.3.4.2 Charged Current quasi-elastic

The simplest neutrino hadronic reaction is the charge current quasi-elastic (CCQE) interaction:

$$\nu_\ell + n \rightarrow \ell^- + p$$

with a charged lepton and a proton in the final state and the antineutrino analog in which the neutron and the proton are exchanged. We need to extend this definition to the neutrino-nucleus interaction occurring on bound nucleons. The ejected proton is not necessarily seen in a detector because quite often its momentum is below the acceptance threshold. However, events with a single reconstructed charged lepton track can result from a variety of initial interactions e.g. from a two body charged current interaction or from real pion production and its subsequent absorption. Similar problems arise in other type of interactions. It is becoming clear that interpretation of neutrino-nucleus interactions must rely on a careful data/Monte Carlo (MC) comparison done with reliable MC neutrino event generators.

In the case of neutrino nucleus scattering we also use the term CCQE-like reaction to define one in which there are no pions in the final state. It then includes events with real pion production followed by absorption. It also includes interactions on bound-nucleon systems (np-nh or meson-exchange current), which will be discussed shortly.

A theoretical description of the free nucleon target CCQE reaction is based on the conserved vector current (CVC) and the partially conserved axial current (PCAC) hypotheses. The only unknown quantity is the nucleon axial form-factor $G_A(Q^2)$ for which one typically assumes a dipole form

$$G_A(Q^2) = \frac{G_A(0)}{\left(1 + \frac{Q^2}{M_A^2}\right)^2}$$

with one free parameter, the axial mass M_A . This dipole form is an assumption which need not hold. Non-dipole form factors are being investigated in [164].

In the past, several measurements of M_A were performed on a deuterium target for which most of nuclear physics complications are minimal and it seemed that the results converged to a value of the order of 1.03 GeV [165]. There is an additional argument in favor of a similar value of M_A coming from the weak pion-production at low Q^2 . A PCAC based evaluation gives an axial mass value of 1.077 ± 0.039 GeV [166]. On the other hand, all of the more recent high statistics measurements of M_A , with the exception of the NOMAD higher-energy experiment, reported larger values, with the MiniBooNE (carbon, $Q^2 > 0$ GeV²) determination of 1.35 ± 0.17 [167] compared to the NOMAD (carbon, $Q^2 > 0$ GeV²) value of 1.07 ± 0.07 [168]). The most recent MINERvA preliminary results for CCQE antineutrino reaction are still subject to large flux normalization uncertainties but they seem to be consistent with $M_A = 0.99$ GeV [169].

Theoretical approaches to CCQE

Several approaches have been followed to describe the CCQE-like process. For moderate and intermediate neutrino energies, in the few GeV region, the most relevant ones are: the involvement of one nucleon, or a pair of nucleons or even three nucleon mechanisms and the excitation of Δ or higher resonances.

A review of theoretical model results can be found in [170]. Almost all approaches used at intermediate neutrino energies rely on the impulse approximation (IA) and neutrino-nucleus CCQE interactions and are viewed as a two step process: primary interaction and Final State Interactions (FSI), and then the propagation of resulting hadrons through the nucleus. In addition they consider several nuclear effects such as the Random Phase Approximation (RPA) or Short Range Correlations (SRC). In the neutrino-nucleus cross section measurements, a goal is to learn about neutrino free nucleon target scattering parameters (an obvious exception is coherent pion production). *Effective* parameters, like the sometimes discussed quasi-elastic axial mass M_A^{eff} , are of little use as their values can depend on the neutrino flux, target and perhaps also on the detection technique or the acceptance.

The simplest model, commonly used in Monte Carlo event generators, is the relativistic Fermi gas (RFG) model proposed by Smith and Moniz more than 40 years ago [171]. The model combines the bare nucleon

physics with a model to account for Fermi motion and nucleon binding within the specific nucleus. The model can be made more realistic in many ways to achieve better agreement with a broad range of electron scattering data. For example, the inclusion of a realistic joint distribution of target nucleon momenta and binding energies based on short range correlation effects leads to the spectral function (SF) approach. Spectral functions for nuclei, ranging from carbon ($A = 12$) to iron ($A = 56$) have been modeled [172]. Calculations by Benhar *et al.*, [173] and Ankowski *et al.*, [174] show that the SF effects only moderately modify the muon neutrino differential cross sections, leading to reductions of the order of 15% in the total cross sections. Inclusion of nucleon-nucleon long-range correlations leads to RPA effects which improves predictions at lower momentum transfers (and also low Q^2).

Multinucleon mechanisms

A plausible solution to the large axial mass puzzle was first pointed out by M. Martini¹¹ *et al.*, [176, 177], and later corroborated by the IFIC group [178, 179]. In the MiniBooNE measurement of Ref. [167], QE is related to processes in which only a muon is detected in the final state. As was already discussed above, besides genuine QE events, this definition includes multinucleon processes. The MiniBooNE analysis of the data attempts to correct (through a Monte Carlo estimate) for real pion production that escapes detection through absorption in the nucleus leading to multinucleon emission. But, it seems clear that to describe the data of Ref. [167], it is necessary to consider, at least, the sum of the genuine QE (absorption by just one nucleon), and the multinucleon contributions, respectively. The sum of these two contributions contribute to the CCQE-like cross section.

The inclusion of the 2p2h (multinucleon) contributions enables [178, 180] the double differential cross section $d^2\sigma/dE_\mu d\cos\theta_\mu$ and the integrated flux unfolded cross section measured by MiniBooNE, to be described with values of M_A (nucleon axial mass) around 1.03 ± 0.02 GeV [166, 168]. This is re-assuring from the theoretical point of view and more satisfactory than the situation envisaged by some other work that described the MiniBooNE data in terms of a larger value of M_A of around 1.3–1.4 GeV, as mentioned above.

Neutrino energy reconstruction

Neutrino oscillation probabilities depend on the neutrino energy, unknown for broad fluxes and, for CCQE, often estimated from the measured angle and energy of the outgoing charged lepton ℓ only. It is common to define a reconstructed neutrino energy E_{rec} (neglecting binding energy and the difference of proton and neutron masses) as:

$$E_{\text{rec}} = \frac{ME_\ell - m_\ell^2/2}{M - E_\ell + |\mathbf{p}_\ell| \cos\theta_\ell} \quad (26)$$

which would correspond to the energy of a neutrino that emits a lepton, of energy E_ℓ and three-momentum \mathbf{p}_ℓ , with a gauge boson W being absorbed by a free nucleon of mass M *at rest* in a CCQE event. The actual (“true”) energy, E , of the neutrino that has produced the event will not be exactly E_{rec} . Actually, for each E_{rec} , there exists a distribution of true neutrino energies that give rise to events whose muon kinematics would lead to the given value of E_{rec} . In the case of genuine QE events, this distribution is sufficiently peaked (the Fermi motion broadens the peak and binding energy shifts it a little) around the true neutrino energy to make the algorithm in Eq. (26) accurate enough to study the neutrino oscillation phenomenon [181]. However, due to the presence of multinucleon events, there is a long tail in the distribution of true energies associated to each

¹¹The papers of Martini *et al.* are based on the older investigation by Marteau *et al.*, [175]. The relevant features of the model were known already at the end of 1990s and at that time the goal was to understand better the SuperKamiokande atmospheric neutrino oscillation signal.

E_{rec} that makes the use of Eq. (26) unreliable. The effects of the inclusion of multinucleon processes on the energy reconstruction have been noticed in [182] and investigated in Ref. [183], within the Lyon 2p2h model and also estimated in Ref. [184], using the simplified model of Ref. [185] for the multinucleon mechanisms.

Monte Carlo event generators

Monte Carlo codes (GENIE, NuWro, Neut, Nuance, etc) describe CCQE events using a simple RFG model, with FSI effects implemented by means of a semi-classical intranuclear cascade. NuWro also offers a possibility to run simulations with a spectral function and an effective momentum dependent nuclear potential. It is also currently the only MC generator with implementation of MEC dynamics. Since the primary interaction and the final state effects are effectively decoupled, FSI do not change the total and outgoing lepton differential cross sections.

4.3.4.3 The Pion-production Region

In the so-called resonant (RES) region the channels of interest are mainly hadronic resonances, with the most important being the $\Delta(1232)$. Typical final states are those with a single pion. During the last five years several new pion production measurements have been performed. In all of them, the targets were nuclei (most often carbon) and interpretation of the data in terms of the neutrino-nucleon cross section needed to account for nuclear effects, impossible to do in a model-independent manner. On the other hand, there has been a lot of activity in the area of coherent pion production and this subject will be discussed separately.

NC π^0

Neutral current π^0 production (NC π^0) is a background to the ν_e appearance oscillation signal. One is interested in a π^0 leaving the nucleus and recent experimental data are given in this format with all the FSI effects included. Signal events originate mostly from: NC1 π^0 primary interaction with a π^0 not being affected by FSI and NC1 π^+ primary interaction with the π^+ being transformed into π^0 in a charge exchange FSI reaction. There are four recent measurements of NC π^0 production (K2K [186], MiniBooNE neutrinos, MiniBooNE antineutrinos [187] and SciBooNE [188]) that use three different fluxes: (K2K, Fermilab Booster neutrinos and anti-neutrinos) and three targets: H_2O (K2K), CH_2 (MiniBooNE) and C_8H_8 (SciBooNE). Final results are presented as flux averaged distributions of events as a function of the π^0 momentum and, in the case of MiniBooNE and SciBooNE, also as a function of the π^0 production angle.

CC π^+

MiniBooNE measured CC 1 π^+ production cross sections, where the signal is defined as exactly one π^+ in the final state with no other mesons [189]. A variety of flux integrated differential and doubly differential cross sections, were reported in Q^2 and the final state particles' momenta. The cross section results are much larger than NUANCE MC predictions and the difference is on average 23%. In Fig. 74 on the left GiBUU and NuWro predictions for CC π^+ are compared to the MiniBooNE data.

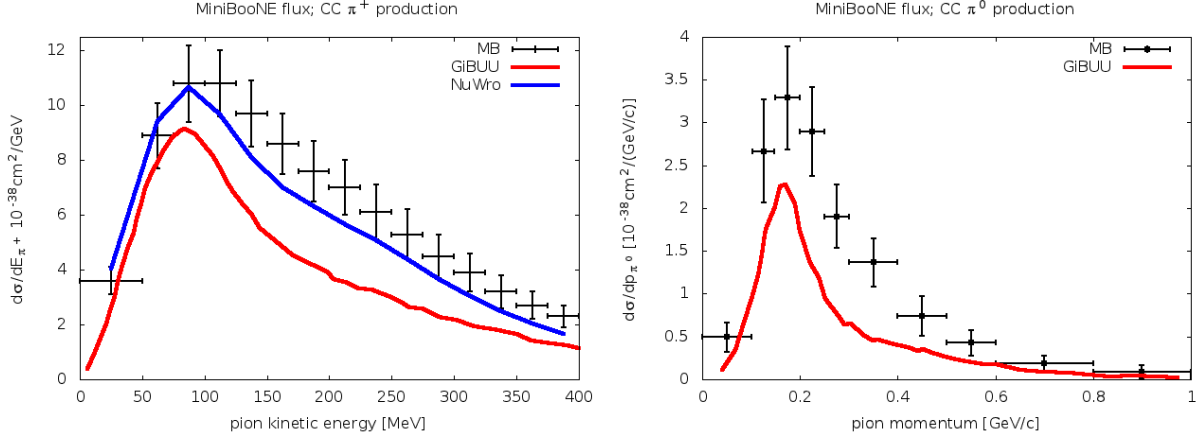


Figure 74: Left: Differential cross section for $CC1\pi^+$ production in the final state (all the FSI effects are included). MiniBooNE measurement [189] is compared to GiBUU [190] and NuWro computations. Right: the same for $CC\pi^0$ production, but only GIBUU results are shown.

CC π^0

MiniBooNE also measured $CC1\pi^0$ production cross sections. As before, the signal is defined as exactly one π^0 in the final state [191]. Various differential distributions are available. There is a dramatic discrepancy between the measured $CC1\pi^0$ production cross section as a function of neutrino energy and NUANCE MC predictions in the region of lower energies. On average the data is larger by $56 \pm 20\%$, but for $E_\nu < 1$ GeV the disagreement is as large as a factor of 2. In Fig. 74 on the right, GiBUU predictions for $CC\pi^0$ are compared to the MiniBooNE data.

Theoretical Considerations

Due to nuclear effects, a comparison to the new data is possible only for MC event generators, sophisticated computation tools like GiBUU and also a few theoretical groups which are able to evaluate FSI effects.

Most of the interesting work was done within GiBUU. It turned out to be very difficult to reproduce the MiniBooNE $CC1\pi^+$ and $CC1\pi^0$ results: the measured cross section is much larger than theoretical computations. In the case of $CC1\pi^+$ production, the discrepancy is as large as 100%. It was also noted that the reported shape of the distribution of π^+ kinetic energies is different from theoretical calculations and does not show a strong decrease at $T_{\pi^+} > 120$ MeV located in the region of maximal probability for pion absorption.

The authors of [190] mention three possible reasons for the data/GiBUU predictions discrepancy: (i) the fact that the Δ excitation axial form factor was chosen to agree with the ANL data only, neglecting the larger cross section measured in the BNL experiment; (ii) a hypothetical $2p-2h-1\pi$ pion production contribution analogous to $2p-2h$ discussed in Section 4.3.4.2; (iii) flux underestimation in the MiniBooNE experiment. Support for the latter arises from the better data/theory agreement found for the ratio, as discussed below.

In the case of $NC\pi^0$ production, a systematic comparison was performed with NuWro MC predictions with an updated FSI model for pions [192]. The overall agreement is satisfactory. Shapes of the distributions of final state π^0 s are affected by an interplay between pion FSI such as absorption and *formation time* effects, understood here as an effect of a finite Δ life-time. It is argued that $NC\pi^0$ production data can be very useful for benchmarking neutrino MC event generators.

In addition, it has been known since ANL and BNL pion production measurements that Δ excitation alone

cannot reproduce the data, although it is a dominant mechanism, and that non-resonant background terms must be included in the theoretical models. There were many attempts in the past to develop suitable models but usually they were not very well justified from the theoretical point of view.

Coherent pion production

In coherent pion production (COH) the target nucleus remains in the ground state. There are four possible channels: CC and NC reactions using neutrinos or anti-neutrinos. A clear experimental signal for the COH reaction for high energies was observed and the aim of recent measurements was to fill a gap in the knowledge of COH cross sections with energies around ~ 1 GeV. At larger neutrino energies a recent measurement was made by MINOS, which reported a NC reaction cross section at $\langle E_\nu \rangle = 4.9$ GeV to be consistent with the predictions of the Berger-Sehgal model (see below). In the case of the NC reaction, MiniBooNE [193] and SciBooNE [194] searched for the COH component. SciBooNE [194] evaluated the ratio of the COH NC π^0 production to the total CC cross section as $(1.16 \pm 0.24)\%$.

MiniBooNE evaluated the NC COH component (plus a possible hydrogen diffractive contribution about which little is known) in the NC π^0 production as 19.5% (at $\langle E_\nu \rangle \sim 1$ GeV) and then the overall flux averaged overall NC π^0 cross section as $(4.76 \pm 0.05 \pm 0.76) \cdot 10^{-40} \text{cm}^2/\text{nucleon}$. Unfortunately, it is difficult to translate both measurements into the absolutely normalized value of the NC COH cross section because of strong dependence on the NUANCE MC generator used in the data analysis.

In the case of the CC reaction, K2K [195] and SciBooNE [196] reported no evidence for the COH component. For the K2K analysis, the 90% confidence limit upper bound for the COH cross sections on carbon was estimated to be 0.6% of the inclusive CC cross section. The SciBooNE upper limits (also for the carbon target) are: 0.67% at $\langle E_\nu \rangle \sim 1.1$ GeV, and 1.36% at $\langle E_\nu \rangle \sim 2.2$ GeV. SciBooNE also reported the measurement of the ratio of CC COH π^+ to NC COH π^0 production and estimated it as $0.14_{-0.28}^{+0.30}$. This is a surprisingly low value, which disagrees with results from the theoretical models which, at SciBooNE energies, typically predict values somewhat smaller than 2. For massless charged leptons, isospin symmetry implies the value of 2 for this ratio and the finite mass corrections make the predicted ratio smaller. Higher neutrino energy ($E_\nu > \sim 2$ GeV) COH production data (including recent NOMAD measurements) were successfully explained with a PCAC based model [197]. Adler's theorem relates $\sigma_{COH}(\nu + X \rightarrow \nu + X + \pi^0)$ at $Q^2 \rightarrow 0$ to $\sigma(\pi^0 + X \rightarrow \pi^0 + X)$. Subsequently, the model for the CC reaction, has been upgraded [198] to include lepton mass effects important for low E_ν studies. The new model predicts the $\sigma_{COH}(\pi^+)/\sigma_{COH}(\pi^0)$ ratio at $E_\nu = 1$ GeV to be 1.45 rather than 2. Another important improvement is to use a better model for $d\sigma(\pi + {}^{12}\text{C} \rightarrow \pi + {}^{12}\text{C})/dt$ in the region of pion kinematic energy $100 \text{ MeV} < T_\pi < 900 \text{ MeV}$. As a result, the predicted COH cross section from the model became reduced by a factor of 2-3 [199]. The PCAC based approach is also discussed in [200] and critically re-derived in Ref. [201]. At lower energies the microscopic Δ dominance models for the COH reaction [202–205] are believed to be more reliable.

Monte Carlo generators

Almost all Monte Carlo (MC) event generators rely on the Rein-Sehgal resonance model for pion resonance production [206]. The model is based on the quark resonance model and includes contributions from 18 resonances covering the region $W < 2$ GeV. The model is easily implementable in MC generators and it has only one set of vector and axial form factors. In the original model, the charged lepton is assumed to be massless and prescriptions to cope with this problem were proposed in Refs. [207]. It was also realized that the Rein-Sehgal model can be improved in the Δ region by modifying both vector and axial form factors using either old deuterium or new MiniBooNE pion production data [208, 209].

For coherent pion production, all the MCs use the Rein-Sehgal COH model [197] analysis of MC event generators and theoretical models described in [170] show that in the 1 – 2 GeV energy region, the Rein Sehgal COH model predictions disagree significantly with all the recent theoretical computations and experimental results. None of the microscopic models, which are believed to be more reliable in the 1 GeV region, have been implemented in Monte Carlo codes yet.

Duality

Bridging the region between RES and DIS (where interactions occur on quarks, to a good approximation) dynamics is a practical problem which must be resolved in all MC event generators. In MC event generators “DIS” is defined as “anything but QE and RES”. This is usually expressed as a condition on a lower limit for the invariant hadronic mass, such as $W > 1.6$ GeV for example. Notice, however, that such a definition of “DIS” contains a contribution from the kinematical region $Q^2 < 1$ GeV² which is beyond the applicability of the genuine DIS formalism. The RES/DIS transition region is not only a matter of an arbitrary choice, but is closely connected with the hypothesis of quark-hadron duality.

Investigation of structure functions introduced in the formalism of the inclusive electron-nucleon scattering led Bloom and Gilman to the observation that the average over resonances is approximately equal to the leading twist contribution measured in the completely different DIS region. One can distinguish two aspects of duality: (i) resonant structure functions oscillate around a DIS scaling curve; (ii) the resonant structure functions for varying values of Q^2 slide along the DIS curve evaluated at fixed Q_{DIS}^2 .

As a practical procedure for addressing this region, Bodek and Yang [210] have introduced and refined a model that is used by many contemporary neutrino event generators, such as NEUGEN and its successor GENIE, to bridge the kinematic region between the Delta and full DIS. The model has been developed for both neutrino- and electron-nucleon inelastic scattering cross sections using leading order parton distribution functions and introducing a new scaling variable they call ξ_w .

At the juncture with the DIS region, the Bodek-Yang model incorporates the GRV98 [211] LO parton distribution functions replacing the variable x with ξ_w . They introduce “K-factors”, different for sea and valence quarks, to multiply the PDFs so that they are correct at the low Q^2 photo-production limit. A possible criticism of the model is the requirement of using the rather dated GRV98 parton distribution functions in the DIS region to make the bridge to the lower W kinematic region seamless.

4.3.4.4 ν -A Deep-inelastic Scattering

Introduction

Although deep-inelastic scattering (DIS) is normally considered to be a topic for higher energy neutrinos, a 10 GeV neutrino factory has real contributions from DIS that are particularly important in feed-down to the background that must be carefully considered. In addition, there are x -dependent nuclear effects that should be taken into account when comparing results from detectors with different nuclei and even when comparing results from “identical” near and far detectors when the neutrino spectra entering the near and far detectors are different.

For this report, the definition of deep-inelastic scattering (DIS) is the kinematic based definition with $W \geq 2.0$ GeV and $Q^2 \geq 1.0$ GeV. This is mostly out of the resonance production region and allows a fit to parton distribution functions. This is unfortunately not the definition used by several modern Monte Carlo generators that do not differentiate between simply “inelastic” interactions and deep-inelastic interactions, calling everything beyond the Δ simply DIS. Unfortunately, this is a confusing use of nomenclature by the generators.

In general, deep-inelastic scattering offers an opportunity to probe the partonic structure of the nucleon both in its free state and when the nucleon is bound in a nucleus. Description of the partonic structure can include *parton distribution functions (PDFs)* giving the longitudinal, transverse and spin distributions of quarks within the nucleon as well as, for example, the hadron formation zone giving the time/length it takes for a struck quark to fully hadronize into a strong-interacting hadron.

Neutrino scattering can play an important role in the extraction of these fundamental parton distribution functions (PDFs) since only neutrinos via the weak-interaction can resolve the flavor of the nucleon's constituents: ν interacts with d , s , \bar{u} and \bar{c} while the $\bar{\nu}$ interacts with u , c , \bar{d} and \bar{s} . The weak current's unique ability to "taste" only particular quark flavors significantly enhances the study of parton distribution functions. A high-statistics measurement of the nucleon's partonic structure, using neutrinos, could complement studies with electromagnetic probes.

In the pursuit of precision measurements of neutrino oscillation parameters, large data samples and a dedicated effort to minimize systematic errors could allow neutrino experiments to independently isolate all six of the weak structure functions $F_1^{\nu N}(x, Q^2)$, $F_1^{\bar{\nu} N}(x, Q^2)$, $F_2^{\nu N}(x, Q^2)$, $F_2^{\bar{\nu} N}(x, Q^2)$, $x F_3^{\nu N}(x, Q^2)$ and $x F_3^{\bar{\nu} N}(x, Q^2)$ for the first time. A neutrino factory would be able to carry out these measurements with unprecedented precision. By taking differences and sums of these structure functions, specific parton distribution functions in a given (x, Q^2) bin can in turn be better isolated. Extracting this full set of structure functions will rely on the y -variation of the structure function coefficients in the expression for the cross-section. In the helicity representation, for example:

$$\begin{aligned} \frac{d^2\sigma^\nu}{dx dq^2} &= \frac{G_F^2}{2\pi x} \left[\frac{1}{2} (F_2^\nu(x, dq^2) + x F_3^\nu(x, dq^2)) + \right. \\ &\quad \left. \frac{(1-y)^2}{2} (F_2^\nu(x, dq^2) - x F_3^\nu(x, dq^2)) - 2y^2 F_L^\nu(x, dq^2) \right]. \end{aligned} \quad (27)$$

where F_L is the longitudinal structure function representing the absorption of longitudinally polarized Intermediate Vector Bosons. By analyzing the data as a function of $(1-y)^2$ in a given (x, dq^2) bin for both ν and $\bar{\nu}$, all six structure functions could be extracted.

Somewhat less demanding in statistics and control of systematics, the "average" structure functions $F_2(x, Q^2)$ and $x F_3(x, Q^2)$ can be determined from fits to combinations of the neutrino and antineutrino differential cross sections and several assumptions. The sum of the ν and $\bar{\nu}$ differential cross sections, yielding F_2 then can be expressed as:

$$\frac{d^2\sigma^\nu}{dx dy} + \frac{d^2\sigma^{\bar{\nu}}}{dx dy} = \frac{G_F^2 M E}{\pi} \left[2 \left(1 - y - \frac{Mxy}{2E} + \frac{y^2}{2} \frac{1 + 4M^2 x^2 / Q^2}{1 + R_L} \right) F_2 + y \left(1 - \frac{y}{2} \right) \Delta x F_3 \right] \quad (28)$$

where R_L is equal to σ_L / σ_T and now F_2 is the *average* of F_2^ν and $F_2^{\bar{\nu}}$ and the last term is proportional to the difference in $x F_3$ for neutrino and antineutrino probes, $\Delta x F_3 = x F_3^\nu - x F_3^{\bar{\nu}}$. In terms of the strange and charm parton distribution functions s and c , at leading order, assuming symmetric s and c seas, this is $4x(s - c)$.

The cross sections are also corrected for the excess of neutrons over protons in the target (for example the Fe correction is 5.67%) so that the presented structure functions are for an isoscalar target. A significant step in the determination of $F_2(x, Q^2)$ in this manner that affects the low- x values is the assumed $\Delta x F_3$ and $R_L(x, Q^2)$. Recent analyses use, for example, a NLO QCD model as input (TRVFS [212, 213]) and assume an input value of $R_L(x, Q^2)$ that comes from a fit to the world's charged-lepton measurements [214]. This could be an additional problem since, as will be suggested, $R_L(x, Q^2)$ can be different for neutrino as opposed to charged-lepton scattering.

The structure function $x F_3$ can be determined in a similar manner by taking the difference in ν and $\bar{\nu}$ differential cross sections.

The Physics of Deep-inelastic Scattering

There have been very few recent developments in the theory of deep-inelastic scattering. The theory has been well-established for years. The most recent developments in neutrino DIS scattering involve the experimental determination of parton distribution functions of nucleons within a nucleus, so-called *nuclear* parton distribution functions (nPDF). The more contemporary study of ν nucleus deep-inelastic scattering using high-statistics experimental results with careful attention to multiple systematic errors began with the CDHSW, CCFR/NuTeV ν Fe, the NOMAD ν C and the CHORUS ν Pb experiments. Whereas the NuTeV [215] and CHORUS [216] Collaborations have published their full data sets, NOMAD [161] has not yet done so. This short summary of DIS physics will concentrate on nuclear/nucleon parton distribution functions.

Low-and-High Q^2 Structure Functions: Longitudinal and Transverse

Since the current and future neutrino beams designed for neutrino oscillation experiments will be concentrating on lower energy neutrinos (1 - 5 GeV), many of the interactions will be at the lower-Q edge of DIS or even in the "soft" DIS region - namely, $W \geq 2.0$ GeV however, with $Q^2 \leq 1.0$ GeV². Understanding the physics of this kinematic region is therefore important.

Since both the vector and axial-vector part of the transverse structure function F_T go to 0 at $Q^2 = 0$ (similar to ℓ^\pm charged-lepton vector current scattering), the low- Q^2 region ν and $\bar{\nu}$ cross sections are dominated by the longitudinal structure function F_L . The longitudinal structure function is composed of a vector and axial-vector component F_L^{VC} and F_L^{AC} and the low- Q^2 behavior of these components is not the same as in the transverse case. The conservation of the vector current (CVC) suggests that F_L^{VC} behaves as the vector current in charged-lepton scattering and vanishes at low Q^2 . However, the axial-vector current is not conserved and is related to the pion field via PCAC, so there is a surviving low Q^2 contribution from this component [217] and F_L^{AC} dominates the low Q^2 behavior. Consequently, the ratio $R = F_L/F_T$ is divergent for neutrino interactions. This is substantially different from the scattering of charged leptons for which R is vanishing as Q^2 and using measurement of R from charged lepton scattering to determine F_2 for neutrino scattering is obviously wrong for lower Q. In addition, this non-vanishing and dominant longitudinal structure function could be important for the interpretation of low- Q^2 nuclear effects with neutrinos to be described shortly.

Low-and-High Q^2 Structure Functions: $1/Q^2$ Corrections

Using a notation similar to that of reference [218], the total structure function can be expressed in a phenomenological form:

$$F_i(x, Q^2) = F_i^{LT}(x, Q^2) \left(1 + \frac{C_4(x)}{Q^2} \right), \quad (29)$$

where $i = 1, 2, 3$ refers to the type of the structure function. Using $i = 2$ as an example, then F_2^{LT} is the leading twist component that has already included target mass corrections (TMC) and C_4 is the coefficient of the twist-4 term, the first higher-twist term proportional to $1/Q^2$. There are, of course, further higher-twist terms $\frac{H_i^{(T=6)}(x)}{Q^4} + \dots$ proportional to ever increasing powers of $1/Q^2$ however, for most phenomenological fits, the dominant leading twist plus twist-4 term are sufficient to describe the data. The target mass corrections are kinematic in origin and involve terms suppressed by powers of M^2/Q^2 while the higher twist terms are dynamical in origin and are suppressed as mentioned by powers of $1/Q^2$. These higher-twist terms are associated with multi-quark or quark and gluon fields and it is difficult to evaluate their magnitude and shape from first

principles. As with the kinematic target mass corrections, these must be taken into account in analyses of data at low Q^2 and especially at large x . At higher Q^2 the contribution of the HT terms is negligible and there are various global fits [219, 220] to the structure functions (among various scattering input) to determine the parton distribution functions (PDFs) that do not include any HT terms.

The analysis of nuclear PDFs to be described shortly uses data from a Tevatron neutrino experiment at very high neutrino energies and thus is one of the analyses that does not need to be concerned with higher-twist corrections. However, the current neutrino-oscillation oriented beam-lines and the 10 GeV neutrino factory are not high-energy so the analyses of these data may indeed need to consider both target mass corrections and higher-twist. If indeed inclusion of higher-twist in these analyses becomes necessary, the authors of [218] stress the importance of explicitly including *both* the target mass corrections *and* the higher twist corrections, even though they have very different physical origin and can have very different x dependence. It is important to note, as mentioned, that there are both *nucleon* and *nuclear* PDFs depending on the target. The relation between them, called nuclear correction factors, are currently being studied for both ν -A and $\ell^\pm A$. There are early indications that the nuclear correction factors for these two processes may not be the same.

Recent DIS measurements: Neutrino Iron Scattering Results

The difficulty, of course, is that modern neutrino oscillation experiments demand high statistics which means that the neutrinos need massive nuclear targets to acquire these statistics. This, in turn, complicates the extraction of free nucleon PDFs and demands nuclear correction factors that scale the results on a massive target to the corresponding result on a nucleon target. The results of the latest study of QCD using neutrino scattering comes from the NuTeV experiment [215]. The NuTeV experiment was a direct follow-up of the CCFR experiment using nearly the same detector as CCFR but with a different neutrino beam. The NuTeV experiment accumulated over 3 million ν and $\bar{\nu}$ events in the energy range of 20 to 400 GeV off a mainly Fe target.

A comparison of the NuTeV results with those of CCFR and the predictions of the major PDF-fitting collaborations (CTEQ and MRST [219, 220]) was carried out. The main points are that the NuTeV F_2 agrees with CCFR for values of $x_{Bj} \leq 0.4$ but is systematically higher for larger values of x_{Bj} culminating at $x_{Bj} = 0.65$ where the NuTeV result is 20% higher than the CCFR result. NuTeV agrees with charged lepton data for $x_{Bj} \leq 0.5$ but there is increasing disagreement for higher values. Although the NuTeV F_2 and xF_3 agree with theory for medium x , they find a different Q^2 behavior at small x and are systematically higher than theory at high x . These results can be summarized in four main questions to ask subsequent neutrino experiments:

- At high x , what is the behavior of the valence quarks as $x \rightarrow 1.0$?
- At all x and Q^2 , what is yet to be learned if we can measure all six ν and $\bar{\nu}$ structure functions to yield maximal information on the parton distribution functions?
- At all x , how do nuclear effects with incoming neutrinos differ from nuclear effects with incoming charged leptons?

This last item highlights an overriding question when trying to get a global view of structure functions from both neutrino and charged-lepton scattering data. How do we compare data off nuclear targets with data off nucleons and, the associated question, how do we scale nuclear target data to the comparable nucleon data? In most PDF analyses, the nuclear correction factors were taken from ℓ^\pm -nucleus scattering and used for both charged-lepton and neutrino scattering. Recent studies by a CTEQ-Grenoble-Karlsruhe collaboration (called nCTEQ) [221] have shown that there may indeed be a difference between the charged-lepton and neutrino correction factors.

The data from the high-statistics ν -DIS experiment, NuTeV summarized above, was used to perform a dedicated PDF fit to neutrino-iron data [222]. The methodology for this fit is parallel to that of the previous global analysis [223] *but* with the difference that only Fe data has been used and no nuclear corrections have been

applied to the analyzed data; hence, the resulting PDFs are for a proton in an iron nucleus - nuclear parton distribution functions¹²

By comparing these iron PDFs with the free-proton PDFs (appropriately scaled) a neutrino-specific heavy target nuclear correction factor R can be obtained which should be applied to relate these two quantities. It is also of course possible to combine these fitted nPDFs to form the individual values of the average of $F_2(\nu A)$ and $F_2(\bar{\nu} A)$ for a given x , Q^2 to compare directly with the NuTeV published values of this quantity. This was recently done and the nCTEQ preliminary results [225] for low- Q^2 are shown in Figure 75. Although the neutrino fit has general features in common with the charged-lepton parameterization, the magnitude of the effects and the x -region where they apply are quite different. The present results are noticeably flatter than the charged-lepton curves, especially at low- and moderate- x where the differences are significant. The comparison between the nCTEQ fit, that passes through the NuTeV measured points, and the charged-lepton fit is very different in the lowest- x , lowest- Q^2 region and gradually approaches the charged-lepton fit with increasing Q^2 . However, the slope of the fit approaching the shadowing region from higher x where the NuTeV measured points and the nCTEQ fit are consistently below the charged-lepton fit as a function of nuclear mass A , make it difficult to reach the degree of shadowing evidenced in charged-lepton nucleus scattering at even higher Q^2 .

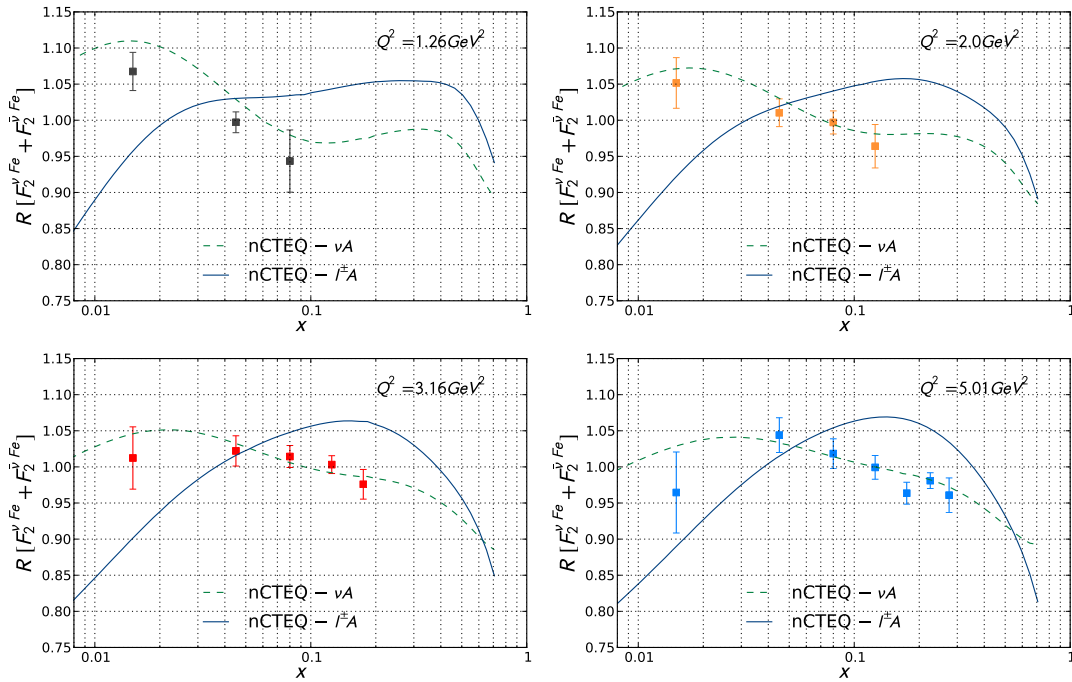


Figure 75: Nuclear correction factor R for the average F_2 structure function in charged current νFe scattering at $Q^2 = 1.2, 2.0, 3.2$ and 5.0 GeV^2 compared to the measured NuTeV points. The green dashed curve shows the result of the nCTEQ analysis of $\nu - A$ (CHORUS, CCFR and NuTeV) differential cross sections plotted in terms of the average F_2^{Fe} divided by the results obtained with the reference fit (free-proton) PDFs. For comparison, the nCTEQ fit to the charged-lepton data is shown by the solid blue curve.

The general trend is that the anti-shadowing region is shifted to smaller x values, and any turn-over at low x

¹²For more details of the fitting techniques and resulting comparisons with charged-lepton scattering see Part II of reference [224].

is minimal given the PDF uncertainties. More specifically, there is no indication of "shadowing" in the NuTeV neutrino results at low- Q^2 . In general, these plots suggest that the size of the nuclear corrections extracted from the NuTeV data are smaller than those obtained from charged lepton scattering.

Comparison of the $\ell^\pm A$ and νA Nuclear Correction Factors

For the nCTEQ analysis, the contrast between the charged-lepton ($\ell^\pm A$) case and the neutrino (νA) case is striking. While the nCTEQ fit to charged-lepton and Drell-Yan (DY) data generally align with the other charged-lepton determinations, the neutrino results clearly yield different behavior as a function of x , particularly in the shadowing/anti-shadowing region. In the $\bar{\nu}$ case, these differences are smaller but persist in the low- x shadowing region. The nCTEQ collaboration emphasize that both the charged-lepton and neutrino results come directly from global fits to the data, there is no model involved. They further suggest that this difference between the results in charged-lepton and neutrino DIS is reflective of the long-standing "tension" between the light-target charged-lepton data and the heavy-target neutrino data in the historical global PDF fits [226, 227]. Their latest results suggest that the tension is not only between charged-lepton *light-target* data and neutrino heavy-target data, but also between neutrino and charged-lepton *heavy-target* data. In other words a difference between charged-lepton ($\ell^\pm A$) and the neutrino (νA) when comparing the same A .

Concentrating on this interesting difference found by the nCTEQ group, if the nuclear corrections for the $\ell^\pm A$ and νA processes are indeed different there are several far-reaching consequences. Considering this, the nCTEQ group has performed a unified global analysis [221] of the $\ell^\pm A$, DY, and νA data (accounting for appropriate systematic and statistical errors) to determine if it is possible to obtain a "compromise" solution including both $\ell^\pm A$ and νA data. Using a hypothesis-testing criterion based on the χ^2 distribution that can be applied to both the total χ^2 as well as to the χ^2 of individual data sets, they found it was *not possible* to accommodate the data from νA and $\ell^\pm A$ DIS by an acceptable combined fit.

That is, when investigating the results in detail, the tension between the $\ell^\pm Fe$ and νFe data sets permits *no possible compromise fit* which adequately describes the neutrino DIS data along with the charged-lepton data and, consequently, $\ell^\pm Fe$ and νFe based on the NuTeV results, have different nuclear correction factors.

A compromise solution between νA and $\ell^\pm A$ data can be found *only* if the full correlated systematic errors of the νA data are not used and the statistical and all systematic errors are combined in quadrature thereby neglecting the information contained in the correlation matrix. In other words the larger errors resulting from combining statistical and all systematic errors in quadrature reduces the discriminatory power of the fit such that the difference between νA and $\ell^\pm A$ data are no longer evident. This conclusion underscores the fundamental difference [221] of the nCTEQ analysis with other contemporary analyses.

On the other hand, a difference between νA and $\ell^\pm A$ is not completely unexpected, particularly in the shadowing region, and has previously been discussed in the literature [228, 229]. The charged-lepton processes occur (dominantly) via γ -exchange, while the neutrino-nucleon processes occur via W^\pm -exchange. The different nuclear corrections could simply be a consequence of the differing propagation of the hadronic fluctuations of the intermediate bosons (photon, W) through dense nuclear matter. Furthermore, since the structure functions in neutrino DIS and charged lepton DIS are distinct observables with different parton model expressions, it is clear that the nuclear correction factors will not be exactly the same. What is, however, unexpected is the degree to which the R factors differ between the structure functions $F_2^{\nu Fe}$ and $F_2^{\ell Fe}$. In particular the lack of evidence for shadowing in neutrino scattering at low Q^2 down to $x \sim 0.02$ is quite surprising.

Should subsequent experimental results confirm the rather substantial difference between charged-lepton and neutrino scattering in the shadowing region at low- Q^2 it is interesting to speculate on the possible cause of the difference. A recent study of EMC, BCDMS and NMC data by a Hampton University - Jefferson Laboratory collaboration [230] suggests that anti-shadowing in charged-lepton nucleus scattering may be dominated by the

longitudinal structure function F_L . As a by-product of this study, their figures hint that shadowing in the data of EMC, BCDMS and NMC μA scattering was being led by the transverse cross section with the longitudinal component crossing over into the shadowing region at lower x compared to the transverse.

As summarized earlier, in the low- Q^2 region, the neutrino cross section is dominated by the longitudinal structure function F_L via axial-current interactions since F_T vanishes as $Q^2 \rightarrow 0$ similar to the behavior of charged lepton scattering. If the results of the NuTeV analysis are verified, one contribution to the different behavior of shadowing at low- Q^2 demonstrated by νA and ℓA , in addition to the different hadronic fluctuations in the two interactions, could be due to the different mix of longitudinal and transverse contributions to the cross section of the two processes in this kinematic region.

Another hypothesis of what is causing the difference between neutrino and charged-lepton shadowing results comes from V. Guzey [231] who speculates that at low- x , low- Q^2 the value of y is close to unity and the neutrino interactions primarily probe the down and strange quarks. This is very different to the situation with charged-lepton scattering where the contribution from down and strange quarks are suppressed by a factor of 1/4 compared to the up and charm. Therefore, the discrepancy between the observed nuclear shadowing in the lepton-nucleus total cross section at small x and shadowing in the total neutrino-nucleus cross section could be caused by the absence of nuclear shadowing in the nuclear strange quark distributions as extracted from the neutrino-nucleus data or even the poor knowledge of the strange-quark distribution in the free-nucleon that affects the neutrino-nucleus ratio more than the charged-lepton ratio.

4.3.5 Near detector baseline design

The current near detector design anticipates three sub-detectors (Fig. 76): a high granularity detector for charm/ τ measurement; a high resolution tracker for precise measurement of the event close to the vertex and a mini-MIND detector for muon measurement.

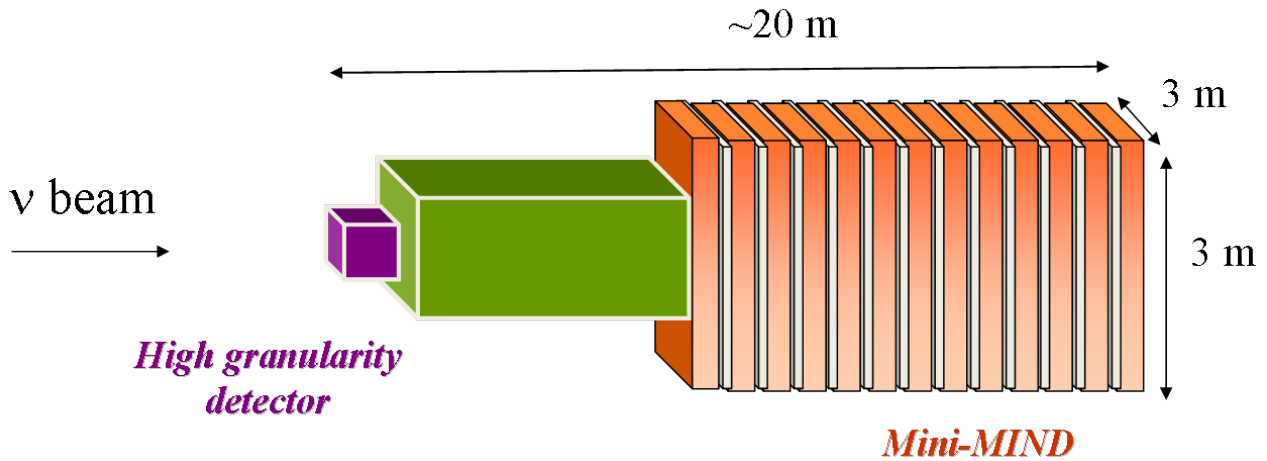


Figure 76: Block diagram design of the near detector

4.3.5.1 Option A - scintillating fibre tracker

A schematic drawing of a scintillating fiber tracker with an incorporated calorimeter is shown in Fig. 77. The detector consists of 20 square shaped modules placed perpendicular to the beam axis. Each module has

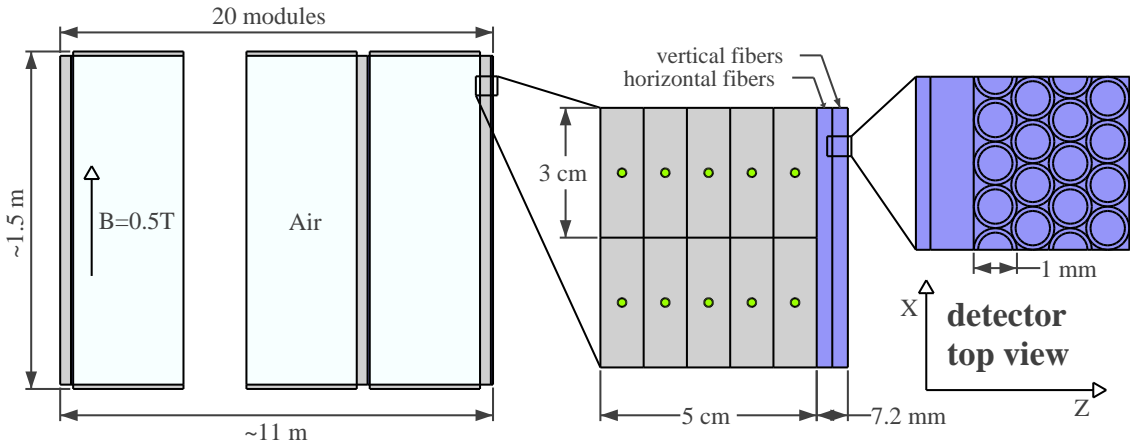


Figure 77: Schematic drawing of the scintillating fiber tracker.

a calorimeter section and a tracker section (also called tracker station). Modules are placed in equidistant positions, forming gaps filled with air. With a larger distance between tracker stations, the X and Y displacement of hits is increased and thus the angular resolution is improved. The sides of the air gaps are covered with layers of plastic scintillation bars. The detector is placed in a 0.5 T dipole magnetic field. Each station consists of one layer of fibers with horizontal orientation and another one with vertical orientation. Each layer has four planes made of 1 mm cylindrical fibers. They form a hexagonal pattern in the layer, thus minimizing the dead volume. There are 12,000 fibers per station, thus 240,000 fibers in total. The calorimeter sections consist of plastic scintillation bars perpendicular to the magnetic field and arranged in 5 planes in each section. Bars are co-extruded with a wavelength shifting (WLS) fiber inside and have $10 \text{ mm} \times 30 \text{ mm}$ cross section. Both the tracker fibers and WLS fibers in the bars are read from both ends by silicon photomultipliers (SiPMs). Overall dimensions of the detector are $\sim 1.5 \text{ m} \times 1.5 \text{ m} \times 11 \text{ m}$ and the detector mass is $\sim 2.7 \text{ t}$.

Simulation of the detector response

The neutrino flux at the near detector was generated by a Monte Carlo simulation of muon decays along the straight section of the Neutrino Factory decay ring [232, 233]. Neutrino interactions in the detector were simulated by the GENIE package [121]. For the simulation of the detector response, the Geant4 software platform [234] was used.

The presence of a muon catcher (e.g. mini version of MIND) as a sub-detector is essential for the muon identification. For various reasons we have not included it in the simulation. Instead, we assume that a muon having momentum of at least 500 MeV is identified in the near detector with 100% efficiency. Such an assumption is not unreasonable since a muon with momentum of 500 MeV has a range of $\approx 170 \text{ cm}$ in polystyrene, thus it will leave the tracker and enter the catcher, where it will be measured. In the following analysis we impose a veto on events with a muon identified in the muon catcher.

Precise and efficient momentum determination of electrons by measuring their track curvature is not possible in the rather dense polystyrene tracker due to bremsstrahlung and partial electromagnetic shower development. Therefore, electron energy should be measured by calorimetric means. The scintillating fiber tracker is an excellent totally active electromagnetic calorimeter, but not all the energy is captured in it due to its rather large radiation length. This implies the need for a dense electromagnetic calorimeter surrounding the scintillating fiber tracker. We assume that in such an enclosing detector almost all of the electromagnetic energy is captured

and measured with a resolution of $6\%/\sqrt{E/\text{GeV}}$ ¹³. In the current simulation, if the electromagnetic energy deposition (as estimated from the MC) of an event without a muon is less than 500 MeV, the event is discarded.

Digitization

A simple Monte Carlo algorithm was developed to simulate the processes of scintillation, photon propagation inside the fibers and SiPM response. For each charged particle hit in a fiber, a random number of scintillation photons is drawn according to the energy deposition and scintillation yield of the material. The fraction of photons remaining in the fiber (trapping efficiency) and light attenuation are taken into account. The photons from multiple hits are summed up and an optical coupling efficiency factor is applied to get the number of incident photons on the SiPM surface. Multiplying the latter by the photon detection efficiency, one obtains the number of primary avalanche triggers in the SiPMs. Dark counts are simulated by further adding a Poisson distributed number to the primary triggers. The final electronic signal response is parametrized by a function that takes into account cross-talk effect and the single pixel response distribution. Only signals with amplitude larger than a threshold equivalent to 2.5 fired pixels in each of the photo-detectors at the ends of the fibers are retained.

It seems that the dark counts are not a major problem for 1 mm fibers and for modern SiPMs, which have less than 1 MHz/mm² dark count rate at room temperature. With the imposed signal threshold and required coincidence of the signals from both ends of a fiber, the number of “false” fiber digits is below 1% of all the fibers in the detector. Therefore, the probability to have two or more adjacent “false” fiber digits which would mimic true particle hits is negligible.

The bar signals are digitized by smearing energy deposits with a 20% Gaussian. Signals below a threshold equivalent to a deposited energy of 0.5 MeV are discarded.

Reconstruction of the lepton candidate

First, the neighbouring fired fibers are grouped into clusters. Depending on the fiber orientation, the (x, z) or (y, z) position of the cluster is calculated by taking the weighted average of the fiber positions. All clusters consistent with a single particle traversing the layer at small angle (with respect to the z axis) are marked.

To measure the angle of the scattered lepton track, only events with one cluster per orientation in the first two stations are considered. This selection has low efficiency, because an event with a single charged particle in the final state might still have more than one cluster in either of the first stations. (For example, consider δ -electrons or interactions of bremsstrahlung photons.) Using measured points from subsequent stations do not improve the angle measurement precision.

Then, Monte Carlo information for the neutrino interaction is used to get the total electromagnetic energy deposition. We iterate over the final state particles of the neutrino reaction and sum the energies of all e^\pm, γ and π^0 . The summed up energy is then smeared with the assumed resolution ($6\%/\sqrt{E/\text{GeV}}$). Since in the following analysis we are interested in events with a single lepton in the final state, the value obtained this way is assumed to be the energy of the electron candidate track. The fraction of leptonic events remaining after the above reconstruction procedure is 43% .

As a result of the reconstruction procedure, for the scattered lepton track we obtain: the initial position, initial slopes ($x'_0 = dx/dz$ and $y'_0 = dy/dz$), initial momentum and charge. Distributions of the differences between reconstructed and true value of the lepton scattering angle and momentum are shown in Figure 78.

¹³A possible realisation of such a calorimeter could follow the design of the EM calorimeter of the HiResM ν detector [235] proposed to serve as the near detector in the LBNE experiment at Fermilab [236]. The energy resolution was obtained by MC simulation.

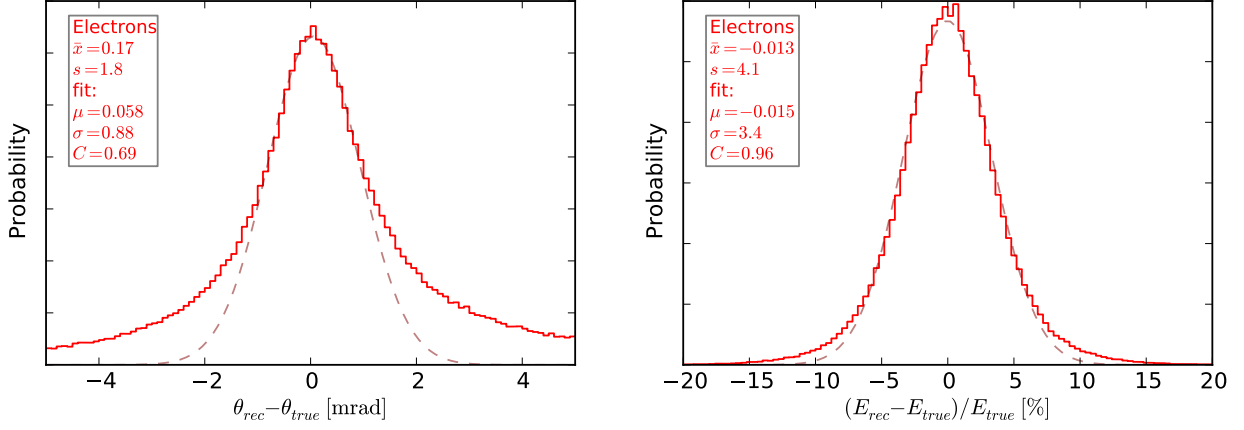


Figure 78: Detector angular (left) and energy (right) resolution for the scattered lepton track in leptonic events. The Gaussian fits are shown with dashed lines. The sample mean, standard deviation and fit parameters are shown in the upper left corners.

Selection of leptonic events

The ES events have low energy deposition near the vertex (consistent with a single particle). To exploit this property, a cut on energy deposition in the vertex bar of 4 MeV is imposed. If the vertex is in a cluster of fibers, a cut is made on the sum of the fiber amplitudes. In some background events, energetic charged hadrons (hundreds of MeV) escape through the air gaps leaving small or no depositions in the calorimetric sections. Therefore, it is required that there is no activity in the side bars covering the air gaps adjacent to the vertex. Another vertex related cut is the requirement that there are no energy depositions upstream of the vertex (backward depositions).

In the ES events the scattered electron/positron could induce a shower in the detector. In order to suppress such events a variable characterizing the transverse spread of the fired bars relative to the lepton track, x_{dev} , is constructed. A selection cut on x_{dev} exploits the spatial symmetry of energy depositions relative to the track in the non-bending plane for events with a single scattered particle. The distribution of the x_{dev} variable is shown in Figure 79. A cut at 15 cm is applied.

The next cut exploits the significant difference in shape of the total EM energy distributions for leptonic and background events, see Figure 80. This enables us to reject events with a total EM energy of more than 5 GeV. With such a cut, the background is reduced by a factor of ≈ 3 , while reducing the signal selection efficiency by $\approx 20\%$.

Background subtraction

It is evident, that an absolutely clean sample of signal events cannot be selected with a reasonable efficiency by employing selection cuts only. Therefore, the estimation of certain background distributions and their extrapolation to the signal region should be made, with the aim of statistically subtracting the background in the selected event samples.

We have chosen to do background subtraction in terms of the scattered lepton angle and energy, measured in the detector. They provide the most powerful signal-to-background separation due to the kinematic properties of the signal processes (19)-(20). For simplicity, we perform a one dimensional analysis.

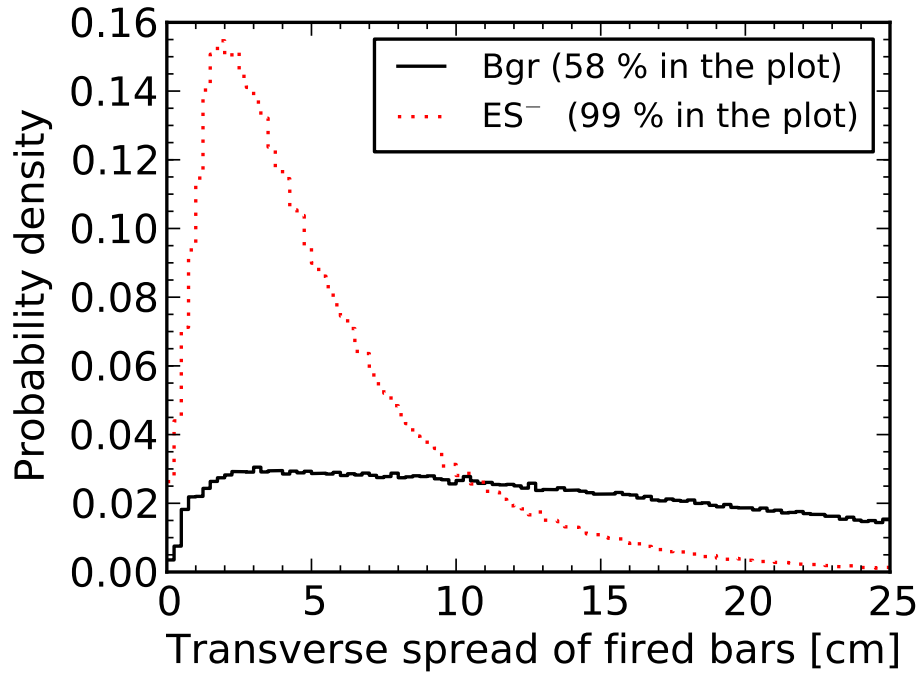


Figure 79: Distribution over the x_{dev} variable for the μ^- mode. The fraction of events contained in the plot is indicated in the legend. The distributions are normalized to a unit area. This plot shows only events for which the reconstructed vertex is in a scintillator bar.

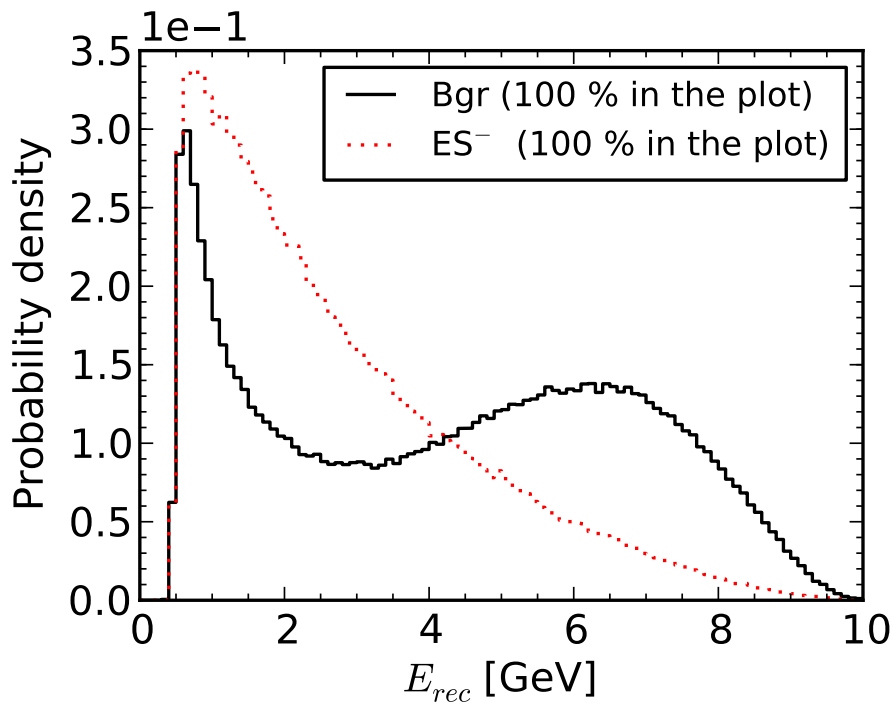


Figure 80: Distribution of measured total electromagnetic energy for ES^- (red) and background (black) events in the μ^- decay mode. The fraction of events contained in the plot is indicated in the legend. The distributions are normalized to a unit area.

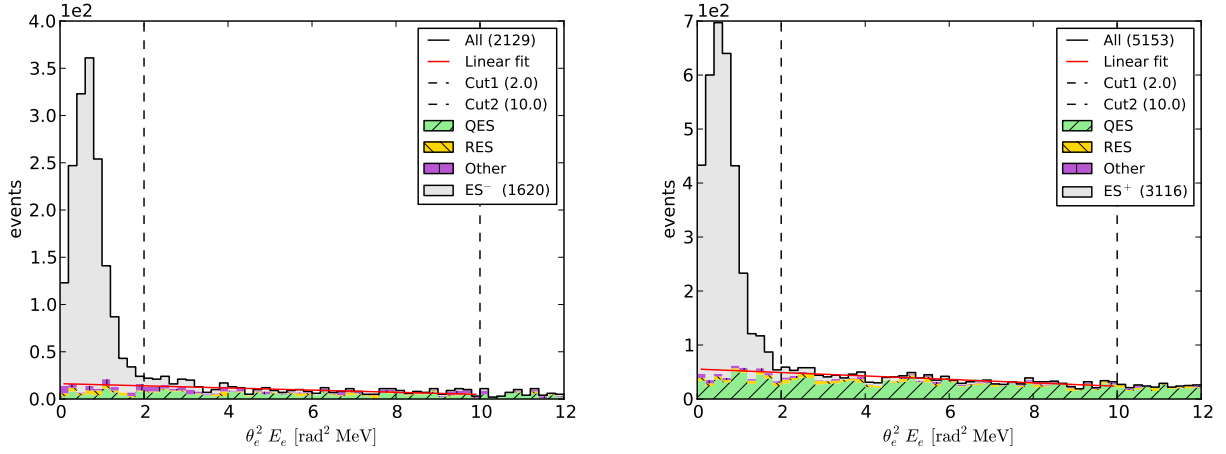


Figure 81: Distributions over $\theta_\ell^2 E_\ell$ for the ES^- sample (left) and ES^+ sample (right). In each histogram the distribution of the leptonic events is filled with solid grey, the distribution of the hadronic events is hatched and the total spectrum is in black. The two cuts bounding the fit interval are drawn with dashed lines. The red line indicates the background extrapolation.

Linear fit method

The linear fit method relies on the nearly flat shape of the corresponding background distribution. The idea is to estimate the background under the signal peak by linear extrapolation from the signal-free region. First, an interval over the $\theta_\ell^2 E_\ell$ distribution is defined so that its lower limit is close to the signal peak, there are almost no signal events in the interval (according to the MC simulation) and the background is approximately linear. Then, a straight line is fitted over the interval. Finally, the line is extrapolated towards zero to estimate the number of background events under the signal peak. The histograms over $\theta_\ell^2 E_\ell$ and the linear fits for the event samples under consideration are shown in Figure 81. Comparison between the estimated and the true number of signal events is given in Table 33. It is seen that the true values lie within the 95% confidence intervals of the predictions.

The main source of systematic errors related to the method is the assumption about the linearity of the background shape. From the fit of the ES^- and ES^+ samples it is estimated that a systematic error of less than 1% can be achieved. However, to give a conclusive estimation, one should investigate if and how various parameters of the simulation and selections influence the background shape.

Table 33: Estimated number of signal events for the two event samples. The statistics correspond to 5×10^{19} μ^- decays and as many μ^+ decays, which is equivalent to 10% of a nominal year running time.

Event sample	Selection eff.	Overall eff.	Purity	All events	Signal events	Signal events linear fit
ES^-	68 %	29 %	92 %	1637	1511	1486 ± 40
ES^+	64 %	28 %	86 %	3414	2951	2892 ± 58

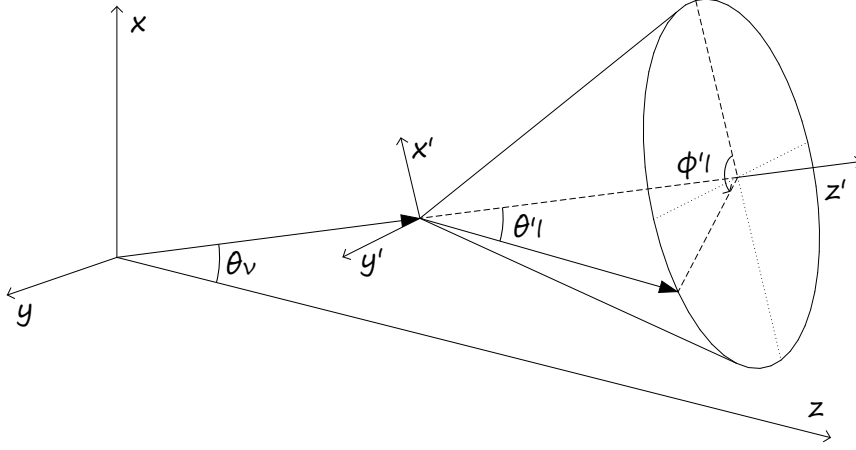


Figure 82: Reference frame of the near detector (and the neutrino beam) - xyz and frame of the neutrino electron scattering - $x'y'z'$ (z' is along with the neutrino momentum).

Reconstruction of the neutrino energy

Kinematics of the $\nu e^- \rightarrow l\nu$ scattering

The energy-momentum conservation leads to the following expression for the incoming neutrino energy in the laboratory frame for a neutrino electron scattering process:

$$E_\nu = \frac{2E_l m_e - m_l^2 - m_e^2}{2(m_e - E_l + p_l \cos \theta'_l)}, \quad (30)$$

where E_ν is the incoming neutrino energy, E_l and p_l are the outgoing lepton energy and momentum, θ'_l is the outgoing lepton angle with respect to the incoming neutrino direction and m_e and m_l are the electron and outgoing lepton (electron or positron in our case) masses. In the near detector the angle of the outgoing lepton with the z axis - θ_l is measured, rather than the angle θ'_l . Let the coordinate system be as shown in Figure 82. The azimuthal angle of the neutrino can be determined by the position of the vertex in the detector. For simplicity, let us assume that it is zero. Then, the relation between θ'_l and θ_l is given by

$$\cos \theta'_l = \cos \theta_\nu \cos \theta_l + \sin \theta_\nu \sin \theta_l \cos \varphi_l, \quad (31)$$

where θ_ν is the neutrino angle with respect to the z axis and φ_l is the azimuthal angle of the lepton (in the xyz frame).

Naive neutrino energy reconstruction

Let us use Equation (30) with a simple assumption that $\theta'_l = \theta_l$ to obtain the reconstructed neutrino energy E_ν^{rec} . Such an assumption is well justified when the neutrino source length is small compared to the distance to the detector. Unfortunately, this is not the case here. To demonstrate the problem we take the lepton energy and angle with respect to the z axis from the simulation (i.e. no detector resolution is involved). The migration matrix (E_ν^{rec} vs. E_ν^{true}) and the relative difference $(E_\nu^{rec} - E_\nu^{true})/E_\nu^{true}$ for the ES^- event sample are shown in Figure 83. It is seen that the difference has a broad distribution with a sample standard deviation of 33.6 %.

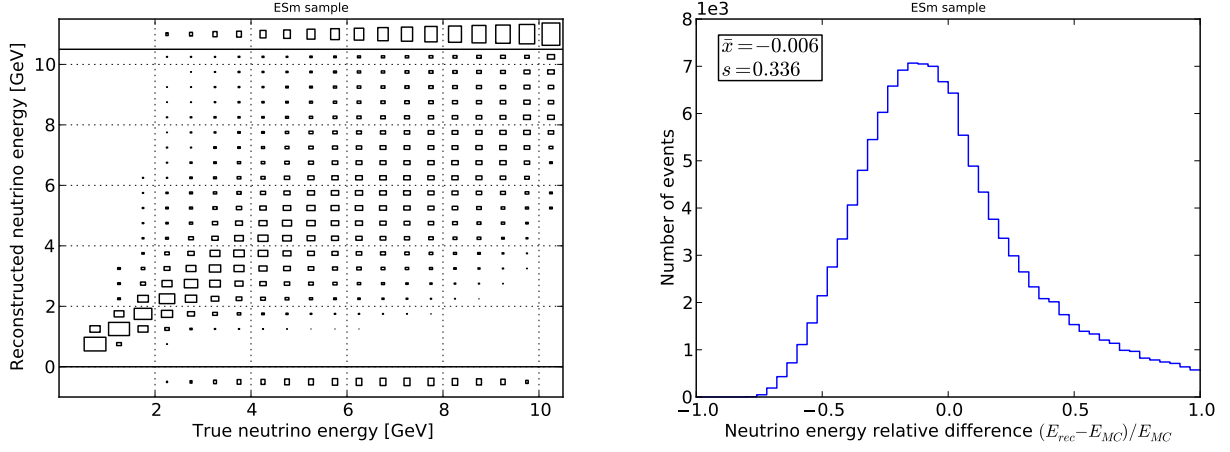


Figure 83: Naive reconstruction of the neutrino energy (background excluded). Left - migration matrix (the sum over each column is normalized to unity). The overflow and underflow bins are separated with horizontal lines. Right - relative difference $(E_{\nu}^{rec} - E_{\nu}^{true})/E_{\nu}^{true}$.

Improved neutrino energy reconstruction

The unknown angle θ_{ν} can be constrained from the radial position of the vertex r_{vtx} , the possible muon decay positions and the $E_{\nu} < E_{beam}$ limit. Then one can average on the possible θ_{ν} angles and estimate θ'_{ν} by using Equation (31). A generalisation of that method for measurement of neutrino energy on an event-by-event basis can be constructed by using a likelihood function $f(\eta|\mathbf{x})$, where η represents unmeasurable (e.g. E_{ν}) variables, \mathbf{x} stands for quantities measured with the detector (e.g. E_l) and the value of the function is the event probability. The likelihood function should include as much information as possible: detector resolutions, kinematics, differential cross sections and beam properties. In our case, we have constructed a likelihood function using the kinematic relations, the differential cross sections and the true neutrino flux shapes (assuming a fair knowledge will be available from the beam instrumentation and Monte Carlo). The estimate for the neutrino energy is then obtained from

$$E_{\nu}^{meas} = \int E_{\nu}(\eta) f(\eta|\mathbf{x}) d\eta, \quad (32)$$

where $\mathbf{x} = (E_l, \theta_l, \varphi_l, r_{vtx})$. Significant improvement is achieved with this method. As is seen in Figure 84, the resolution for the reconstructed energy can be as good as 13%, see Figure 84. Nevertheless, the ambiguity coming from the unknown neutrino angle (or muon decay position) cannot be fully eliminated on an event-by-event basis.

Migration matrices and resolutions for the reconstructed neutrino energy E_{ν}^{meas} obtained by using quantities measured in the detector are shown in Figure 85. The neutrino energy resolution is now typically around 30%.

Estimation of the neutrino flux energy distribution

We have demonstrated that with the near detector we can measure neutrino-electron interaction rates and, in addition, we can estimate the neutrino energy on an event-by-event basis. However, there are two components with different flavour (ν_{μ} and $\bar{\nu}_e$ for the μ^{-} beam or $\bar{\nu}_{\mu}$ and ν_e for the μ^{+} beam) that contribute to each event sample (ES^{-} , ES^{+}). Thus, one needs to disentangle the two components using a fitting procedure and/or Monte

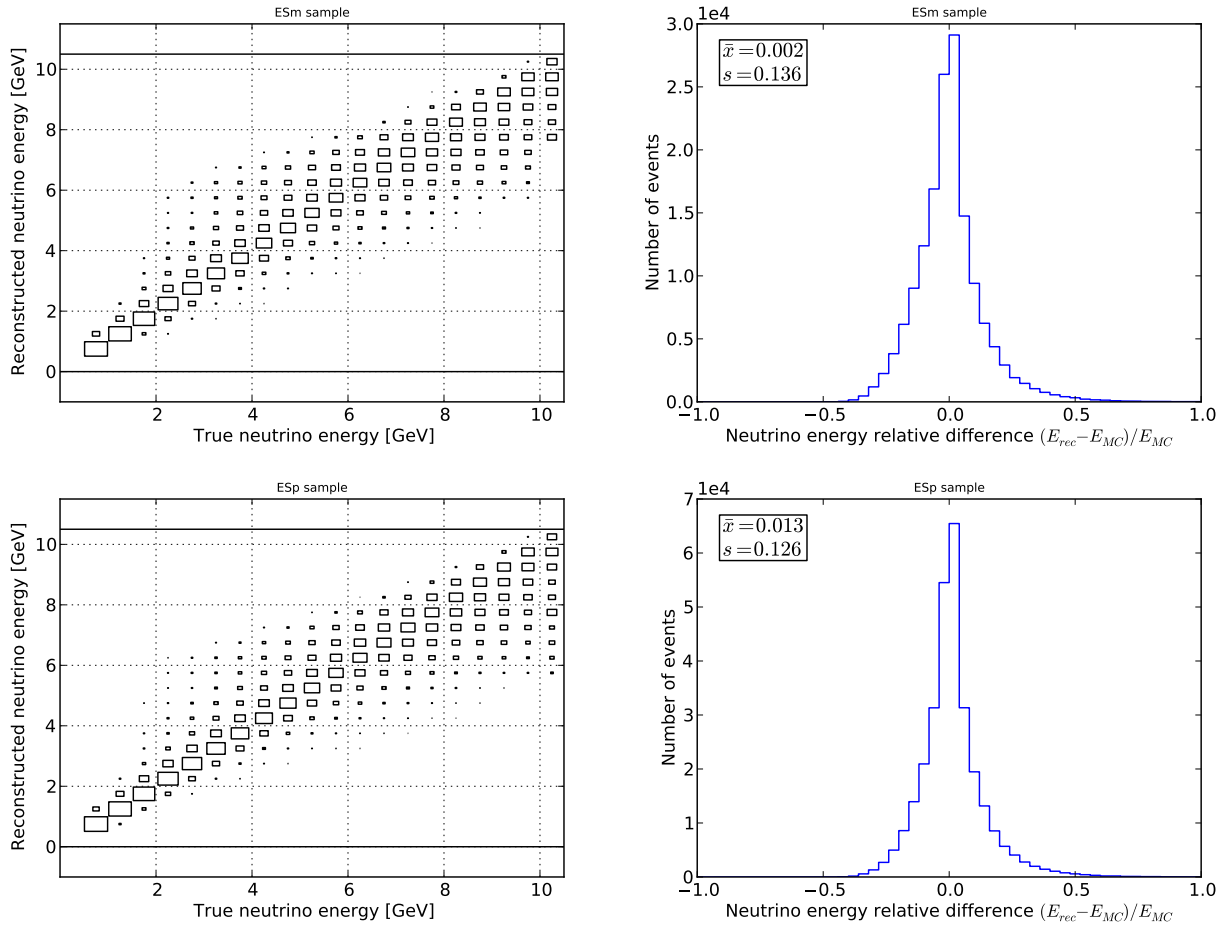


Figure 84: Improved reconstruction of the neutrino energy. Left - migration matrix (the sum over each column is normalized to unity). The overflow and underflow bins are separated with horizontal lines. Right - relative difference $(E_{\nu}^{rec} - E_{\nu}^{true})/E_{\nu}^{true}$ for the respective leptonic event sample (background excluded). Top - ES^{-} sample, bottom - ES^{+} sample.

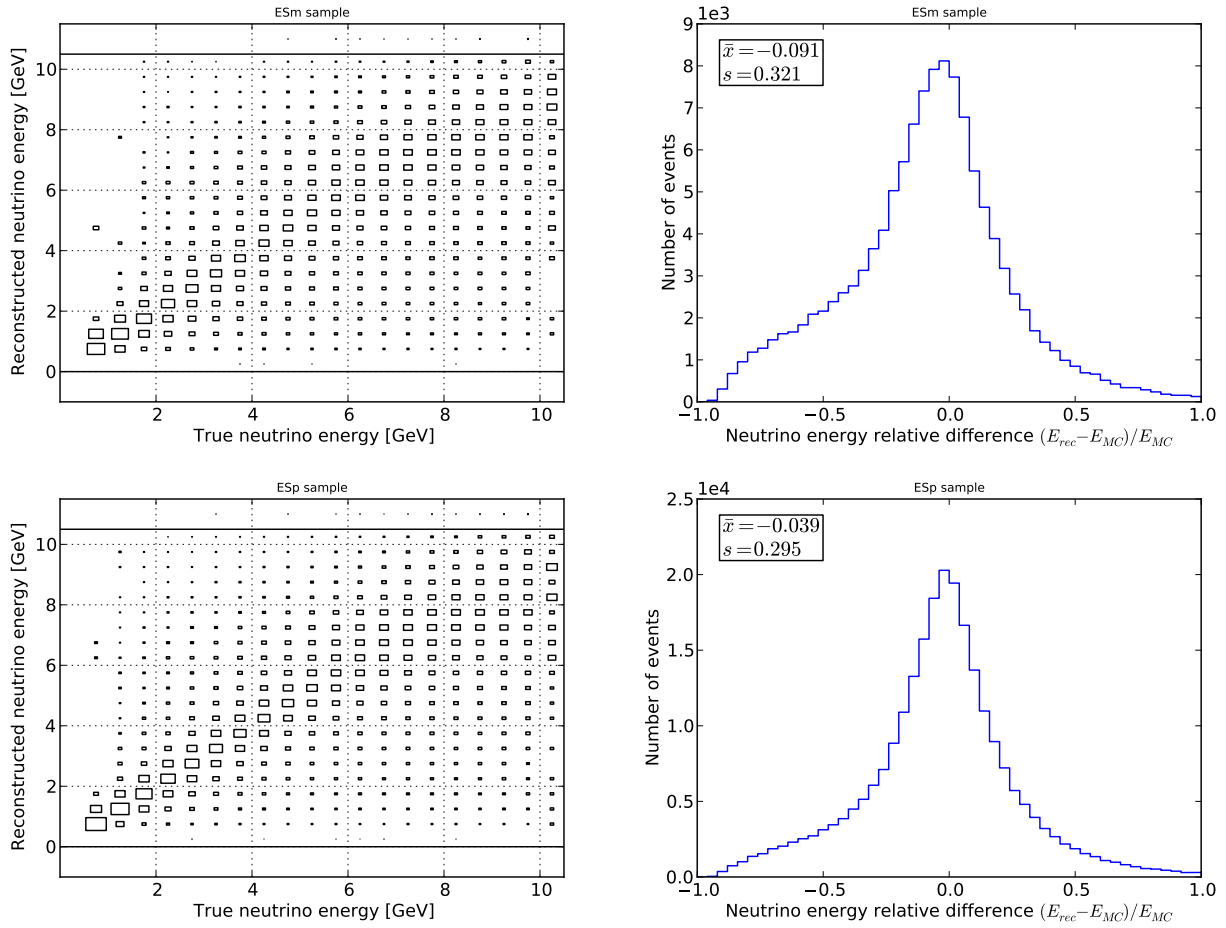


Figure 85: Reconstruction of the neutrino energy using measured quantities. Left: Migration matrix (the sum over each column is normalized to unity). The overflow and underflow bins are separated with horizontal lines. Right: Relative difference $(E_{\nu}^{meas} - E_{\nu}^{true})/E_{\nu}^{true}$ for the respective leptonic event sample (background excluded). Top - ES^{-} sample, bottom - ES^{+} sample.

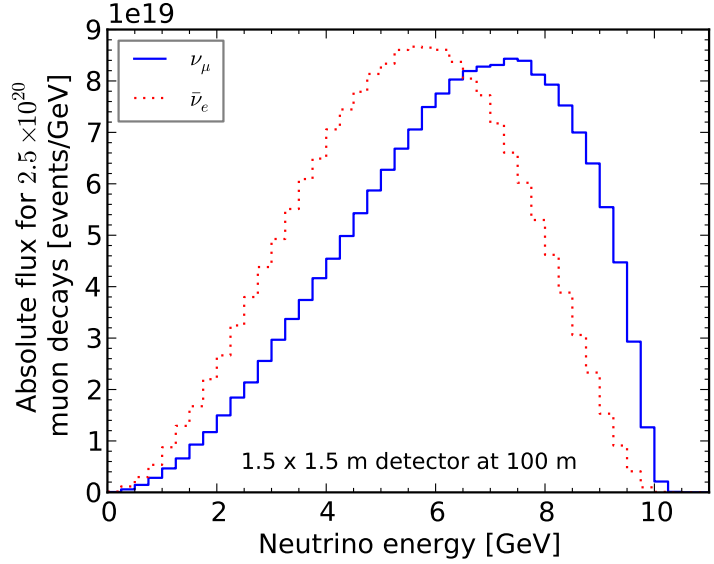


Figure 86: Energy distributions of the ν_μ and $\bar{\nu}_e$ coming from the decay ring in μ^- mode.

Carlo shape assumptions. For example, in μ^- running mode one measures:

$$N_{\text{ES}^-}(E) = N_{\nu_\mu e^-}(E) + N_{\bar{\nu}_e e^-}(E) = \phi_{\nu_\mu}(E)\sigma_{\nu_\mu e^-}^{\text{NC}}(E) + \phi_{\bar{\nu}_e}(E)\sigma_{\bar{\nu}_e e^-}^{\text{NC}}(E), \quad (33)$$

where $N(E)$ denotes event rates, $\phi(E)$ - beam fluxes and $\sigma(E)$ - cross sections.

To resolve the fluxes in this case one can make use of the different shapes of the electron and muon neutrino spectra, see Figure 86. However, neutrinos from both flavors are produced by the decays of muons from the same beam. Therefore, a strong correlation exists between the two spectral shapes as seen by the near detector and it can be exploited to disentangle the spectra. Of course, the extent of validity of a fitting procedure exploiting such correlation needs to be verified by respective Monte Carlo simulations.

4.3.5.2 Option B - High resolution straw tube tracker

A second option is possible high resolution straw tube tracker inspired by the HiResM ν near detector [237] being considered for the LBNE project at Fermilab [238, 239]. In this section we describe the detector being considered for LBNE, which would have identical features to the one at a Neutrino Factory.

Building upon the NOMAD-experience [161], this option includes a low-density tracking detector with a fiducial mass of 7.4 Ton as a neutrino target. The active target tracker will have a factor of two more sampling points along the z -axis (ν -direction) and a factor of six more sampling points in the plane transverse to the neutrino compared to the NOMAD experiment. The proposed detector will further enhance the resolving power by having an order of magnitude more tracking points and coverage for side-exiting neutrals and muons.

We are proposing straw-tube trackers (STT) for the active neutrino target, similar to the ATLAS Transition Radiation Tracker [240–242] and the COMPASS detector [243]. The tracker will be composed of straw tubes with 1 cm diameter, in the vertical (y) and horizontal (x) direction. In front of each module a plastic radiator made of many thin foils allows the identification of electrons through their Transition Radiation. The nominal fiducial volume for CC analysis is: $350 \times 350 \times 600 \text{ cm}^3$, corresponding to 7.4 tons of mass with an overall density $\rho < 0.1 \text{ g/cm}^3$.

The STT will be surrounded by an electromagnetic calorimeter (sampling Pb/scintillator) covering the forward and side regions. Both sub-detectors will be installed inside a dipole magnet providing a magnetic field of $\sim 0.4 \text{ T}$. An external muon detector based upon Resistive Plate Chambers (RPC) will be placed outside of the magnet (see figure 87).

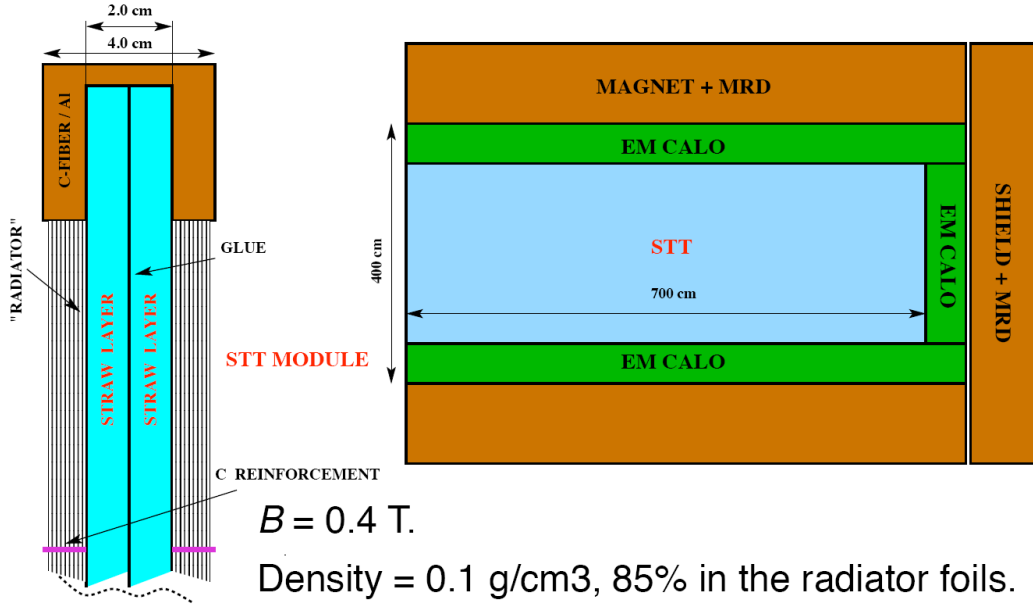


Figure 87: Sketch of the proposed HiRes detector showing the inner straw tube tracker (STT), the electromagnetic calorimeter (EM CALO) and the magnet with the muon range detector (MRD). Also shown is one module of the proposed straw tube tracker (STT). Two planes of straw tubes are glued together and held by an aluminium frame.

The neutrino target will be mainly composed of carbon, with a radiation length of about 5 m and spacepoint resolution around 200 μm . The momentum resolution is dominated by multiple scattering for tracks 1 m long ($\Delta p/p = 0.05$), while the measurement error for $p = 1 \text{ GeV}$ tracks would be $\Delta p/p = 0.006$. The proposed detector will measure track position, dE/dx , and transition radiation (with Xe filling) over the entire instrumented volume. The unconverted photon energy will be measured in the calorimeters with a target energy resolution of $\sim 10\%/\sqrt{E}$. The detector will provide:

- Full reconstruction of charged particles and gammas;
- Identification of electrons, pions, kaons, and protons from dE/dx ;
- Electron (positron) identification from Transition Radiation ($\gamma > 1000$);
- Full reconstruction and identification of protons down to momenta of 250 MeV;
- Reconstruction of electrons down to momenta of 80 MeV from curvature in the B-field.

The proposed near detector will measure the relative abundance, the energy spectrum, and the detailed topologies for $\nu_\mu, \bar{\nu}_\mu, \nu_e$ and $\bar{\nu}_e$ induced interactions, including the momentum vectors of negative, positive and neutral (π^0, K_s^0, Λ and $\bar{\Lambda}$) particles composing the hadronic system. A NC event candidate in NOMAD, shown in figure 88, gives an idea of the precision with which the charged-particles and the forward gammas were measured. Detailed simulations of this detector have been carried out in the context of the LBNE proposals [236]. These simulations were adapted to the neutrino spectra at a Neutrino Factory to derive the performance parameters of this detector in this context.

4.3.5.3 Charm and τ Detector

The near detector at the Neutrino Factory needs to measure the charm cross section to validate the size of the charm background in the far detector, since this is one of the backgrounds that contribute to the wrong-sign

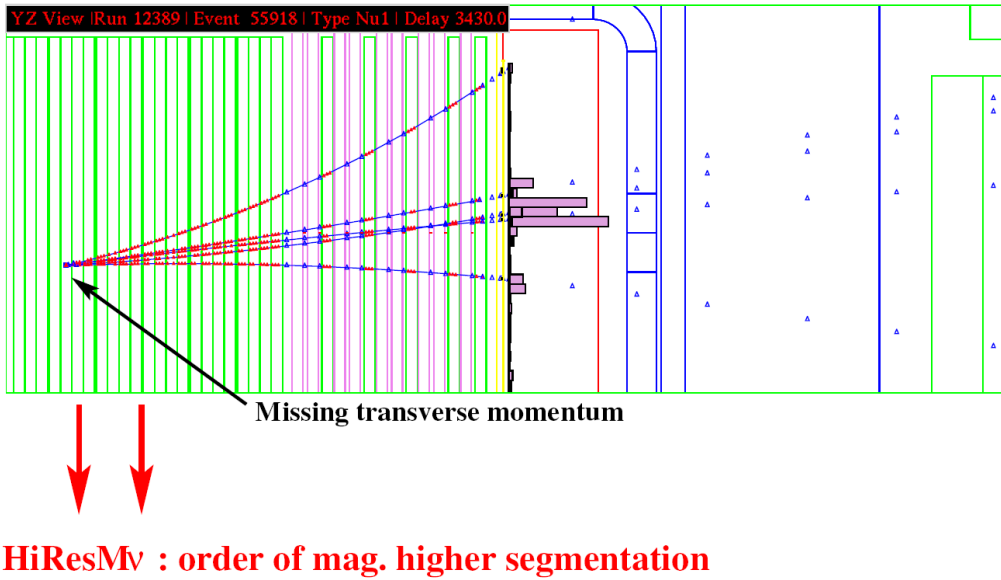


Figure 88: Candidate NC Event in NOMAD. Tracking charged particles in the HiRes detector will provide a factor of two higher segmentation along z-axis and a factor of six higher segmentation in the transverse-plane compared to NOMAD.

muon signature. The best measurements of the charm cross section and branching fractions are from NOMAD [244], but the accuracy close to the charm threshold and below 10 GeV remains at $\sim 10\%$. The theoretical uncertainty in the charm cross-section arises from the errors in the strange sea content of the nucleon, the semi-leptonic charm to muon branching fraction, the longitudinal structure function (F_L) and higher-twist effects. For this reason, it is paramount to make an independent near detector measurement of the charm cross section below 10 GeV and make the error in the charm cross section negligible in the estimation of the neutrino oscillation background.

Furthermore, a near detector should be able to also measure τ -leptons in the final state in order to explore couplings of Non Standard Interactions (NSI) at source $\epsilon_{\tau\mu}^s, \epsilon_{\tau e}^s$ or detection $\epsilon_{\tau\mu}^d, \epsilon_{\tau e}^d$ (see [132] for a comprehensive treatment). A semiconductor vertex detector is capable of detecting both charm and τ -leptons, be able to operate at a high event rate and still have very good spatial resolution. The primary neutrino interaction vertex is distinguished from the secondary vertex due to the short lived charm hadron or the τ -lepton in the silicon vertex detector. The vertex detector is similar in design to the NOMAD–STAR detector [245] that was installed in NOMAD [161] and was used to measure the impact parameter and double vertex resolution of short-lived events [246]. A τ -lepton event can be identified by an impact parameter signature with a dedicated silicon vertex detector with a B_4C target (see NAUSICAA proposal [247]). Standard ν_μ CC interactions have an impact parameter *r.m.s* of $28 \mu\text{m}$, while tau decays have an impact parameter *r.m.s* of $62 \mu\text{m}$. By performing a cut on the impact parameter significance (σ_{IP}/IP) one can separate one prong decays of the tau from the background. For three prong decays of the tau, a double vertex signature is used to separate signal from background. The total net efficiency of the tau signal in NAUSICAA was found to be 12%.

A silicon strip vertex detector would be in the upstream section of the near detector and would consist of a target of 10 modules of B_4C , which has the largest density 2.49 g/cm^3 for the longest radiation length 21.7 cm. The dimensions are $100 \times 100 \times 2 \text{ cm}^3$ per module for a total mass of 498 kg (see figure 89). There are 40 ladders of silicon detectors of 50 cm length in each plane and there are 12 silicon planes in each detector. This implies 480 ladders, with 9 silicon detectors per ladder, for a total of 4320 silicon detectors, covering a total area of 12 m^2 . Assuming 640 channels per ladder, this constitutes a total of 307,200 readout channels.

At a 10 GeV Neutrino Factory the charm branching fraction is of about 2% and the ν_μ CC interaction rate per year is approximately 1.3×10^7 in a 500 kg detector. Therefore, with a similar detection efficiency to the NOMAD-STAR detector [245], one expects 2×10^4 charm events per year. A search for tau events from non-standard interactions can also be carried out in this detector. With the tau detection efficiency found in NAUSICAA and a ratio of cross-sections of $\sigma_\tau/\sigma_\mu \sim 0.2$, we obtain $P_{\mu\tau} < 7 \times 10^{-7}$ at 90% C.L for a 10 year run, assuming no background. This improves the current limits from NOMAD and CHORUS by two orders of magnitude [248, 249].

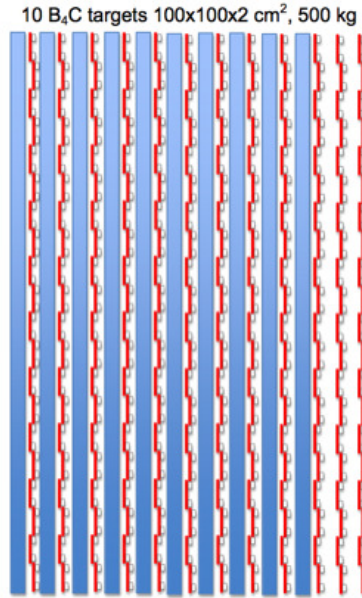


Figure 89: Conceptual design for a vertex detector at a near detector of a Neutrino Factory.

5 Conclusions

Lead author: KL

Acknowledgements

Lead author: KL

References

- [1] B. Pontecorvo, “Mesonium and antimesonium,” *Sov. Phys. JETP* **6** (1957) 429.
- [2] B. Pontecorvo, “Inverse beta processes and nonconservation of lepton charge,” *Sov. Phys. JETP* **7** (1958) 172–173.
- [3] Z. Maki, M. Nakagawa, and S. Sakata, “Remarks on the unified model of elementary particles,” *Prog. Theor. Phys.* **28** (1962) 870–880.
- [4] S. M. Bilenky, S. Pascoli, and S. T. Petcov, “Majorana neutrinos, neutrino mass spectrum, CP-violation and neutrinoless double beta-decay. I: The three-neutrino mixing case,” *Phys. Rev. D* **64** (2001) 053010, arXiv:0102265 [hep-ph].
- [5] **Particle Data Group** Collaboration, J. Beringer *et al.*, “Review of Particle Physics (RPP),” *Phys.Rev.* **D86** (2012) 010001.
- [6] M. Gonzalez-Garcia, M. Maltoni, J. Salvado, and T. Schwetz, “Global fit to three neutrino mixing: critical look at present precision,” *JHEP* **1212** (2012) 123, arXiv:1209.3023 [hep-ph].
- [7] H. Georgi, “Particles and fields,” in *Proceedings of the APS Div. of Particles and Fields*, C. Carlson, ed., p. 575 et seq. 1975.
- [8] H. Fritzsch and P. Minkowski, “Unified Interactions of Leptons and Hadrons,” *Annals Phys.* **93** (1975) 193–266.
- [9] J. C. Pati and A. Salam, “Unified Lepton-Hadron Symmetry and a Gauge Theory of the Basic Interactions,” *Phys.Rev.* **D8** (1973) 1240–1251.
- [10] H. Georgi and S. Glashow, “Unity of All Elementary Particle Forces,” *Phys.Rev.Lett.* **32** (1974) 438–441.
- [11] G. Altarelli and F. Feruglio, “Discrete Flavor Symmetries and Models of Neutrino Mixing,” *Rev.Mod.Phys.* **82** (2010) 2701–2729, arXiv:1002.0211 [hep-ph].
- [12] H. Ishimori, T. Kobayashi, H. Ohki, Y. Shimizu, H. Okada, *et al.*, “Non-Abelian Discrete Symmetries in Particle Physics,” *Prog.Theor.Phys.Suppl.* **183** (2010) 1–163, arXiv:1003.3552 [hep-th].
- [13] S. F. King and C. Luhn, “Neutrino Mass and Mixing with Discrete Symmetry,” *Rept.Prog.Phys.* **76** (2013) 056201, arXiv:1301.1340 [hep-ph].
- [14] P. Minkowski, “ $\mu \rightarrow e\gamma$ at a Rate of One Out of 1-Billion Muon Decays?,” *Phys. Lett.* **B67** (1977) 421.
- [15] T. Yanagida, “Horizontal symmetry and masses of neutrinos,” *Conf. Proc.* **C7902131** (1979) 95.
- [16] P. Ramond, “The Family Group in Grand Unified Theories,” arXiv:hep-ph/9809459 [hep-ph].
- [17] M. Gell-Mann, P. Ramond, and R. Slansky, “Complex Spinors and Unified Theories,” *Conf.Proc.* **C790927** (1979) 315–321, arXiv:1306.4669 [hep-th].
- [18] **ISS Physics Working Group** Collaboration, A. Bandyopadhyay *et al.*, “Physics at a future Neutrino Factory and super-beam facility,” *Rept. Prog. Phys.* **72** (2009) 106201, arXiv:0710.4947 [hep-ph].

- [19] T. Edgecock, O. Caretta, T. Davenne, C. Densham, M. Fitton, *et al.*, “The EUROnu Project,” *Phys.Rev.ST Accel.Beams* **16** (2013) 021002, arXiv:1305.4067 [physics.acc-ph].
- [20] A. Cervera, A. Laing, J. Martin-Albo, and F. J. P. Soler, “Performance of the MIND detector at a Neutrino Factory using realistic muon reconstruction,” *Nucl. Instrum. Meth. A* **624** (2010) 601–614, arXiv:1004.0358 [hep-ex].
- [21] R. Bayes, A. Laing, F. Soler, A. Cervera Villanueva, J. Gomez Cadenas, *et al.*, “The Golden Channel at a Neutrino Factory revisited: improved sensitivities from a Magnetised Iron Neutrino Detector,” *Phys.Rev.* **D86** (2012) 093015, arXiv:1208.2735 [hep-ex].
- [22] A. Bross, R. Wands, R. Bayes, A. Laing, F. Soler, *et al.*, “A Toroidal Magnetised Iron Neutrino Detector (MIND) for a Neutrino Factory,” *Phys.Rev. ST Accel. Beams* **16** (2013) 081002, arXiv:1306.5327 [physics.ins-det].
- [23] M. C. Gonzalez-Garcia and M. Maltoni, “Phenomenology with Massive Neutrinos,” *Phys. Rept.* **460** (2008) 1–129, arXiv:0704.1800 [hep-ph].
- [24] R. Mohapatra, S. Antusch, K. Babu, G. Barenboim, M. Chen, *et al.*, “Theory of neutrinos: A White paper,” *Rept. Prog. Phys.* **70** (2007) 1757–1867, arXiv:hep-ph/0510213 [hep-ph].
- [25] **Particle Data Group** Collaboration, K. Nakamura *et al.*, “Review of particle physics,” *J.Phys.* **G37** (2010) 075021.
- [26] G. Fogli, E. Lisi, A. Marrone, D. Montanino, A. Palazzo, *et al.*, “Global analysis of neutrino masses, mixings and phases: entering the era of leptonic CP violation searches,” *Phys.Rev.* **D86** (2012) 013012, arXiv:1205.5254 [hep-ph].
- [27] K. Abazajian, M. Acero, S. Agarwalla, A. Aguilar-Arevalo, C. Albright, *et al.*, “Light Sterile Neutrinos: A White Paper,” arXiv:1204.5379 [hep-ph].
- [28] T. Ohlsson, “Status of non-standard neutrino interactions,” *Rep. Prog. Phys.* **76**, **044201** (2013) 044201, arXiv:1209.2710 [hep-ph].
- [29] **Double Chooz Collaboration** Collaboration, Y. Abe *et al.*, “Reactor electron antineutrino disappearance in the Double Chooz experiment,” *Phys.Rev.* **D86** (2012) 052008, arXiv:1207.6632 [hep-ex].
- [30] **RENO collaboration** Collaboration, J. Ahn *et al.*, “Observation of Reactor Electron Antineutrino Disappearance in the RENO Experiment,” *Phys.Rev.Lett.* **108** (2012) 191802, arXiv:1204.0626 [hep-ex].
- [31] **DAYA-BAY Collaboration** Collaboration, F. An *et al.*, “Observation of electron-antineutrino disappearance at Daya Bay,” *Phys.Rev.Lett.* **108** (2012) 171803, arXiv:1203.1669 [hep-ex].
- [32] Y. Itow *et al.*, “The JHF-Kamioka neutrino project,” *Nucl. Phys. Proc. Suppl.* **111** (2001) 146–151, arXiv:0106019 [hep-ex].
- [33] **NOvA Collaboration** Collaboration, D. Ayres *et al.*, “NOvA: Proposal to build a 30 kiloton off-axis detector to study $\nu(\mu) \rightarrow \nu(e)$ oscillations in the NuMI beamline,” arXiv:hep-ex/0503053 [hep-ex].

- [34] **PINGU collaboration** Collaboration, T. IceCube, “PINGU Sensitivity to the Neutrino Mass Hierarchy,” arXiv:1306.5846 [astro-ph.IM].
- [35] Y. Wang, “Daya bay ii: current status and future plan.” talk at Daya Bay II meeting, IHEP, Jan, 2013.
- [36] **LBNE Collaboration** Collaboration, T. Akiri *et al.*, “The 2010 Interim Report of the Long-Baseline Neutrino Experiment Collaboration Physics Working Groups,” arXiv:1110.6249 [hep-ex].
- [37] A. Lenz, U. Nierste, J. Charles, S. Descotes-Genon, H. Lacker, *et al.*, “Constraints on new physics in $B - \bar{B}$ mixing in the light of recent LHCb data,” *Phys.Rev.* **D86** (2012) 033008, arXiv:1203.0238 [hep-ph].
- [38] S. King, “Predicting neutrino parameters from SO(3) family symmetry and quark-lepton unification,” *JHEP* **0508** (2005) 105, arXiv:hep-ph/0506297 [hep-ph].
- [39] A. de Gouvea and H. Murayama, “Neutrino Mixing Anarchy: Alive and Kicking,” arXiv:1204.1249 [hep-ph].
- [40] M. Fukugita and T. Yanagida, “Baryogenesis Without Grand Unification,” *Phys. Lett.* **B174** (1986) 45.
- [41] S. Davidson, E. Nardi, and Y. Nir, “Leptogenesis,” *Phys. Rept.* **466** (2008) 105–177, arXiv:0802.2962 [hep-ph].
- [42] M. Buckley and H. Murayama, “How can we test seesaw experimentally?,” *Phys. Rev. Lett.* **97** (2006) 231801, arXiv:hep-ph/0606088 [hep-ph].
- [43] M. L. Mangano *et al.*, “Physics at the front end of a neutrino factory: A Quantitative appraisal,” arXiv:0105155 [hep-ph]. Report of the nuDIS Working Group for the ECFA-CERN Neutrino-Factory study.
- [44] A. de Gouvêa and J. Jenkins, “What can we learn from neutrino electron scattering?,” *Phys. Rev. D* **74** (2006) 033004, arXiv:0603036 [hep-ph].
- [45] J. Aysto *et al.*, “Physics with low-energy muons at a neutrino factory complex,” arXiv:0109217 [hep-ph]. Report of the Stopped Muons Working Group for the ECFA - CERN study on Neutrino Factory and Muon Storage Rings at CERN.
- [46] B. Pontecorvo, “Neutrino experiments and the question of leptonic-charge conservation,” *Sov. Phys. JETP* **26** (1968) 984–988.
- [47] V. N. Gribov and B. Pontecorvo, “Neutrino astronomy and lepton charge,” *Phys. Lett.* **B28** (1969) 493.
- [48] **Super-Kamiokande Collaboration** Collaboration, Y. Fukuda *et al.*, “Evidence for oscillation of atmospheric neutrinos,” *Phys. Rev. Lett.* **81** (1998) 1562–1567, arXiv:hep-ex/9807003 [hep-ex].
- [49] **SNO Collaboration** Collaboration, Q. Ahmad *et al.*, “Direct evidence for neutrino flavor transformation from neutral current interactions in the Sudbury Neutrino Observatory,” *Phys. Rev. Lett.* **89** (2002) 011301, arXiv:nucl-ex/0204008 [nucl-ex].
- [50] **KamLAND Collaboration** Collaboration, T. Araki *et al.*, “Measurement of neutrino oscillation with KamLAND: Evidence of spectral distortion,” *Phys. Rev. Lett.* **94** (2005) 081801, arXiv:hep-ex/0406035 [hep-ex].

- [51] **MINOS Collaboration**, P. Adamson *et al.*, “Measurement of neutrino oscillations with the MINOS detectors in the NuMI beam,” *Phys. Rev. Lett.* **101** (2008) 131802, arXiv:0806.2237 [hep-ex].
- [52] M. Kobayashi and T. Maskawa, “CP Violation in the Renormalizable Theory of Weak Interaction,” *Prog. Theor. Phys.* **49** (1973) 652–657.
- [53] **DOUBLE-CHOOZ Collaboration** Collaboration, Y. Abe *et al.*, “Indication for the reactor anti-neutrino disappearance in the Double Chooz experiment,” *Phys.Rev.Lett.* **108** (2012) 131801, arXiv:1112.6353 [hep-ex].
- [54] **T2K Collaboration** Collaboration, K. Abe *et al.*, “Indication of Electron Neutrino Appearance from an Accelerator-produced Off-axis Muon Neutrino Beam,” *Phys.Rev.Lett.* **107** (2011) 041801, arXiv:1106.2822 [hep-ex].
- [55] **MINOS Collaboration** Collaboration, P. Adamson *et al.*, “Improved search for muon-neutrino to electron-neutrino oscillations in MINOS,” *Phys.Rev.Lett.* **107** (2011) 181802, arXiv:1108.0015 [hep-ex].
- [56] NuFit webpage, www.nu-fit.org.
- [57] P. Huber, “On the determination of anti-neutrino spectra from nuclear reactors,” *Phys.Rev.* **C84** (2011) 024617, arXiv:1106.0687 [hep-ph].
- [58] D. Forero, M. Tortola, and J. Valle, “Global status of neutrino oscillation parameters after Neutrino-2012,” *Phys.Rev.* **D86** (2012) 073012, arXiv:1205.4018 [hep-ph].
- [59] **MINOS Collaboration** Collaboration, P. Adamson *et al.*, “Measurement of Neutrino and Antineutrino Oscillations Using Beam and Atmospheric Data in MINOS,” *Phys.Rev.Lett.* **110** (2013) 251801, arXiv:1304.6335 [hep-ex].
- [60] **LSND Collaboration** Collaboration, A. Aguilar-Arevalo *et al.*, “Evidence for neutrino oscillations from the observation of anti-neutrino(electron) appearance in a anti-neutrino(muon) beam,” *Phys. Rev.* **D64** (2001) 112007, arXiv:hep-ex/0104049 [hep-ex].
- [61] **MiniBooNE Collaboration** Collaboration, A. Aguilar-Arevalo *et al.*, “Improved Search for $\bar{\nu}_\mu \rightarrow \bar{\nu}_e$ Oscillations in the MiniBooNE Experiment,” arXiv:1303.2588 [hep-ex].
- [62] M. A. Acero, C. Giunti, and M. Laveder, “Limits on nu(e) and anti-nu(e) disappearance from Gallium and reactor experiments,” *Phys.Rev.* **D78** (2008) 073009, arXiv:0711.4222 [hep-ph].
- [63] C. Giunti and M. Laveder, “Statistical Significance of the Gallium Anomaly,” *Phys. Rev.* **C83** (2011) 065504, arXiv:1006.3244 [hep-ph].
- [64] T. Mueller, D. Lhuillier, M. Fallot, A. Letourneau, S. Cormon, *et al.*, “Improved Predictions of Reactor Antineutrino Spectra,” *Phys.Rev.* **C83** (2011) 054615, arXiv:1101.2663 [hep-ex].
- [65] K. Schreckenbach, G. Colvin, W. Gelletly, and F. Von Feilitzsch, “DETERMINATION OF THE ANTI-NEUTRINO SPECTRUM FROM U-235 THERMAL NEUTRON FISSION PRODUCTS UP TO 9.5-MEV,” *Phys.Lett.* **B160** (1985) 325–330.
- [66] A. Hahn, K. Schreckenbach, G. Colvin, B. Krusche, W. Gelletly, *et al.*, “ANTI-NEUTRINO SPECTRA FROM PU-241 AND PU-239 THERMAL NEUTRON FISSION PRODUCTS,” *Phys.Lett.* **B218** (1989) 365–368.

- [67] F. Von Feilitzsch, A. Hahn, and K. Schreckenbach, “Experimental beta spectra from Pu239 and U235 thermal neutron fission products and their correlated anti-neutrino spectra,” *Phys.Lett.* **B118** (1982) 162–166.
- [68] P. Vogel, G. Schenter, F. Mann, and R. Schenter, “Reactor anti-neutrino spectra and their application to anti-neutrino induced reactions. 2.,” *Phys.Rev.* **C24** (1981) 1543–1553.
- [69] G. Mention, M. Fechner, T. Lasserre, T. Mueller, D. Lhuillier, *et al.*, “The Reactor Antineutrino Anomaly,” *Phys. Rev.* **D83** (2011) 073006, arXiv:1101.2755 [hep-ex].
- [70] J. Kopp, P. A. N. Machado, M. Maltoni, and T. Schwetz, “Sterile Neutrino Oscillations: The Global Picture,” arXiv:1303.3011 [hep-ph].
- [71] J. Conrad, C. Ignarra, G. Karagiorgi, M. Shaevitz, and J. Spitz, “Sterile Neutrino Fits to Short Baseline Neutrino Oscillation Measurements,” *Adv.High Energy Phys.* **2013** (2013) 163897, arXiv:1207.4765 [hep-ex].
- [72] C. Giunti, M. Laveder, Y. Li, and H. Long, “A Pragmatic View of Short-Baseline Neutrino Oscillations,” arXiv:1308.5288 [hep-ph].
- [73] S. M. Bilenky, C. Giunti, and W. Grimus, “Neutrino mass spectrum from the results of neutrino oscillation experiments,” *Eur. Phys. J.* **C1** (1998) 247–253, hep-ph/9607372.
- [74] N. Okada and O. Yasuda, “A sterile neutrino scenario constrained by experiments and cosmology,” *Int. J. Mod. Phys.* **A12** (1997) 3669–3694, hep-ph/9606411.
- [75] M. Maltoni and T. Schwetz, “Testing the statistical compatibility of independent data sets,” *Phys. Rev. D* **68** (2003) 033020, arXiv:0304176 [hep-ph].
- [76] G. Karagiorgi *et al.*, “Leptonic CP violation studies at MiniBooNE in the (3+2) sterile neutrino oscillation hypothesis,” *Phys. Rev. D* **75** (2007) 013011, arXiv:0609177 [hep-ph].
- [77] M. Maltoni and T. Schwetz, “Sterile neutrino oscillations after first MiniBooNE results,” *Phys. Rev. D* **76** (2007) 093005, arXiv:0705.0107 [hep-ph].
- [78] **The International Design Study for the Neutrino Factory** Collaboration, T. I.-N. S. Group, “Neutrino factory: specification of baseline.”. <https://www.ids-nf.org/wiki/FrontPage/Documentation?action=AttachFile&do=get&target=IDS-NF-002-v1.1.pdf>.
- [79] S. K. Agarwalla, P. Huber, J. Tang, and W. Winter, “Optimization of the Neutrino Factory, revisited,” *JHEP* **01** (2011) 120, arXiv:1012.1872 [hep-ph].
- [80] P. Huber and W. Winter, “Neutrino factories and the ‘magic’ baseline,” *Phys. Rev.* **D68** (2003) 037301, arXiv:hep-ph/0301257.
- [81] V. Barger, D. Marfatia, and K. Whisnant, “Breaking eight fold degeneracies in neutrino CP violation, mixing, and mass hierarchy,” *Phys. Rev.* **D65** (2002) 073023, arXiv:hep-ph/0112119 [hep-ph].
- [82] A. M. Dziewonski and D. L. Anderson, “Preliminary reference earth model,” *Phys. Earth Planet. Interiors* **25** (1981) 297–356.

- [83] P. Huber, M. Lindner, and W. Winter, “Simulation of long-baseline neutrino oscillation experiments with GLOBES (General Long Baseline Experiment Simulator),” *Comput. Phys. Commun.* **167** (2005) 195, arXiv:hep-ph/0407333 [hep-ph].
- [84] P. Huber, J. Kopp, M. Lindner, M. Rolinec, and W. Winter, “New features in the simulation of neutrino oscillation experiments with GLOBES 3.0: General Long Baseline Experiment Simulator,” *Comput. Phys. Commun.* **177** (2007) 432–438, arXiv:hep-ph/0701187 [hep-ph].
- [85] J. Conrad, A. de Gouvea, S. Shalgar, and J. Spitz, “Atmospheric Tau Neutrinos in a Multi-kiloton Liquid Argon Detector,” *Phys.Rev.* **D82** (2010) 093012, arXiv:1008.2984 [hep-ph].
- [86] **Super-Kamiokande Collaboration** Collaboration, K. Abe *et al.*, “A Measurement of the Appearance of Atmospheric Tau Neutrinos by Super-Kamiokande,” *Phys.Rev.Lett.* **110** (2013) 181802, arXiv:1206.0328 [hep-ex].
- [87] **Intensity Frontier Neutrino Working Group** Collaboration, A. de Gouvea *et al.*, “Neutrinos,” arXiv:1310.4340 [hep-ex].
- [88] M. Blennow, P. Coloma, P. Huber, and T. Schwetz, “Quantifying the sensitivity of oscillation experiments to the neutrino mass ordering,” arXiv:1311.1822 [hep-ph].
- [89] P. Coloma and P. Huber, “Impact of nuclear effects on the extraction of neutrino oscillation parameters,” arXiv:1307.1243 [hep-ph].
- [90] P. Coloma, P. Huber, J. Kopp, and W. Winter, “Systematic uncertainties in long-baseline neutrino oscillations for large θ_{13} ,” arXiv:1209.5973 [hep-ph].
- [91] **LBNE Collaboration** Collaboration, C. Adams *et al.*, “Scientific Opportunities with the Long-Baseline Neutrino Experiment,” arXiv:1307.7335 [hep-ex].
- [92] A. Stahl, C. Wiebusch, A. Guler, M. Kamiscioglu, R. Sever, *et al.*, “Expression of Interest for a very long baseline neutrino oscillation experiment (LBNO),”.
- [93] E. Baussan, M. Dracos, T. Ekelof, E. F. Martinez, H. Ohman, *et al.*, “The use the a high intensity neutrino beam from the ESS proton linac for measurement of neutrino CP violation and mass hierarchy,” arXiv:1212.5048 [hep-ex].
- [94] **MEMPHYS Collaboration** Collaboration, L. Agostino *et al.*, “Study of the performance of a large scale water-Cherenkov detector (MEMPHYS),” *JCAP* **1301** (2013) 024, arXiv:1206.6665 [hep-ex].
- [95] L. Agostino, M. Buizza-Avanzini, M. Marafini, T. Patzak, A. Tonazzo, *et al.*, “Future large-scale water-Cherenkov detector,” *Phys.Rev. ST Accel. Beams* **16**, **061001** (2013), arXiv:1306.6865 [physics.ins-det].
- [96] J. Conrad and M. Shaevitz, “Multiple Cyclotron Method to Search for CP Violation in the Neutrino Sector,” *Phys. Rev. Lett.* **104** (2010) 141802, arXiv:0912.4079 [hep-ex].
- [97] J. Alonso, F. Avignone, W. Barletta, R. Barlow, H. Baumgartner, *et al.*, “Expression of Interest for a Novel Search for CP Violation in the Neutrino Sector: DAEdALUS,” arXiv:1006.0260 [physics.ins-det].

- [98] S. Agarwalla, P. Huber, J. Link, and D. Mohapatra, “A new approach to anti-neutrino running in long baseline neutrino oscillation experiments,” *JHEP* **1104** (2011) 099, arXiv:1005.4055 [hep-ph].
- [99] C. Aberle, A. Adelman, J. Alonso, W. Barletta, R. Barlow, *et al.*, “Whitepaper on the DAEdALUS Program,” arXiv:1307.2949 [physics.acc-ph].
- [100] P. Huber, M. Mezzetto, and T. Schwetz, “On the impact of systematical uncertainties for the CP violation measurement in superbeam experiments,” *JHEP* **0803** (2008) 021, arXiv:0711.2950 [hep-ph].
- [101] D. Adey, S. Agarwalla, C. Ankenbrandt, R. Asfandiyarov, J. Back, *et al.*, “Neutrinos from Stored Muons nuSTORM: Expression of Interest,” arXiv:1305.1419 [physics.acc-ph].
- [102] F. Gerigk *et al.*, “Conceptual design of the SPL II: A high-power superconducting h^- linac at CERN,” Tech. Rep. CERN-2006-006, CERN, Geneva, Switzerland, July, 2006.
- [103] R. Garoby, “SPL at CERN,” in *Proceedings SRF 2009, 14th International Conference on RF Superconductivity, DBB Forum, Berlin September 20–25, 2009*, pp. 930–933. Helmholtz-Zentrum Berlin, Berlin, 2009.
- [104] F. Gerigk *et al.*, “Layout and machine optimisation for the SPL at CERN,” Tech. Rep. CERN-ATS-2010-208, CERN, Geneva, Switzerland, 2010.
- [105] D. Neuffer, “Design of muon storage rings for neutrino oscillation experiments,” *IEEE Trans. Nucl. Sci.* **28** (1981) 2034.
- [106] R. C. Fernow *et al.*, “Targets and magnetic elements for pion collection in muon collider drivers,” *AIP Conf. Proc.* **352** (1995) 134.
- [107] R. Chehab, “A second order calculation of the adiabatic invariant of a charged particle spiraling in a longitudinal magnetic field,” *J. Math. Phys.* **19** (1978) 937.
- [108] R. B. Palmer *et al.*, “Muon colliders,” *AIP Conf. Proc.* **372** (1996) 3.
- [109] K. T. McDonald *et al.*, “The MERIT high-power target experiment at the CERN PS,” in *Proceedings of IPAC’10, Kyoto, Japan* [266], p. 3527.
- [110] T. McManamy *et al.*, “Overview of the SNS target system testing and initial beam operation experience,” *J. Nucl. Mat.* **377** (2008) 1.
- [111] X. Ding *et al.*, “Optimized parameters with a mercury jet target,” in *Proceedings of PAC09, Vancouver, BC, Canada*, p. 2748. 2009.
- [112] M. D. Bird *et al.*, “The NHMFL hybrid magnet projects,” *IEEE Trans. Appl. Supercon.* **19** (2009) 1612.
- [113] J. H. Schultz, “Radiation resistance of fusion magnet materials,” in *20th IEEE/NPSS Symposium on Fusion Engineering, 2003*, p. 423. IEEE, 2003.
- [114] J. H. Schultz *et al.*, “The ITER central solenoid,” in *Twenty-First IEEE/NPSS Symposium on Fusion Engineering, 2005*. IEEE, 2005.
- [115] A. Hervé *et al.*, “Experience gained from the construction, test and operation of the large 4-T CMS coil,” *IEEE Trans. Appl. Supercon.* **18** (2004) 346.

- [116] K. H. Tanaka *et al.*, “Development of radiation resistant magnets for JHF/J-PARC,” *IEEE Trans. Appl. Supercon.* **14** (2004) 402.
- [117] **Neutrino Factory/Muon Collider Collaboration** Collaboration, C. H. Albright *et al.*, “The neutrino factory and beta beam experiments and development,” arXiv:physics/0411123 [physics].
- [118] A. Cervera, A. Donini, M. Gavela, J. Gomez Cadenas, P. Hernandez, *et al.*, “Golden measurements at a neutrino factory,” *Nucl. Phys.* **B579** (2000) 17–55, arXiv:hep-ph/0002108 [hep-ph].
- [119] A. Cervera-Villanueva, “MIND performance and prototyping,” *AIP Conf. Proc.* **981** (2008) 178–180.
- [120] **ISS Detector Working Group** Collaboration, T. Abe *et al.*, “Detectors and flux instrumentation for future neutrino facilities,” *JINST* **4** (2009) T05001, arXiv:0712.4129 [physics.ins-det].
- [121] C. Andreopoulos *et al.*, “The GENIE Neutrino Monte Carlo Generator,” *Nucl. Instrum. Meth. A* **614** (2010) 87–104, arXiv:0905.2517 [hep-ph].
- [122] J. Allison *et al.* *Nuclear Science, IEEE Transactions on* feb.
- [123] A. Cervera-Villanueva, J. J. Gomez-Cadenas, and J. A. Hernando, “RecPack a reconstruction toolkit,” *Nucl. Instrum. Meth.* **A534** (2004) 180–183.
- [124] D. Groom, N. Mikhov, and S. Striganov, “Muon stopping power and range tables 10 mev-100 tev,” *Atomic Data and Nuclear Data Tables* **78** (2001) 183–356.
- [125] P. Adamson *et al.*, “The MINOS calibration detector,” *Nucl. Instrum. Meth.* **A556** (2006) 119–133.
- [126] “AIDA: Advanced european infrastructures for detectors at accelerators,” 2010. <http://cern.ch/aida>.
- [127] A. Hocker, J. Stelzer, F. Tegenfeldt, H. Voss, K. Voss, *et al.*, “TMVA - Toolkit for Multivariate Data Analysis,” *PoS ACAT* (2007) 040, arXiv:physics/0703039 [PHYSICS].
- [128] **MINOS collaboration** Collaboration, P. Adamson *et al.*, “First direct observation of muon antineutrino disappearance,” *Phys.Rev.Lett.* **107** (2011) 021801, arXiv:1104.0344 [hep-ex].
- [129] J. Burguet-Castell, M. Gavela, J. Gomez-Cadenas, P. Hernandez, and O. Mena, “On the Measurement of leptonic CP violation,” *Nucl. Phys.* **B608** (2001) 301–318, arXiv:hep-ph/0103258 [hep-ph].
- [130] J. Burguet-Castell, M. B. Gavela, J. J. Gomez-Cadenas, P. Hernandez, and O. Mena, “Superbeams plus neutrino factory: The golden path to leptonic CP violation,” *Nucl. Phys.* **B646** (2002) 301–320, arXiv:hep-ph/0207080.
- [131] J. Burguet-Castell, D. Casper, E. Couce, J. J. Gómez-Cadenas, and P. Hernández, “Optimal beta-beam at the CERN-SPS,” *Nucl. Phys.* **B725** (2005) 306–326, arXiv:hep-ph/0503021.
- [132] **IDS-NF Collaboration** Collaboration, S. Choubey *et al.*, “International Design Study for the Neutrino Factory, Interim Design Report,” arXiv:1112.2853 [hep-ex].
- [133] **MINOS** Collaboration, P. Adamson *et al.*, “New constraints on muon-neutrino to electron-neutrino transitions in MINOS,” *Phys. Rev. D* **82** (2010) 051102, arXiv:1006.0996 [hep-ex].
- [134] **MINOS Collaboration** Collaboration, P. Adamson *et al.*, “Neutrino and Antineutrino Inclusive Charged-current Cross Section Measurements with the MINOS Near Detector,” *Phys. Rev.* **D81** (2010) 072002, arXiv:0910.2201 [hep-ex].

- [135] C. Tunnell, *Sensitivity to electronvolt-scale sterile neutrinos at a 3.8-GeV/c muon decay ring*. PhD thesis, University of Oxford, 2013.
- [136] **MINOS** Collaboration, K. Lang, “MINOS detectors for neutrino interactions,” *Nucl. Instrum. Meth.* **A461** (2001) 290–292.
- [137] **VLHC Design Study Group** Collaboration, G. Ambrosio *et al.*, “Design study for a staged very large hadron collider,”. SLAC-R-591; FERMILAB-TM-2149.
- [138] A. Devred *et al.*, “Status of ITER Conductor Development and Production,” *IEEE Trans. Appl. Supercond.* **22** (2012) 4804909.
- [139] **MINOS** Collaboration, D. G. Michael *et al.*, “The Magnetized steel and scintillator calorimeters of the MINOS experiment,” *Nucl. Instrum. Meth.* **A596** (2008) 190–228, arXiv:0805.3170 [physics.ins-det].
- [140] A. Y. Rodriguez Marrero, “Measurement of the exclusive ($\nu_\mu p \rightarrow \mu^- p \pi^+$) and inclusive ($\nu_\mu N \rightarrow \mu^- N' \pi^+$) single pion ν interaction cross section in a carbon target using the SciBar ,”.
- [141] **T2K** Collaboration, Y. Kudenko, “The near neutrino detector for the T2K experiment,” *Nucl. Instrum. Meth.* **A598** (2009) 289–295, arXiv:0805.0411 [physics.ins-det].
- [142] D. Greiner, T. Lachenmaier, J. Jochum, and A. Cabrera, “Double Chooz detectors design,” *Nucl. Instrum. Meth.* **A581** (2007) 139–142.
- [143] **MINERvA** Collaboration, K. S. McFarland, “MINERvA: A dedicated neutrino scattering experiment at NuMI,” *Nucl. Phys. Proc. Suppl.* **159** (2006) 107–112, arXiv:physics/0605088.
- [144] Z. Sadygov, 1996. Russian patent No. 2102820.
- [145] N. Bacchetta *et al.*, “New type of metal-resistive layer-silicon avalanche detectors for visible and UV light detection,” *Nucl. Instrum. Meth.* **A383** (1996) 263–265.
- [146] D. Renker and E. Lorenz, “Advances in solid state photon detectors,” *JINST* **4** (2009) P04004.
- [147] V. Balagura *et al.*, “Study of scintillator strip with wavelength shifting fiber and silicon photomultiplier,” *Nucl. Instrum. Meth.* **A564** (2006) 590–596, arXiv:physics/0504194.
- [148] M. Yokoyama *et al.*, “Performance of Multi-Pixel Photon Counters for the T2K near detectors,” *Nucl. Instrum. Meth.* **A622** (2010) 567–573, arXiv:1007.2712 [physics.ins-det].
- [149] “Hamamatsu Photonics.”. <http://www.hamamatsu.com/>.
- [150] L. B. Okun, *Leptons and quarks*. Nauka, Moscow, 2 ed., 1990.
- [151] **EURO ν** Collaboration, M. Bogomilov *et al.*, “Neutrino factory near detector,” *Phys. Rev. Special Topics - Accelerators and Beams* **16** (2013) 081001.
- [152] W. J. Marciano and Z. Parsa, “Neutrino-Electron Scattering Theory,” *J. Phys.* **G29** (2003) 2629–2645, arXiv:hep-ph/0403168.
- [153] A. Laing and F. J. P. Soler, “Oscillation probability fits using near detector data at a neutrino factory,” *PoS NFACT08* (2008) 129.

- [154] **MINOS Collaboration** Collaboration, D. Michael *et al.*, “Observation of muon neutrino disappearance with the MINOS detectors and the NuMI neutrino beam,” *Phys. Rev. Lett.* **97** (2006) 191801, arXiv:hep-ex/0607088 [hep-ex].
- [155] **T2K Collaboration** Collaboration, K. Abe *et al.*, “The T2K Experiment,” *Nucl.Instrum.Meth.* **A659** (2011) 106–135, arXiv:1106.1238 [physics.ins-det].
- [156] J. e. Morfin, “The Minerva Technical Design Report,” 2006.
http://minerva-docdb.fnal.gov/0007/000700/028/TDR_v1.3.pdf.
- [157] **MINERvA Collaboration**, T. Kafka and V. Paolone, “Prospects and status of the MINERvA experiment at FNAL,” *Prog. Part. Nucl. Phys.* **64** (2010) 181–183.
- [158] I. Stancu *et al.*, “Letter of Intent to Build a MiniBooNE Near Detector:BooNE,”.
- [159] **MiniBooNE Collaboration** Collaboration, A. Aguilar-Arevalo *et al.*, “The MiniBooNE Detector,” *Nucl.Instrum.Meth.* **A599** (2009) 28–46, arXiv:0806.4201 [hep-ex].
- [160] **SciBooNE Collaboration** Collaboration, A. Aguilar-Arevalo *et al.*, “Bringing the SciBar detector to the booster neutrino beam,” arXiv:hep-ex/0601022 [hep-ex].
- [161] **NOMAD Collaboration**, J. Altegoer *et al.*, “The NOMAD experiment at the CERN SPS,” *Nucl. Instrum. Meth. A* **404** (1998) 96–128.
- [162] **MicroBooNE Collaboration** Collaboration, H. Chen *et al.*, “Proposal for a New Experiment Using the Booster and NuMI Neutrino Beamlines: MicroBooNE,”.
- [163] J. G. Morfin, J. Nieves, and J. T. Sobczyk, “Recent Developments in Neutrino/Antineutrino - Nucleus Interactions,” arXiv:1209.6586 [hep-ex].
- [164] B. Bhattacharya, R. Hill, and G. Paz, “Model independent determination of the axial mass parameter in quasielastic neutrino-nucleon scattering,” *Phys. Rev.* **D84** (2011) 073006, arXiv:1108.0423 [hep-ph].
- [165] A. Bodek, S. Avvakumov, R. Bradford, and H. S. Budd, “Extraction of the axial nucleon form-factor from neutrino experiments on deuterium,” *J.Phys.Conf.Ser.* **110** (2008) 082004, arXiv:0709.3538 [hep-ex].
- [166] V. Bernard, L. Elouadrhiri, and U. Meissner, “Axial structure of the nucleon: Topical Review,” *J.Phys.* **G28** (2002) R1–R35, arXiv:hep-ph/0107088 [hep-ph].
- [167] **MiniBooNE Collaboration** Collaboration, A. Aguilar-Arevalo *et al.*, “First Measurement of the Muon Neutrino Charged Current Quasielastic Double Differential Cross Section,” *Phys. Rev.* **D81** (2010) 092005, arXiv:1002.2680 [hep-ex].
- [168] **NOMAD Collaboration** Collaboration, V. Lyubushkin *et al.*, “A Study of quasi-elastic muon neutrino and antineutrino scattering in the NOMAD experiment,” *Eur.Phys.J.* **C63** (2009) 355–381, arXiv:0812.4543 [hep-ex].
- [169] **MINERvA Collaboration** Collaboration, J.G.Morfin. Poster presented at neutrino2012 conference, kyoto, 2012.

- [170] S. Boyd, S. Dytman, E. Hernandez, J. Sobczyk, and R. Tacik, “Comparison of models of neutrino-nucleus interactions,” *AIP Conf.Proc.* **1189** (2009) 60–73.
- [171] R. Smith and E. Moniz, “NEUTRINO REACTIONS ON NUCLEAR TARGETS,” *Nucl.Phys.* **B43** (1972) 605.
- [172] O. Benhar, A. Fabrocini, S. Fantoni, and I. Sick, “Spectral function of finite nuclei and scattering of GeV electrons,” *Nucl.Phys.* **A579** (1994) 493–517.
- [173] O. Benhar and D. Meloni, “Total neutrino and antineutrino nuclear cross-sections around 1-GeV,” *Nucl.Phys.* **A789** (2007) 379–402, arXiv:hep-ph/0610403 [hep-ph].
- [174] A. M. Ankowski and J. T. Sobczyk, “Construction of spectral functions for medium-mass nuclei,” *Phys.Rev.* **C77** (2008) 044311, arXiv:0711.2031 [nucl-th].
- [175] J. Marteau, “Effects of the nuclear correlations on the neutrino oxygen interactions,” *Eur.Phys.J.* **A5** (1999) 183–190, arXiv:hep-ph/9902210 [hep-ph].
- [176] M. Martini, M. Ericson, G. Chanfray, and J. Marteau, “A Unified approach for nucleon knock-out, coherent and incoherent pion production in neutrino interactions with nuclei,” *Phys.Rev.* **C80** (2009) 065501, arXiv:0910.2622 [nucl-th].
- [177] M. Martini, M. Ericson, G. Chanfray, and J. Marteau, “Neutrino and antineutrino quasielastic interactions with nuclei,” *Phys.Rev.* **C81** (2010) 045502, arXiv:1002.4538 [hep-ph].
- [178] J. Nieves, I. Ruiz Simo, and M. Vicente Vacas, “The nucleon axial mass and the MiniBooNE Quasielastic Neutrino-Nucleus Scattering problem,” *Phys.Lett.* **B707** (2012) 72–75, arXiv:1106.5374 [hep-ph].
- [179] J. Nieves, I. Ruiz Simo, and M. Vicente Vacas, “Inclusive Charged-Current Neutrino-Nucleus Reactions,” *Phys.Rev.* **C83** (2011) 045501, arXiv:1102.2777 [hep-ph].
- [180] M. Martini, M. Ericson, and G. Chanfray, “Neutrino quasielastic interaction and nuclear dynamics,” *Phys.Rev.* **C84** (2011) 055502, arXiv:1110.0221 [nucl-th].
- [181] D. Meloni and M. Martini, “Revisiting the T2K data using different models for the neutrino-nucleus cross sections,” *Phys.Lett.* **B716** (2012) 186–192, arXiv:1203.3335 [hep-ph].
- [182] J. T. Sobczyk, “Multinucleon ejection model for Meson Exchange Current neutrino interactions,” *Phys.Rev.* **C86** (2012) 015504, arXiv:1201.3673 [hep-ph].
- [183] M. Martini, M. Ericson, and G. Chanfray, “Neutrino energy reconstruction problems and neutrino oscillations,” *Phys.Rev.* **D85** (2012) 093012, arXiv:1202.4745 [hep-ph].
- [184] U. Mosel and O. Lalakulich, “Neutrino-Long-Baseline Experiments and Nuclear Physics,” *PoS BORMIO2012* (2012) 034, arXiv:1204.2269 [nucl-th].
- [185] O. Lalakulich, K. Gallmeister, and U. Mosel, “Many-Body Interactions of Neutrinos with Nuclei - Observables,” *Phys.Rev.* **C86** (2012) 014614, arXiv:1203.2935 [nucl-th].
- [186] **K2K Collaboration** Collaboration, S. Nakayama *et al.*, “Measurement of single π^0 production in neutral current neutrino interactions with water by a 1.3-GeV wide band muon neutrino beam,” *Phys. Lett.* **B619** (2005) 255–262, arXiv:hep-ex/0408134 [hep-ex].

- [187] **MiniBooNE Collaboration** Collaboration, A. Aguilar-Arevalo *et al.*, “Measurement of $\nu(\mu)$ and anti- $\nu(\mu)$ induced neutral current single π^0 production cross sections on mineral oil at $E(\nu) \sim O(1\text{-GeV})$,” *Phys. Rev.* **D81** (2010) 013005, arXiv:0911.2063 [hep-ex].
- [188] **SciBooNE Collaboration** Collaboration, Y. Kurimoto *et al.*, “Measurement of Inclusive Neutral Current Neutral π^0 Production on Carbon in a Few-GeV Neutrino Beam,” *Phys.Rev.* **D81** (2010) 033004, arXiv:0910.5768 [hep-ex].
- [189] **MiniBooNE Collaboration** Collaboration, A. Aguilar-Arevalo *et al.*, “Measurement of Neutrino-Induced Charged-Current Charged Pion Production Cross Sections on Mineral Oil at $E_\nu \sim 1\text{ GeV}$,” *Phys. Rev.* **D83** (2011) 052007, arXiv:1011.3572 [hep-ex].
- [190] O. Lalakulich, K. Gallmeister, T. Leitner, and U. Mosel, “Pion production in the MiniBooNE,” *AIP Conf.Proc.* **1405** (2011) 127–133, arXiv:1107.5947 [nucl-th].
- [191] **MiniBooNE Collaboration** Collaboration, A. Aguilar-Arevalo *et al.*, “Measurement of ν_μ -induced charged-current neutral pion production cross sections on mineral oil at $E_\nu \in 0.5 - 2.0\text{ GeV}$,” *Phys. Rev.* **D83** (2011) 052009, arXiv:1010.3264 [hep-ex].
- [192] T. Golan, C. Juszczak, and J. T. Sobczyk, “Final State Interactions Effects in Neutrino-Nucleus Interactions,” *Phys.Rev.* **C86** (2012) 015505, arXiv:1202.4197 [nucl-th].
- [193] **MiniBooNE Collaboration** Collaboration, A. Aguilar-Arevalo *et al.*, “First Observation of Coherent π^0 Production in Neutrino Nucleus Interactions with $E_\nu < 2\text{ GeV}$,” *Phys. Lett.* **B664** (2008) 41–46, arXiv:0803.3423 [hep-ex].
- [194] **SciBooNE Collaboration** Collaboration, Y. Kurimoto *et al.*, “Improved measurement of neutral current coherent π^0 production on carbon in a few-GeV neutrino beam,” *Phys.Rev.* **D81** (2010) 111102, arXiv:1005.0059 [hep-ex].
- [195] **K2K Collaboration** Collaboration, M. Hasegawa *et al.*, “Search for coherent charged pion production in neutrino-carbon interactions,” *Phys. Rev. Lett.* **95** (2005) 252301, arXiv:hep-ex/0506008 [hep-ex].
- [196] **SciBooNE Collaboration** Collaboration, K. Hiraide *et al.*, “Search for Charged Current Coherent Pion Production on Carbon in a Few-GeV Neutrino Beam,” *Phys.Rev.* **D78** (2008) 112004, arXiv:0811.0369 [hep-ex].
- [197] D. Rein and L. M. Sehgal, “Coherent π^0 Production in Neutrino Reactions,” *Nucl.Phys.* **B223** (1983) 29.
- [198] C. Berger and L. Sehgal, “Lepton mass effects in single pion production by neutrinos,” *Phys.Rev.* **D76** (2007) 113004, arXiv:0709.4378 [hep-ph].
- [199] C. Berger, “PCAC and coherent pion production by neutrinos,” *AIP Conf.Proc.* **1189** (2009) 218–223, arXiv:0908.2758 [hep-ph].
- [200] E. Paschos and D. Schalla, “Coherent Pion Production by Neutrinos,” *AIP Conf.Proc.* **1189** (2009) 213–217, arXiv:0910.2852 [hep-ph].
- [201] E. Hernandez, J. Nieves, and M. Vicente-Vacas, “Neutrino Induced Coherent Pion Production off Nuclei and PCAC,” *Phys.Rev.* **D80** (2009) 013003, arXiv:0903.5285 [hep-ph].

- [202] S. Nakamura, T. Sato, T.-S. Lee, B. Szczerbinska, and K. Kubodera, “Dynamical Model of Coherent Pion Production in Neutrino-Nucleus Scattering,” *Phys.Rev.* **C81** (2010) 035502, arXiv:0910.1057 [nucl-th].
- [203] M. Valverde, J. Amaro, E. Hernandez, and J. Nieves, “Coherent Neutrino Scattering,” *Acta Phys.Polon.* **B40** (2009) 2551–2557, arXiv:0906.1516 [nucl-th].
- [204] E. Hernandez, J. Nieves, and M. Valverde, “Coherent pion production off nuclei at T2K and MiniBooNE energies revisited,” *Phys.Rev.* **D82** (2010) 077303, arXiv:1007.3685 [hep-ph].
- [205] L. Alvarez-Ruso, L. Geng, S. Hirenzaki, M. Vicente Vacas, T. Leitner, *et al.*, “Neutrino-induced coherent pion production,” *AIP Conf.Proc.* **967** (2007) 201–204, arXiv:0709.3019 [nucl-th].
- [206] D. Rein and L. M. Sehgal, “Neutrino Excitation of Baryon Resonances and Single Pion Production,” *Annals Phys.* **133** (1981) 79–153.
- [207] K. M. Graczyk and J. T. Sobczyk, “Lepton mass effects in weak charged current single pion production,” *Phys.Rev.* **D77** (2008) 053003, arXiv:0709.4634 [hep-ph].
- [208] **MiniBooNE Collaboration** Collaboration, J. A. Nowak, “Four Momentum Transfer Discrepancy in the Charged Current π^+ Production in the MiniBooNE: Data vs. Theory,” *AIP Conf.Proc.* **1189** (2009) 243–248, arXiv:0909.3659 [hep-ph].
- [209] K. M. Graczyk and J. T. Sobczyk, “Form Factors in the Quark Resonance Model,” *Phys.Rev.* **D77** (2008) 053001, arXiv:0707.3561 [hep-ph].
- [210] A. Bodek and U.-k. Yang, “NUFACT09 update to the Bodek-Yang unified model for electron- and neutrino- nucleon scattering cross sections,” *AIP Conf.Proc.* **1222** (2010) 233–237.
- [211] M. Gluck, E. Reya, and A. Vogt, “Dynamical parton distributions revisited,” *Eur.Phys.J.* **C5** (1998) 461–470, arXiv:hep-ph/9806404 [hep-ph].
- [212] R. Thorne and R. Roberts, “A Practical procedure for evolving heavy flavor structure functions,” *Phys.Lett.* **B421** (1998) 303–311, arXiv:hep-ph/9711223 [hep-ph].
- [213] A. D. Martin, R. Roberts, W. J. Stirling, and R. Thorne, “Estimating the effect of NNLO contributions on global parton analyses,” *Eur.Phys.J.* **C18** (2000) 117–126, arXiv:hep-ph/0007099 [hep-ph].
- [214] L. Whitlow, S. Rock, A. Bodek, E. Riordan, and S. Dasu, “A Precise extraction of $R = \sigma_L / \sigma_T$ from a global analysis of the SLAC deep inelastic e p and e d scattering cross-sections,” *Phys.Lett.* **B250** (1990) 193–198.
- [215] **NuTeV Collaboration** Collaboration, M. Tzanov *et al.*, “Precise measurement of neutrino and anti-neutrino differential cross sections,” *Phys.Rev.* **D74** (2006) 012008, arXiv:hep-ex/0509010 [hep-ex].
- [216] **CHORUS Collaboration** Collaboration, G. Onengut *et al.*, “Measurement of nucleon structure functions in neutrino scattering,” *Phys.Lett.* **B632** (2006) 65–75.
- [217] **NOMAD Collaboration** Collaboration, R. Petti, “Cross-section measurements in the NOMAD experiment,” *Nucl.Phys.Proc.Suppl.* **159** (2006) 56–62, arXiv:hep-ex/0602022 [hep-ex].

- [218] A. Accardi *et al.*, “New parton distributions from large- x and low- Q^2 data,” *Phys. Rev.* **D81** (2010) 034016, arXiv:0911.2254 [hep-ph].
- [219] J. Pumplin, D. Stump, J. Huston, H. Lai, P. M. Nadolsky, *et al.*, “New generation of parton distributions with uncertainties from global QCD analysis,” *JHEP* **0207** (2002) 012, arXiv:hep-ph/0201195 [hep-ph].
- [220] W. Stirling, A. Martin, R. Roberts, and R. Thorne, “MRST parton distributions,” *AIP Conf.Proc.* **747** (2005) 16–21.
- [221] K. Kovarik, I. Schienbein, F. Olness, J. Yu, C. Keppel, *et al.*, “Nuclear corrections in neutrino-nucleus DIS and their compatibility with global NPFD analyses,” *Phys.Rev.Lett.* **106** (2011) 122301, arXiv:1012.0286 [hep-ph].
- [222] I. Schienbein, J. Yu, C. Keppel, J. Morfin, F. Olness, *et al.*, “Nuclear parton distribution functions from neutrino deep inelastic scattering,” *Phys.Rev.* **D77** (2008) 054013, arXiv:0710.4897 [hep-ph].
- [223] J. Owens, J. Huston, J. Pumplin, D. Stump, C. Keppel, *et al.*, “Nuclear corrections and parton distribution functions: Lessons learned from global fitting,” *AIP Conf.Proc.* **967** (2007) 259–263.
- [224] B. Kopeliovich, J. Morfin, and I. Schmidt, “Nuclear Shadowing in Electro-Weak Interactions,” *Prog.Part.Nucl.Phys.* **68** (2013) 314–372, arXiv:1208.6541 [hep-ph].
- [225] “XX International Workshop on Deep-Inelastic Scattering and Related Subjects.” http://www.praktika.physik.uni-bonn.de/conferences/dis-2012?set_language=en.
- [226] **CTEQ Collaboration** Collaboration, J. Botts *et al.*, “CTEQ parton distributions and flavor dependence of sea quarks,” *Phys.Lett.* **B304** (1993) 159–166, arXiv:hep-ph/9303255 [hep-ph].
- [227] H. Lai, J. Botts, J. Huston, J. Morfin, J. Owens, *et al.*, “Global QCD analysis and the CTEQ parton distributions,” *Phys.Rev.* **D51** (1995) 4763–4782, arXiv:hep-ph/9410404 [hep-ph].
- [228] S. J. Brodsky, I. Schmidt, and J.-J. Yang, “Nuclear antishadowing in neutrino deep inelastic scattering,” *Phys.Rev.* **D70** (2004) 116003, arXiv:hep-ph/0409279 [hep-ph].
- [229] J.-W. Qiu and I. Vitev, “Nuclear shadowing in neutrino nucleus deeply inelastic scattering,” *Phys.Lett.* **B587** (2004) 52–61, arXiv:hep-ph/0401062 [hep-ph].
- [230] V. Guzey, L. Zhu, C. E. Keppel, M. E. Christy, D. Gaskell, *et al.*, “Impact of nuclear dependence of $R = \sigma_L/\sigma_T$ on antishadowing in nuclear structure functions,” *Phys.Rev.* **C86** (2012) 045201, arXiv:1207.0131 [hep-ph].
- [231] “Nuclear shadowing in charged-lepton-nucleus and neutrino-nucleus scattering.” Work in progress.
- [232] Y. Karadzhov, “Neutrino Factory Near Detector Simulation,” *AIP Conf. Proc.* **1222** (2010) 467–470. <http://link.aip.org/link/?APCPCS/1222/467/1>.
- [233] Y. Karadzhov and R. Tsenov, “Neutrino Factory Near Detector Simulation,” *Annual of the University of Sofia, Faculty of Physics* **103** (2010) . http://phys.uni-sofia.bg/annual/arch/103/arch_en.html.
- [234] S. Agostinelli *et al.*, “GEANT4—a simulation toolkit,” *Nucl. Instrum. Methods A* **506** (2003) 250–303.

- [235] S. Mishra, “Near Detector with a straw tube tracker,” in *Seventh IDS-NF Plenary Meeting, 17-19 October 2011, Arlington, VA USA*. 2011.
<https://www.ids-nf.org/wiki/VTECH-2011-10-17/Agenda>.
- [236] M. Bass *et al.*, “A study of the physics potential of the long-baseline neutrino experiment project with an extensive set of beam, near detector and far detector configurations,” Tech. Rep. LBNE-PWG-002, 2010.
- [237] S. R. Mishra, R. Petti, and C. Rosenfeld, “A High Resolution Neutrino Experiment in a Magnetic Field for Project-X at Fermilab,” *PoS NFACT08* (2008) 069, arXiv:0812.4527 [hep-ex].
- [238] “Preparation for p5 meetings on physics with a high intensity proton source,” 2007.
http://www.fnal.gov/directorate/Longrange/Steering_Public/P5.html.
- [239] “Fermilab steering group report,” 2007.
http://www.fnal.gov/pub/directorate/steering/pdfs/SGR_2007.pdf.
- [240] **ATLAS TRT** Collaboration, T. Akesson *et al.*, “Status of design and construction of the Transition Radiation Tracker (TRT) for the ATLAS experiment at the LHC,” *Nucl. Instrum. Meth.* **A522** (2004) 131–145.
- [241] **ATLAS TRT** Collaboration, T. Akesson *et al.*, “ATLAS Transition Radiation Tracker test-beam results,” *Nucl. Instrum. Meth.* **A522** (2004) 50–55.
- [242] **ATLAS TRT** Collaboration, E. Abat *et al.*, “The ATLAS Transition Radiation Tracker (TRT) proportional drift tube: Design and performance,” *JINST* **3** (2008) P02013.
- [243] V. N. Bychkov *et al.*, “Construction and manufacture of large size straw-chambers of the COMPASS spectrometer tracking system,” *Part. Nucl. Lett.* **111** (2002) 64–73.
- [244] **NOMAD** Collaboration, O. Samoylov *et al.*, “A Precision Measurement of Charm Dimuon Production in Neutrino Interactions from the NOMAD Experiment,” *Nucl. Phys.* **B876** (2013) 339–375, arXiv:1308.4750 [hep-ex].
- [245] M. Ellis and F. J. P. Soler, “Charm identification using silicon detectors in a neutrino experiment,” *J. Phys. G* **G29** (2003) 1975–1979.
- [246] G. Barichello, A. Cervera-Villanueva, D. Daniels, E. do Couto e Silva, M. Ellis, *et al.*, “Performance of the NOMAD-STAR detector,” *Nucl. Instrum. Meth.* **A506** (2003) 217–237.
- [247] J. J. Gomez-Cadenas, J. A. Hernando, and A. Bueno, “A Neutrino apparatus with improved capabilities for a short baseline muon-neutrino (electron-neutrino) \rightarrow tau- neutrino search,” *Nucl. Instrum. Meth.* **A378** (1996) 196–220.
- [248] **NOMAD** Collaboration, P. Astier *et al.*, “Final NOMAD results on $\nu_\mu \rightarrow \nu_\tau$ and $\nu_e \rightarrow \nu_\tau$ oscillations including a new search for ν_τ appearance using hadronic τ decays,” *Nucl. Phys. B* **611** (2001) 3–39, arXiv:0106102 [hep-ex].
- [249] **CHORUS** Collaboration, E. Eskut *et al.*, “Final results on ν_μ to ν_τ oscillation from the CHORUS experiment,” *Nucl. Phys.* **B793** (2008) 326–343, arXiv:0710.3361 [hep-ex].
- [250] **ISS Physics Working Group** Collaboration, A. Bandyopadhyay *et al.*, “Physics at a future Neutrino Factory and super-beam facility,” *Rept. Prog. Phys.* **72** (2009) 106201, arXiv:0710.4947 [hep-ph].

- [251] Muon Accelerator Program, “Muon accelerator program snowmass whitepaper,” 2013. in preparation.
- [252] E. Christensen, P. Coloma, and P. Huber, “Physics Performance of a Low-Luminosity Low Energy Neutrino Factory,” arXiv:1301.7727 [hep-ph].
- [253] <http://www-ap.fnal.gov/MARS/>.
- [254] S. A. Bogacz, “Recirculating linac acceleration—end-to-end simulation,” in *Neutrino Factories, Superbeams and Beta Beams: 11th International Workshop on Neutrino Factories, Superbeams and Beta Beams—NuFact09*, M. C. Goodman, D. M. Kaplan, and Z. Sullivan, eds., vol. 1222 of *AIP Conference Proceedings*, pp. 363–367. American Institute of Physics, Melville, NY, 2010.
- [255] T. Roberts, “G4beamline.” <http://g4beamline.muonsinc.com>.
- [256] S. A. Bogacz, “Beam Dynamics of Muon Acceleration for Neutrino Factory,” *J. Phys. G: Nucl. Part. Phys* **29** (2003) 1723.
- [257] S. A. Bogacz, “Maximizing number of passes in muon RLA,” in *Neutrino Factories, Superbeams and Betabeams: 9th International Workshop on Neutrino Factories, Superbeams, and Betabeams - NuFact 07*, O. Yasuda, N. Mondal, and C. Ohmori, eds., vol. 981 of *AIP Conference Proceedings*, pp. 324–326. AIP, 2008.
- [258] S. A. Bogacz, K. B. Beard, and R. P. Johnson, “Recirculating linear accelerators for future muon facilities,” in *Proceedings of IPAC’10, Kyoto, Japan* [266], pp. 3602–3604.
- [259] S. Bogacz, V. Morozov, Y. Roblin, K. Beard, A. Kurup, *et al.*, “Recent Progress Toward a Muon Recirculating Linear Accelerator.”
- [260] V. Lebedev, “Optim.” [HTTP://WWW-BDNEW.FNAL.GOV/PBAR/ORGANIZATIONALCHART/LEBEDEV/OPTIM/OPTIM.HTM](http://www-bdnew.fnal.gov/pbar/organizationalchart/lebedev/optim/optim.htm).
- [261] C. Ankenbrandt *et al.*, “Low-energy neutrino factory design,” *Phys. Rev. ST Accel. Beams* **12** (2009) 070101.
- [262] S. A. Bogacz, “Low Energy Stages - ‘Dogbone’ Muon RLA,” *Nucl. Phys. B Proc. Suppl.* **149** (2005) 309–312.
- [263] “Mad-x.” [HTTP://MAD.HOME.CERN.CH/MAD/](http://MAD.HOME.CERN.CH/MAD/).
- [264] S. D. H. *et al.*, ““project x - accelerator reference design report””
<https://proecjtx-docdb.fnal.gov:440/cgi-bin/documentdatabase>. Tech. Rep. Project-X-doc-776-v7, Fermilab.
- [265] ““design of accumulator and compressor rings for project-x based proton driver.”. TUPPC043.
- [266] *Proceedings of IPAC’10, Kyoto, Japan*. IPAC’10 and Asian Committee for Future Accelerators, 2010.

A Incremental Development of a 10 GeV Neutrino Factory

Chris Rogers, Patrick Huber

The Neutrino Factory facility will provide an intense beam of high energy neutrinos for precision measurement of CP violation. Here a series of stages are examined that may permit incremental development of a facility with physics at each stage and with a relatively small increase in the overall facility cost. The advantage of constructing such a facility incrementally is that it may be easier to fit within presumed funding profiles and the technical risk can be spread more evenly over the project lifetime.

A.1 Neutrino Factory baseline

The Neutrino Factory facility baseline design makes a beam of muons by firing a high power and short pulse proton beam onto a target. The resultant secondary particles contain many charged pions along with other secondaries. These pions are captured into a solenoidal field, during which most decay to muons. Subsequently the muons are taken through a solenoidal chicane and proton absorber to remove protons and particles outside the momentum acceptance of the capture system. An adiabatic buncher and phase rotator is used to capture muons longitudinally. Transverse ionisation cooling is used to reduce the transverse emittance of the muon beam, leading to the capture of a significant number of useful muons.

In the baseline design, these muons are subsequently accelerated in a linac from 0.2 GeV to 0.8 GeV; and in two RLAs, first from 0.8 GeV to 2.8 GeV and secondly from 2.8 GeV to 10 GeV.

The muons are finally injected into a storage ring at 10 GeV where they decay into neutrinos and electrons. The neutrino decay products are directed towards a remote detector where the flux of different neutrino species can be measured.

In this paper the Neutrino Factory baseline is considered the final design goal of the facility, and staging schemes are considered that would deliver this facility as the final stage.

A.2 Staging Schemes

In this paper, the number of neutrino interactions is considered as the means to providing an incremental approach to a Neutrino Factory facility.

The number of neutrino interactions can be modified either by modifying the number of muons reaching the storage ring, typically by modifying the design of the capture channel; or by reducing the detector size.

The scheme chosen is driven by a balance between physics need, cost and perceived technical risk. Delaying the construction of certain elements can spread cost and risk more evenly over the project lifetime. It is perceived that, for example, gaining experience with muon beam handling and radiation issues with a low rate beam may enable a better design and lower risk associated with higher rate beams.

A.3 Rate Staging

More than half of the projected Neutrino Factory cost is associated with the proton driver and capture section, which are the sections that mostly impact the rate of muons in the storage ring. Additionally, these are expected to be the most technically challenging parts of the Neutrino Factory design, while the accelerator and decay ring designs are expected to be relatively low risk.

It is proposed that an initial stage would be using a lower power proton driver, possibly at an existing facility, a target horn rather than high field capture solenoid and no cooling section. An upgrade scenario would then

be to build a high field solenoid in the capture region, extend the beamline adding a cooling section and as a further stage to increase the proton driver beam power to 4 MW.

Implementing a staged scenario in this way is challenging due to the practicalities of manipulating highly activated targets and beam transport lines. Conventional transport elements like bending magnets would result in a dramatically reduced beam transport due to the exceptionally large beam emittance, both transverse and longitudinal, which cannot be transported efficiently by multipole-type lattices [?] [?].

In this study a solenoidal chicane is proposed to introduce a transverse displacement. A schematic diagram of the proposed scheme is shown in Fig. 90.

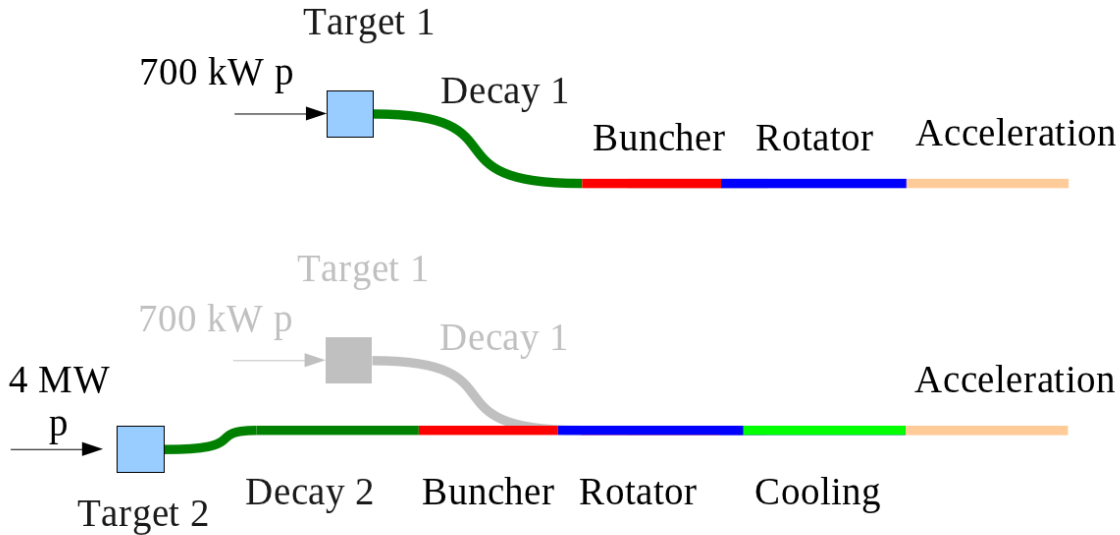


Figure 90: Schematic diagram of (top) stage 1 and (bottom) stage 2 and 3 of the proposed scheme. Stage 3 is to increase the proton beam power on target to 4 MW.

A.3.1 Muon Chicane to Create Transverse Displacement

The muon chicane mentioned above, is designed to remove undesirable secondaries from the beam. A solenoidal chicane is used which has excellent properties for transport of high emittance beams.

Increasing the radius of curvature of the chicane increases the lateral displacement of the beam pipe without significantly affecting the beam transport properties.

A.3.2 Magnetic Field in a Constant Radius Constant Field Bent Solenoid

The magnetic field in a bent solenoid is assumed to have only a radial dependence, such that it can be written as

$$\mathbf{B}_{bs} = f(\rho)\mathbf{s} \quad (34)$$

From Maxwell's equations, in the absence of current sources

$$\begin{aligned}\nabla \times \mathbf{B} &= \left(\frac{1}{\rho} \partial_s B_y - \partial_y B_s\right) \rho + \\ &\quad (\partial_y B_\rho - \partial_\rho B_y) \mathbf{s} + \\ &\quad \frac{1}{\rho} (\partial_\rho \rho B_s - \partial_s B_\rho) \mathbf{y} = 0.\end{aligned}$$

Substituting for \mathbf{B}_{bs} gives

$$\partial_\rho \rho f(\rho) = 0 \quad (35)$$

which has the solution

$$f(\rho) = \frac{b_0}{\rho} = \frac{b_s \rho_0}{\rho}. \quad (36)$$

Here b_s is the magnetic field strength on the reference orbit at radius ρ_0 .

A.3.3 Helical Motion

In the presence of a field of this nature, some particles can be shown to travel in a helix. Starting from the Lorentz equations,

$$\mathbf{F} = \frac{d\mathbf{p}}{dt} = q\mathbf{v} \times \mathbf{B} \quad (37)$$

it is possible to derive the criterion for helical motion. Assume no radial velocity, so that

$$\mathbf{v} = c \frac{p_y \mathbf{y} + p_s \mathbf{s}}{E} \quad (38)$$

with speed of light c . Then if the particle is travelling at radius ρ

$$\mathbf{F} = qc \frac{p_y b_0}{E \rho} \quad (39)$$

For circular or helical motion, with constant energy,

$$\mathbf{F} = m\gamma\rho\omega^2 = \frac{m\gamma\beta_s^2 c^2}{\rho} = \frac{c^2 p_s^2}{Er_0}. \quad (40)$$

By equating the two expressions for \mathbf{F}

$$\frac{c^2 p_s^2}{E\rho} = qc \frac{p_y b_0}{E\rho}. \quad (41)$$

Then if

$$p_y = \frac{qp_s^2}{b_0} \quad (42)$$

particle motion will be on a helix. It should be noted that the slope of the helix is independent of the radius.

A.3.4 Vertical Displacement

In a chicane-type geometry vertical displacement into a collimator used to reject high momentum particles. The vertical displacement is given by

$$\delta_y = \frac{dy}{ds} \delta_s \quad (43)$$

where δ_s is the total path length through the circular orbit,

$$\delta_s = \rho\delta_\theta \quad (44)$$

and δ_θ is the total bend angle of the chicane. The vertical divergence is given by

$$\frac{dy}{ds} = \frac{p_y}{p_s} = \frac{qp_s}{b_0} \quad (45)$$

so

$$\delta_y = \frac{qp_s}{b_0} \rho\delta_\theta = \frac{qp_s}{b_s} \delta_\theta \quad (46)$$

and the vertical displacement is independent of the radius of the helix. This is a useful feature as the chicane radius of curvature can be increased to provide a larger transverse displacement of the beam pipe. This may provide space for the beam pipe and tunnel to pass from the second target station, past the decommissioned first target station and into the existing tunnel for acceleration.

A.3.5 Tracking through a Dual Chicane System

The effect of introducing a second chicane was studied in a full Monte Carlo simulation. In this study, the initial 10 m long chicane, used for removing undesirable pollutants from the beam, was left in situ and a second, 40 m long chicane was placed immediately after the proton absorber, replacing almost all of the drift section with a chicane. The total bending angle in each half of both chicanes was left unchanged at 12.5° , resulting in a radius of curvature of 22.9 m and 91.7 m respectively and a horizontal transverse displacement of 1.08 m and 4.34 m respectively.

The tracking results for the two front ends are shown in Fig. 91. There is a slight degradation in capture performance, with peak muon yield reduced from 0.0672 muons per proton to 0.06495 muons per proton. (TODO: update that number on final design; errors?)

By introducing a second chicane, it is possible to introduce a lateral displacement of the target region that would enable a target station upgrade as part of the staging scheme.

A.3.6 Removing the cooling channel

Removal of the cooling channel would necessitate moving, reinstalling and recommissioning the buncher and phase rotator in an upstream position. While this may be time consuming, the dominant cost of the front end is in the capital cost of RF power supplies and so it is thought that it will only increment the total cost by a small fraction. It would, however, necessitate rebuilding the target station and initial capture region as following operation of the facility any existing target station or capture region would be too active to handle.

Removing the cooling channel would decrease the capture efficiency from the baseline 0.0672 to 0.0298 good muons per proton, where the latter number includes the effect of adding another chicane. (TODO: 0.0672 number is not final; errors?)

A.3.7 Replacing the target with a horn design

The effect of replacing the solenoidal capture target with a horn was studied in [250]. The main affect was shown to be that only one sign of muon could be captured at any one time. The study showed that the capture efficiency of the horn was between 40 % and 50 % compared to the capture efficiency of a solenoid-like target station. It should be noted that the capture efficiency of the Study 2a target station is very similar to the one presented in the RDR.

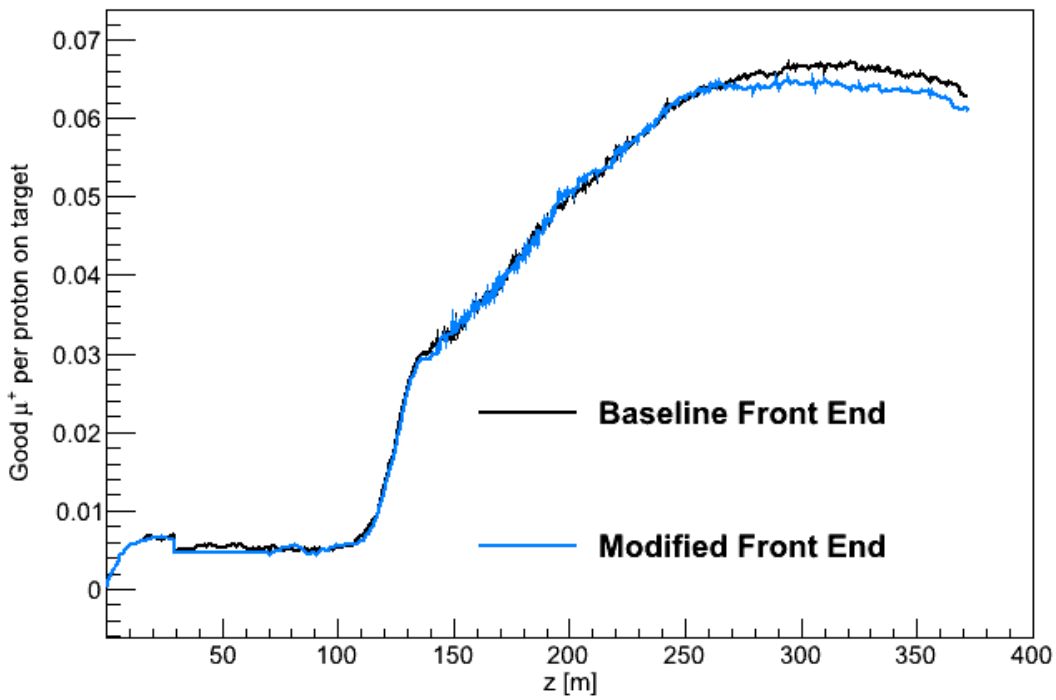


Figure 91: Capture performance of the baseline front end and the modified front end including a long chicane to provide a transverse displacement of the beamline. The cooling channel starts at 129.1 m. Good muons are counted using the standard criterion that muons should be within a momentum band of 100 MeV/c to 300 MeV/c, within a transverse acceptance of 30 mm and a longitudinal acceptance of 150 mm, which corresponds to the acceptance of the accelerator system.

	Stage 1	Stage 2	Stage 3
700 kW proton driver	0.18	0.18	
CERN 400 kA Horn	0.52		
No cooling channel	0.44		
Total	0.041	0.18	1

Table 34: Fraction of the baseline capture rate that would be achieved by each of the staging options discussed above. The total is found by taking the product of cells in the column above.

A.3.8 Target Geometry Considerations

Despite the introduction of a chicane, the front end beam axis following upgrade would still be 5.4 m from the target station. Some clearance is required for the tunnel in which the front end is expected to sit.

The NuMi/NovA target station has been successfully operated with 400 kW of proton beam power and an upgrade is planned for operation at 700 kW. (TODO: check those numbers) The target station half-width is 3 m. If a similar target station were installed 2.4 m would be available for additional supports and infrastructure associated with a tunnel.

If it were desired to provide a target horn that could operate at 4 MW, additional space may be required. The advantage of operation at 4 MW is that an initial low power proton driver may be replaced by a high power proton driver as an incremental upgrade; followed by a target station and front end upgrade at a later date. Much of the construction work for these upgrades could be performed during operation of the existing facility.

The front end beam pipe in this region is 0.3 m in diameter, with tightly packed RF cavities extending to 0.6 m. In the current design superconducting coils sit outside the RF cavity radius, providing a 1.5 T field. RF power is fed through gaps between adjacent coils. No full magnet design exists but a similar magnet under construction for the MICE experiment has a cryostat outer half width of 1.3 m, leaving 1.1 m for tunnel infrastructure. It may be possible, but would require some care in the design to ensure that the equipment does indeed fit in the tunnel. (TODO: do we want some images here? NOvA? MICE CC? (copyright/authorship issue))

A.3.9 Using a lower powered proton driver

Implicit in the discussion above is the assumption that one may use a lower powered proton driver to feed the target horn. There are several existing facilities that can deliver proton beams of the required beam power, and it is assumed that an existing facility would be used in this case. An additional buncher and bunch compression ring would be required for the protons, as no existing facility has the capability to deliver protons with the required 1-3 ns bunch length.

A.3.10 Rate reduction in proposed staging schemes

The rate of particle interactions in the detector at each stage, as a proportion of the rate for the final stage, is shown in Table 34.

TODO: costing table should be updated with numbers from RDR nf costing - TODO: here I have used scaled costing from euronu with modification to TODO: accomodate lower energy NF

	Stage 1	Stage 2	Stage 3
Proton Driver	6	0	21
Target, capture, decay	8	15	0
Front End	6	12	0
Acceleration	27	0	0
Decay Ring	9	0	0
Detector	13	0	0
Total Cost	65	21	27

Table 35: Cost for the proposed stages, based on [?]. Units are cost units [cu], where 1 cu is the cost for 1 % of the euronu accelerator facility cost, based on the upper bound estimate for cost.

A.4 Physics Reach of a Staged Facility

The physics reach of the various stages has been examined in detail for configurations with 0.04, 0.25 and 1 times 10^{21} useful muon decays which corresponds to accelerator stage I-III as described in Tab. 35. The detector lends itself well to continuous staging, which practically is implied due to the considerable time span required for construction and the fact that a partial detector can be fully operational. A 50 kt partial and a 100 kt full detector are considered. Combined with the three accelerator stages this corresponds to eight luminosity scenarios: 0.02, 0.04, 0.125, 0.25, 0.5, 1. The corresponding physics reach using a 10 GeV muon energy in terms of the accuracy on δ_{CP} is shown in Fig. 92. The two lines labeled 0.02 and 0.04 correspond to the stage I accelerator facility with a 50 kt or 100 kt detector respectively and fall in between the physics reaches of LBNE10 and full LBNE with a 2.3 MW proton driver. This implies that even a minimal stage I facility is competitive to current superbeam experiments. and at the same time provides a clear upgrade path to 5° accuracy without running into systematics issues.

An energy stage at 5 GeV was also investigated and it was found that running at 5 GeV and 2000 km baseline reduces the physics reach by a similar amount as reducing the luminosity by a factor of 2. Combined with the fact that at 5 GeV the acceptance of the 10 GeV storage ring would reduce the actual flux by a factor of ~ 2 , makes a 5 GeV energy stage rather unattractive from a physics point of view.

This is to be contrasted with the case where the baseline is changed to 1300 km and the detector technology is changed as well to a liquid argon detector. In this case it can be shown that the overall sensitivity is quite good because now oscillation maximum, beam flux and detection efficiencies are well matched again. This scenario is studied in detail in the MASS report [251, 252]. On the one hand it demonstrates the flexibility of the neutrino factory concept, on the other hand it makes it obvious that the beam flux, the oscillation maximum and detection efficiencies have to be carefully matched at the beginning. Therefore, neither baseline or energy should be changed as part of a staging scenario; in the initial choice, however, there exists quite some latitude.

B Conclusion

The feasibility of incrementally developing a 10 GeV Neutrino Factory has been examined and it has been found that the cost and risk can be spread over several stages while delivering competitive physics at each stage and finally enabling a greater degree of precision to be reached.

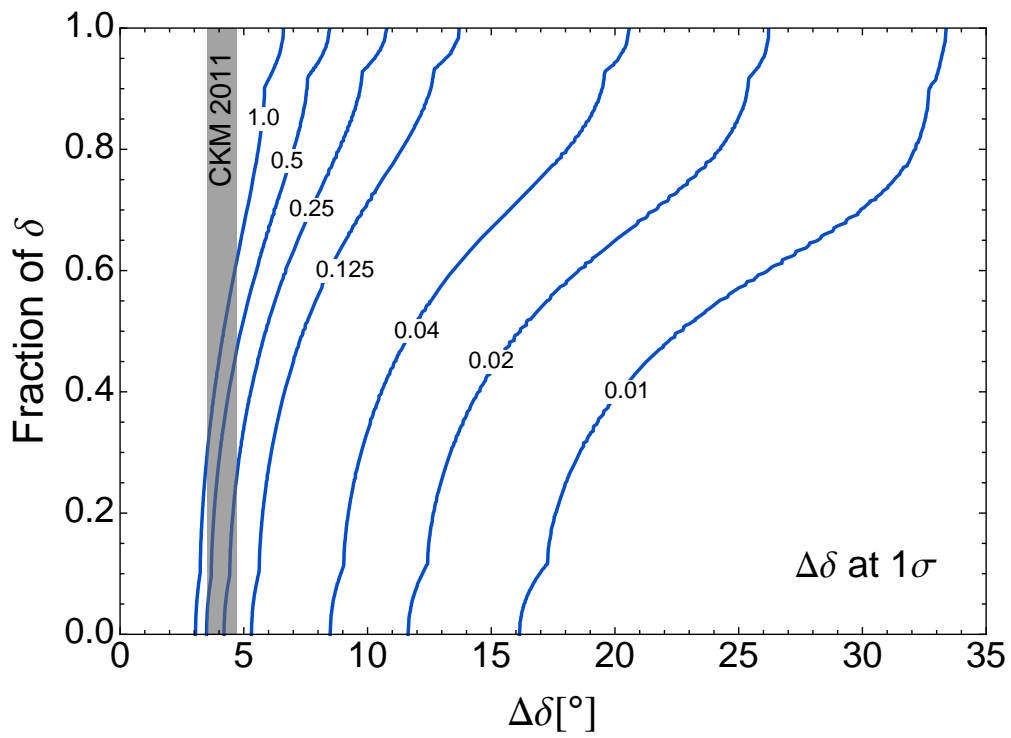


Figure 92: PRELIMINARY – This figure shows the fraction of CP for which a measurement of CP phase δ_{CP} is possible with a certain accuracy at 1σ . The labels correspond the fractional luminosities relative to the full facility, *i.e.* fractions of 10^{21} muons, 100 kt detector and 10 years running time.

C PPEG appendices

Lead author: PH

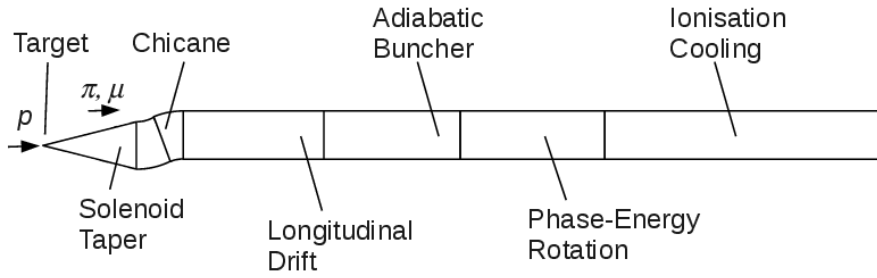


Figure 93: Schematic of the overall front end section.

D The Muon Front End

C. T. Rogers D. Stratakis G. Prior S. Gilardoni D. Neuffer P. Snopok A. Alekou J. Pasternak

The front end is described in outline in Sec. 3.4. In this section some of the details of the lattice simulations are described. Lattice files are available on the launchpad web service [?] either by direct download or using the bazaar distributed version control system [?].

Three simulation codes were used to track the beam in the muon front end. ICOOL version 3.20 [?] and G4Beamline version 2.14 (G4BL) [?] were used to track the front end, assess capture performance and transmission losses. Initial particle distributions and detailed studies of activation in the decay and chicane region were generated using MARS `VERSION`.

D.1 Decay Region

The target is immersed in a 20 T solenoidal field which tapers to 1.5 T over a distance of about 15 m. In this region, the aperture is considered by the front end group to be a volume of rotation with radius r given by

$$r = \frac{75^2 - 300^2}{15000}z + 75^2 \quad (47)$$

where z is the position along the beamline and units are mm. In G4BL this is modelled as a volume of rotation and in ICOOL a series of cylinders are used with inner edges at 5 mm steps in radius.

Both simulation codes generate fields using infinitely thin current sheets, where an analytical solution exists for the generated fields. In G4BL this is handled automatically by the code, given a certain field tolerance. In ICOOL the sheets are generated manually with 5 sheets generated per coil, with current spread evenly across the coil cross sectional area. The nominal coils used in the simulations are outline in table 6.

A cartoon schematic of the decay region, chicane, proton absorber and longitudinal drift is shown in fig. 18

D.2 Particle Selection System

Protons and particles with momentum above 500 MeV/c are rejected from the front end by means of a solenoidal chicane and Beryllium plug. The chicane filters particles with momentum above 500 MeV/c. The Beryllium plug ranges out low energy protons.

D.2.1 Chicane and Proton Absorber Conceptual Design

Given that it is challenging to get good muon transmission over the desired range of momenta, and that both positive and negative muon species need to be captured, a stellarator-type solenoidal chicane is proposed. Solenoidal chicanes induce a vertical dispersion in the beam, resulting in symmetric transmission of both particle charges. Matching from the constant solenoid field of the front end to the bent solenoid field is relatively easy. The main problem with this sort of lattice is that it is not possible to make an open midplane solenoid. Either very high radius superconducting coils with significant shielding or normal conducting coils exposed to beam power in the hundred kW range are required. Clearly these components would become active and it is expected that they would be treated as part of the remote handling facility in the target area.

The addition of a Beryllium proton absorber after the chicane serves to lower the overall energy of particles in the system. This stops almost all of the protons, while leaving most muons in the beam. Increasing the absorber thickness and increasing the chicane angle reduce the good muon yield slightly, while producing a dramatic reduction in the proton beam power escaping the system. Based on that, a 12.5° chicane angle and 100 mm proton absorber thickness were chosen. Some details on optimisation of the particle selection system are given in [?].

D.2.2 Simulation of the Chicane and Proton Absorber in G4BL and ICOOL

The main text describes how the chicane was simulated in G4BL. In ICOOL, the solenoid taper field was cut at 15 m and a constant 1.5 T field was used for the following 4 m match. The chicane was modelled using BSOL model 1, which presents a 1.5 T field along the nominal curved trajectory and a $1/r$ dependence off that axis. Two regions were modelled, one with positive radius of curvature and one with negative radius of curvature. No end field was used for the chicane, leading to a discontinuity in field lines at the interfaces between the BSOL regions.

D.3 Chicane Energy Deposition Studies

The initial configuration of the chicane as simulated in MARS15 [253] and shown in fig. 94 starts at the end of the target/capture region, 30 meters downstream from the target, which corresponds to zero in TODO: Check should be 20m Fig. 94. Field maps for MARS simulations were generated by G4BL [?]. Coils have inner radius of 43 cm, outer radius of 53 cm, length of 18 cm, with on-axis field of 1.5 T throughout the channel. Either copper or a standard MARS material SCON consisting of 90% superconductor (60% Cu and 40% NbTi) and 10% Kapton ($C_{22}H_{10}N_2O_5$) are used for simulations. The proton absorber is a 10 cm Be disk of outer radius 30 cm.

Two conceptual designs for managing the radiation losses in the chicane are available and both are discussed here. The chicane could be implemented using normal conducting copper coils with inorganic insulators to accommodate the significant radiation load. Alternately, the chicane could be implemented using superconducting coils with significant shielding inside the coils.

The case of a chicane without shielding is used as a reference. In this case the peak total deposited power density in the coils is 15.8 mW/g, while a common limit for superconducting coils is 0.15 mW/g. In terms of peak linear power density for the geometry described above that corresponds to 42.6 kW/m for Cu coils, see fig. 95, or 33.3 kW/m for SCON coils. That is significantly larger than the typical 1 W/m limit for hands-on operation. Since these numbers represent averages over the whole coil, a more thorough analysis is required by subdividing the coils into smaller segments in order to localize energy deposition peaks.

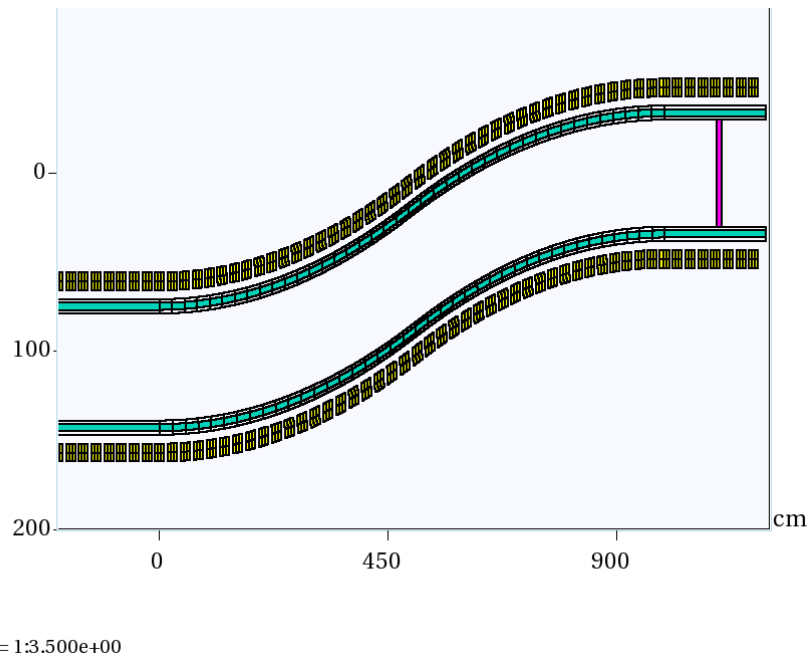


Figure 94: Chicane as simulated in MARS, top view. Yellow: solenoidal coils, cyan: pure W shielding, gray: SS beam pipe and shield pipe around W shield, magenta: 100 mm Be proton absorber.

D.3.1 MARS simulations, ROOT framework

A recently developed ROOT-based geometry framework for MARS was used for modelling the chicane. The TGeoCtube elementary volume (cut tubes with arbitrary entrance and exit angles) was used to generate segments of the toroidal beam pipe. The chicane as defined using ROOT is shown in fig. 96.

D.3.2 Coil segmentation

The energy deposition in the chicane is highly asymmetric. Dispersion is excited vertically for particles of intermediate momenta, while high momenta particles are lost transversely on the inside of the bend. Few particles are expected to be lost on the outside of the bend.

In order to correctly account for this effect each coil was represented as a set of segments: 12 azimuthal segments (uniform, 30° each), 2 radial segments, and 3 longitudinal segments, for a total of 72 segments per coil. As expected, even though the average energy deposition per coil is reduced dramatically with the introduction of shielding, there are peaks in the individual segments.

D.3.3 Shielding effect: alternative layouts

The beam pipe in the chicane is wider than in the rest of the front end to permit the dispersion to develop. Two models for beampipe aperture were considered here:

- Bore radius of 42 cm with shielding of radial thickness 35 cm everywhere in the chicane.
- Non-uniform shielding with 30 cm of shielding and bore radius of 30 cm away from the center of the chicane and 40 cm of shielding and bore radius 42 cm around the center of the chicane where the beam is wider.

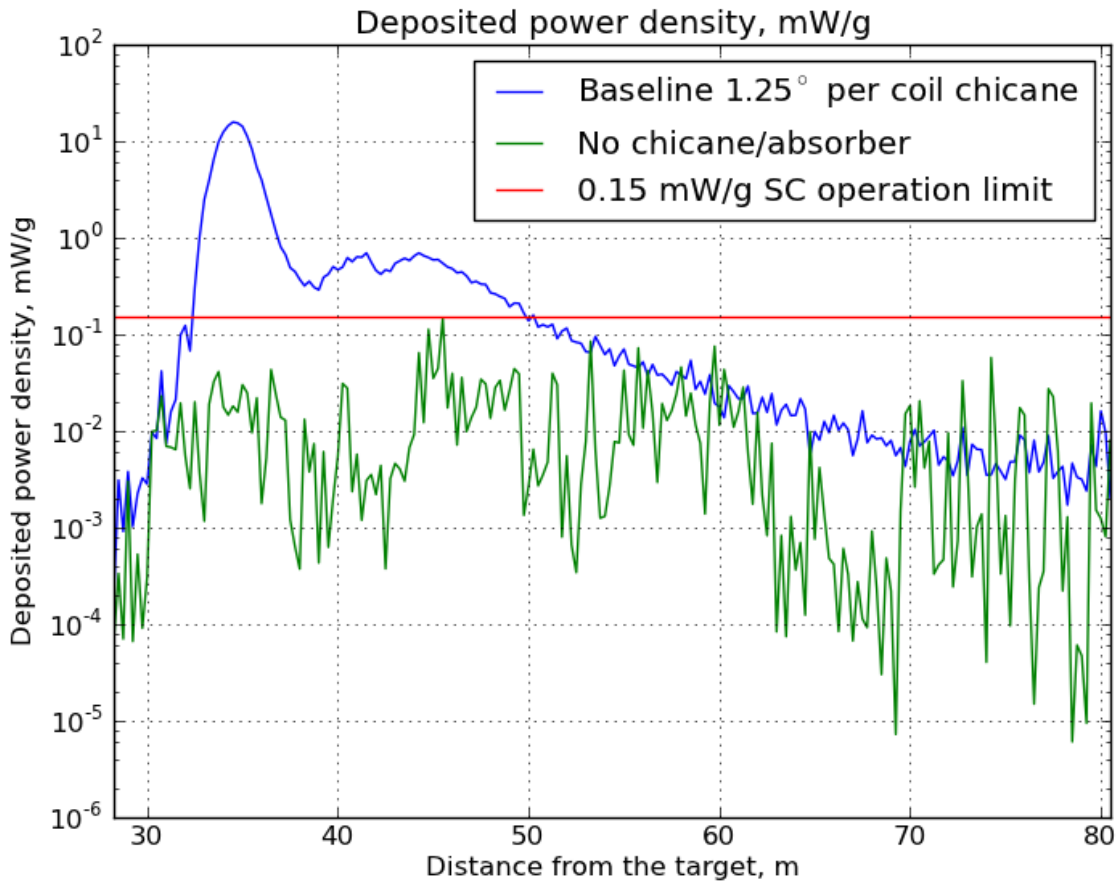


Figure 95: Energy deposition in the coils of the chicane with no shielding, mW/g, nominal 12.5° chicane, used as a reference.

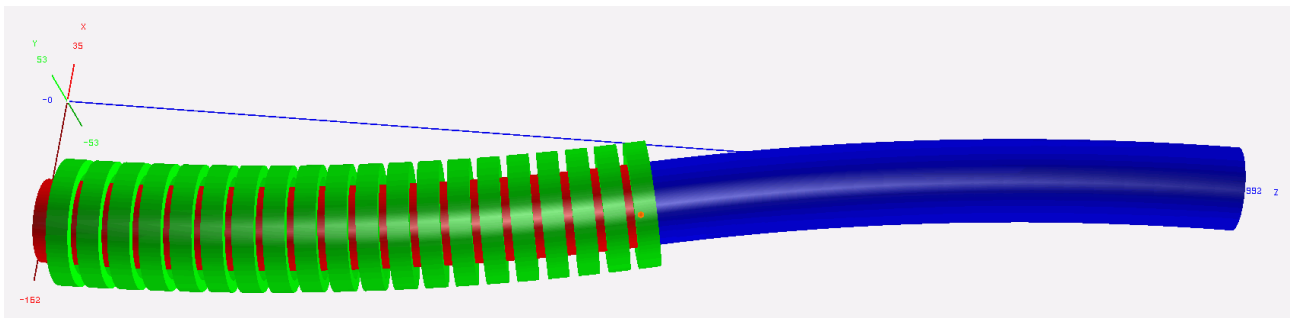


Figure 96: Chicane geometry as defined using ROOT. Red: shield, bend in; blue: shield, bend out; green: half of all the solenoidal coils. Some coils have been removed from the visualisation to display the beam pipe.

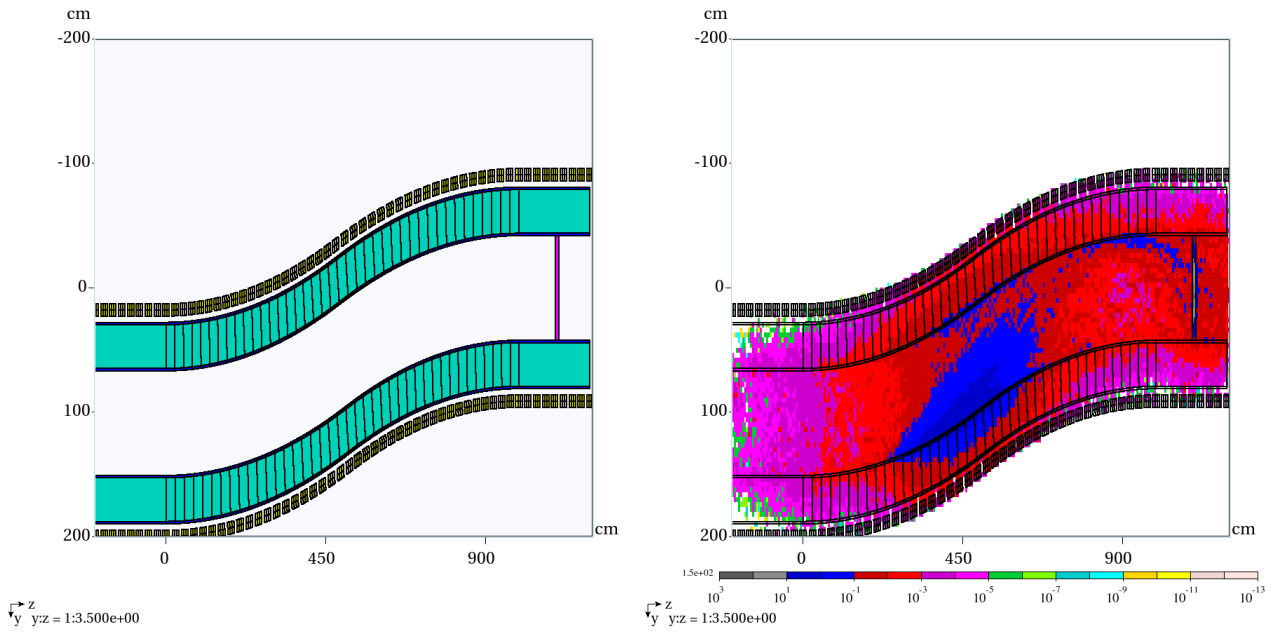


Figure 97: Layout of the chicane with uniform shielding of 35 cm, constant bore radius of 42 cm accommodates beam widening at the center of the chicane. Total power density plot on the right shows that power deposition in the coils is of the order of 0.1 mW/g; however, the quantitative segmented coil analysis shows several peaks larger than the 0.15 mW/g limit.

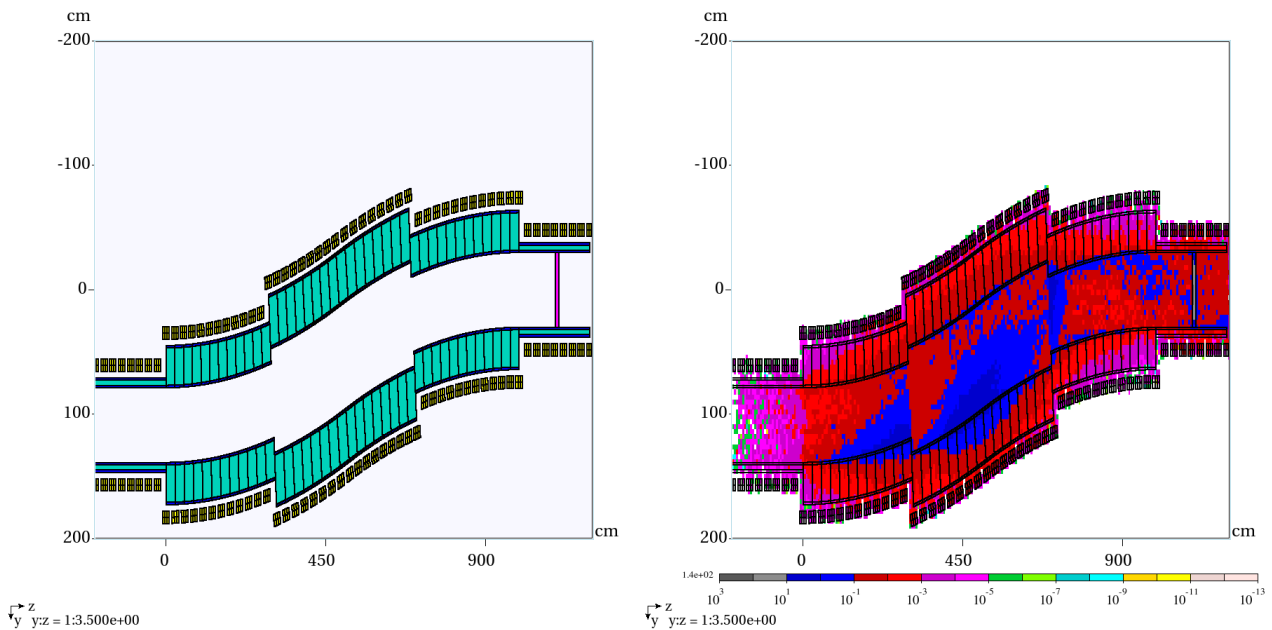


Figure 98: Layout of the chicane with non-uniform shielding of 40 cm around the center of the chicane with a constant bore radius of 42 cm to accommodate beam widening, 30 cm elsewhere in the chicane with a constant bore radius of 30 cm to keep the coil radius smaller. Total power density plot on the right shows that power deposition in the coils within the chicane is of the order of 0.1 mW/g; however, the quantitative segmented coil analysis shows several peaks larger than the 0.15 mW/g limit.

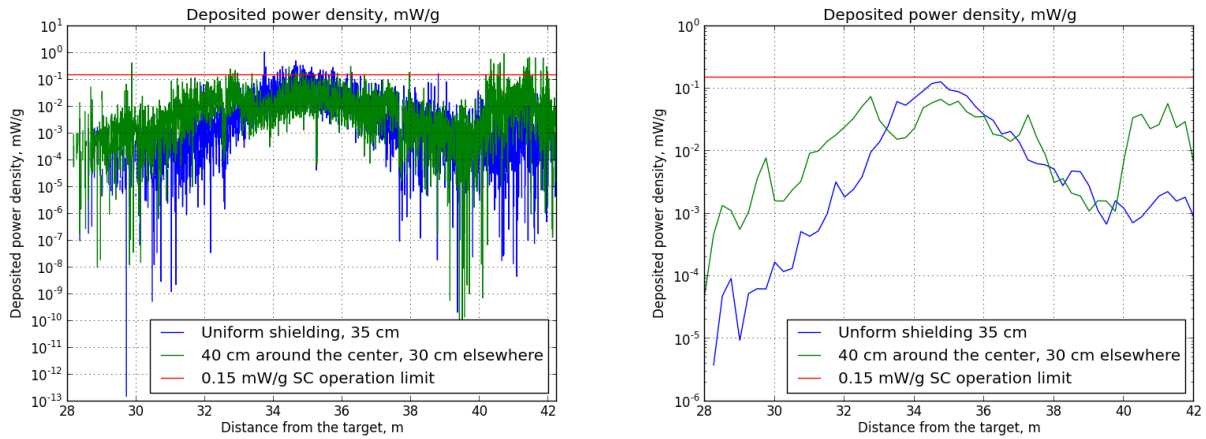


Figure 99: Left: maximum deposited power density for segmented coils, showing a few peaks larger than the 0.15 mW/g limit. Right: average deposited power density per coil is within the 0.15 mW/g limit.

The chicane layout and the total deposited power density are shown in Fig. 97 for the case of the uniform shielding, and in Fig. 98 for the case of the variable thickness shielding. The density of W is reduced to 60% to account for the tungsten bead packing fraction. The total deposited power density peaks at 1 mW/g for the uniform shielding as represented by the blue line in fig. 99 and at 0.4 mW/g for the non-uniform shielding as represented by the green line in Fig. 99. Where $z \geq 40$ m, electromagnetic showering from the proton absorber produces some energy deposition and additional shielding needs to be considered. The average power density per coil is lower than the 0.15 mW/g limit for the superconducting coils for both cases.

D.3.4 Remaining beam power

The beam power that remains in the beamline downstream of the initial particle selection scheme is shown in fig. 100 for different particle species. The particle selection system is successful at removing the large majority of proton beam power from the beam, although a noticeable fraction of particles do remain.

The remaining protons originate from a few high energy particles which seem to scatter through the chicane. The energy distribution of different beam components before the particle selection system, after the particle selection system and at the end of the cooling channel is shown in fig. 101.

D.4 Modifications to the RF capture system

The RF capture system is designed to capture the beam into RF buckets and rotate the longitudinal phase space so that buckets have the same energy. The conceptual design of the system was outlined in [?]. Here we describe the parameters of the lattice updated for the modified longitudinal distribution introduced by the particle selection system.

As relevant to the RF capture system, the main effect of the particle selection system is to introduce a mean energy loss of 34 MeV/c for the higher momentum reference particle with initial momentum 270 MeV/c and 41 MeV/c for the lower momentum reference particle with initial momentum 185 MeV/c. This introduces a translation and a slight shear in the longitudinal phase space. A modified capture system is required to capture this distribution efficiently.

Additionally, the position of the RF cavities has been modified to place them every 0.75 m with power feeds envisaged to pass between individual magnet coils.

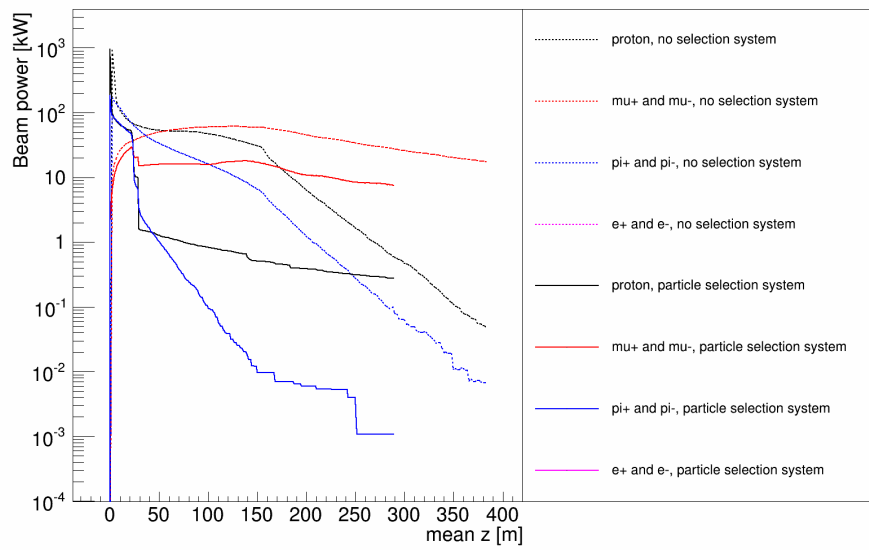
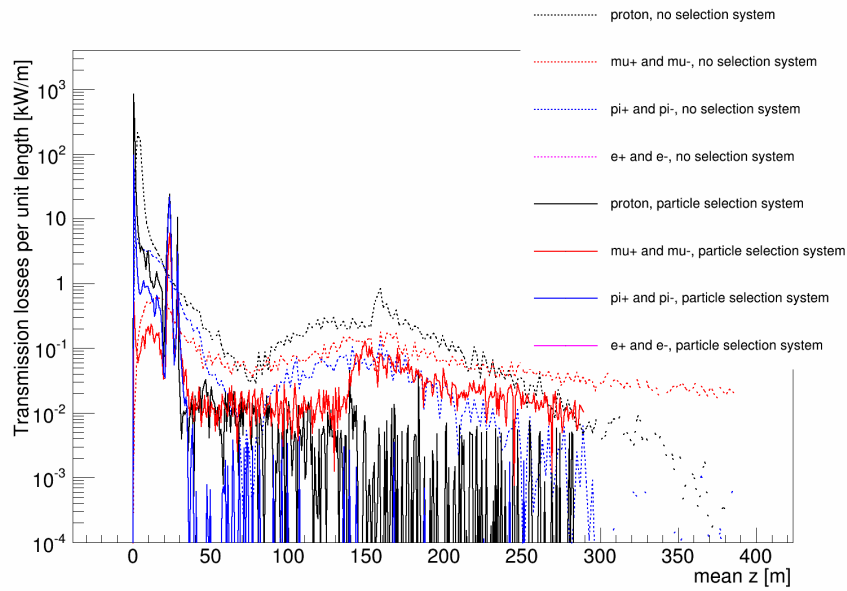


Figure 100: (top) Transmission losses and (bottom) remaining beam power following the particle selection system. Simulation in G4BL 2.14.

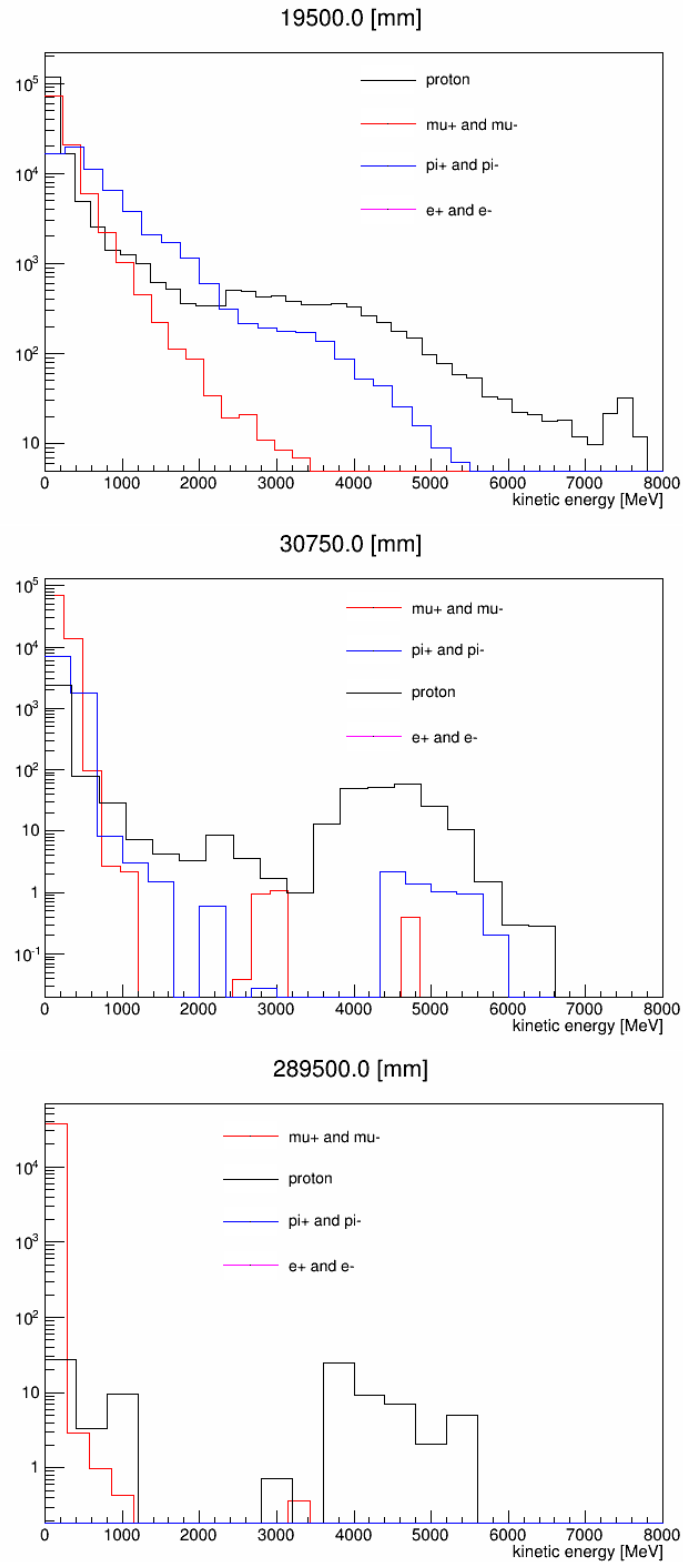


Figure 101: Remaining beam energy, separated by particle type, for position (top) before the particle selection system, (middle) after the particle selection system and (bottom) at the end of the cooling channel. The exact z-position is shown in the plot titles. Simulation in G4BL. 2.14.

D.4.1 Longitudinal Drift

In order to bunch and phase rotate the beam, it is necessary to make a longitudinal drift to allow a time-energy correlation to develop. In ICOOL, a constant 1.5 T region with beam pipe radius 0.3 m and length 40.80 metres is used.

A slightly more complicated model is required in G4BL due to the way the geometry is handled. The coil model as outlined in the chicane section is extended for 4.5 m after the end of the chicane. The last 2.5 m of this region is written to a field map file; and then this file is read into G4BL with a scale factor of -1, providing cancellation of the last 2.5 m of field. This creates an abrupt stop to the field map at the nominal end of the particle selection system, some 2 m downstream of the equivalent point in ICOOL. The drift and RF capture can then be simulated using an idealised 1.5 T field.

D.5 Ionisation Cooling Channel

The ionisation cooling channel design is essentially the same as in the Feasibility Study 2A documentation [?]. The cell length has been made longer, to provide space for insulation and support structure for the cooling channel. Additionally, RF and absorbers have been removed from every sixth cell to provide space for bellows.

D.5.1 Matching from RF capture to cooling

The quality of the transverse match between the RF capture system and the cooling channel can be observed in fig. 102. Some large beta function oscillations and emittance growth can be seen at the interface between the two systems, and this is likely to be due to transverse mismatch in some portion of the phase space occupied by the beam.

Long term beta-beating is observed in the cooling lattice. The origin of the beta-beating is likely to be a longitudinal mismatch which leads to some momentum oscillation within the cooler and a corresponding oscillation in the beta function.

The effect of the longitudinal mismatch on the longitudinal phase space of the beam can be seen in fig. 103. There is a significant longitudinal emittance growth in the beamline. No longitudinal match has been attempted between the cooling channel, and this could likely reduce the emittance growth. There are also significant longitudinal-transverse correlations in the beam that may lead to high transverse amplitude muons becoming dephased from the RF and lost.

D.6 Summary

The Neutrino Factory muon front-end captures a substantial proportion of the muons produced by the Neutrino Factory target. Longitudinal capture is achieved using a buncher and energy-time phase-rotation system while transverse capture is achieved using a high field solenoid adiabatically tapered to 1.5 T and enhanced by ionisation cooling.

Technical risks to the muon front-end are presented by the requirement for high peak RF fields in the presence of intense magnetic fields and irradiation of the accelerator hardware due to uncontrolled particle losses. Strategies have been outlined by which these risks can be mitigated. Overall, the muon front-end increases the capture rate of muons in the nominal accelerator acceptance by a factor 10.

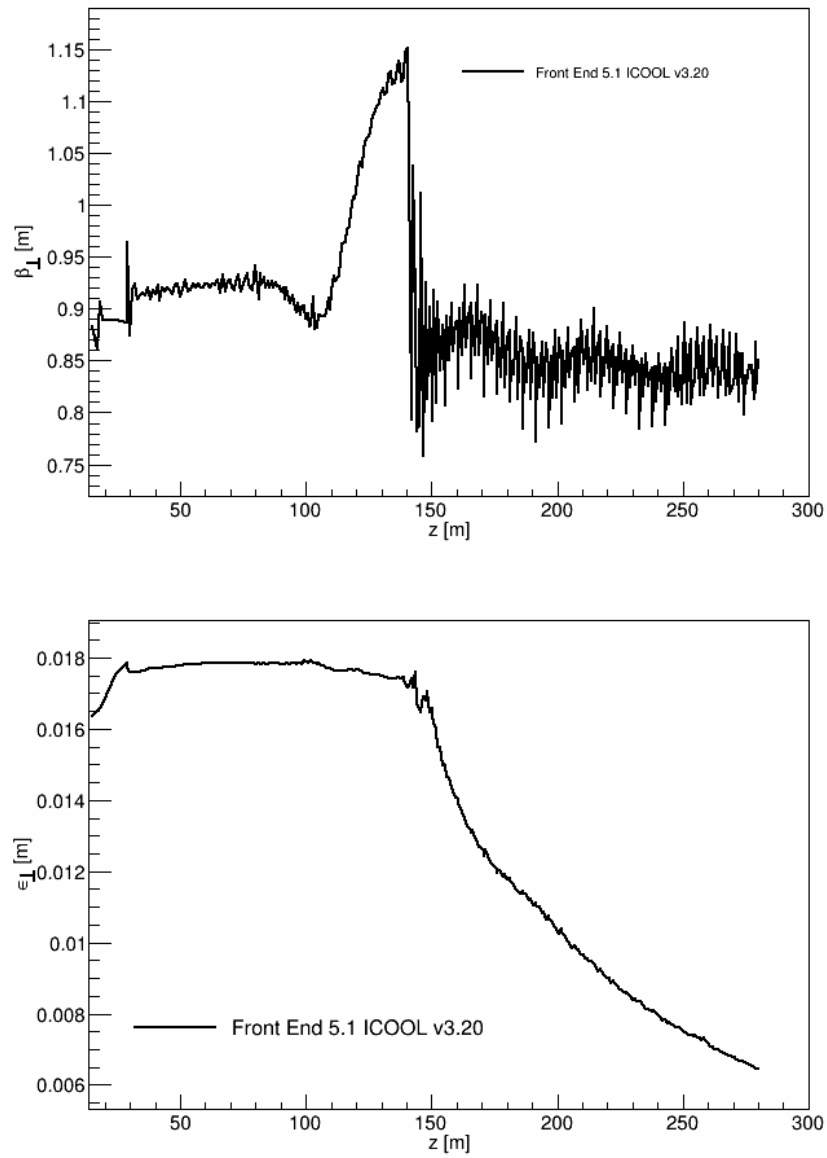


Figure 102: Transverse beam optics following the RF capture system: (top) optical 4D β function [m] (bottom) 4D normalised emittance

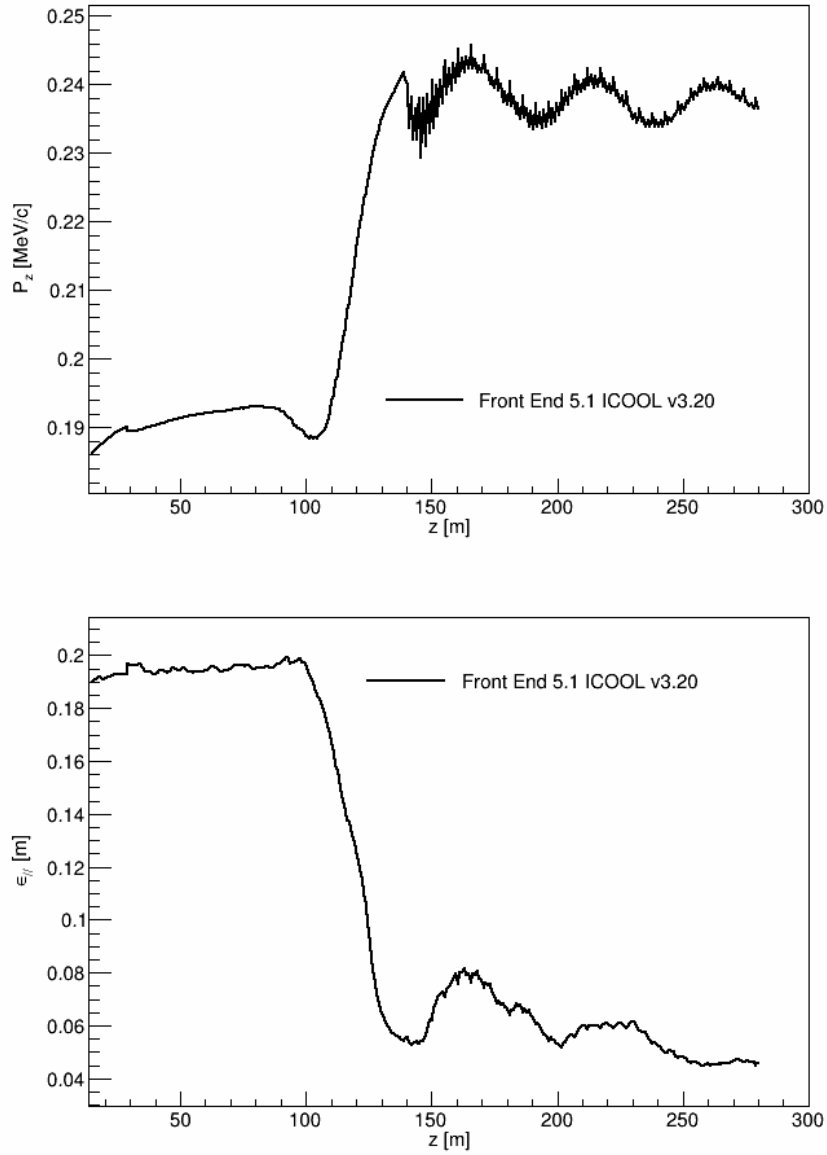


Figure 103: Longitudinal beam parameters following the RF capture system (top) mean longitudinal momentum and (bottom) longitudinal emittance.

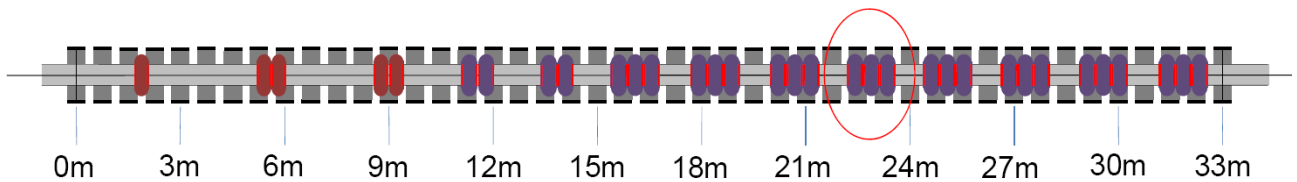


Figure 104: Buncher initial schematic.

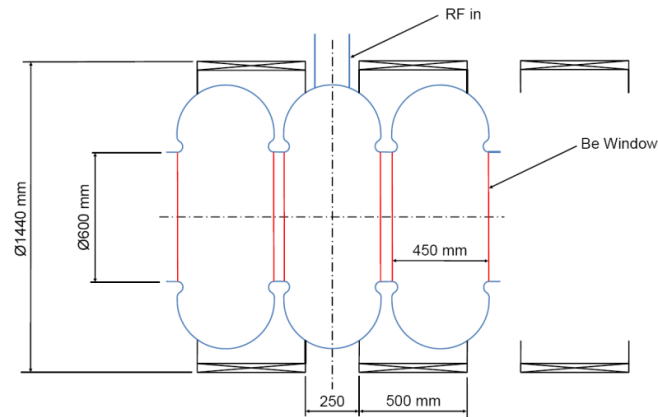


Figure 105: Enlarged illustration of encircled area in Fig. 104.

E Front End Engineering

We produced mechanical designs of modules for the bunching, phase rotation, and cooling stages of the front end. All systems consist of RF cavities within a magnetic field. For the buncher and phase rotation sections, that field is a roughly constant 1.5 T, whereas in the cooling the field alternates in sign from one cell to the next. All solenoids are superconducting, while the RF cavities are room temperature with frequencies varying between 201 and 359 MHz. The cavity apertures are closed with beryllium windows are used, similarly to the buncher section, to achieve high gradients. This becomes more challenging as gradients increase in the buncher section, and in the phase rotation and cooling sections, due to the difficulty of removing heat from the windows.

E.1 Buncher and Phase Rotation

An initial design proposal for an earlier version of the buncher lattice is shown in Fig. 104 with a more detailed depiction of the encircled area in Fig. 105. Due to low gradients required at the beginning of the buncher, fewer cavities with a high gradient were used instead of many cavities with a low gradient. The required voltage increases down the line, and the cavities are grouped into multi-cell modules as this occurs.

The phase rotation has a similar configuration, but due to the consistently high gradient required, an arrangement of cavities and coils shown in Fig. 106 was proposed.

The coil configurations depicted in these figures are in practice not feasible due to the conflicts between the solenoid coils and the RF input coupler. An engineering feasibility study provided a proposal as depicted in Fig. 107. This first iteration modified the schematic to include the RF coupler access to the individual cavities. A bellows was included in every cell to allow cavities to be assembled one-by-one. The design also permits a lattice cell to lack a cavity (depicted to the right of Fig. 107) so that a module of a group of cavities and coils can be removed without disassembling the entire beam line. The coil geometry for this new configuration is shown in Table 36. The design increases the distance between the coils to accommodate the bellows without

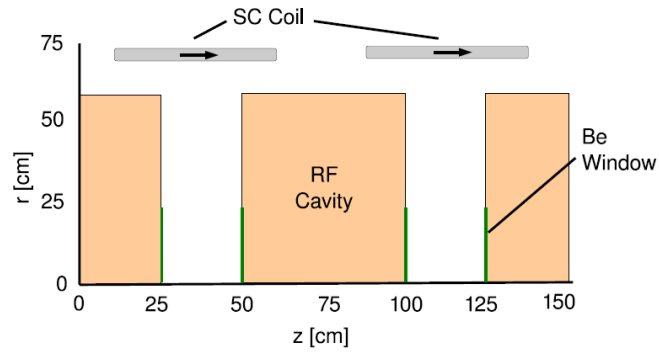


Figure 106: depicting the theoretical layout of the phase rotation module.

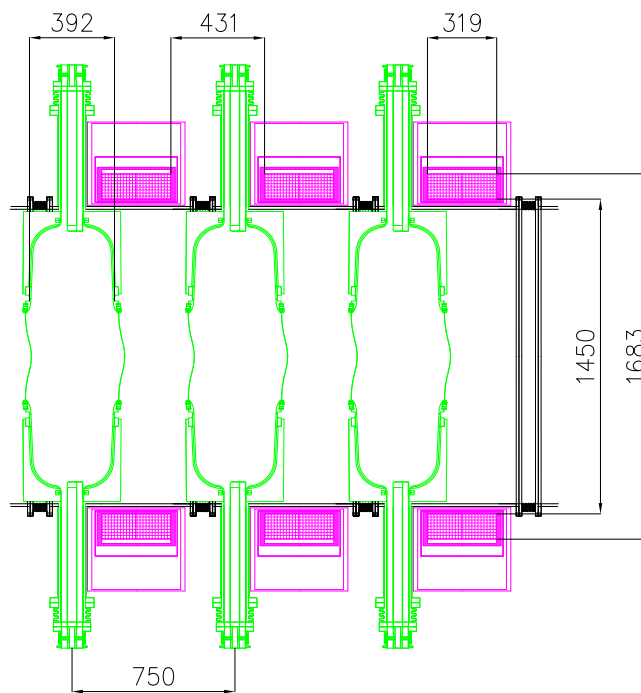


Figure 107: A buncher cell CAD cavity/coil model based on MICE.

Table 36: Solenoid coil parameters for the theoretical lattice design (Original), the engineering design with bellows in every cell (Bellows), and the engineering design with bellows only in cells that are missing cavities (Module). The current density in the original coil was 47.5 A/mm².

	Original	Bellows	Module
Length (cm)	50	31.9	50
Inner radius (cm)	68	72.5	72.5
Radial thickness (cm)	4	11.65	11.65

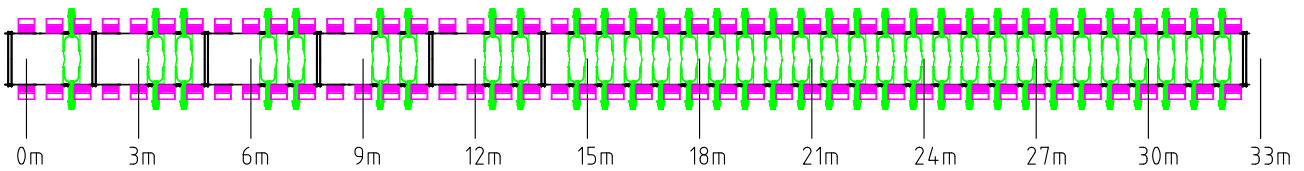


Figure 108: Buncher section with the cell design containing a bellows in each lattice cell.

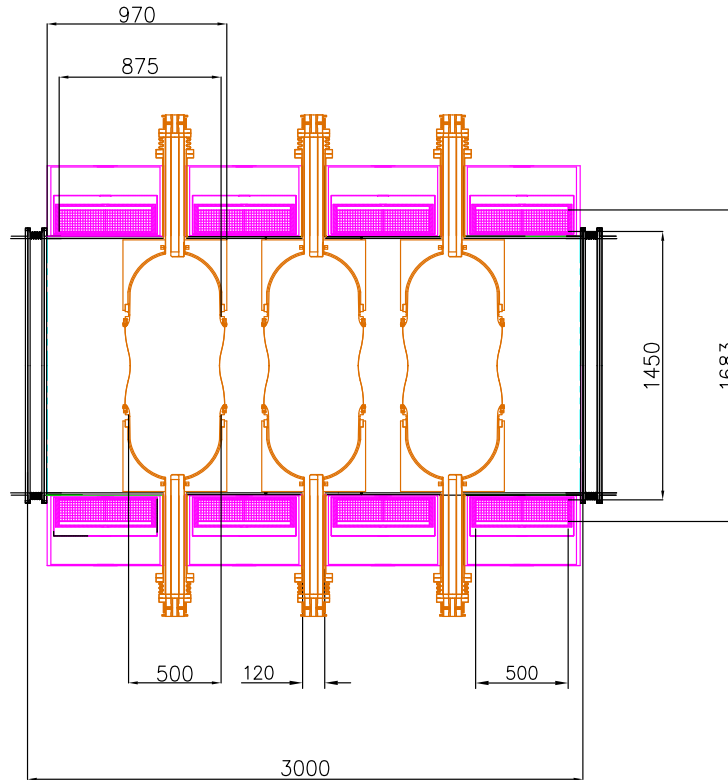


Figure 109: depicting a 3m phase rotation module

changing the 0.75 cm cell length. The buncher lattice in Fig. 104 with these new cells is depicted in Fig. 108. Breaking the design into 3 or 4-cell modules is straightforward at the beginning since there is significant space between cavities at the beginning of the buncher in the earlier design. However, in the latter part of the buncher, splitting into modules becomes more difficult: Figure 108 depicts a large number of cavities in a single module, which may be impractical.

It is preferable to have the cavities grouped into modules, even in the region with higher gradients. Every module can be removed for maintenance or replacement purposes to ensure minimum machine down time. Figure 109 depicts such a module with 4 lattice cells and 4 cavity cells. The disadvantage of this arrangement, in particular for the phase rotation, is that the requirement to periodically remove RF cavities reduces the average RF gradient available. However, raising the 13 MV/m gradient in the phase rotation design to 16 MV/m (the gradient in the cooling), and using modules with 5 lattice cells and 4 cavity cells, gives an essentially identical average RF gradient. The cavity modules can be strung together to increase cost effectiveness further by a common cryogenic feed. A more detailed study will need to be carried out which leads to points being addressed such as additional couplings, enclosure vessels, access areas for instance.

Note that the lattice designs described in appendix BLAH have a constant 1.5 T solenoid field, and have

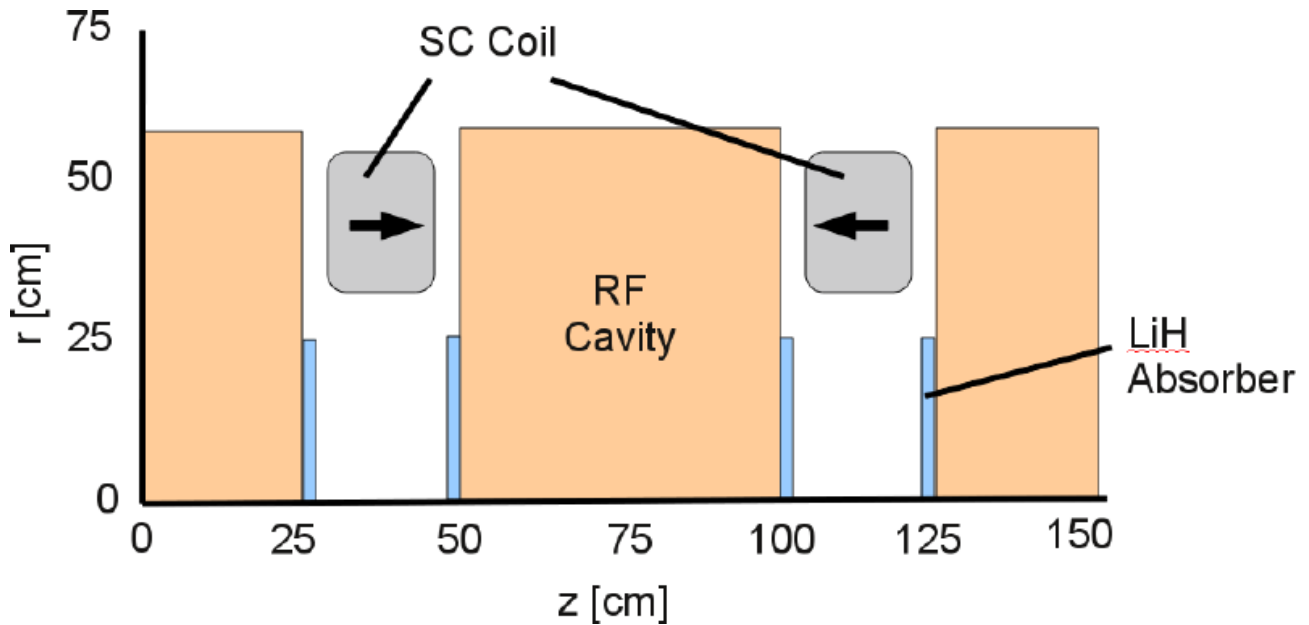


Figure 110: Illustrating the theoretical schematic for a two cell model

Table 37: summary of coil parameters

Length (cm)	15
Inner Radius (cm)	70
Radial thickness (cm)	15
Current Density (A/mm^2)	107

cavities in each cell, even at the beginning of the buncher. Future studies should simulate the design described here to determine the impact of the non-constant solenoid field and the missing cavities on the beam dynamics.

E.2 Cooling

The ionisation cooling channel cells differ from those in the buncher and phase rotator in that the solenoids alternate in sign from one cell to the next, the solenoids have a smaller radius, and the cavities have a LiH absorber at their ends. The cavities are 201 MHz with a gradient of 16 MV/m.

Fig. 110 illustrates the cooling cell layout for the original proposal. This schematic indicates the components required and their relative position. Table 37 gives the solenoid coil parameters.

As for the buncher and phase rotation, the cavities should be grouped into individually-removable modules. We designed such a module, depicted in Fig. 111. The module shown contains 7 coils and 6 cavities is provisionally. From the original specification, the lattice cell increased from 75 cm to 86 cm, but the coil geometry remained the same. The required bellows at the left hand side is the width of one cavity to maintain beam dynamics and provide access to mechanical systems including the vacuum arrangement.

This design is being used in the lattice described in Section XXX, except modules of 6 coils and 5 cavities are used.

The technology and design solution are comparable to the MICE RF Coupling Coil. Fig. 112 demonstrates the size in context. The MICE RFCC module is being built and commissioned at the time of writing.

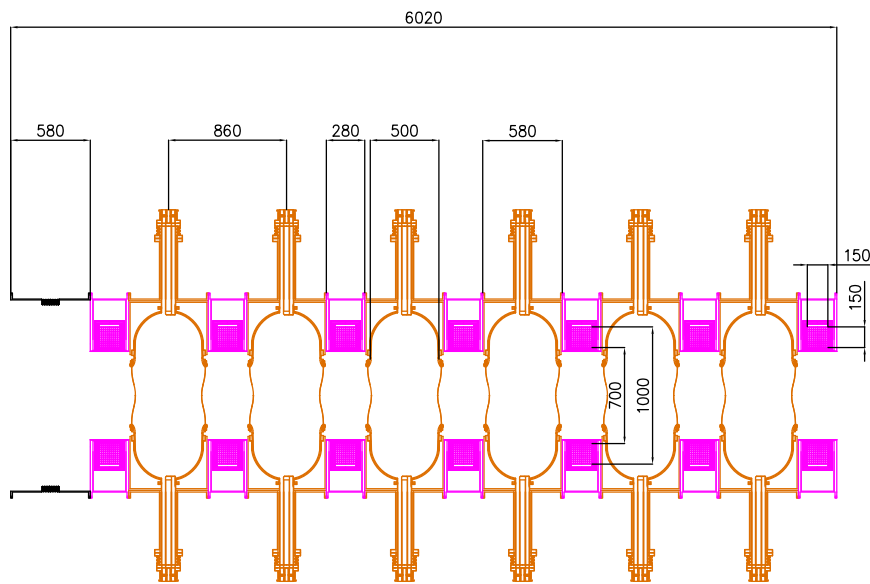


Figure 111: A 6 cavity and 7 coil module. The cavity is 50 cm long. Each solenoid coil cross-section is 15 cm × 15 cm. The cell length is 86 cm instead of 75 cm to accommodate the required vacuum vessels. The vacuum chamber in the empty cell to the left has a bellows at its center.

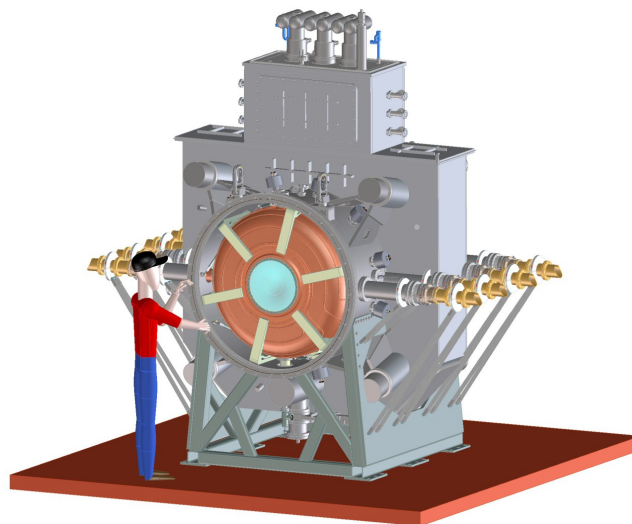


Figure 112: shows a CAD model for the MICE RF Coupling Coil

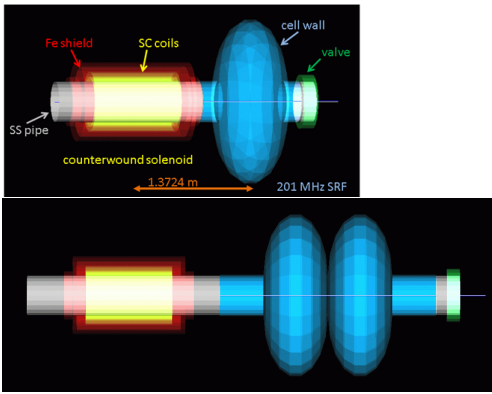


Figure 113: Layout of the two cryo-module types: short cryo (top), medium cryo (bottom). They share the same solenoid and cavity type throughout in this study.

F Acceleration Lattice Details

F.1 Overall Lattice Description

The linac is required to accelerate 0.244 GeV muons coming from the muon front-end to 0.8 GeV and, given these relatively low energies, solenoidal transverse focusing has been chosen, so that the beam preserves its initial horizontal-vertical phase-space coupling. The transfer to RLA I is performed through the Double Arc Chicane, which consists of a vertical dipole spreader (at the beginning), a sequence of horizontally bending magnets (horizontal arc), and a vertical dipole combiner (at the end). Here, quadrupoles were chosen for transverse focusing [254]. In this manner both positive and negative muons can be transferred, while keeping RLA I at the same height as the linac, a decision taken to simplify the civil engineering. With the beam now being relativistic, quadrupole focusing in a FODO-lattice is preferred for the Double Arc Chicane. Entering RLA I, the beam performs 4.5 passes at an average gain of 0.45 GeV/pass with an excursion along the return arcs after each pass. Single-cell, superconducting cavities provide acceleration along RLA I while transverse focusing is achieved by quadrupoles in a FODO arrangement along RLA I and its arcs. Similarly, through another Double Arc Chicane, the 2.8 GeV beam is transferred to RLA II where it again performs 4.5 passes, but now at an average gain of 1.6 GeV/pass.

For the remainder of this section, we will describe in detail the above beam lines one-by-one.

F.2 Pre-linac

A single-pass linac raises the total energy from 0.244 GeV to 0.8 GeV. This makes the muons sufficiently relativistic to facilitate further acceleration in the RLA. The initial phase-space of the beam, as delivered by the muon front-end, is characterized by significant energy spread; the linac has been designed, so that it first confines the muon bunches in longitudinal phase-space, then adiabatically super-imposes acceleration over the confinement motion, and finally boosts the confined bunches to 0.8 GeV. The Pre-linac uses counter wound, shielded superconducting solenoids and 201 MHz superconducting cavities. It is configured with two types of cryomodules, both with a bore radius of 23 cm. The first is a short-cryo (3 m long) with a single RF cell, while the second is a medium-cryo (5 m long) with a double RF cell. G4beamline [255] model of both style cryo modules is illustrated in Fig. 113.

To achieve a manageable beam-size in the front-end of the linac, short focusing cells are used for the first

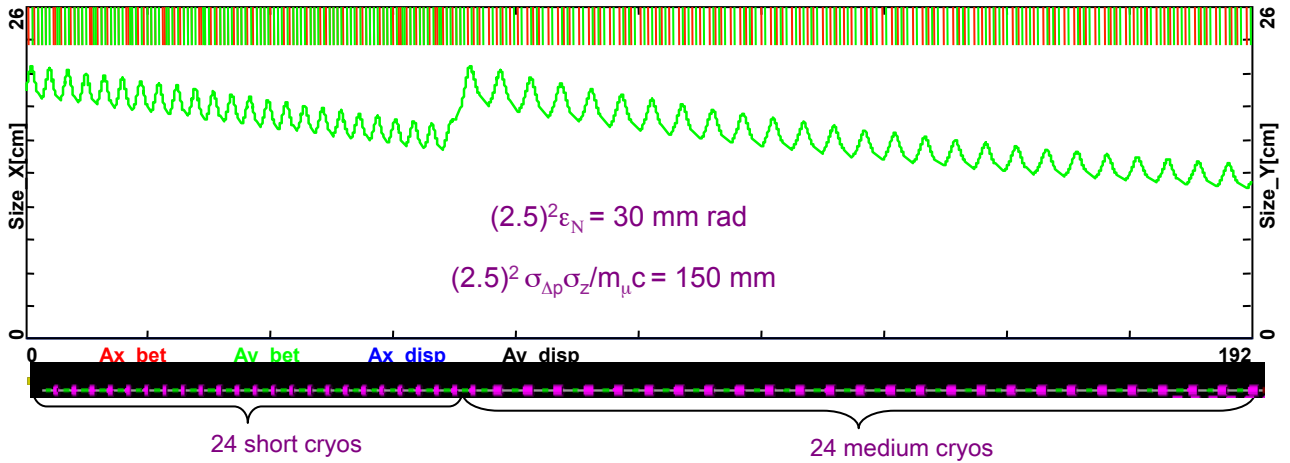


Figure 114: Transverse FOFO optics of the entire linac in terms of the beam envelope at 2.5σ ; the upper and middle periodic sections are uniformly matched at the junction.

24 cryo-modules [256]. The beam size is adiabatically damped with acceleration, allowing the short cryo-modules to be replaced with again 24 medium length cryo-modules. Consequently, the linac was split into two consecutive sections (referred as: the upper and middle linac sections) each section being built of a particular type of cryo-module as shown in Fig. 113. Each linac section is configured with periodic FOFO cells, matched at the section junctions [257], as illustrated in Fig. 114. Periodicity within each section is maintained by scaling the solenoid fields in consecutive cryo-modules linearly with increasing momentum as summarized in Table 38.

One of the main requirements of the single-pass pre-accelerator linac is to compress adiabatically the longitudinal phase-space volume in the course of acceleration. The initial longitudinal acceptance of the linac (chosen to be 2.5σ) calls for “full bucket acceleration”; with an initial momentum acceptance of $\Delta p/p = \pm 17\%$ and a bunch length of $\Delta \phi = \pm 102^\circ$ (in RF phase). To perform adiabatic bunching one needs to drive rather strong synchrotron motion along the linac. The profile of the RF-cavity phases is organized so that the phase of the first cavity is shifted by 73° (off crest) and then the cavity phase is gradually changed to zero by the end of the linac, see Table 38 and Fig. 115a.

In the initial part of the linac, when the beam is still not relativistic, the far-off-crest acceleration induces rapid synchrotron motion (one full period, see Fig. 115c), which allows bunch compression in both bunch-length and momentum spread as illustrated in Fig 115.

To maximize the longitudinal acceptance, the initial position of the bunch is shifted relative to the center of the bucket, to keep the beam boundary inside the separatrix [258], as illustrated in Fig. 115d. The synchrotron motion also suppresses the sag in acceleration for the bunch head and tail. In our tracking simulation [259] we have assumed a particle distribution that is Gaussian in 6D phase space with the tails of the distribution truncated at 2.5σ , which corresponds to the beam acceptance. Despite the large initial energy spread, the particle tracking simulation through the linac does not predict any significant emittance growth [259]. Results of the simulation are illustrated in Fig. 116, which shows the longitudinal phase-space at the end of the linac as simulated by a simple matrix based code OptiM [260] (Fig. 116b). One can see good agreement between the design phase-space (red contour) and the results of realistic multi-particle tracking.

Table 38: Linac parameters for short cryomodules (left) and medium cryomodules (right). RF phases are degrees from crest. Solenoid fields alternate sign. Kinetic energy is at the end of the module.

Kinetic			Kinetic		
RF phase (deg.)	Field (T)	Energy (MeV)	RF phase (deg.)	Field (T)	Energy (MeV)
73.34	1.06	141.37	45.51	1.37	279.87
72.19	1.08	144.55	43.69	1.43	295.74
71.05	1.09	147.93	41.89	1.49	312.10
69.90	1.11	151.52	40.11	1.56	328.93
68.75	1.13	155.31	38.36	1.63	346.21
67.61	1.15	159.30	36.63	1.70	363.92
66.46	1.17	163.50	34.93	1.77	382.02
65.32	1.19	167.90	33.26	1.84	400.51
64.17	1.22	172.50	31.62	1.91	419.35
63.03	1.24	177.29	30.00	1.99	438.52
61.82	1.26	182.30	28.41	2.06	458.00
60.68	1.29	187.50	26.87	2.14	477.78
59.53	1.32	192.90	25.35	2.21	497.82
58.38	1.34	198.49	23.86	2.29	518.12
57.24	1.37	204.27	22.41	2.37	538.64
56.09	1.40	210.25	21.00	2.45	559.38
54.95	1.43	216.41	19.62	2.53	580.30
53.81	1.47	222.75	18.28	2.62	601.41
52.67	1.50	229.27	16.97	2.70	622.68
51.54	1.53	235.98	15.70	2.78	644.09
50.41	1.56	242.86	14.47	2.87	665.63
49.30	1.60	249.91	13.29	2.95	687.28
48.18	1.64	257.13	12.13	3.03	709.04
47.07	1.67	264.51	11.02	3.12	730.89

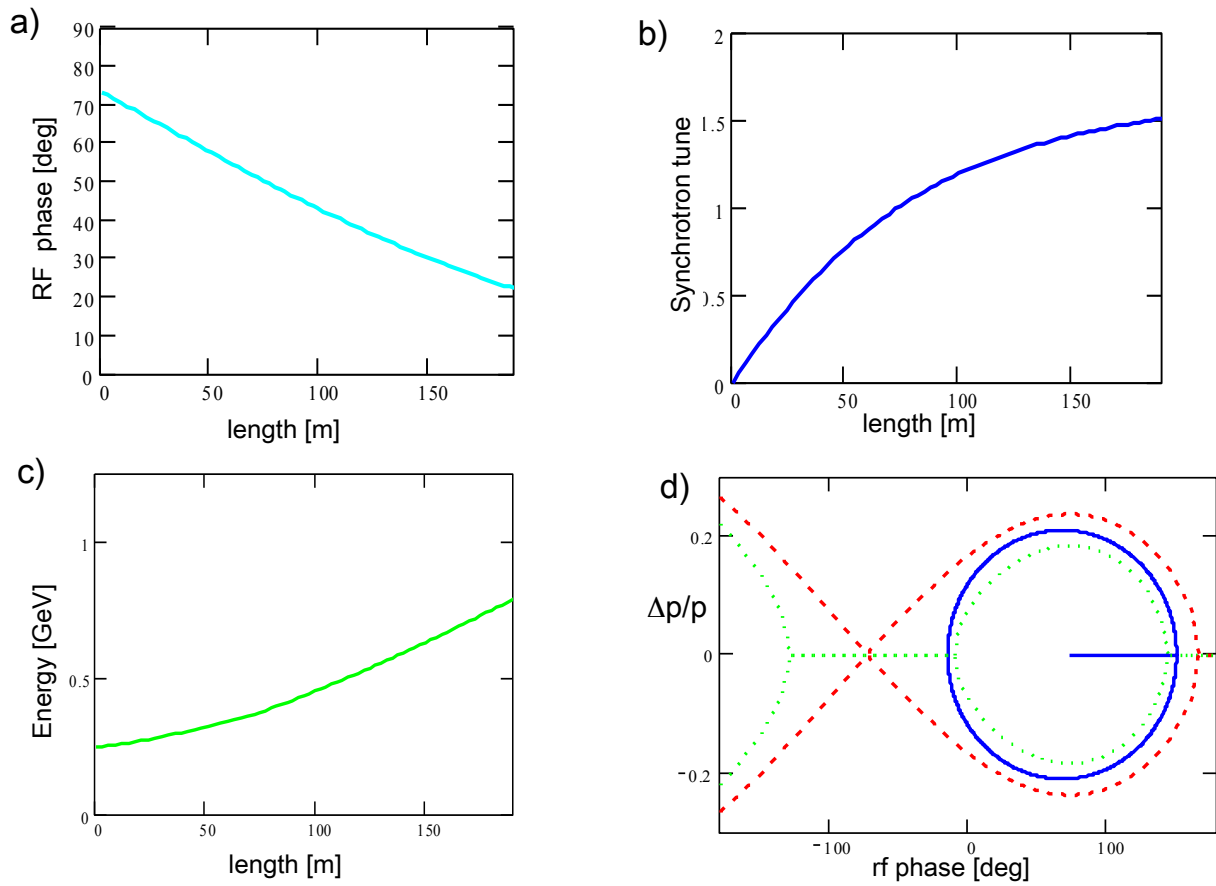


Figure 115: Longitudinal matching of a single-pass linac: a) The bunch starts far off-crest to capture the beam at low energy and then moves to the crest as the energy increases and the longitudinal acceptance improves. b) The synchrotron phase advances by 1.5 of a full period from the beginning to the end of the linac. c) The rate of energy gain increases as the bunch moves closer to crest. d) Longitudinal acceptance matched inside the separatrix and optimized for “full bucket” acceleration.

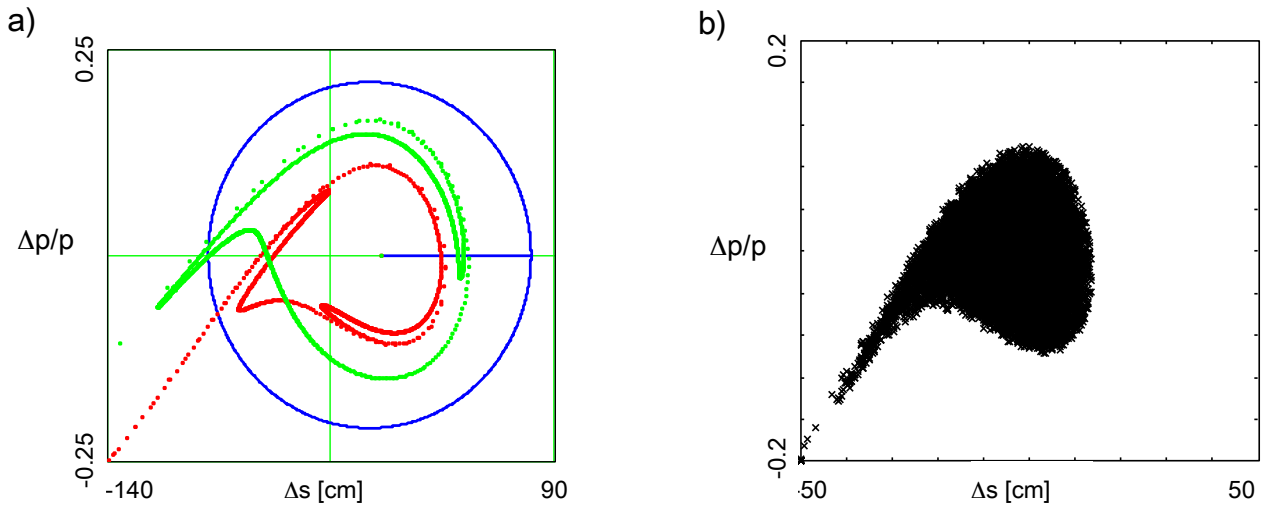


Figure 116: Longitudinal phase-space compression along the linac: a) Evolution of the initial acceptance at the beginning of the linac (blue circle), transformed into the green contour at the middle of the linac (after 24 short cryo-modules) and finally mapped into the red contour at the linac end. b) Results of a multi particle tracking (10,000 particles); longitudinal phase-space the at the linac end as simulated by a matrix code OptiM.

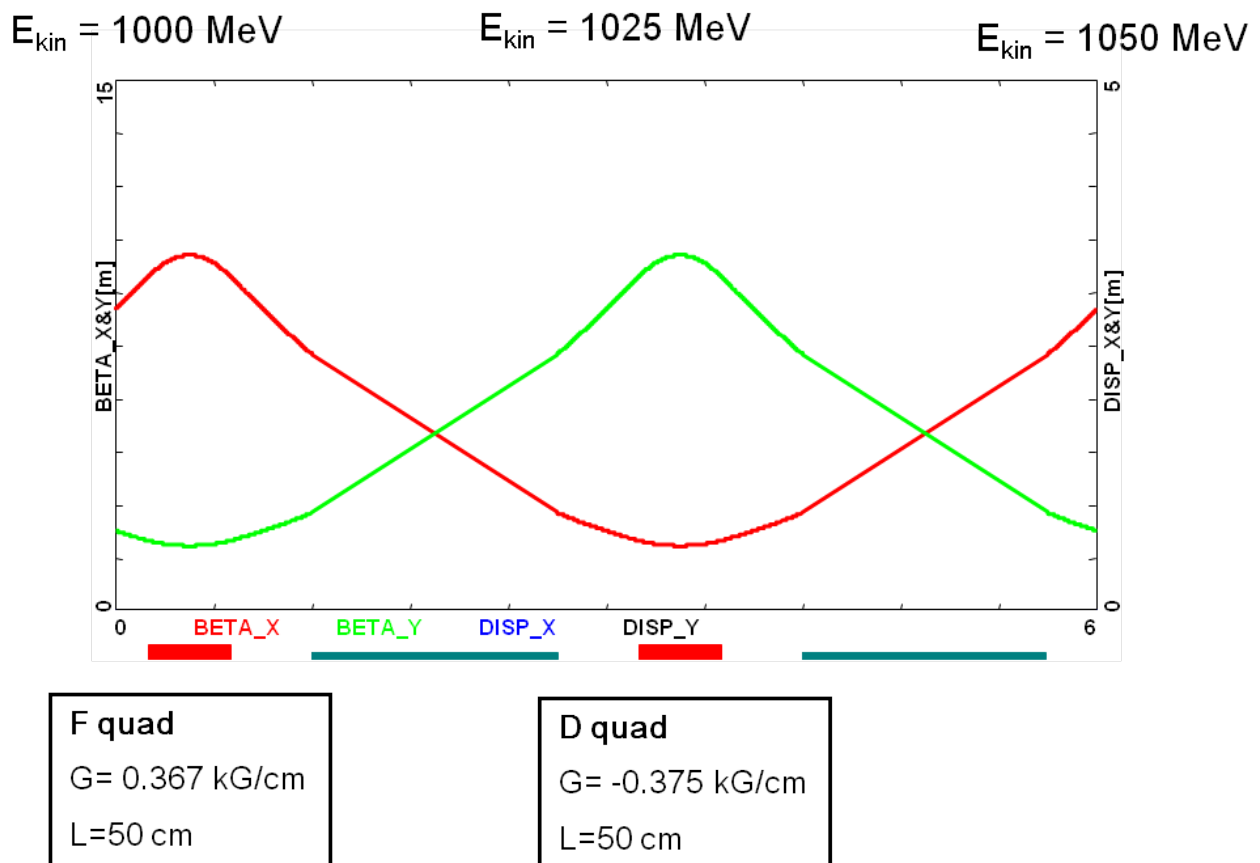


Figure 117: Periodic 90° FODO 6 m linac cell. A pair of 2-cell cavities is interleaved between quadrupoles. The cavity length is 1 RF wavelength and the elements are equally spaced.

3m RLA I LINAC Module core:

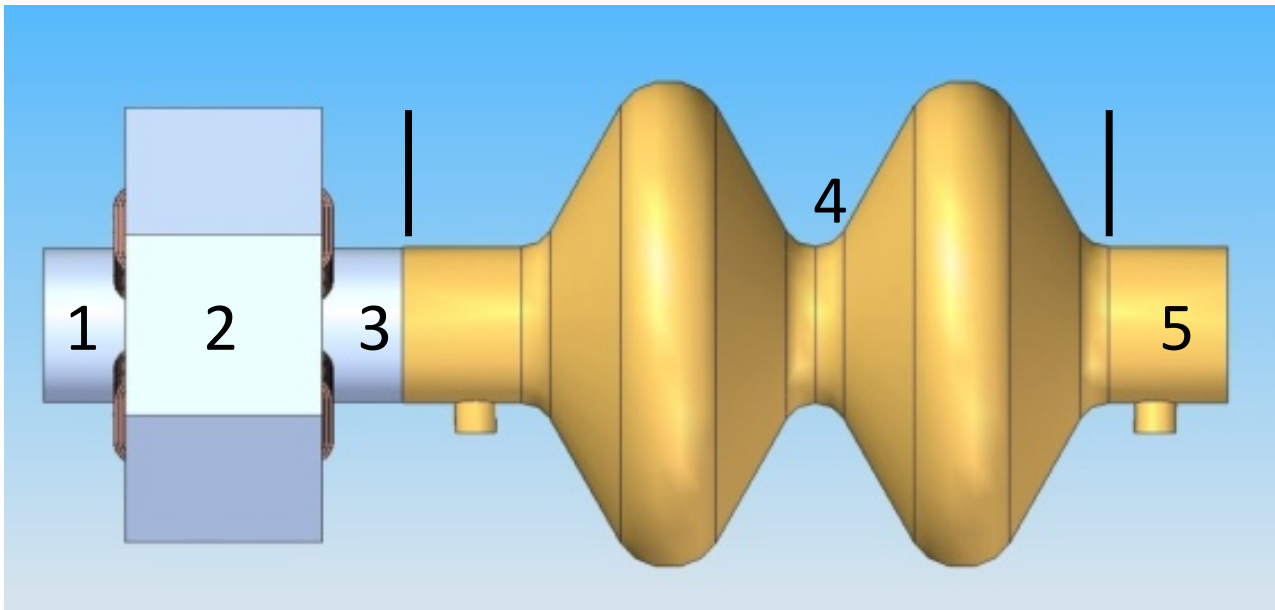


Figure 118: RLA I linac half-cell (3 m), including a single 2-cell cavity and a quadrupole.

F.3 RLA I

The dog-bone RLA I is designed to accelerate simultaneously the μ^+ and μ^- beams from 0.8 GeV to 2.8 GeV. The injection energy into the RLA and the energy gain per RLA linac (0.45 GeV) were chosen so that a tolerable level of RF phase slippage along the linac could be maintained (≈ 200 in RF phase). To suppress chromatic effects, 90° FODO optics was used as a building block for both the linac and the return arcs. The layout and optics of the linac's periodic cell is shown in Fig. 117. The quadrupole centers start at longitudinal position 46 cm with a spacing between quadrupole centers of 3 m, as illustrated in Fig. 118.

The FODO lattice starts at one end of the linac with the first F quad in the table, and is reflection symmetric about the centre of the last D quad shown in the table. There are RF cavities between each of the quadrupoles, except there are no cavities between the central D magnet and its adjacent F quadrupoles. In the first full pass, each cavity causes the beam to gain 25 MeV, starting with a kinetic energy of about 1 GeV at the beginning of that pass. The focusing profile along the linac was chosen so that beams with a large energy spread could be transported within the given aperture. Since the beam is traversing the linac in both directions, a “bisected” focusing profile [261] was chosen for the multi-pass linac.

Here, the quadrupole gradients scale up with momentum to maintain 90° phase advance per cell for the first half of the linac (Fig. 119a), and then are mirror reflected in the second half, as illustrated in Fig. 119b. Higher linac passes (2-nd, 3-rd and 4-th) are illustrated in Fig. 120. Increasing under focusing due to higher energies induces a beta-beat wave across the linac with characteristic nodes at the linac ends.

At the ends of the RLA linac, the beams need to be directed into the appropriate energy-dependent (pass-dependent) droplet arc for recirculation [262]. Each arc starts with a switchyard dipole - a single horizontal bend located at the linac end, common for both recirculated arcs: Arc 1 and 3 at one linac end and Arc 2 and 4 at the other end. The entire droplet-arc architecture is based on 90° phase-advance cells with periodic beta functions. For practical reasons, horizontal rather than vertical beam separation has been chosen. Rather than

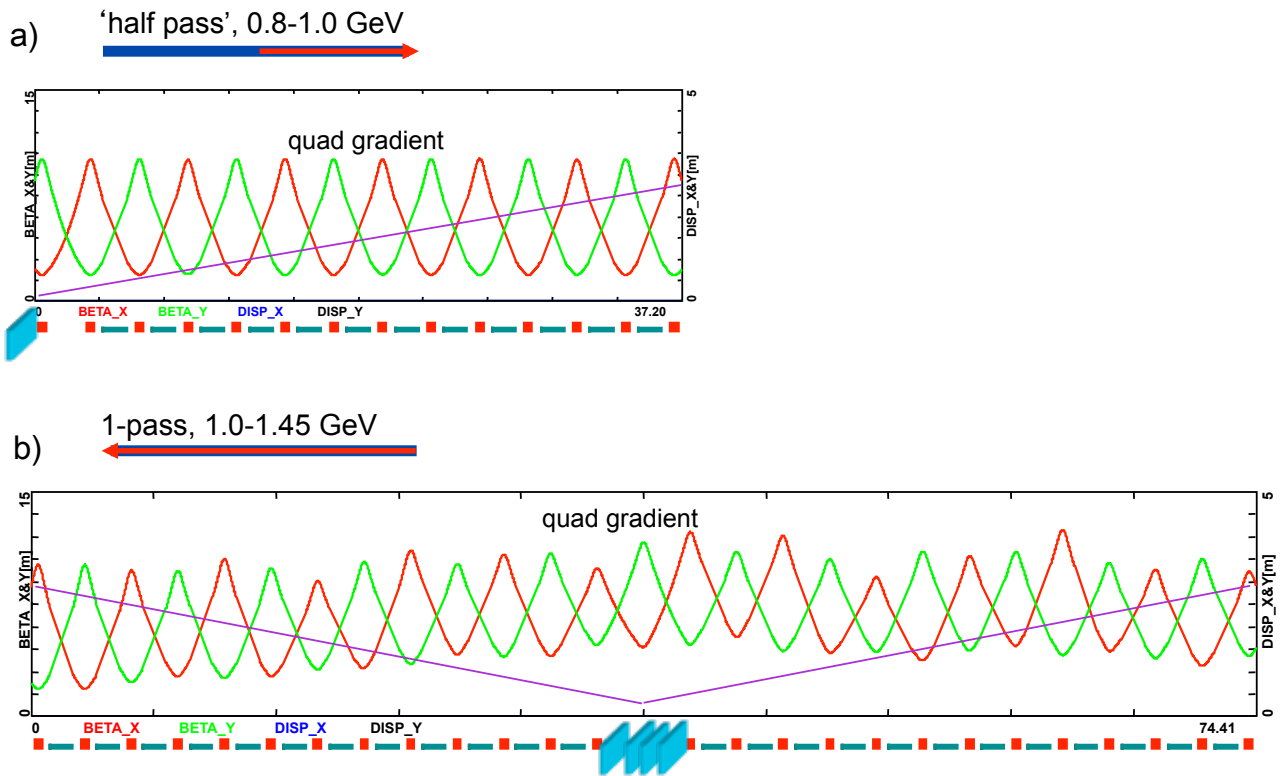


Figure 119: FODO-based multi-pass linac optics. The quadrupole gradients are scaled up with momentum for the first half of the linac, then they are mirror reflected in the second half. The injection chicane magnets are located at the middle of the linac (marked in blue).

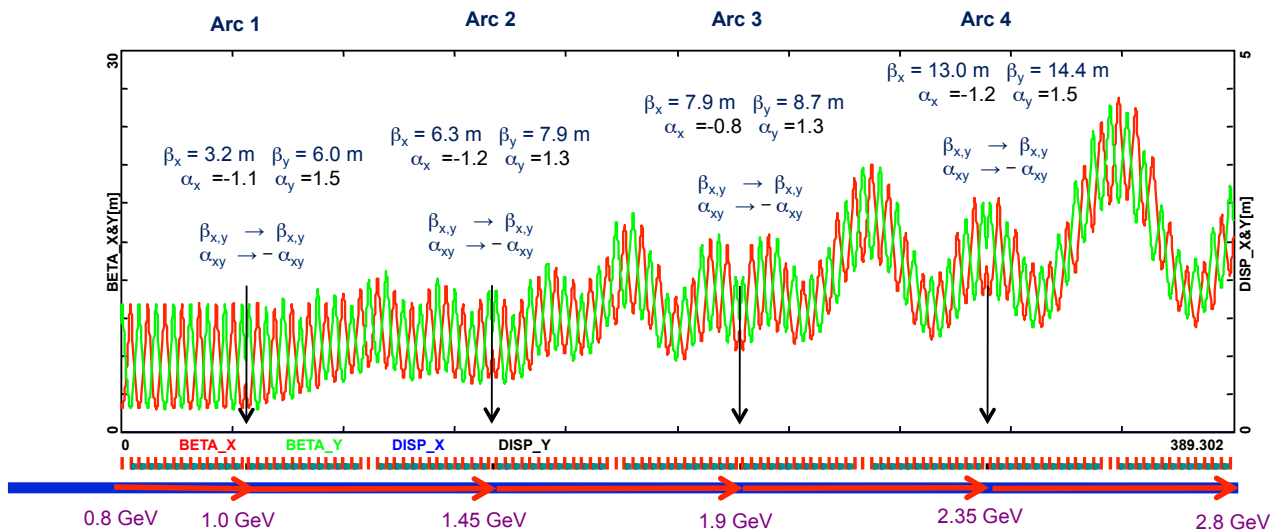


Figure 120: Bisected linac optics for all 4.5 passes. The requirement of simultaneous acceleration of both muon charge species imposes mirror symmetry of the arc optics. This puts a constraint on the exit/entrance Twiss functions for two consecutive linac passes, namely: $\beta_n^{\text{out}} = \beta_{n+1}^{\text{in}}$ and $\alpha_n^{\text{out}} = -\alpha_{n+1}^{\text{in}}$, where $n = 0, 1, 2, \dots$ is the pass index. The consecutive linac passes are connected with $-I$ transfer matrix representing mirror symmetric arcs.

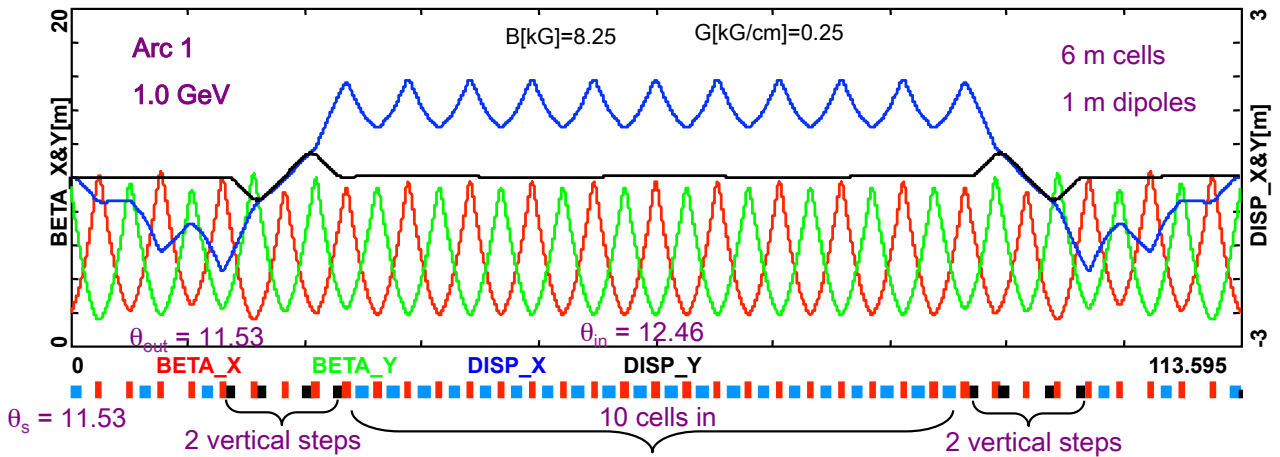


Figure 121: Compact FODO-based droplet arc optics. Horizontal dispersion “flip” is implemented with two “empty cells”, which are perfectly suited to accommodate a pair of vertical steps facilitating a 1 meter “lift” of the inward part of the droplet and hence it solves the “crossing problem” with the second droplet arc (Arc 3 at 1.9 GeV) as illustrated in Figure 11. Again, 90° FODO in the vertical plan guarantees the vertical steps to form an achromat by purely geometric dispersion suppression.

suppressing the horizontal dispersion created by the spreader, it has been matched to that of the outward arc. This is partially accomplished by removing one dipole (the one furthest from the spreader) from each of the two cells following the spreader. To switch from outward to inward bending, two “empty” cells are used, wherein the four dipoles are removed. The two remaining dipoles at the ends bend the same direction as the dipoles to which they are closest. To facilitate simultaneous acceleration of both μ^+ and μ^- bunches, a mirror symmetry is imposed on the droplet arc optics (oppositely charged bunches move in opposite directions through the arcs) [257]. This puts a constraint on the exit/entrance Twiss functions for two consecutive linac passes, namely: $\beta_n^{\text{out}} = \beta_{n+1}^{\text{in}}$ and $\alpha_n^{\text{out}} = -\alpha_{n+1}^{\text{in}}$, where $n = 0, 1, 2, \dots$ is the pass index.

Complete droplet arc optics for the lowest energy arc (1.0 GeV) is shown in Fig. 121.

All higher arcs (Arc 2, 3 and 4, returning: 1.45 GeV, 1.9 GeV and 2.35 GeV beams respectively) follow the same “blue print” and they all share the optics architecture of Arc 1. The higher arcs are configured with longer and longer 90° FODO cells, composed with progressively longer dipoles: Arc 2 (7 meter cell based

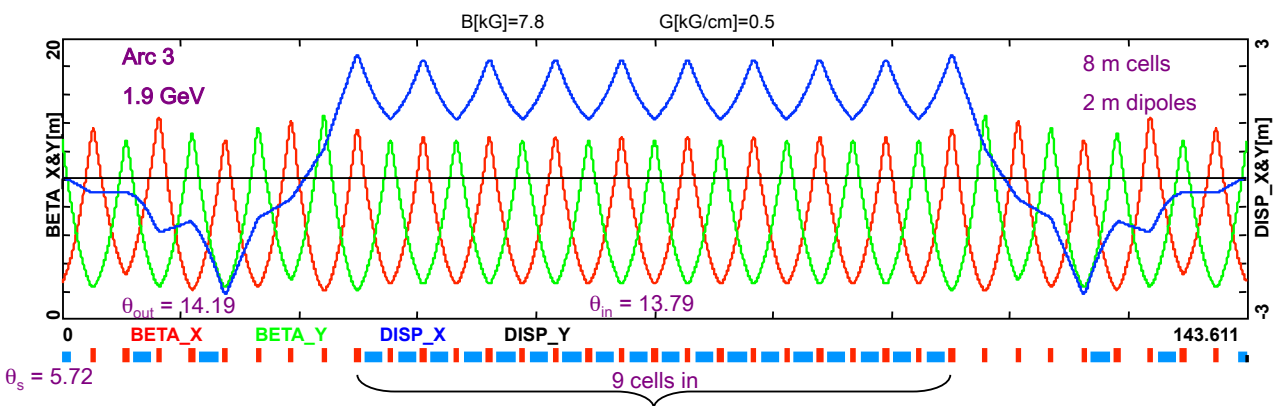


Figure 122: Arc 3 optics at 1.9 GeV based on the same lattice architecture as Arc 1. Here, the in-plane horizontal layout was implemented; therefore no vertical steps are present.

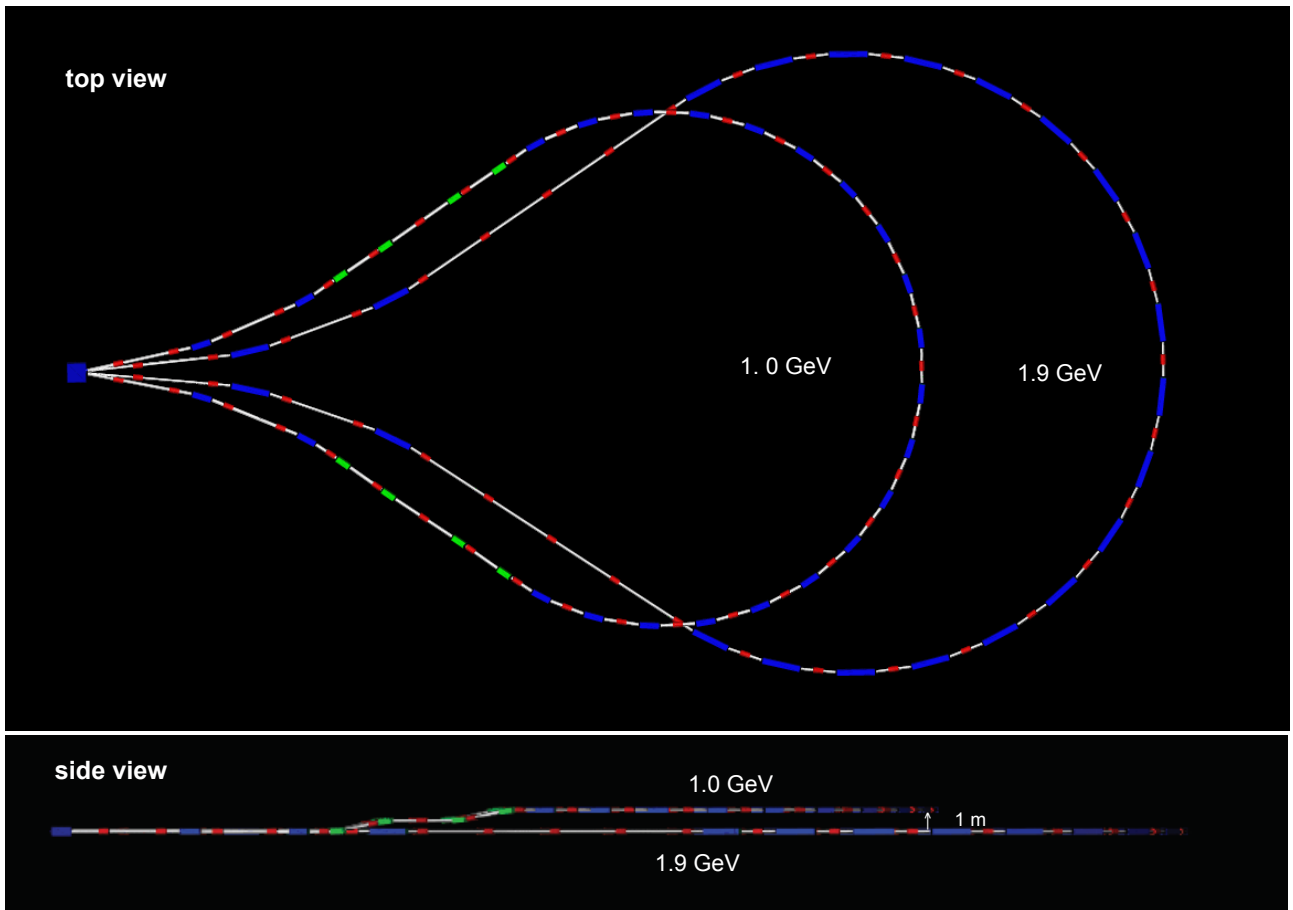


Figure 123: Top and side views of a G4beamline model of the two arcs: Arc 1 (1.0 GeV) and Arc 3 (1.9 GeV).

on 1.5 meter dipoles), Arc 3 (8 meter cell based on 2 meter dipoles) and Arc 4 (9 meter cell based on 2.5 meter dipoles). The quadrupole strengths in the arcs are scaled up linearly with momentum to preserve the 90° FODO lattice. The choice of using longer and longer FODO cells for the arcs is compatible with increasing Twiss functions at the linac ends for bisected linac optics. Hence it facilitates arc-to-linac match by design, eliminating needs for matching optics in arc's Spreader/Recombiner sections. All the arc cells maintain 90° FODO optics, which guarantees intrinsic cancelation of chromatic effects, alleviating horizontal emittance dilution in the arcs. Therefore, there is no need for sextupole corrections at the Spreader/Recombiner sections as in the previous design.

The momentum compaction in the arcs is relatively large (6.5-8 m), which guarantees significant rotation in longitudinal phase-space as the beam passes through the arc. This effect, combined with off-crest acceleration in the subsequent linac, yields further compression of the longitudinal phase-space as the beam is accelerated [254].

F.4 RLA II

The dog-bone RLA II is designed to accelerate simultaneously the μ^+ and μ^- beams from 2.8 GeV to 10.2 GeV. The injection energy into the RLA and the energy gain per RLA linac (1.6 GeV) were chosen so that a tolerable level of RF phase slippage along the linac could be maintained (~ 200 in RF phase). The optics configuration is almost identical to that of RLA I. It is again based on a 90° FODO lattice and a bisected multi-pass linac. The main difference is that the fundamental cell-length was extended to 12 m (cf. 6 m for RLA I).

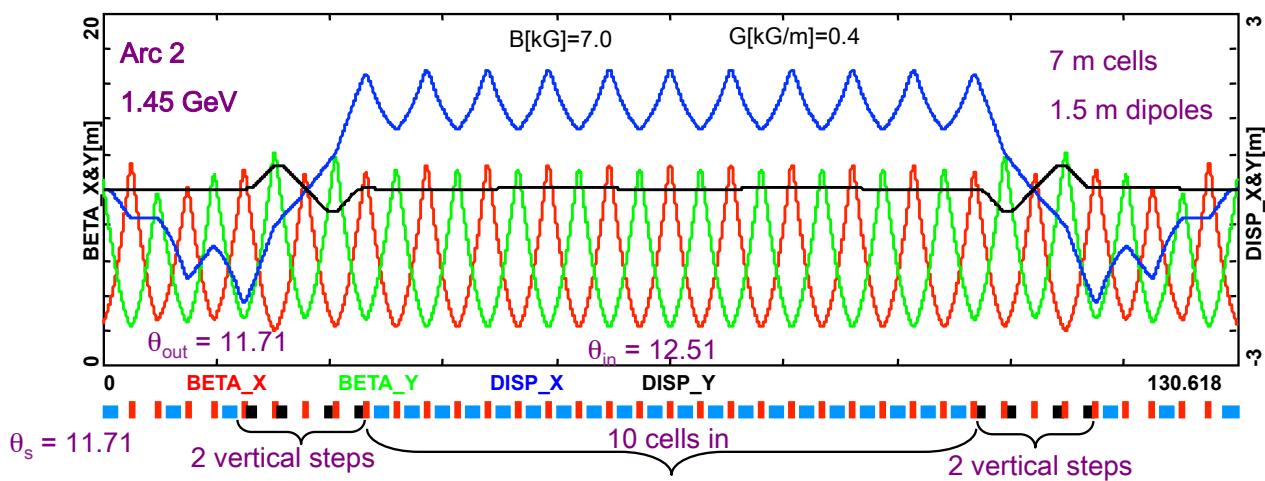


Figure 124: Arc 2 optics sharing the same lattice architecture as Arc 1. Here, the inward lob of Arc 2 is “dropped down” via a pair of vertical steps (see Figure 14).

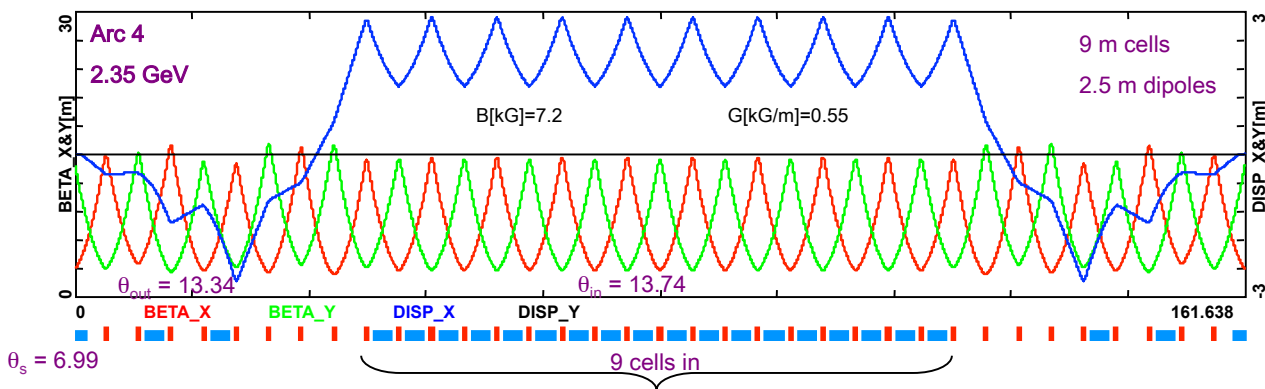


Figure 125: Arc 4 optics sharing the same lattice architecture as Arc 3. Here, the in-plane horizontal layout was implemented; therefore no vertical steps are present.

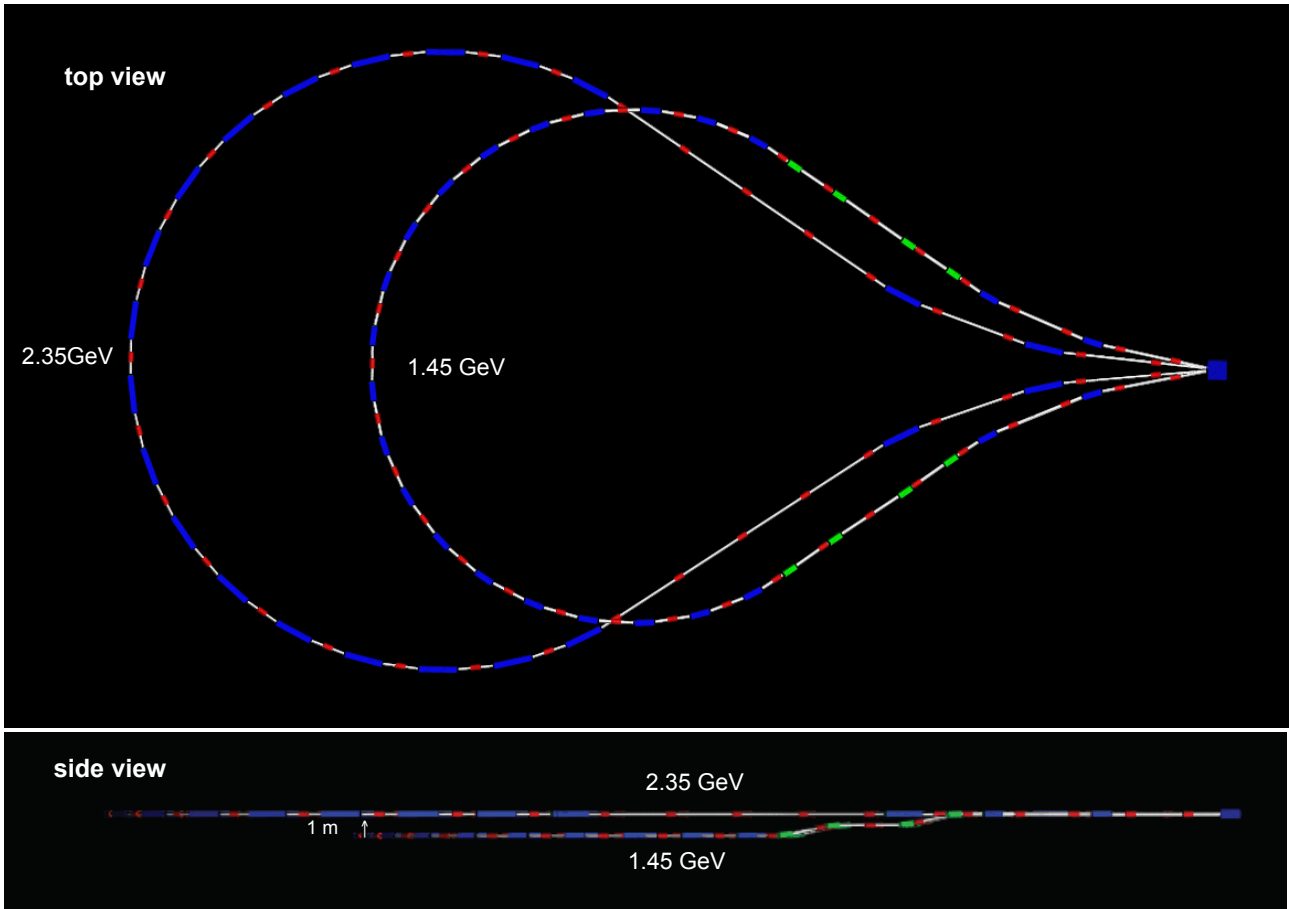


Figure 126: Top and side views of a G4beamline model of the two arcs: Arc 2 (1.45 GeV) and Arc 4 (2.35 GeV).

6m RLA II LINAC Module core:

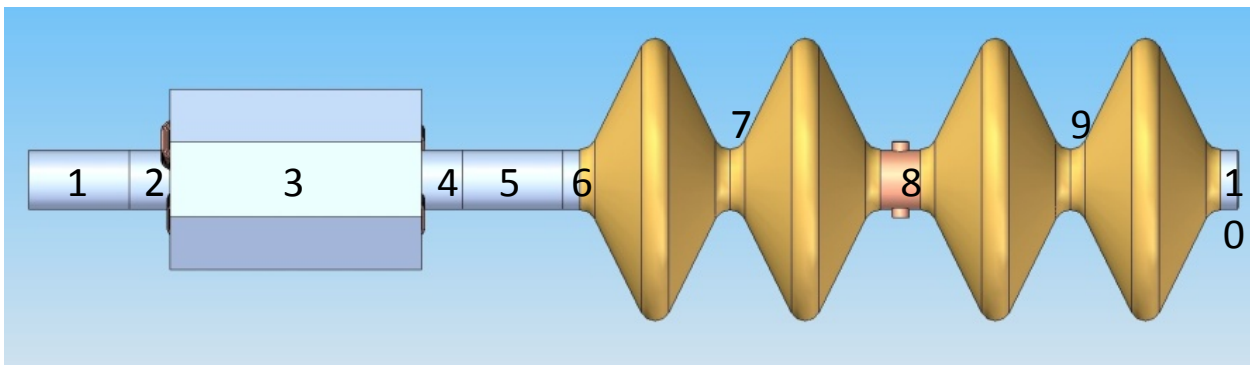


Figure 127: RLA II linac half-cell (6 m), including a pairs of 2-cell cavities and a quadrupole.

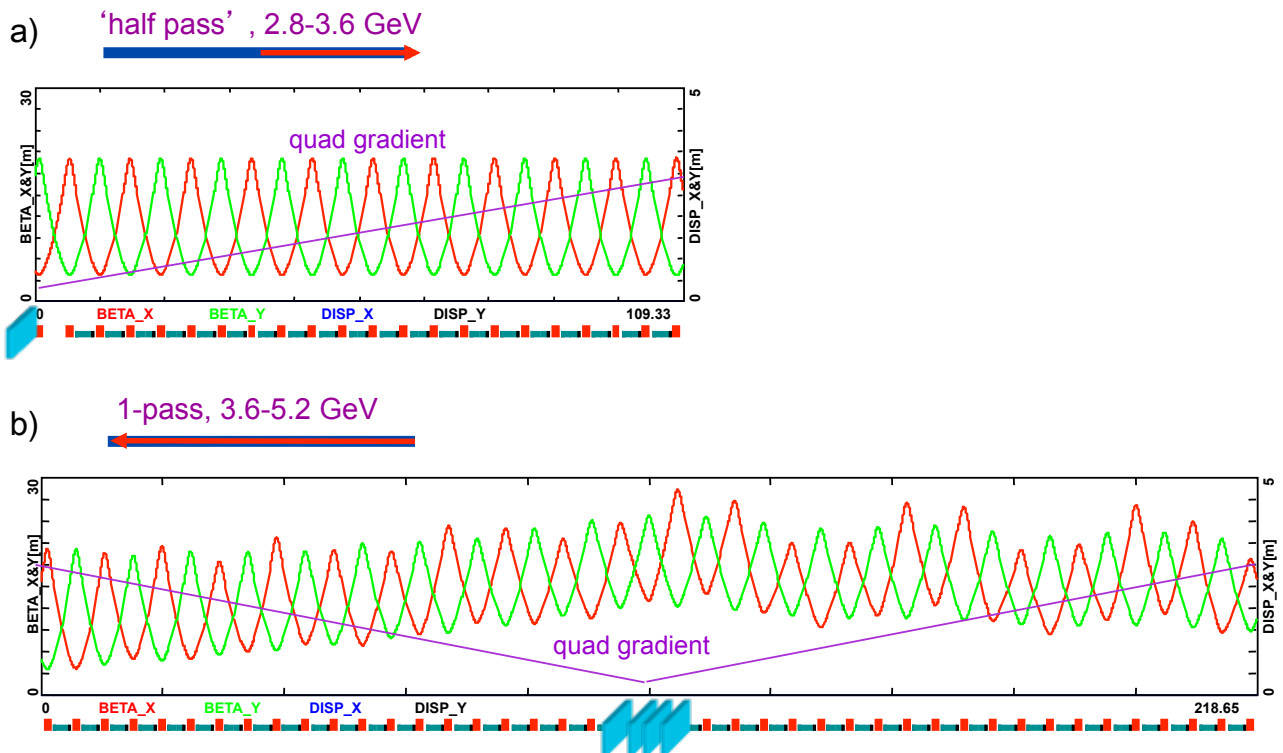


Figure 128: Bisected multi-pass linac optics. The quadrupole gradients are scaled up with momentum for the first half of the linac and mirror reflected in the second half.

The layout of a half-cell is illustrated in Fig. 127.

As for RLA I, a bisected focusing profile was chosen for the multi-pass linac in RLA II, with the quadrupole gradients scaled up with momentum in the first half of the linac and mirror reflected in the second half, as illustrated in Fig. 128.

The optics configuration for the return droplet arcs is almost identical to that of RLA I. It is again based on a 90° FODO. Complete droplet arc optics for the lowest energy arc (3.6 GeV) is shown in Fig. 129.

All higher arcs (Arc 2, 3 and 4, returning: 5.2 GeV, 6.8 GeV and 8.4 GeV beams respectively) are configured with longer and longer 90° FODO cells, composed with progressively longer dipoles: Arc 2 (14 meter cell based on 3 meter dipoles), Arc 4 (16 meter cell based on 2×2 meter dipoles) and Arc 4 (18 meter cell based on 2×2.5 meter dipoles). The quadrupole strengths in the arcs are scaled up linearly with momentum to preserve the 90° FODO lattice.

F.5 Double Arc Chicane

To transfer both μ^+ and μ^- bunches from one accelerator to the next, we use a compact double arc chicane, which layout is illustrated in Fig. 130a). Both muon charge species are split vertically in opposite directions (by the first “blue” dipole) and then leveled horizontally (by the second pair of “blue” dipoles). Then they are bent horizontally by a sequence of “green” dipoles forming a vertically stacked pair of arcs. Finally, both beams are recombined vertically by a mirror symmetric pair of “blue” dipoles closing the vertical chicane. The net horizontal arc bend is appropriately chosen to link two desired points. As for the Double Arc chicane optics, a FODO lattice is used with a 90° phase advance in both the horizontal and vertical plane. Each “leg” of the chicane involves four vertical bending magnets and a horizontal arc at the middle, forming a double achromat in the horizontal and vertical planes, while preserving periodicity of the beta functions. The overall optics is

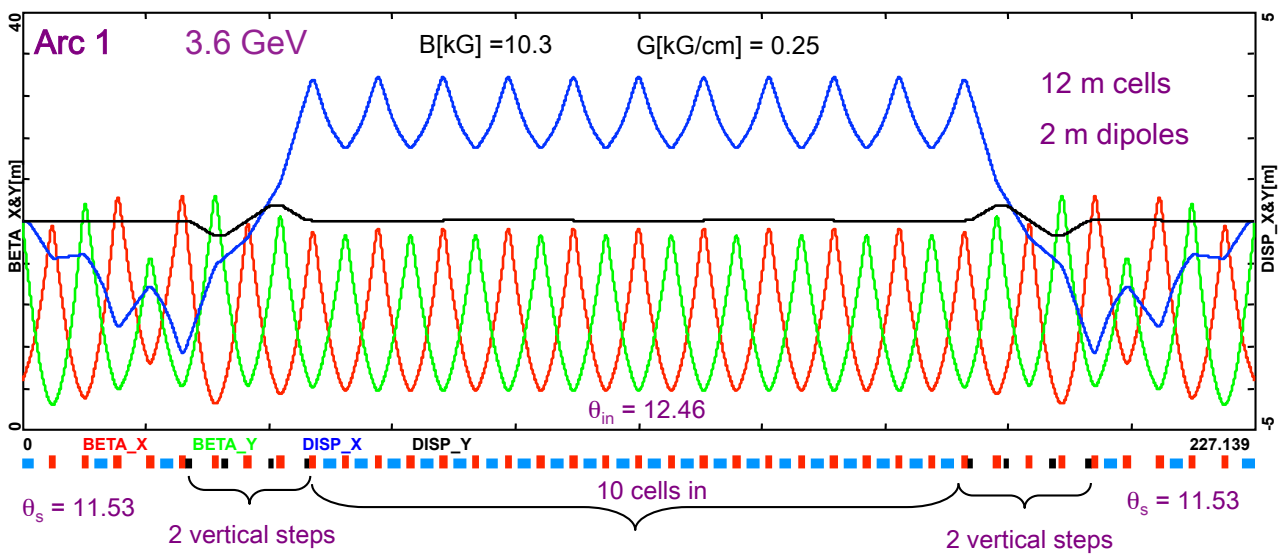


Figure 129: Arc 1 optics (at 3.6 GeV) sharing the same lattice architecture as Arc 1 in RLA I. Again, the inward lobe of Arc 2 is “lifted up” via a pair of vertical steps.

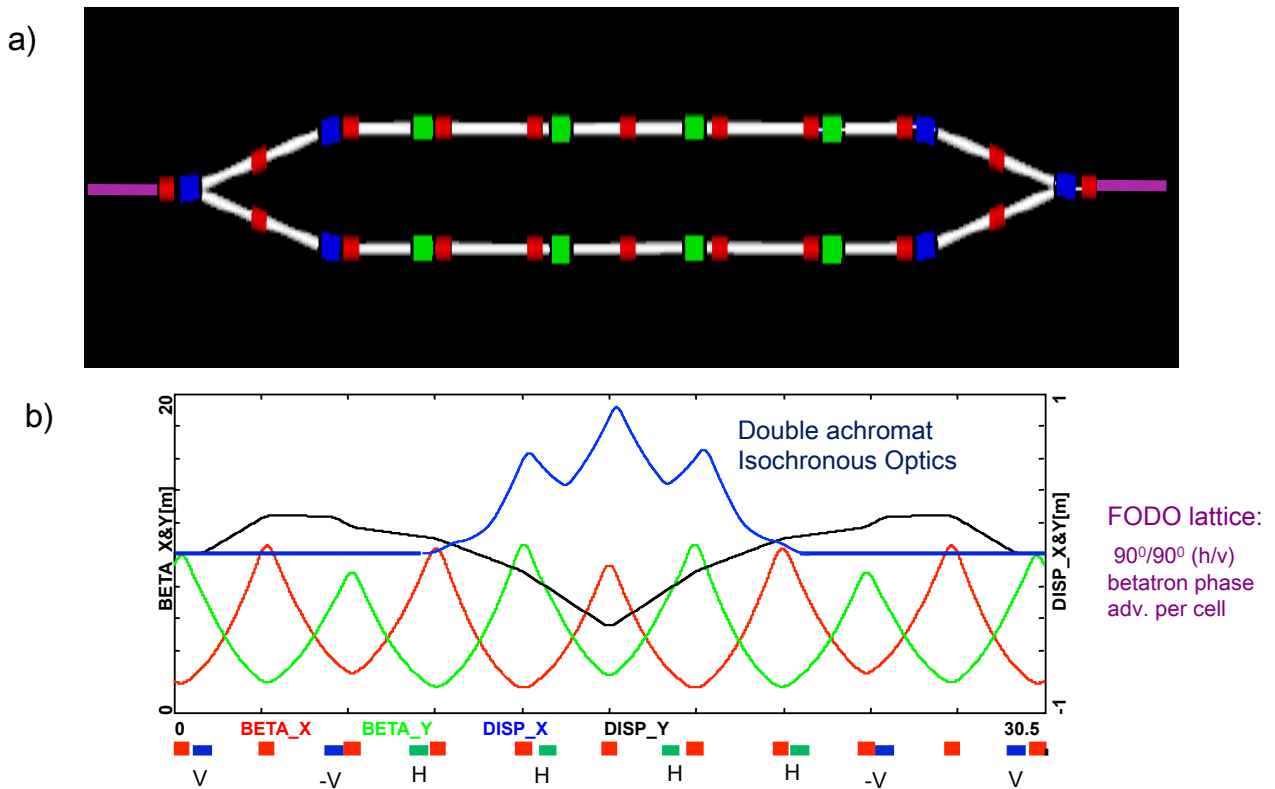


Figure 130: Lattice layout and optics of the Double Arc Chicane.

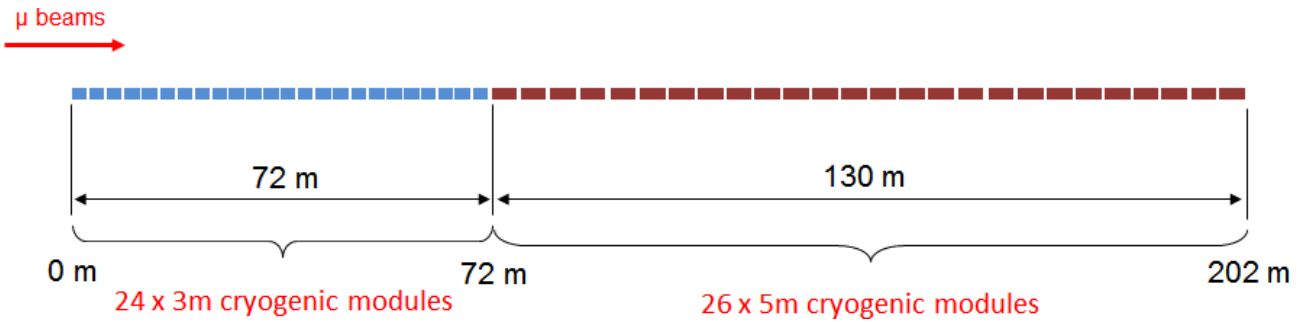


Figure 131: Pre-LINAC sketch to illustrate the basic layout

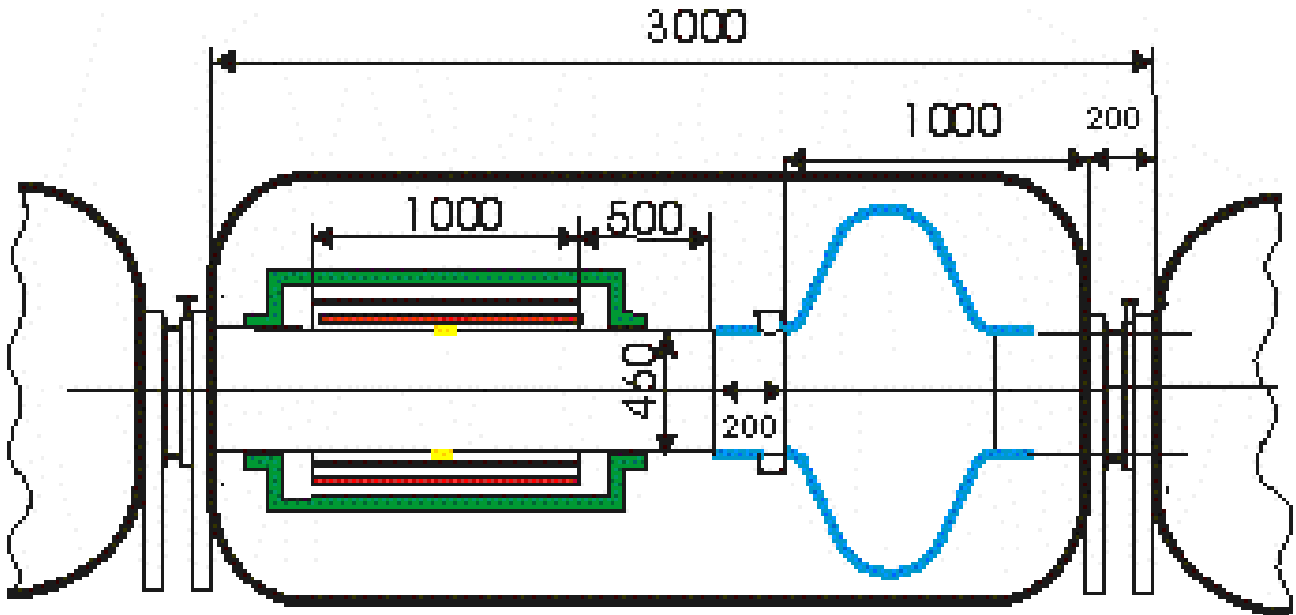


Figure 132: depicting a schematic for the 3 m module containing the solenoid (1.5 Tesla) and single cell cavity (201.25 MHz, gain per cavity: 11.17 MeV)

illustrated in Fig. 130b); it shows both the horizontal and vertical dispersion being suppressed through stacking even number of 90° FODO cells (2 cells to close the horizontal dispersion and 4 cells to close the vertical one).

G Acceleration Engineering

Acceleration of the muon beam occurs in a number of stages. The first stage is a pre-linac, which accelerates the beam to 0.8 GeV total energy. This is followed by two recirculating linear accelerators (RLAs), taking the beam to 2.8 GeV and 10.0 GeV, respectively. RLAs are preferable to a series of single-pass linacs since the beam makes multiple passes through the RF cavities (4.5 passes in our design), consequently reducing the cost of the acceleration system. The RLA technique cannot be applied at lower energies, however, since the beam has a low velocity which, combined with its large relative-energy spread and large geometric emittance, would make a linac phased for a higher energy inefficient at the lower, initial energy.

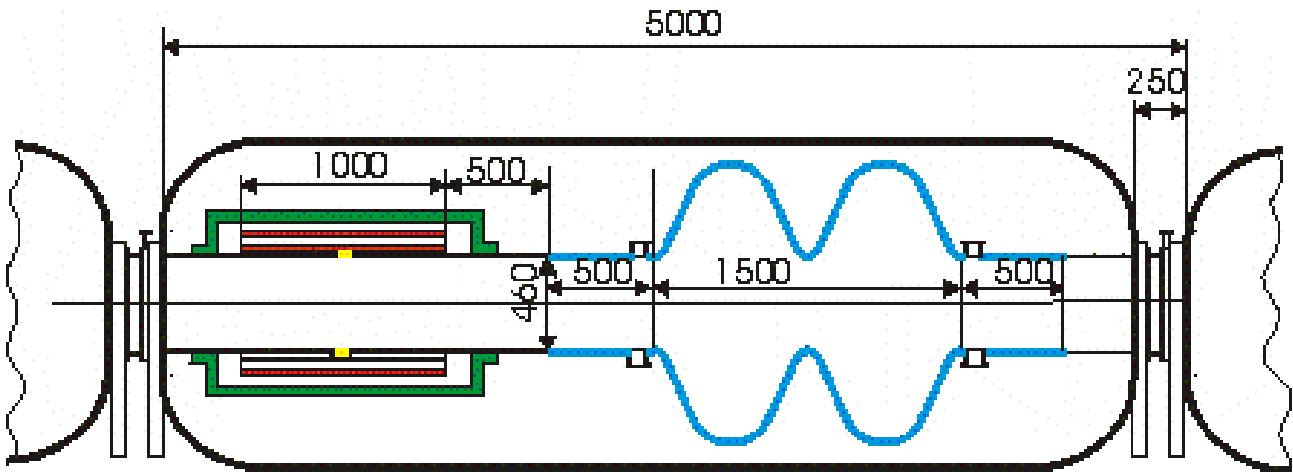


Figure 133: illustrating the initial sketch for the 5 m module containing a solenoid (2 Tesla) and a 2 cell cavity (201.25 MHz, gain per cavity 22.34: MeV):

G.1 Pre-LINAC

To increase the energy sufficiently to apply the RLA technique a Linear pre-accelerator raises the total energy from 0.244 GeV to 0.775 GeV. The Pre-LINAC consists of two distinct sections to retain an acceptable beam envelope. See Figure 131 for a sketch of the Pre-LINAC overview. The first part is comprised of a solenoid-single cell cavity module as depicted in Fig. 132 followed by a solenoid-two cell cavity module as shown in Fig. 133.

An initial engineering evaluation led to a reiteration of the design shown in Figures 132 and 133 as the geometry has to be modified to cater for mechanical components such as bellows, vessel enclosures and their interfaces. The challenge of the extremely compact layout coupled with the magnetic shielding requirement requires further investigation. Since solenoids produce strayfields that have adverse effects on the superconducting RF cavities; therefore, a very important design feature of the solenoids is the need to eliminate the strayfields. The solenoids satisfy the following conditions:

1. Are designed to produce zero net magnetic moment. This means that the coil that produces the solenoidal field is bucked by a coil or coils that are larger in diameter.
2. The field from the bucking coils is to be distributed in the same way as the solenoid field. This suggests that the bucking solenoid be around the focusing solenoid so that the return flux from the focusing solenoid is returned between the focusing solenoid and the bucking solenoid.
3. The solenoid pair is surrounded by iron, except where the muon beam passes through it.
4. An iron flux shield is installed between the solenoid magnet package and the RF cavity cells.
5. The superconducting RF cells nearest the focusing solenoid are covered with a type 2 superconducting shield. This will not shield the earth's magnetic field, but it will shield the remaining strayflux from a nearby solenoid.

It can be seen that a distance of 500mm must be maintained in order to negate the effect of the solenoid strayfields on the RF cavity. The physical length of the coils and iron shield had to be reduced by 200mm to accommodate mechanical items and provide minimum spacing for vessels for cryogenic purposes. At the same time, the overall length of 3 m could be maintained pending verification by the lattice designer. Note also that the solenoid field increases along the Pre-LINAC from 1.06 T to 3.34 T progressively. Table B.1.b shows the maximum nominal values.

A technology solution for the cryogenic requirement is proposed, based on the above parameters and cost

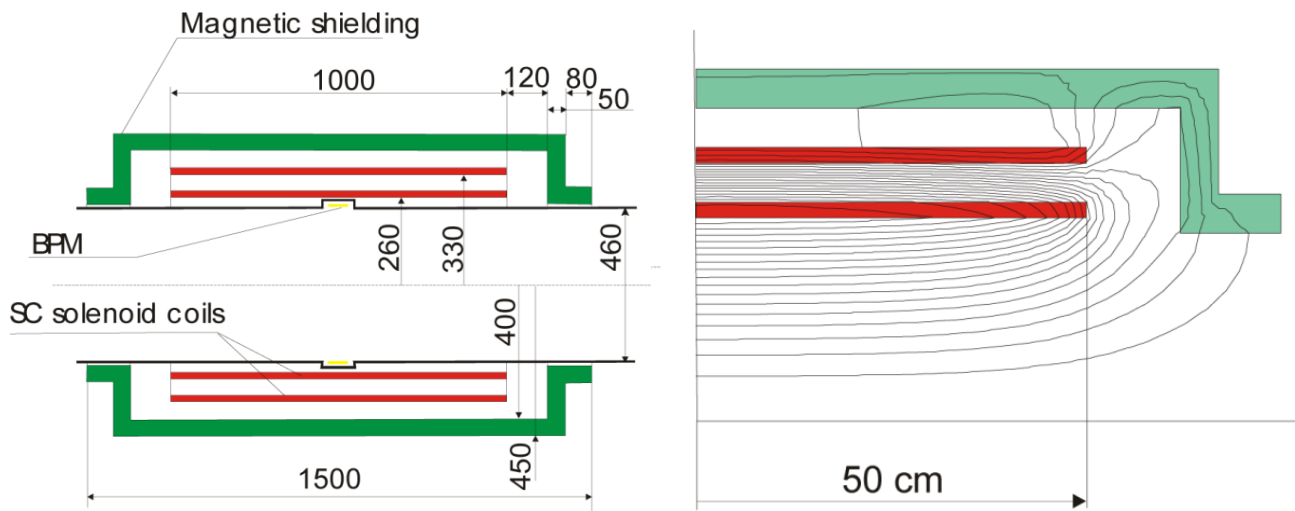


Figure 134: depicting a more detailed schematic of the solenoid including dimensions (on the left) and magnetic field lines (on the right):

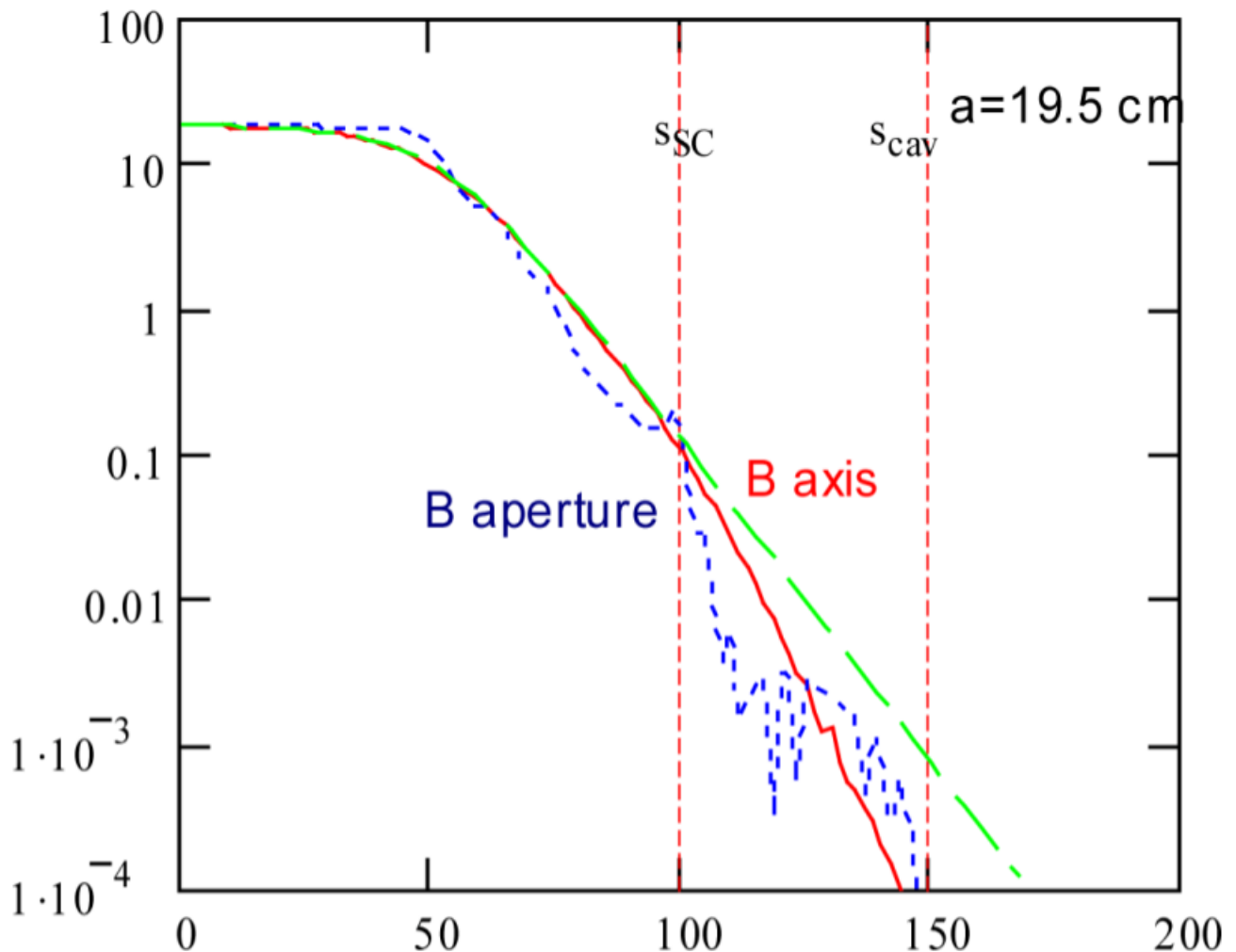


Figure 135: The magnetic field as a function of the longitudinal position. The solid red line is the field on axis. The blue short-dashed line is the field at a radius of 23 cm. The green long-dashed line is a fit to $B(s) = (B_0/2)\{1 - \tanh[(s - L/2)/a]\}$, where $a = 19.5 \text{ cm}$.

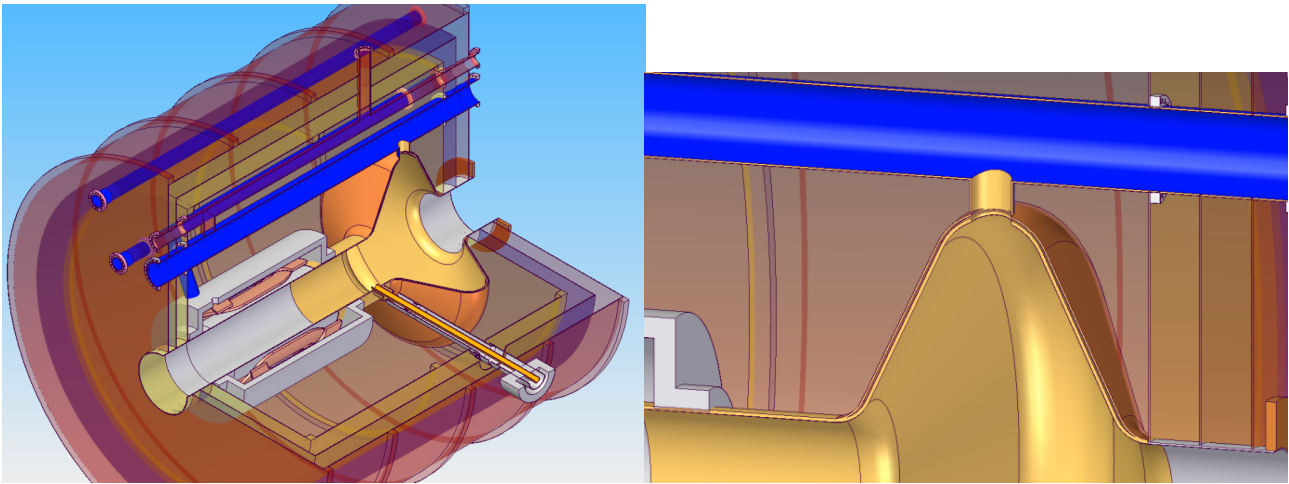


Figure 136: Images of 3m Module (Fig. B.1.6) depicting the general layout first and detail image of the RF cavity 1.8K jacket.

Table 39: Pre-linac RF parameters

RF cavity parameters:	3m Module	5m Module
RF frequency (MHz)	201.25	201.25
Aperture Diameter (mm)	460	460
Cells per cavity	1	2
Energy gain/cavity (MeV)	11.2	22.4
Stored energy/cavity (J)	966	1932
Input power/cavity (kW)	490	980
RF on time (ms)	3	3
Loaded Q	106	106

constraints. Investigations into cryogenics design lead to the decision to adopt a string cooling approach rather than an individual module for the Pre-LINAC section. A CAD schematic is illustrating this in Fig. B.1.6.

A 2-phase common vessel provides the RF cavity jacket with cooling to 1.8K. This jacket surrounding the cavity is kept to a minimum volume in order to reduce the amount of liquid Helium required. Using a 1.8K temperature alleviates the requirement to invest in exotic materials for the cavities and a Niobium coating suffices to maintain the gradient prerequisite.

Surrounding the 1.8K cavity jacket is a 5K chamber. The solenoid is located in this chamber ensuring it will be superconducting, resulting in the negation of the need to manufacture the coils from Powder In Tube (PIT) or Yttrium Barium Copper Oxide (YBCO) for instance.

The subsequent vessel in turn is a 40K shield acting as the intermediate temperature insulation. The outer structure bringing it to room temperature and contains a magnet shield. It further provides the overall interface bellow between modules.

The input coupler features similar insulation layers to prevent its cooling. A cooling spiral may need to be applied in the 5 K region due to its length. It has intercepts at the 5K and 40K shields before passing through the room temperature outer mantle. The design input power is 1016 kW with an RF on-time of 3 ms giving a RF duty factor of 4.5%. This equates to an RF coupler CW of approximately 45.7 kW.

This solution applies to the single cell 3m module and the two cell 5m module.

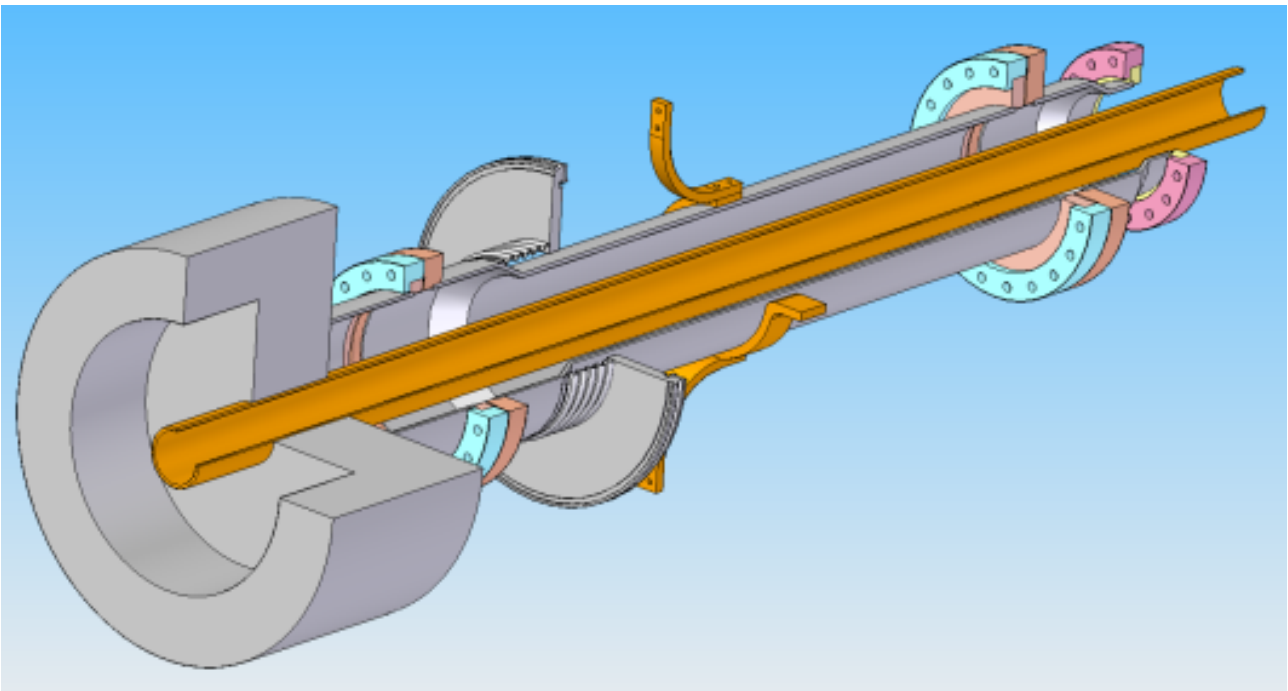


Figure 137: Input coupler showing the coaxial cable separated from the cold mass by surrounding it with a vacuum isolation chamber. A more detailed study may prove that a further insulate is required.

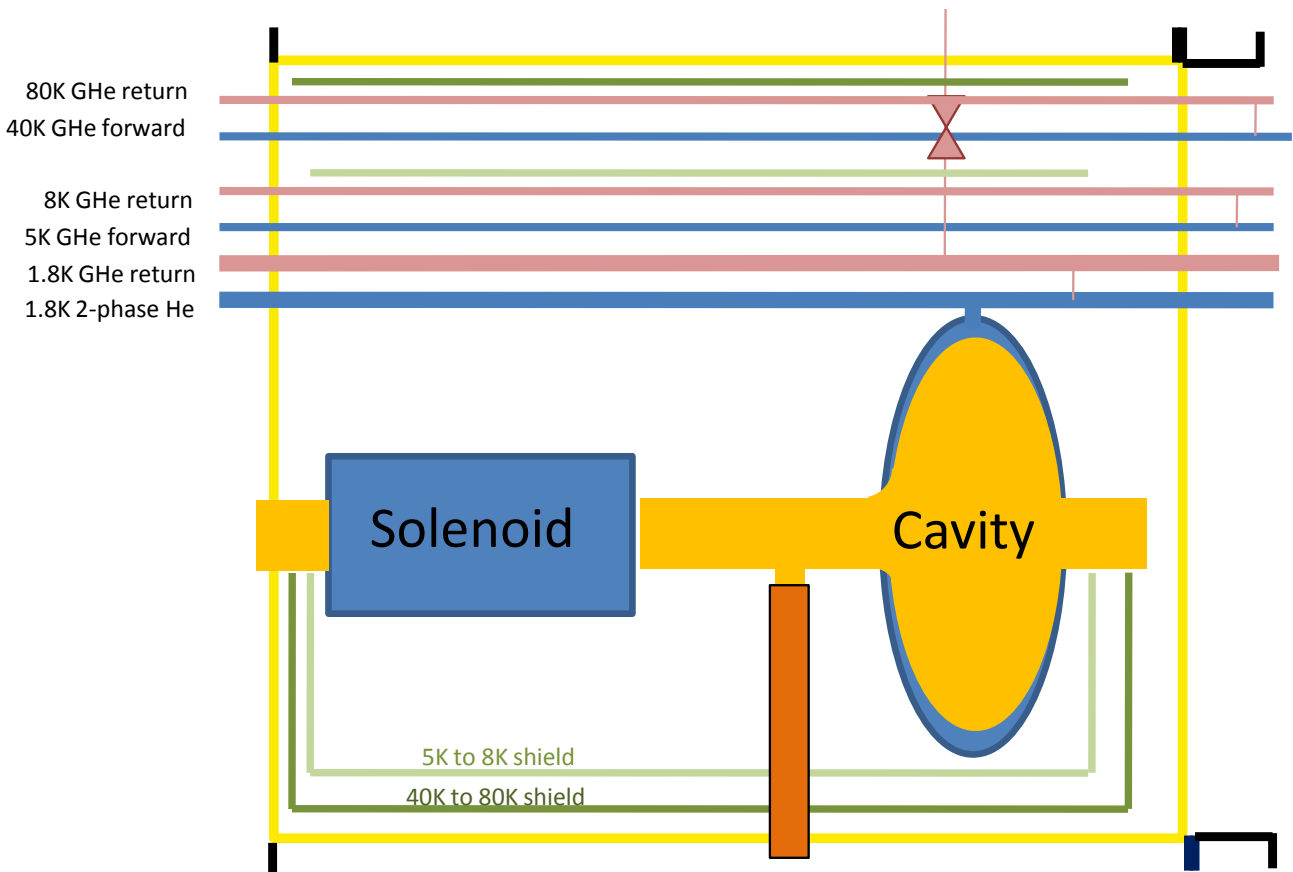


Figure 138: Cryo schematic depicting the cryogenic arrangement. During the Technical Design Phase a detailed heat analysis is required which may determine the need for a 5K feed to the iron shield and a return to the 8K GHe line as provisionally sketched into Fig. B.1.6



Figure 139: Module interface image (JParc 50 GeV neutrino beamline SC module)

Table 40: Pre-linac solenoid parameters.

	3 m Module	5 m Module
Magnetic Induction max. (T)	1.5	3.5
Inner Coil Radius (mm)	254	254
Inner Coil Thickness (mm)	10.5	25.7
Inner Coil Layers	8	19
Outer Coil Radius (mm)	521	521
Outer Coil Thickness (mm)	3	7
Outer Coil Layers	2	5
Physical/Magnetic Length (mm)	900/1000	900/1000
Design Current (A)	335.4	771.4

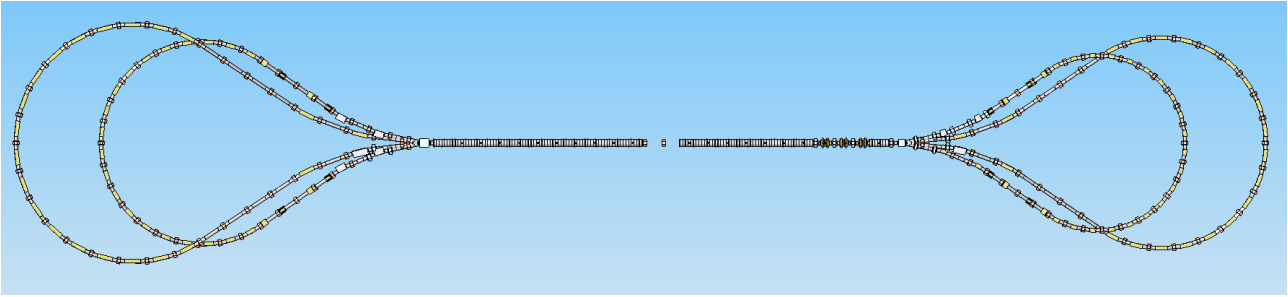


Figure 140: CAD image depicting the linear accelerator with the droplet arcs (odd numbered arcs on the right, even numbered arcs on the left).

Table 41: RF cavity parameters: 3m Module

RF frequency (MHz)	201.25
Aperture Diameter (mm)	460
Cells per cavity	2
Energy gain/cavity (MeV)	22
Stored energy/cavity (J)	1932
Input power/cavity (kW)	980
RF on time (ms)	3
Loaded Q	106

The design is very conceptual at this stage and further studies must be carried out to investigate the feasibility further.

G.2 Recirculating Linear Accelerator 1

CAD image depicting the Linear Accelerator with the droplet arcs (odd numbered arcs on the right, even numbered arcs on the left).

The Recirculating Linear Accelerator 1 consists of 5 distinct sections. The LINAC section in which the beam is accelerated after being injected in the centre is a series of a quadrupole magnet and a two-cell cavity module. 22 of these modules are required for acceleration with two modules at the centre where the cavities have been replaced by drifts for injection purposes. The quadrupole gradient increases systematically from the centre towards the arc to retain the beam characteristics. This is achieved in an arrangement of 25 quadrupoles in a mirror symmetric pattern about the centre.

The beam entering has an energy of 775 MeV increasing to 1000 MeV at the end where it enters the first re-circulating 'droplet' arc (Arc1). This closed mirror symmetric droplet arc returns the beam to the LINAC where further acceleration increases the energy to 1.45 GeV. This re-circulation process repeats three times more before the beam is extracted at an energy of 2.8 GeV. Hence, during the 4.5 passes a 0.45 GeV gain per pass is achieved.

G.2.1 RLA1 LINAC

See Table 41 for the 3 m module parameters and Fig. 142 for a depiction of the schematic components.

An initial technology solution was the exclusion of the quadrupole magnet from the cryogenic system after first calculations proofed that the magnet can be normal conducting. This would have eliminated the need to

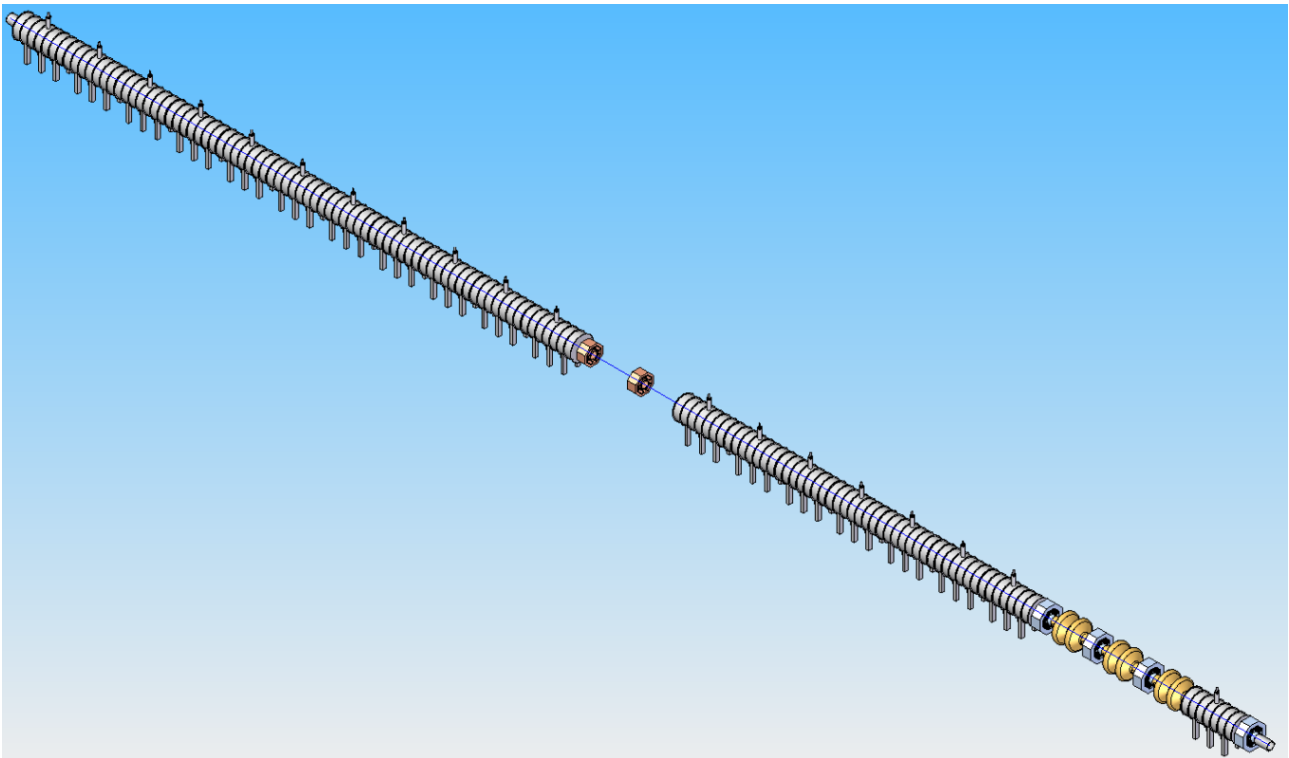


Figure 141: a CAD image illustrating module place holders. Note in the centre a yet to be defined injection system “empty space.” Towards the bottom right are two module core systems shown, consisting of the quadrupole magnet and a 2 cell cavity.

mitigate the heat load by taking it out of the cold system leading to a compact and efficient cryomodule. In addition, the cryogenic enclosures contained a magnetic shield which in turn negates the magnetic influence of the magnet on the cavity. Upon closer investigation, it was found that the physical space required to accommodate the required components is insufficient. The approach of having cold-warm sections furthermore requires bellows and vacuum systems. Fig. 143 illustrates a typical arrangement.

Previously omitted systems such as diagnostics and corrector systems may need to be incorporated. A comparison between the ideal schematic and the typical arrangement illustrated in the previous figure is shown in Fig. 144.

It is evident that a reiteration in the system and lattice design is required. Using one input coupler would provide some space and coupled with a cold magnet to eliminate the warm-cold transitions would further contribute to the possibility to maintain the distances between cavity and magnet. In addition, this solution would follow closely the Pre-LINAC approach.

G.2.2 Mirror Symmetric Droplet Arcs (odd numbers)

The RLA1 Arcs use existing technology for the required systems. Table 42 lists the Quadrupole and 43 Dipole Magnet details. The figures in the tables and a first approximate magnet analysis was carried out to verify that all magnet systems can be normal conducting. This reduces development time and reduces risk as the technology is well understood.

A challenge exists in the area designated the switch-yard. See Fig. 146 for a depiction of the odd Arc number switch-yard area. As the beam exits the LINAC at different energies, the trajectories vary accordingly. Investigations revealed that a pulsed dipole magnet technology is beyond today's possibility based on the field

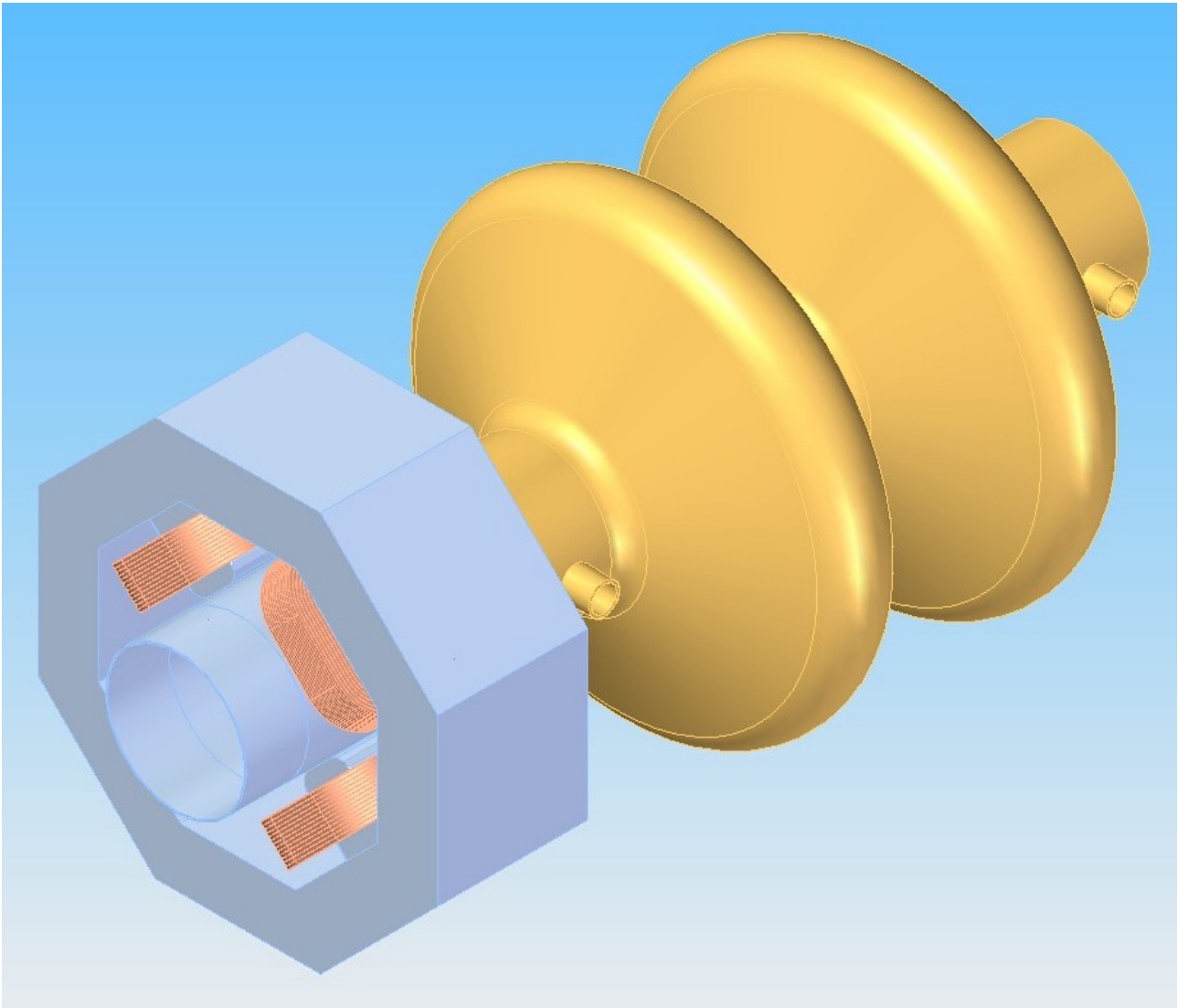


Figure 142: Depiction of the 3m module components indicating a normal conducting quadrupole magnet (bottom left) and the 2 cell cavity with the input coupler ports pointing to the bottom right,

Table 42: name, gradient, aperture, magnetic length and quantity for the Quadrupole magnets. The RLA1 “A” for Arc and “Arc-number” plus focusing-defocusing approach is used in the naming convention.

RLA1 Arc Quadrupole Magnets:	Gradient G[T/m]	Aperture [mm]	length [mm]	Qty
RLA1A1F	3.76115	476	500	19
RLA1A1D	-3.82471	476	500	18
RLA1A2F	5.03572	476	500	19
RLA1A2D	-4.73199	476	500	18
RLA1A3F	5.83838	476	500	18
RLA1A3D	-5.44503	476	500	17
RLA1A4F	6.46735	476	500	18

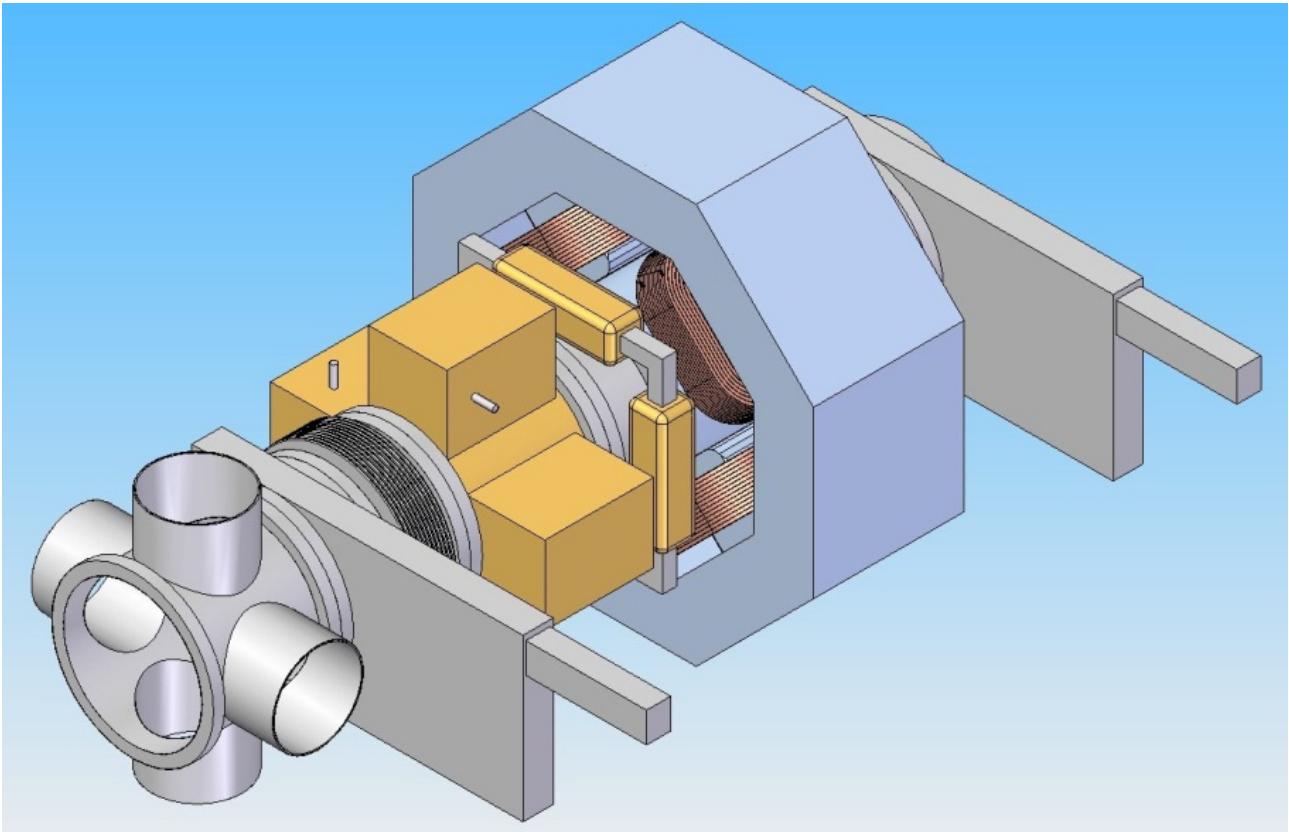


Figure 143: placeholders for a 4 way cross (426mm), gate valve (176mm), bellow (252mm), RF cell BPM (476mm), a corrector magnet (226mm) and on the opposite side a further 252mm long bellow followed by a 176mm gate valve.

Table 43: dipole magnets. The naming convention shows “H” for horizontal, “VU” for vertical up and “VD” for vertical down.

RLA1 Arc Dipole Magnets:	Field B[T]	Aperture [mm]	length [mm]	Qty:
RLA1A1H	-0.987059	476	1000	24
RLA1A2H	0.870892	476	1500	24
RLA1A3H	-0.960028	476	2000	22
RLA1A4H	0.956984	476	2500	22
RLA1A1VU	-0.987059	476	753.3	4
RLA1A1VD	0.987059	476	753.3	4
RLA1A2VU	-0.995872	476	902.5	4
RLA1A2VD	0.995872	476	902.5	4

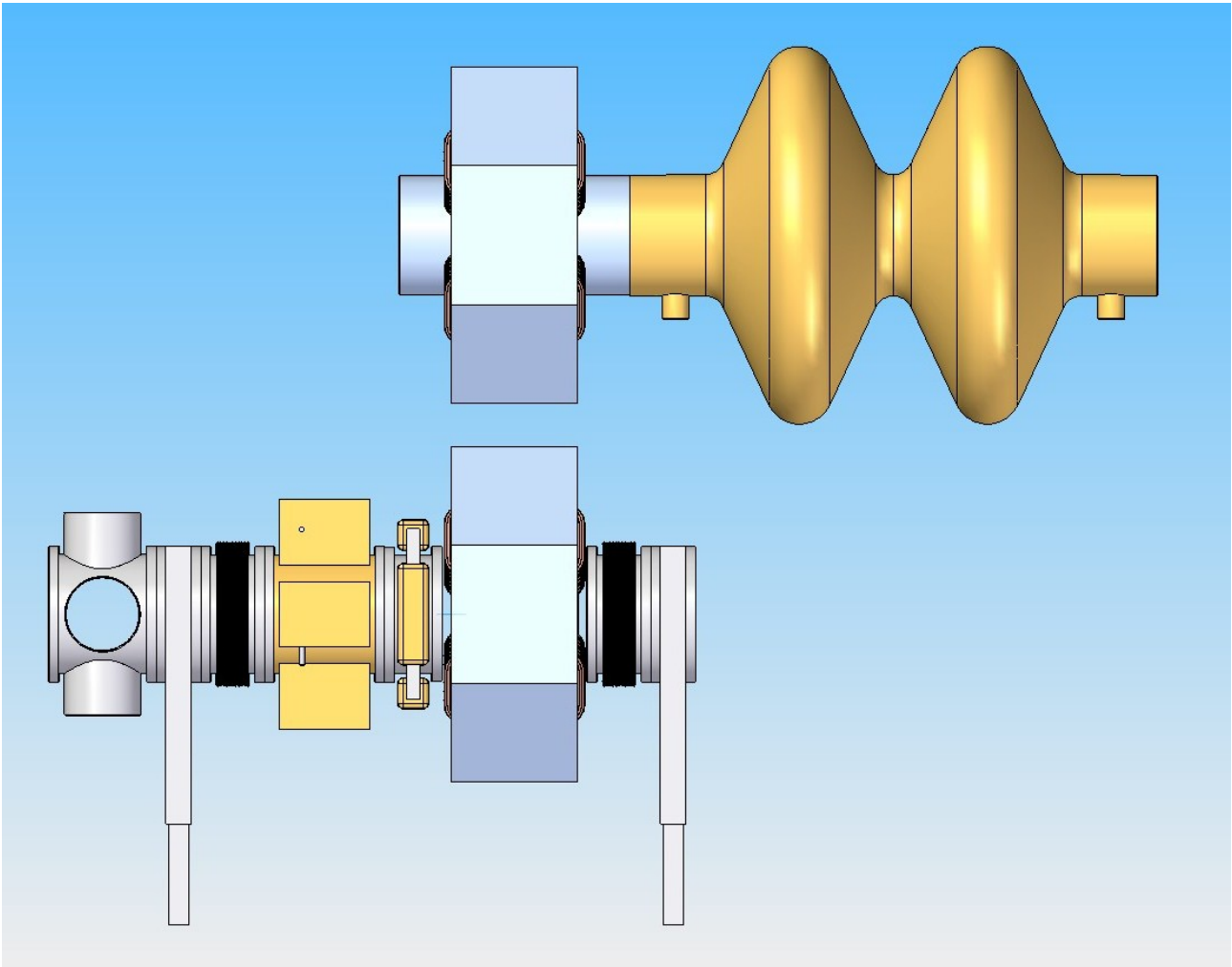


Figure 144: a length comparison. An increase in length per section of 1984mm would be required.

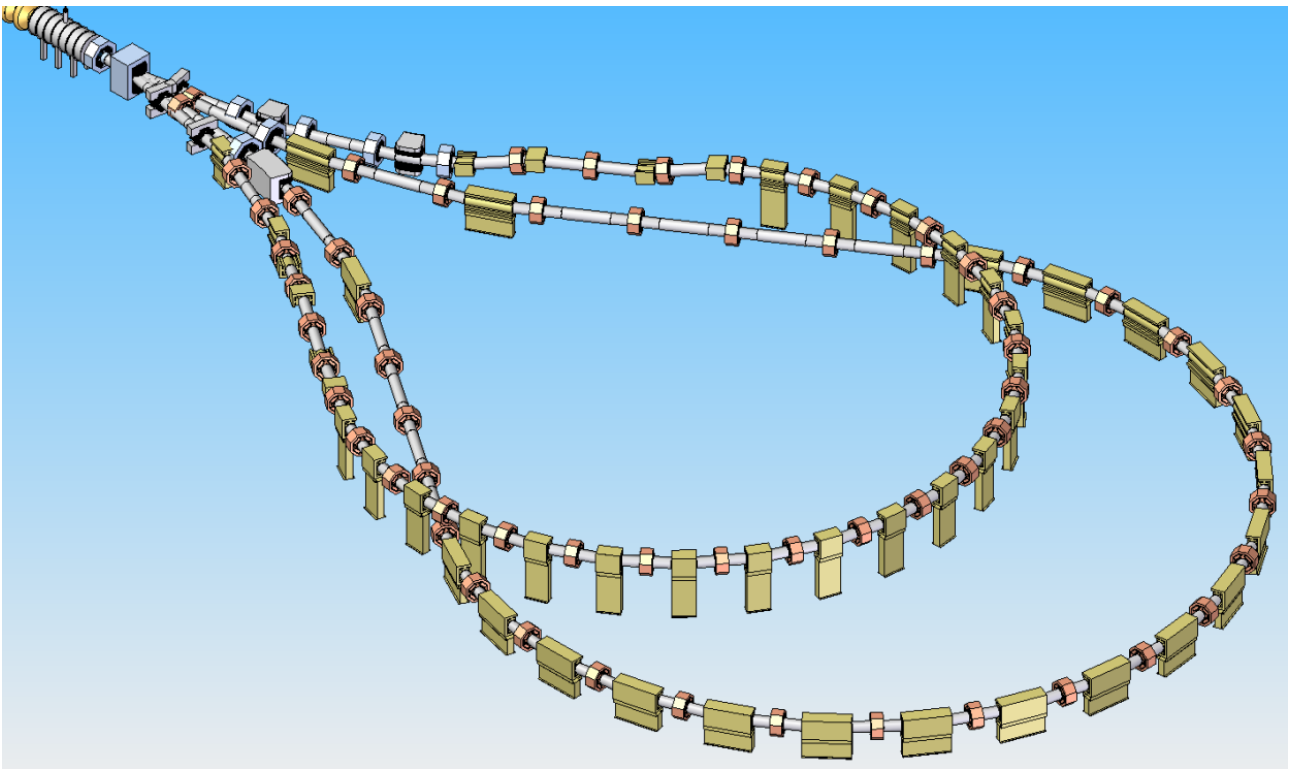


Figure 145: the 'smaller' Arc 1 passing over the 'larger' Arc 3. Initial CAD place holders are shown in green (Dipole Magnets) and skin colour (Quadrupole Magnets).

strength, timing and special requirement of the current lattice design. A feasible alternative solution is to divert the beam using a dipole magnet at fixed field strength. This will cater for both, positive and negative muon signs. Preliminary calculations point to a “window-frame” design providing a cost effective solution for the highest magnetic characteristic quality possible. The real challenge however follows on as the beamlines are in very close proximity of each other and thus leaving very little physical space for systems such as magnets. The RLA1 Arcs 1 and 3 switch yard is the most challenging and particular attention has been paid here to find solutions. As can be seen in Fig. 146, clashes between systems exist which careful design and technology choice can overcome. The first set of Arc3 quadrupole magnets require a new and novel approach in the form of a dedicated “one-piece” vacuum vessel with recesses incorporated to enable quadrupole yokes and windings space. This pair of quadrupoles would need to be manufactured as one “straddling” magnet. Provisional calculations indicate this to be a feasible solution provided the common magnet flux return side in the centre has sufficient thickness and volume to retain linear behaviour. Furthermore, the flux passing through the centre must be such that the direction is the same; i.e. both are focusing in the opposite beam direction. Corrector magnets will be required downstream as the independent alignment is now extremely restricted.

There is currently no technology solution to avoid the clash for the first set of Arc1 quadrupole magnets and a lattice re-design is essential. This will be even more predominant when the extraction lines are incorporated.

The second set of Arc 3 quadrupole magnets requires an open side design solution to avoid interference with the Arc 1 vacuum vessel. This is an existing technology utilising the “Collins” magnets scaled to suit this purpose.

Further magnet systems require careful design and orientation from there onwards using existing technology. For instance “C-type” dipoles facing either inward or outward with steel structures shaped such to avoid clashes.

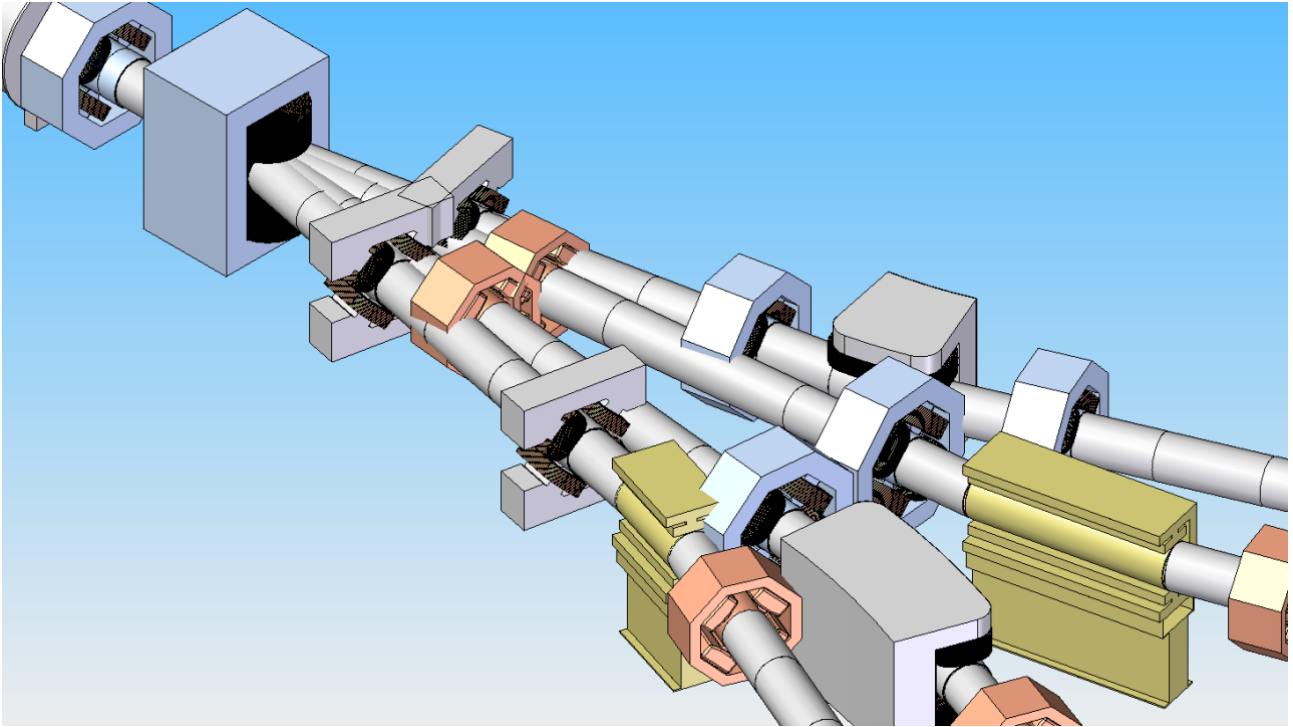


Figure 146: a CAD sketch of the RLA1 odd Arc number switch-yard area. The inner vacuum vessels belong to Arc 1 with the outer belonging to Arc 3. The green initial dipole place holders have been replaced by dimensionally more accurate “grey” models in the area of interest. The skin coloured quadrupole are a first approximation representation replaced by “grey Collins” and “silvery” standard quadrupoles with almost net shape in certain challenging positions.

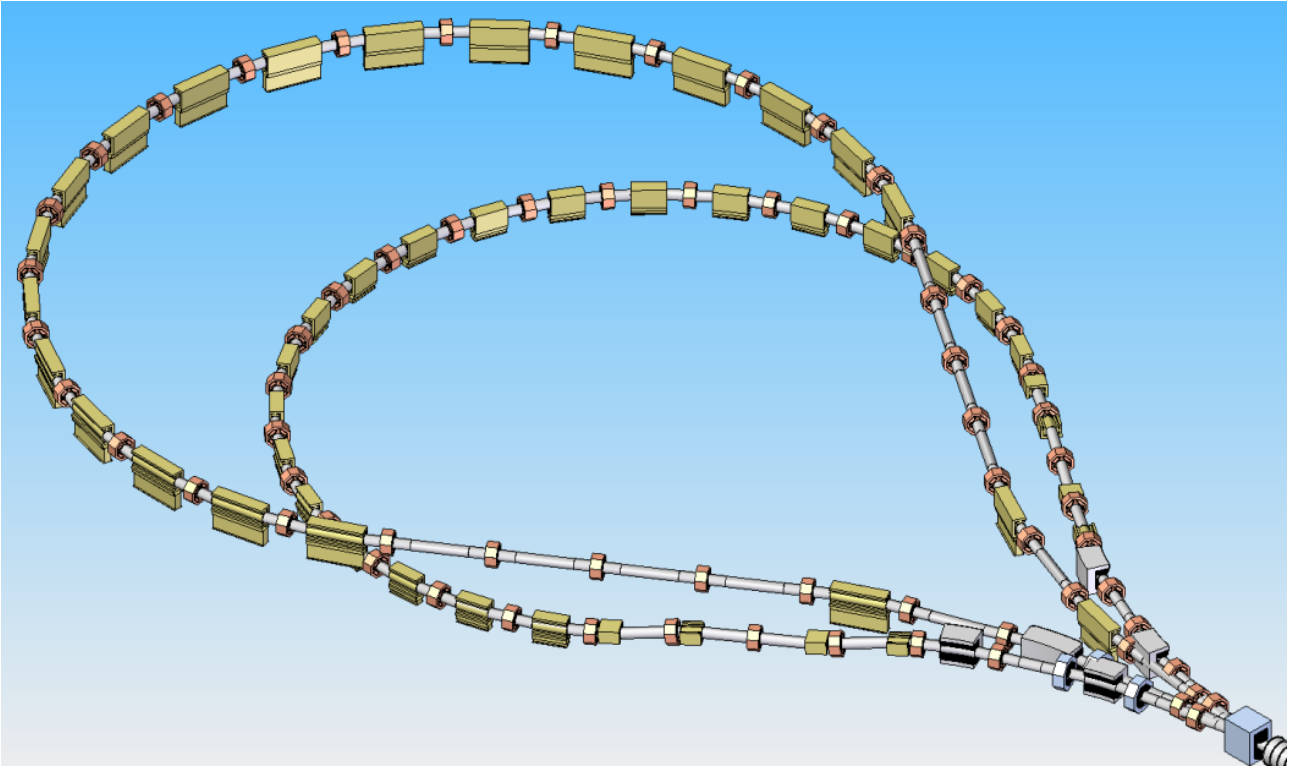


Figure 147: CAD model illustrating the general layout. First approximation dipoles shown in green and quadrupoles in skin colour. Dimensionally truer systems have been placed in areas of interest for a clash analysis coloured “grey” and “silvery.”

G.2.3 Mirror Symmetric Droplet Arcs (even numbers)

These Arcs follow the same design concept as Arcs 1 and 3 with the difference that we do not have to contend with the additional extraction of the beam. The lower energy Arc 2 passes underneath the higher energy Arc 4 on this side. Fig. 147 shows a CAD representation of the general layout.

The clashes that exist here can be solved by adapting the same technology and methodology as described in the odd Arc section. Straddling Quadrupoles need to be developed for the first set in Arc2 and Arc4. Clever design and turning the dipole magnets so they are inward facing further solves clashes with the quadrupoles.

H Decay Ring Lattice Details

H.1 Injection

The six bunches in the ring cross one another alternately at two sets of three crossing points. Injection of each pair of μ^+ and μ^- bunch trains can either be made simultaneously at one of these crossing points or with some delay interleaved between crossing points. The first option is preferred since it allows a longer kicker rise and fall time (Fig. 149) given by

$$\frac{C}{3c} - t_b \quad (48)$$

where C is the ring circumference, c is light speed and t_b is the time duration of a single bunch train. However, simultaneous injection may not be made in the middle of the arc, since muon bunches of each sign would then

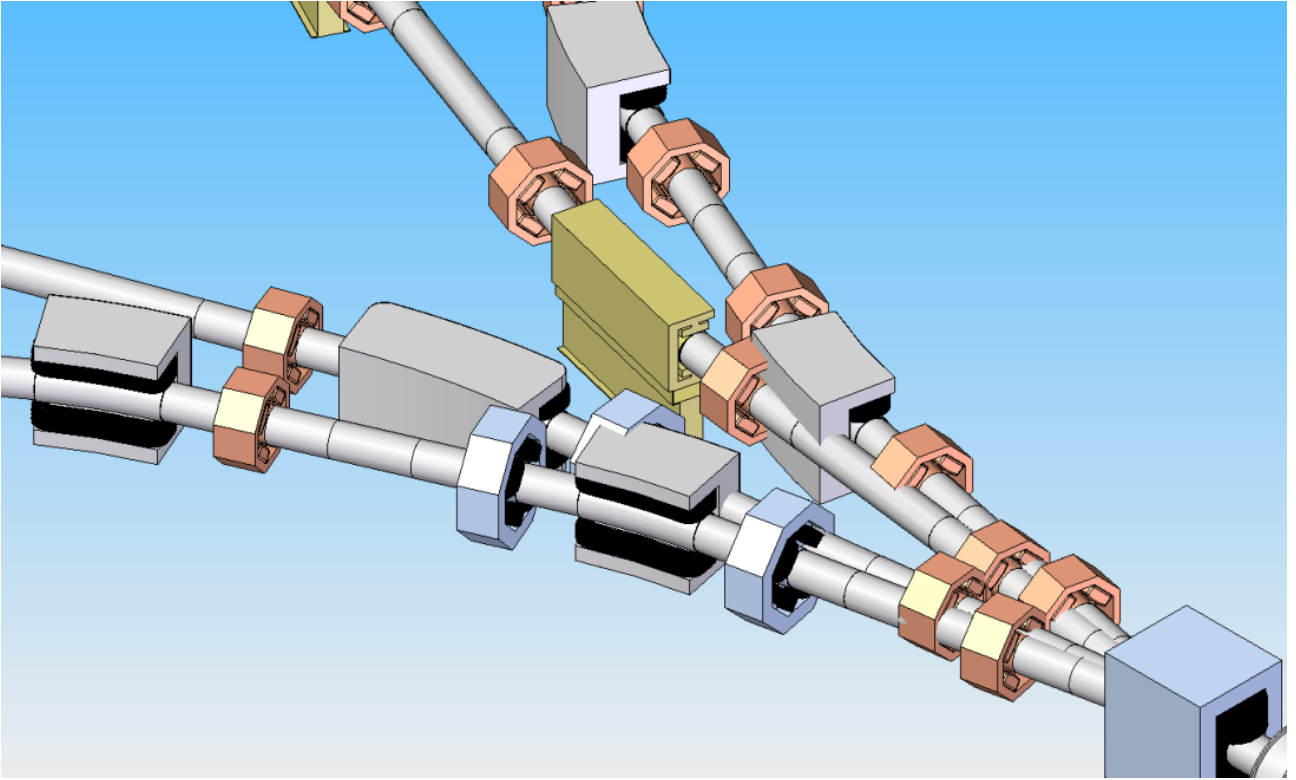


Figure 148: a close up of the RLA1 even Arc switch yard area.

arrive at the end of a production straight simultaneously. In fact, injection must be at least a distance L_{ex} on either side of the arc centre where L_{ex} is given by

$$L_{ex} = \frac{c}{2}(t_b^{ini} + n_\tau \eta T_0 \delta + t_{gap}) \quad (49)$$

where t_b^{ini} is the initial bunch duration (250 ns), t_{gap} is the desired gap between neutrino signals to be maintained for n_τ mean decay times, δ is the fractional total momentum spread, η is the phase slip and T_0 is the revolution time. Placing an insertion in the production straight is also excluded since it would result in an unacceptable increase in beam divergence. Therefore, the insertion can only be placed between the arc and the matching section to the production straight. To maintain left-right symmetry an insertion must be included at either end of the upper arc. However, insertions are not needed in the lower half of the ring and excluding them helps to increase the production efficiency. Since the insertion contributes to the width of the upper half, the lower arc must be increased in length. To reduce the number of distinct elements in the ring, this is done by increasing the drift lengths while leaving the magnet lengths unchanged.

The zero dispersion insertion is made up of four FDF triplet cells with 3.7 m long drifts in which to place injection magnets. As shown in Fig. 150, a symmetric arrangement of septa and kicker magnets about a central empty drift allows injection of both muon signs from opposing directions. The horizontal phase advance per cell is set close to $\pi/2$ to maximise the displacement at each septum owing to kickers located one and three cells away. The peak fields of both kicker magnets must be equal in magnitude to allow simultaneous injection. Injection settings are listed in Table 44. The injected beam reaches the closed orbit after passing through two opposite polarity kicker magnets. The trajectory of the opposite sign muon bunch will be antisymmetric reflected about the centre of the empty drift. This means that injection will be from the outside of the ring for one muon sign and from the inside of the ring for the other (Fig. 151). The available kicker rise/fall time, taking into account debunching up to the point of injection of the final bunch, is approximately $1.37 \mu s$. Apart from the kicker rise/fall time, previous studies indicates that these parameters are realisable [?].

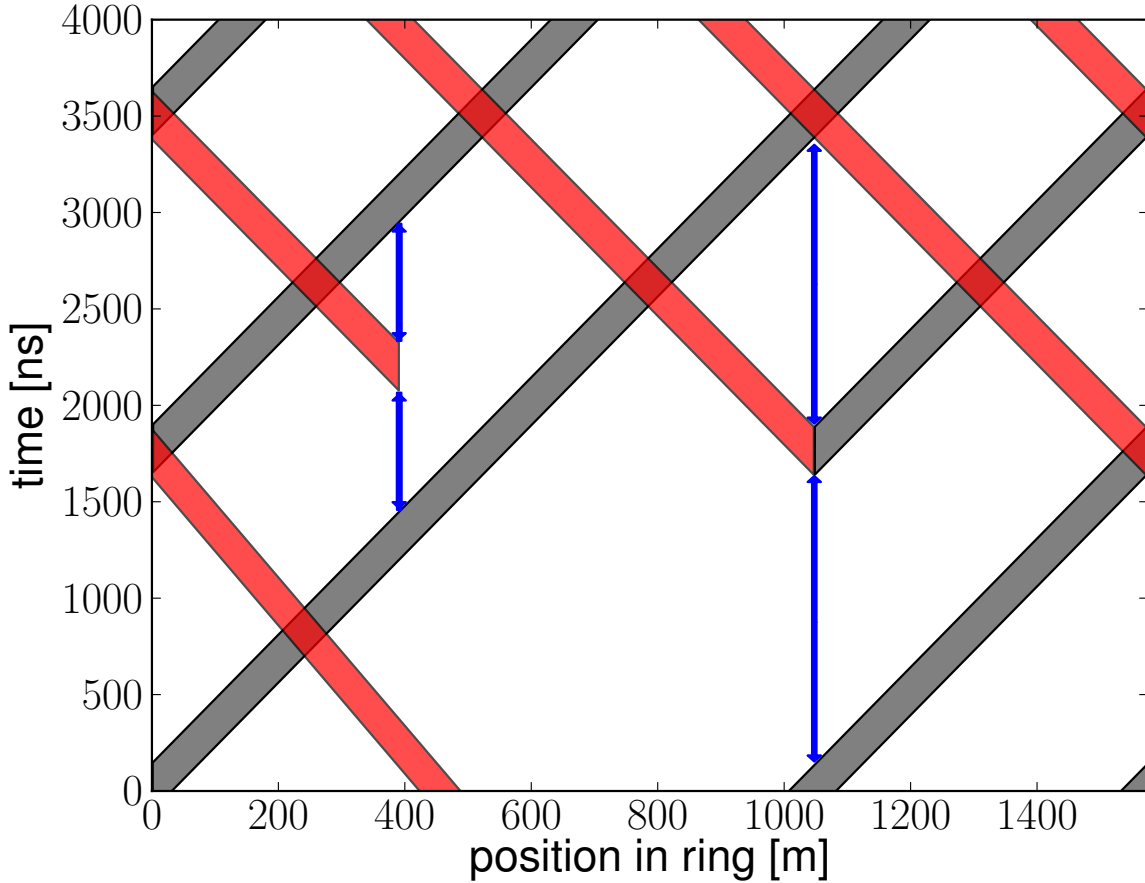


Figure 149: Illustration of two possible injection schemes. The grey and red bands represent muon bunches of opposite sign counter-rotating in the ring. The horizontal axis covers the circumference. The bunch train length is given by the thickness of the band but ignores debunching. The blue arrows on the left and right depict interleaved and simultaneous injection, respectively. The absolute position and time of injection in this figure is arbitrary. The length of the arrows before and after the bunch injection give the available kicker rise and fall time, respectively.

A dispersion suppressor section is needed between the arc and the insertion section. The suppression is done by following eleven normal arc cells with three in which the bend angle is reduced by $\frac{2}{3}$. The total number of cells must be increased by two to conserve the total bend (176.4°) in the arc. Note, since the total bend less than π the insertion does not point in the direction of the detectors. Between the dispersion suppressor and the insertion, an optics matching section comprising four quadrupoles is added. The dispersion suppressor and matching section optics are shown in Fig. 152.

H.2 Dynamic aperture

Tracking studies indicate that the dynamic aperture of the decay ring, assuming no lattice errors, is sufficient to accommodate the required $30\pi\text{mm}$ acceptance for muons with a momentum spread up to 1%. Above this momentum spread, the dynamic aperture is reduced owing to integer or half integer resonances. The momentum acceptance could be improved by introducing sextupoles to reduce the large chromaticity in the ring

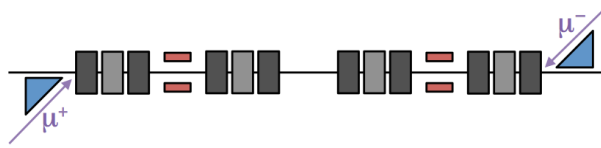


Figure 150: Schematic of the injection insertion showing the septum (blue triangles) and kicker (red squares) magnets.

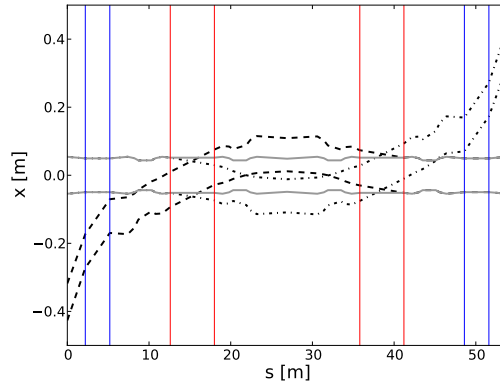


Figure 151: Beam envelope for injection trajectories (dashed and dash-dot black lines) and circulating beam (solid grey line). The envelope represents the 30π mm acceptance. The location of the septa and kicker magnets is indicated by the vertical blue and red lines, respectively.

(Table 17). The phase space up to the last stable amplitude is shown for on-momentum muons in Fig. 153 and the dependence of dynamic aperture on momentum spread is shown in Fig. 154.

I FNAL Proton Driver Annex

FNAL proposes to build Project X [264] as a new high intensity proton source. Project X has four goals:

1. To provide neutrino beams for long baseline neutrino oscillation experiments;
2. To provide intense kaon and muon beams for precision experiments;
3. To provide MW-class beam at 1 GeV to support a broad range of materials studies and energy application; and
4. To develop a path toward a muon source for a possible Neutrino Factory

The fourth goal provides the beam needed for a Neutrino Factory but additional accelerator rings will be needed to provide the correct time structure for the beam. A schematic layout of the Project X reference design is shown in figure 155.

Anticipated financial constraints have led to consideration of a staged approach to implementing Project X. Three stages are envisioned before Project X could be upgraded to be a Proton Driver for a Neutrino factory.

Table 44: Injection Settings

	Angle (mrad)	Length (m)	Field (T)	Rise/Fall Time (μ s)
Septum	67.5	3.0	0.75	-
Kicker	8.1	5.4	0.05	1.37

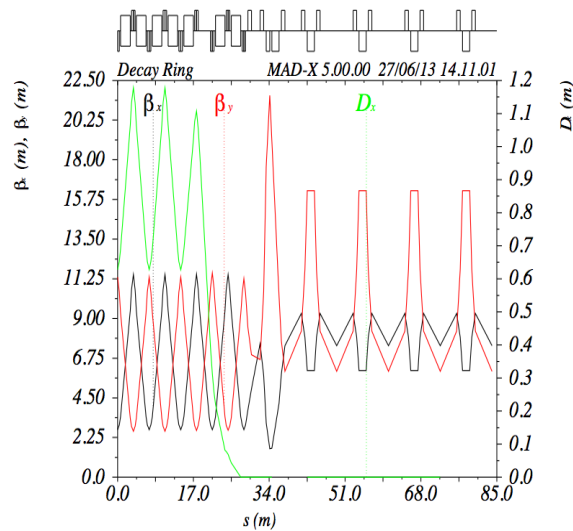


Figure 152: Matching from arc to insertion calculated using MAD-X[263].

The Project X staging is envisaged as follows:

1. Construction of a 1 GeV CW linac operating with an average current of 1 mA which will provide beam to the existing Booster and to a new 1 GeV experimental facility;
2. Addition of a 1-3 GeV CW linac operating with an average current of 1 mA providing beam to a new 3 GeV experimental facility and upgrading the 1 GeV linac to 2 mA average current; and
3. Addition of a 3-8 GeV pulsed linac and accompanying upgrades to the Recycler and Main Injector.

The upgrades to Project X to provide beam for a Neutrino factory can be considered a fourth stage.

The current Project X reference design report [264] describes in detail the accelerator facility. The primary elements are

- An H^- source consisting of a 30 keV DC ion source, Low Energy Beam Transport (LEBT), 2.1 MeV RFQ, and Medium Energy Beam Transport (MEBT) augmented with a wideband bunch-by-bunch chopper capable of generating bunch trains of arbitrary patterns at 162.5 MHz;
- A 3 GeV superconducting linac operating in CW mode, and capable of accelerating an average ($> \mu s$) beam current of 2 mA to 1 GeV and 1 mA to 3 GeV, with a peak beam current of 5 mA;
- A 3 to 8 GeV pulsed superconducting linac capable of accelerating an average current of $43 \mu A$ with a 4.3% duty factor;
- A pulsed dipole that can switch the 3 GeV beam between injection into the pulsed linac and the 3 GeV experimental program;
- An RF beam splitter that can extract 1 mA of beam at 1 GeV;
- An RF beam splitter that can deliver 3 GeV beam to multiple experiments;
- Upgrades to the 8 GeV Booster to support injection at 1 GeV (stages 1 and 2);
- Upgrades to the Main Injector/Recycler complex to support a factor of three increase in beam intensity (stage 3); and
- Target facilities required to produce secondary particle beams needed by the experimental program.

The beam originates from a 1–10 mA DC H^- source; Project X will operate the source at 5 mA. The LEBT will include a gross chopper that will operate at the μs time scale. The beam is bunched and accelerated by a CW normal-conducting RFQ to 2.1 MeV. The RFQ is followed by the MEBT section, which includes a wide band chopper capable of bunch-by-bunch passage or removal dependent upon a pre-programmed time-line to dictate the bunch pattern. To reduce the 5 mA beam current from the source into the CW linac to an average

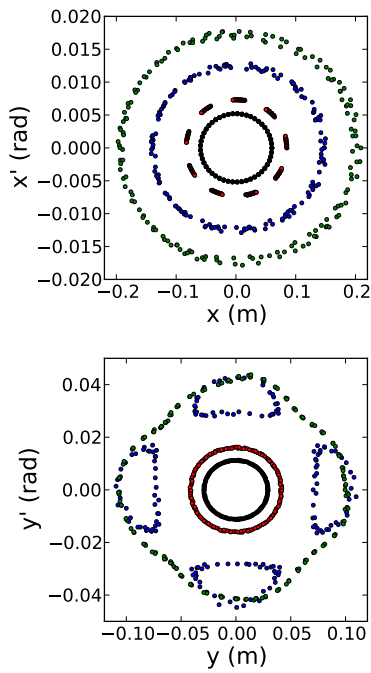


Figure 153: Phase space plots in the horizontal (top) and vertical (bottom) planes up to the maximum stable amplitude in an ideal lattice assuming zero momentum spread. Single particles were tracked for four mean decay times. The innermost black points show the required 30π mm acceptance. The other amplitudes, shown in red, blue and green, are 60π mm, 180π mm and 360π mm, respectively.

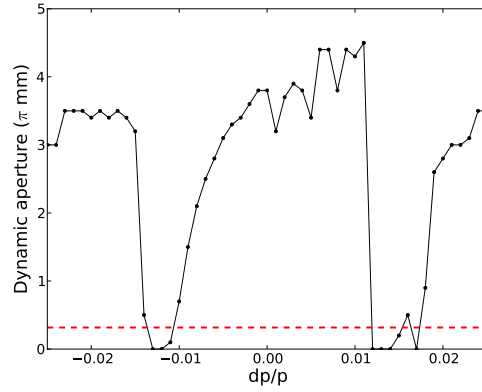


Figure 154: Dynamic aperture for off-momentum particles. The horizontal line shows the required acceptance.

Table 45: Accelerating cavity specifications for the CW linac. β_G is cavity geometrical phase velocity. The type of accelerating structure used in the various sections of the linac are noted on the figure: HWR refers to have-wave resonators; SSR refers to single spoke resonators; the 650 MHz elliptical cavities are optimised for two geometrical phase velocities in the low energy (LB) and high energy (HB) sections of the linac.

Section	β_G	Freq (MHz)	Cavity type	Number of cavities/CM	Gradient (MV/m)	Q_0 (10^{10})	Energy (MeV)
HWR	0.094	162.5	Half Wave	8/1	8.2	0.5	2.1—11
SSR1	0.186	325	Single Spoke	16/2	10	0.5	11—38
SSR2	0.431	325	Single Spoke	35/7	11.2	1.2	38—177
LB650	0.61	650	Elliptic	30/5	16.5	1.5	177—480
HB650	0.9	650	Elliptic	42/7	17.6	2.0	480—1000
HB650	0.9	650	Elliptic	120/15	17.6	2.0	1000—3000

beam current up to 2 mA, the chopper systems will always remove a majority of the beam. The bunch spacing will be 6.15 ns with an intensity of 1.9×10^8 protons per bunch exiting the front end.

Figure 156 shows a schematic of the front end and the linacs. Several types of superconducting RF cavities will be used in the CW linac. Up to 11 MeV, 162.5 MHz half-wave resonator cavities are used. Two types of single-spoke cavities operating at 325 MHz will be used to accelerate beam from to 177 MeV. The rest of the CW linac will use two types of 650 MHz elliptical cavities. Table 45 contains the CW linac cavity parameters. Cavities and focusing elements are grouped within cryomodules. In the 162,5 and 325 MHz section of the linac focusing is provided by solenoids. A standard normal conducting focusing/defocusing (FD) quadrupole doublet is used between all 650 MHz cryomodules; Additional superconducting doublets are located in the centre of the low-beta cryomodules. All magnets are superconducting with built-in dipole correctors for beam steering.

The CW linac accelerates H^- ions having the base bunch frequency of 162.5 MHz set by the RFQ. The beam may be steered toward the high-energy linac (pulsed linac), to the experimental areas, or to the linac dump. The injection to the pulsed linac is controlled by a pulsed switching-magnet. If the switch magnet is off, then the beam encounters another selection dipole magnet to steer it to the 3 GeV experimental area or the dump. In the experimental area, an RF beam separator is used to split the beam.

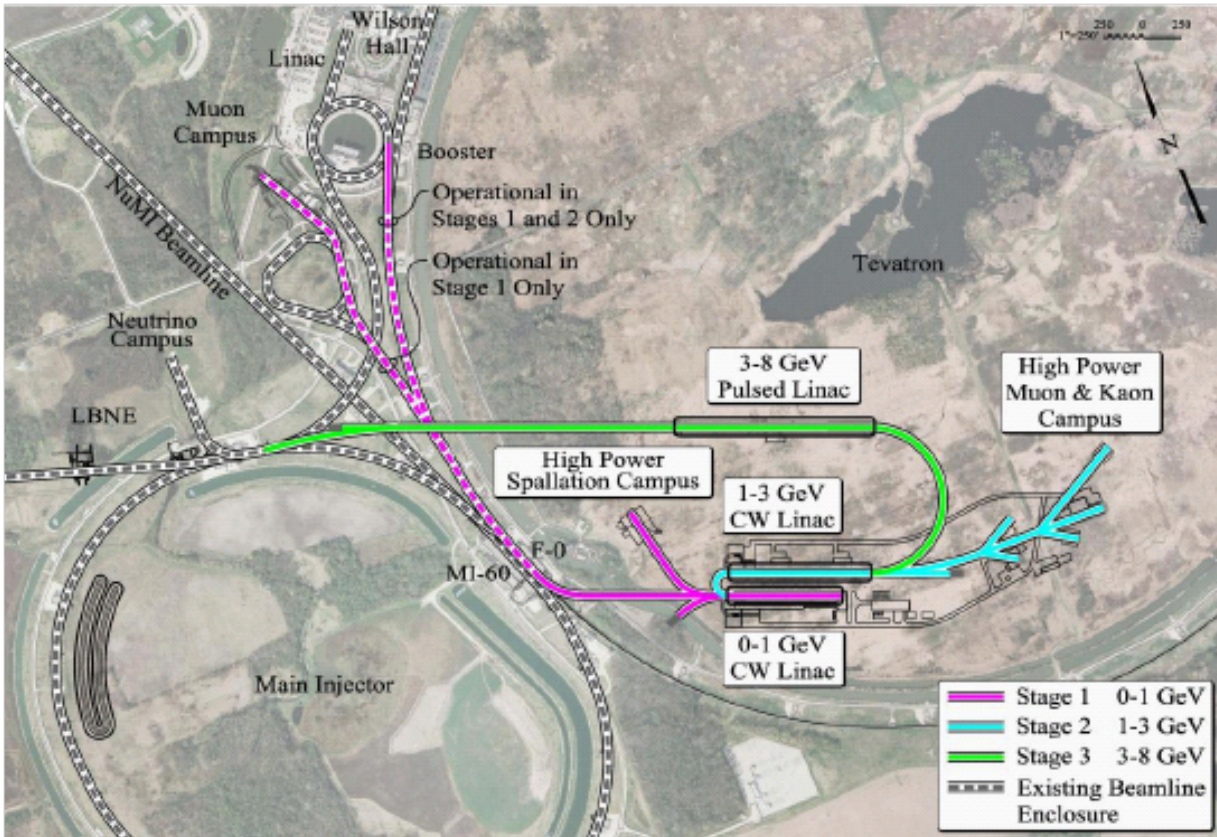


Figure 155: Schematic of FNAL Project X.

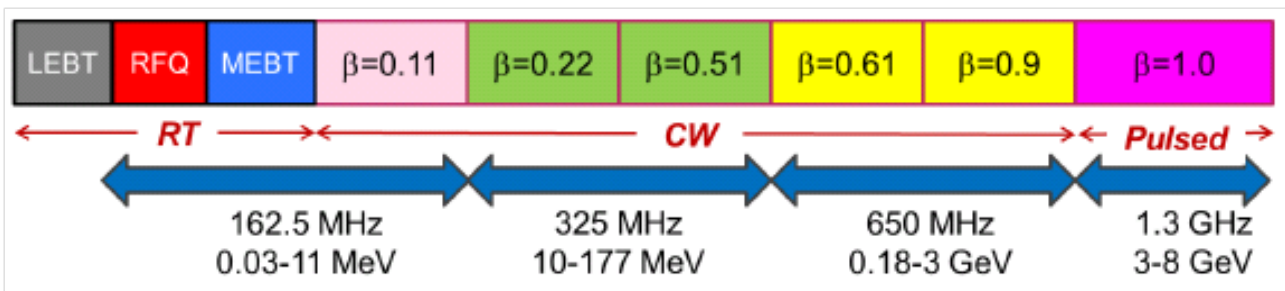


Figure 156: Front-end, CW linac and pulsed linac where the accelerating frequency, energy range and geometrical phase velocity are shown for each section.

The 3–8 GeV pulsed linac is also a superconducting linac based upon XFEL/ILC technology. ILC-type cryomodules with 1.3 GHz 9-cell cavities optimized for $\beta = 1$. A cavity gradient of 25 MV/m, which is readily achieved with current superconducting RF technology, means that 224 cavities are needed to accelerate the H^- beam from 3 to 8 GeV. Six 4.3 ms pulses of beam are provided at a rate of 10 Hz to fill the Recycler. The pulse micro-structure is determined by the Recycler RF bucket and revolution frequencies; the micro-structure is appropriately formed by the MEBT programmable chopper.

Project X fits comfortably within FNAL's Tevatron Ring. The basic idea is that, after upgrading Project X, an accumulation ring will be connected to Project X's 8 GeV transfer line between the pulsed linac and Recycler. The accumulated protons would then be transferred to a separate bunch compression ring. From that ring, beam will be sent to the Neutrino Factory target station. The target station and ensuing muon collection, acceleration and decay ring will fit within the Tevatron Ring as well.

With the initial 1 mA average CW linac current, half of the CW linac beam would have to be accelerated by the pulse linac to achieve 4 MW. This would mean that the high energy linac would have to pulse 50% of the time. Instead of converting the pulsed linac to CW, the average injection current can be raised. Provisions are being designed into Project X to support an upgrade of the CW linac to deliver an averaged beam current of 5 mA. The ion source would be operated at 10 mA and therefore the peak current will also be 10 mA in the downstream linacs. To achieve 4 MW at 8 GeV, the pulsed linac will could deliver beam pulses for 6.67 ms at 15 Hz where the programmable chopper allows half of the beam through to fill the RF buckets of the accumulation ring. The upgrade path to the pulsed linac RF systems to achieve the longer beam pulses at a larger pulsing rate is adding RF power.

The transfer line from the pulsed linac to the accumulator ring will have the same characteristics as the Project X transfer line to the Recycler that is being designed to avoid loss of the H^- ions due to Lorentz stripping, black-body radiation stripping, and stripping through collisions with residual gas in the beam pipe. Dipole fields will be limited to 0.05 T to prevent stripping of the weakly bound second electron. The vacuum of the transfer line will be required to be $\sim 1 \times 10^{-8}$ Torr. To mitigate black-body-radiation stripping, a liquid-nitrogen cryogenic shield will surround the beam pipe. Project X is not planning on a cryogenic shield since with the beam power is 345 kW results in black-body loses of 0.3 W/m at 300 K. Increasing the beam power by more than a factor of ten will result in an unacceptable beam loss rate; therefore the beam pipe will have a cryogenic shield to reduce the black-body radiation stripping to an acceptable level. The transport line will include a transverse collimation scheme for capturing large amplitude particles, a momentum-collimation system for the protection of off-energy particles, and a passive phase-rotator cavity to compensate for energy jitter.

The preliminary design for the accumulator ring has a circumference of ≈ 300 m [265]. Injection will incorporate a stripping system to convert H^- -ions to protons. Foil or laser stripping of electrons from a beam of such power will need to be developed. The stripping processes are quantum mechanical which could leave $\sim 1\%$ of the H^- ions unaffected. The non-stripped beam results in a need for a ≈ 50 kW beam dump integrated into the proton accumulation ring.

The major concern with a foil stripping system is the survival of the foil. Current systems rely upon short H^- beam pulses. Pulses much longer than 1 ms will deposit enough energy to melt/damage the foil. The foil stripping-injection process will have to employ transverse/longitudinal phase-space painting to spread the energy deposition over the foil. There must be enough time between pulses (≈ 10 ms) such that the foil can radiate. The bulk of the energy deposited in the foil comes from multiple passes of protons. To reduce the number of proton hits, the circulating beam is moved away from the foil when there is no beam being injected into the linac. Development of cooled foils or a rotating foil may also increase the stripping foil survivability.

A demonstration of high efficiency laser stripping system is needed. A laser based stripping system depends upon two abrupt magnetic fields and a bright-broad laser intersecting the beam. The H^- beam is subjected

to an abrupt exposure to a high-field dipole magnet where an electron will immediately Lorentz strip. After the dipole, the hydrogen beam is exposed to a laser that excites the remaining electron. A second high-field dipole magnet Lorentz strips the excited electron. The laser beam is divergent and at an angle with respect to the hydrogen beam so that the spread of Lorentz transformed photon energies matches the spread in hydrogen-beam energies. The laser must be bright enough to ensure a high efficiency for exciting the hydrogen. The laser could be high-powered, pulsing synchronously with the beam. A moderate-power laser with a resonant cavity across the beam could also be used. Either arrangement needs development to survive in the radiation area of an accelerator enclosure.

The CW linac front-end will be programmed to give short bursts, injecting beam repeatedly into the same RF buckets of the proton accumulator ring. When the protons have been loaded into each of four RF buckets, the RF voltage is increased to shorten the bunch lengths. A single proton bunch is then transferred to the compression ring which is the same circumference as the accumulation ring. The compression ring will do a quick bunch rotation, to achieve the desired bunch length for beam on target, followed by extraction. The single bunch transfers will occur to support a 60 Hz rate.

The extracted beam is then directed to the target. The extraction beam line will include collimation, dispersion compensation and a final focus system. The last transfer line magnet element will be outside the target station shielding and equipment; the last focusing and steering elements will be at least 3 m from the target.

J Detector working group appendices

Lead authors: PS, ABr, JM, RT

J.1 Far Detector Migration Matrices

The migration matrices used for the evaluation of the far detector sensitivities to neutrino oscillations for the International Design Study for the Neutrino Factory are presented in this appendix. Four different experimental cases are considered, defined by the charge of the muon contained in the decay ring and the polarity of the toroidal magnetic field in the detector. For each of these experimental states six matrices are provided, representing the response to the Golden Oscillation channel signal (wrong sign ν_μ and $\bar{\nu}_\mu$ appearance) and all the backgrounds due to charge misidentified examples from the associated muon neutrino disappearance channel (same sign ν_μ and $\bar{\nu}_\mu$), the neutral current background, the flavour misidentified electron neutrino (ν_e and $\bar{\nu}_e$) charged current background, the tau neutrino contamination in the signal, and the tau neutrino background of the opposite sign.

The migration matrices for a stored μ^+ , with a μ^+ focusing detector field, are found in tables 46 to 51; those for a stored μ^- , with a μ^+ focusing detector field, are found in tables 52 to 57; for a stored μ^+ , with a μ^- focusing detector field, are found in tables 58 to 63; and for a stored μ^- , with a μ^- focusing detector field, are found in tables 64 to 69. Each entry in the tables is the survival probability for each species in a specific energy range. In all tables, columns represent the true neutrino energy in GeV up to 10 GeV, and rows the reconstructed energy, also in GeV. The final row represents events with a reconstructed energy between 10.0 and 11.0 GeV, which is greater than the known maximum, due to the resolution of the detector.

Table 46: Probability of observing ν_μ CC Signal in units of 10^{-3} , as a function of energy in GeV, for a stored μ^+ with a μ^+ focusing detector field.

	0.0-0.5	0.5-1.0	1.0-1.5	1.5-2.0	2.0-2.5	2.5-3.0	3.0-3.5	3.5-4.0	4.0-4.5	4.5-5.0	5.0-5.5	5.5-6.0	6.0-7.0	7.0-8.0	8.0-9.0	9.0-10.0
0.0-0.5	0.000	0.000	0.318	1.508	0.832	0.280	0.120	0.036	0.056	0.055	0.018	0.018	0.009	0.000	0.010	0.010
0.5-1.0	0.000	0.000	0.834	8.771	7.248	3.410	1.303	0.448	0.414	0.201	0.127	0.073	0.066	0.048	0.010	0.029
1.0-1.5	0.000	0.000	2.742	22.810	22.628	10.354	4.818	1.631	1.016	0.566	0.417	0.290	0.103	0.067	0.029	0.029
1.5-2.0	0.000	0.039	5.782	42.137	49.788	30.274	13.941	4.838	2.991	1.608	0.998	0.635	0.329	0.134	0.108	0.038
2.0-2.5	0.000	0.000	2.782	42.969	74.181	56.088	31.276	13.494	5.662	2.960	1.815	1.398	0.507	0.258	0.118	0.153
2.5-3.0	0.000	0.000	1.113	21.996	73.858	87.481	56.945	31.073	14.842	7.090	3.757	1.979	0.930	0.373	0.167	0.143
3.0-3.5	0.000	0.000	0.437	8.459	45.137	91.836	87.090	55.104	30.004	14.144	6.571	3.740	1.616	0.469	0.304	0.153
3.5-4.0	0.000	0.000	0.238	3.571	18.486	60.373	96.298	86.822	55.530	29.676	14.594	7.008	2.884	1.119	0.441	0.334
4.0-4.5	0.000	0.000	0.040	1.733	7.163	28.752	72.926	98.918	81.791	53.523	29.606	15.541	5.984	1.827	0.667	0.305
4.5-5.0	0.000	0.000	0.099	1.023	3.276	11.963	38.427	78.435	97.442	79.216	52.059	29.594	11.826	3.328	1.148	0.429
5.0-5.5	0.000	0.000	0.040	0.815	1.698	5.107	16.324	46.896	85.572	95.022	77.200	50.763	22.948	6.254	1.923	0.849
5.5-6.0	0.000	0.000	0.060	0.537	1.239	2.361	7.150	22.758	53.461	86.269	89.906	71.661	40.814	12.978	4.189	1.422
6.0-7.0	0.000	0.000	0.020	0.659	1.290	2.483	4.853	14.318	40.820	94.949	151.876	173.169	135.808	60.345	21.103	6.593
7.0-8.0	0.000	0.000	0.040	0.399	0.815	1.119	1.663	3.674	8.540	24.943	61.898	113.764	159.010	125.826	61.053	22.576
8.0-9.0	0.000	0.000	0.020	0.503	0.458	0.735	0.960	1.380	2.464	5.665	15.193	37.419	99.766	154.009	117.475	60.057
9.0-10.0	0.000	0.000	0.020	0.191	0.594	0.542	0.463	0.806	0.997	2.266	3.776	8.733	37.085	108.602	146.211	114.236
10.0-11.0	0.000	0.000	0.079	1.508	1.850	2.081	1.818	2.043	2.878	3.143	5.373	7.244	18.261	72.892	203.811	359.233

Table 48: Probability of observing $\bar{\nu}_\mu$ NC Background in units of 10^{-3} , as a function of energy in GeV, for a stored μ^+ with a μ^+ focusing detector field.

	0.0-0.5	0.5-1.0	1.0-1.5	1.5-2.0	2.0-2.5	2.5-3.0	3.0-3.5	3.5-4.0	4.0-4.5	4.5-5.0	5.0-5.5	5.5-6.0	6.0-7.0	7.0-8.0	8.0-9.0	9.0-10.0
0.0-0.5	0.000	0.000	0.000	0.000	0.000	0.000	0.007	0.000	0.000	0.000	0.004	0.000	0.003	0.000	0.000	0.000
0.5-1.0	0.000	0.000	0.000	0.000	0.000	0.009	0.000	0.000	0.000	0.004	0.000	0.000	0.001	0.000	0.001	0.005
1.0-1.5	0.000	0.000	0.000	0.000	0.000	0.000	0.007	0.035	0.010	0.012	0.014	0.023	0.009	0.014	0.018	0.013
1.5-2.0	0.000	0.000	0.000	0.000	0.000	0.028	0.014	0.018	0.035	0.050	0.065	0.032	0.049	0.072	0.047	0.059
2.0-2.5	0.000	0.000	0.000	0.000	0.000	0.000	0.028	0.018	0.035	0.079	0.061	0.062	0.055	0.061	0.066	0.061
2.5-3.0	0.000	0.000	0.000	0.000	0.000	0.000	0.000	0.035	0.005	0.037	0.014	0.039	0.048	0.042	0.051	0.066
3.0-3.5	0.000	0.000	0.000	0.000	0.000	0.000	0.007	0.018	0.020	0.025	0.022	0.010	0.039	0.031	0.039	0.044
3.5-4.0	0.000	0.000	0.000	0.000	0.000	0.000	0.007	0.006	0.015	0.008	0.011	0.032	0.029	0.040	0.029	0.037
4.0-4.5	0.000	0.000	0.000	0.023	0.000	0.000	0.014	0.000	0.005	0.017	0.011	0.006	0.014	0.011	0.017	0.019
4.5-5.0	0.000	0.000	0.000	0.000	0.000	0.000	0.000	0.006	0.010	0.000	0.000	0.016	0.007	0.004	0.012	0.016
5.0-5.5	0.000	0.000	0.000	0.000	0.000	0.000	0.007	0.000	0.000	0.008	0.000	0.000	0.012	0.004	0.013	0.008
5.5-6.0	0.000	0.000	0.000	0.000	0.000	0.000	0.000	0.000	0.005	0.004	0.000	0.000	0.003	0.006	0.010	0.015
6.0-7.0	0.000	0.000	0.000	0.000	0.000	0.000	0.000	0.000	0.000	0.000	0.004	0.016	0.010	0.007	0.009	0.011
7.0-8.0	0.000	0.000	0.000	0.000	0.000	0.000	0.000	0.000	0.000	0.000	0.004	0.003	0.004	0.006	0.008	0.005
8.0-9.0	0.000	0.000	0.000	0.000	0.000	0.000	0.000	0.012	0.005	0.000	0.000	0.000	0.001	0.004	0.004	0.009
9.0-10.0	0.000	0.000	0.000	0.000	0.000	0.000	0.000	0.000	0.000	0.004	0.004	0.000	0.001	0.001	0.004	0.006
10.0-11.0	0.000	0.000	0.000	0.000	0.000	0.000	0.000	0.000	0.005	0.008	0.004	0.000	0.012	0.004	0.010	0.020

Table 50: Probability of observing ν_τ CC Contamination in units of 10^{-3} , as a function of energy in GeV, for a stored μ^+ with a μ^+ focusing detector field.

	0.0-0.5	0.5-1.0	1.0-1.5	1.5-2.0	2.0-2.5	2.5-3.0	3.0-3.5	3.5-4.0	4.0-4.5	4.5-5.0	5.0-5.5	5.5-6.0	6.0-7.0	7.0-8.0	8.0-9.0	9.0-10.0
0.0-0.5	0.000	0.000	0.000	0.000	0.000	0.000	2.857	0.112	0.118	0.065	0.114	0.053	0.034	0.042	0.048	0.029
0.5-1.0	0.000	0.000	0.000	0.000	0.000	0.000	2.857	0.675	0.826	0.582	0.478	0.550	0.400	0.327	0.237	0.213
1.0-1.5	0.000	0.000	0.000	0.000	0.000	0.000	5.714	1.912	2.124	1.974	1.457	1.704	1.212	1.085	0.861	0.670
1.5-2.0	0.000	0.000	0.000	0.000	0.000	0.000	11.429	4.386	5.250	4.304	3.325	3.319	3.021	2.603	1.871	1.510
2.0-2.5	0.000	0.000	0.000	0.000	0.000	0.000	8.571	6.636	7.550	7.086	5.625	5.928	5.215	4.089	3.359	2.602
2.5-3.0	0.000	0.000	0.000	0.000	0.000	0.000	14.286	10.348	9.320	8.996	8.449	7.916	7.329	6.012	4.777	3.950
3.0-3.5	0.000	0.000	0.000	0.000	0.000	0.000	11.429	11.135	11.266	9.157	9.724	10.525	8.650	7.603	6.051	4.613
3.5-4.0	0.000	0.000	0.000	0.000	0.000	0.000	5.714	7.536	10.795	11.196	10.452	10.702	9.625	8.768	7.026	5.485
4.0-4.5	0.000	0.000	0.000	0.000	0.000	0.000	5.714	5.624	8.553	9.319	9.268	10.400	9.469	8.873	7.460	6.195
4.5-5.0	0.000	0.000	0.000	0.000	0.000	0.000	5.714	4.499	4.955	7.798	9.678	8.910	9.638	9.205	8.413	6.779
5.0-5.5	0.000	0.000	0.000	0.000	0.000	0.000	2.857	2.362	3.244	4.821	6.558	7.436	8.744	8.705	7.820	6.782
5.5-6.0	0.000	0.000	0.000	0.000	0.000	0.000	0.000	0.562	1.652	3.430	4.350	6.105	7.132	7.740	7.285	6.732
6.0-7.0	0.000	0.000	0.000	0.000	0.000	0.000	0.000	0.562	1.652	2.589	4.554	6.514	9.598	12.730	13.349	13.738
7.0-8.0	0.000	0.000	0.000	0.000	0.000	0.000	0.000	0.337	0.472	0.874	0.888	2.165	3.989	7.461	10.604	11.446
8.0-9.0	0.000	0.000	0.000	0.000	0.000	0.000	0.000	0.225	0.118	0.324	0.228	0.763	1.355	3.483	6.398	8.887
9.0-10.0	0.000	0.000	0.000	0.000	0.000	0.000	0.000	0.000	0.000	0.194	0.296	0.124	0.461	1.502	3.465	5.543
10.0-11.0	0.000	0.000	0.000	0.000	0.000	0.000	0.000	0.450	0.649	0.453	0.524	0.799	0.806	1.296	2.525	5.755

Table 52: Probability of observing $\bar{\nu}_\mu$ CC Signal in units of 10^{-3} , as a function of energy in GeV, for a stored μ^- with a μ^+ focusing detector field.

	0.0-0.5	0.5-1.0	1.0-1.5	1.5-2.0	2.0-2.5	2.5-3.0	3.0-3.5	3.5-4.0	4.0-4.5	4.5-5.0	5.0-5.5	5.5-6.0	6.0-7.0	7.0-8.0	8.0-9.0	9.0-10.0
0.0-0.5	0.000	0.000	0.000	0.000	0.000	0.036	0.017	0.018	0.000	0.000	0.000	0.000	0.000	0.000	0.000	0.000
0.5-1.0	0.000	0.000	0.000	0.000	0.527	1.824	1.484	0.559	0.242	0.109	0.106	0.035	0.009	0.000	0.000	0.000
1.0-1.5	0.000	0.000	0.000	0.000	1.653	7.766	6.476	3.283	0.895	0.453	0.265	0.071	0.036	0.009	0.000	0.000
1.5-2.0	0.000	0.000	0.000	0.116	5.959	30.559	23.128	9.920	4.438	1.811	0.899	0.477	0.172	0.082	0.028	0.036
2.0-2.5	0.000	0.000	0.078	0.078	8.847	51.364	54.250	30.194	12.344	5.199	2.081	0.989	0.281	0.100	0.065	0.036
2.5-3.0	0.000	0.000	0.000	0.000	6.431	50.552	76.959	59.577	30.262	12.427	5.573	2.454	0.879	0.329	0.101	0.053
3.0-3.5	0.000	0.000	0.000	0.000	3.779	45.892	87.624	81.185	54.092	28.332	13.227	5.525	2.030	0.740	0.203	0.053
3.5-4.0	0.000	0.000	0.000	0.000	1.472	29.132	90.190	103.443	80.233	50.885	26.507	13.327	4.486	1.123	0.507	0.107
4.0-4.5	0.000	0.000	0.000	0.000	0.509	14.105	67.062	119.045	112.994	79.633	48.411	25.984	9.607	2.146	0.600	0.205
4.5-5.0	0.000	0.000	0.000	0.000	0.236	5.996	35.678	95.507	129.850	110.284	75.606	46.531	18.180	4.255	1.024	0.383
5.0-5.5	0.000	0.000	0.000	0.000	0.127	2.673	15.151	53.264	111.074	132.022	105.852	72.868	33.551	8.738	2.085	0.623
5.5-6.0	0.000	0.000	0.000	0.000	0.073	1.210	6.493	24.404	70.202	122.403	130.278	107.873	55.429	16.974	4.372	1.246
6.0-7.0	0.000	0.000	0.000	0.000	0.109	1.878	5.882	15.746	51.649	131.931	222.197	255.393	193.513	80.339	24.491	6.800
7.0-8.0	0.000	0.000	0.000	0.000	0.055	0.939	2.112	5.465	11.188	31.973	86.135	167.802	243.794	178.045	75.870	24.442
8.0-9.0	0.000	0.000	0.000	0.000	0.018	0.686	1.414	1.930	3.244	7.554	20.440	52.427	152.621	235.485	163.132	72.373
9.0-10.0	0.000	0.000	0.000	0.000	0.055	0.704	0.873	1.479	2.163	2.663	5.696	13.027	53.716	171.891	222.380	152.490
10.0-11.0	0.000	0.000	0.000	0.039	0.127	1.391	2.514	3.391	4.363	5.779	6.949	10.344	23.863	107.685	320.444	561.826

Table 54: Probability of observing ν_μ NC Background in units of 10^{-3} , as a function of energy in GeV, for a stored μ^- with a μ^+ focusing detector field..

	0.0-0.5	0.5-1.0	1.0-1.5	1.5-2.0	2.0-2.5	2.5-3.0	3.0-3.5	3.5-4.0	4.0-4.5	4.5-5.0	5.0-5.5	5.5-6.0	6.0-7.0	7.0-8.0	8.0-9.0	9.0-10.0
0.0-0.5	0.000	0.000	0.000	0.000	0.000	0.000	0.000	0.000	0.000	0.000	0.000	0.000	0.000	0.000	0.000	0.000
0.5-1.0	0.000	0.000	0.000	0.000	0.000	0.000	0.000	0.000	0.000	0.000	0.000	0.000	0.000	0.000	0.000	0.000
1.0-1.5	0.000	0.000	0.000	0.000	0.000	0.000	0.000	0.000	0.000	0.000	0.000	0.000	0.000	0.000	0.000	0.000
1.5-2.0	0.000	0.000	0.000	0.000	0.000	0.000	0.000	0.000	0.000	0.000	0.000	0.000	0.000	0.001	0.000	0.000
2.0-2.5	0.000	0.000	0.000	0.000	0.000	0.000	0.000	0.000	0.000	0.004	0.000	0.000	0.001	0.003	0.006	0.007
2.5-3.0	0.000	0.000	0.000	0.000	0.000	0.000	0.000	0.005	0.004	0.000	0.020	0.003	0.007	0.009	0.010	0.013
3.0-3.5	0.000	0.000	0.000	0.000	0.000	0.000	0.000	0.005	0.000	0.000	0.000	0.003	0.022	0.013	0.019	0.017
3.5-4.0	0.000	0.000	0.000	0.000	0.000	0.000	0.000	0.000	0.000	0.000	0.007	0.000	0.012	0.016	0.012	0.013
4.0-4.5	0.000	0.000	0.000	0.000	0.000	0.000	0.000	0.000	0.000	0.004	0.000	0.000	0.003	0.009	0.016	0.014
4.5-5.0	0.000	0.000	0.000	0.000	0.000	0.000	0.000	0.000	0.000	0.008	0.003	0.000	0.004	0.007	0.010	0.012
5.0-5.5	0.000	0.000	0.000	0.000	0.000	0.000	0.000	0.000	0.000	0.000	0.003	0.003	0.004	0.003	0.002	0.016
5.5-6.0	0.000	0.000	0.000	0.000	0.000	0.000	0.000	0.000	0.000	0.000	0.000	0.000	0.001	0.005	0.006	0.005
6.0-7.0	0.000	0.000	0.000	0.000	0.000	0.000	0.000	0.000	0.000	0.000	0.000	0.000	0.001	0.005	0.004	0.013
7.0-8.0	0.000	0.000	0.000	0.000	0.000	0.000	0.000	0.000	0.000	0.000	0.000	0.000	0.001	0.001	0.005	0.004
8.0-9.0	0.000	0.000	0.000	0.000	0.000	0.000	0.000	0.000	0.000	0.000	0.000	0.000	0.003	0.001	0.000	0.002
9.0-10.0	0.000	0.000	0.000	0.000	0.000	0.000	0.000	0.000	0.000	0.000	0.000	0.000	0.000	0.000	0.001	0.002
10.0-11.0	0.000	0.000	0.000	0.000	0.000	0.000	0.000	0.000	0.000	0.004	0.000	0.000	0.001	0.005	0.002	0.004

Table 56: Probability of observing $\bar{\nu}_\tau$ CC Contamination in units of 10^{-3} , as a function of energy in GeV, for a stored μ^- with a μ^+ focusing detector field.

	0.0-0.5	0.5-1.0	1.0-1.5	1.5-2.0	2.0-2.5	2.5-3.0	3.0-3.5	3.5-4.0	4.0-4.5	4.5-5.0	5.0-5.5	5.5-6.0	6.0-7.0	7.0-8.0	8.0-9.0	9.0-10.0
0.0-0.5	0.000	0.000	0.000	0.000	0.000	0.000	0.000	0.000	0.000	0.000	0.000	0.018	0.000	0.005	0.004	0.007
0.5-1.0	0.000	0.000	0.000	0.000	0.000	0.000	0.000	0.000	0.110	0.044	0.079	0.092	0.054	0.040	0.025	0.063
1.0-1.5	0.000	0.000	0.000	0.000	0.000	0.000	0.000	0.000	0.551	0.568	0.264	0.369	0.222	0.257	0.272	0.160
1.5-2.0	0.000	0.000	0.000	0.000	0.000	0.000	0.000	1.953	1.543	1.224	1.186	1.275	0.949	0.782	0.664	0.574
2.0-2.5	0.000	0.000	0.000	0.000	0.000	0.000	0.000	2.344	2.536	2.710	2.399	2.346	2.477	2.145	1.935	1.552
2.5-3.0	0.000	0.000	0.000	0.000	0.000	0.000	0.000	1.953	3.528	3.933	4.350	4.101	3.971	3.608	2.858	2.534
3.0-3.5	0.000	0.000	0.000	0.000	0.000	0.000	0.000	3.906	2.977	3.933	4.746	5.653	5.001	4.693	4.028	3.456
3.5-4.0	0.000	0.000	0.000	0.000	0.000	0.000	0.000	3.125	4.520	5.113	5.273	6.078	6.253	6.267	5.458	4.636
4.0-4.5	0.000	0.000	0.000	0.000	0.000	0.000	0.000	3.125	3.087	7.080	6.802	6.798	7.814	7.145	6.565	6.052
4.5-5.0	0.000	0.000	0.000	0.000	0.000	0.000	0.000	1.953	3.307	4.632	7.039	7.426	8.009	7.953	7.676	6.818
5.0-5.5	0.000	0.000	0.000	0.000	0.000	0.000	0.000	2.344	2.205	3.452	5.537	6.484	7.457	7.751	7.626	7.051
5.5-6.0	0.000	0.000	0.000	0.000	0.000	0.000	0.000	0.000	1.102	2.054	3.296	4.766	6.576	7.196	7.559	7.375
6.0-7.0	0.000	0.000	0.000	0.000	0.000	0.000	0.000	0.000	0.661	2.273	3.427	5.893	8.958	12.126	13.577	14.040
7.0-8.0	0.000	0.000	0.000	0.000	0.000	0.000	0.000	0.000	0.000	0.437	0.870	1.755	4.011	8.008	10.309	11.568
8.0-9.0	0.000	0.000	0.000	0.000	0.000	0.000	0.000	0.000	0.220	0.131	0.501	0.480	1.279	3.653	6.210	8.520
9.0-10.0	0.000	0.000	0.000	0.000	0.000	0.000	0.000	0.000	0.220	0.131	0.105	0.148	0.485	1.352	3.343	5.513
10.0-11.0	0.000	0.000	0.000	0.000	0.000	0.000	0.000	0.000	0.110	0.087	0.395	0.406	0.693	1.004	2.219	4.942

Table 58: Probability of observing ν_μ CC Signal in units of 10^{-3} , as a function of energy in GeV, for a stored μ^+ with a μ^- focusing detector field.

	0.0-0.5	0.5-1.0	1.0-1.5	1.5-2.0	2.0-2.5	2.5-3.0	3.0-3.5	3.5-4.0	4.0-4.5	4.5-5.0	5.0-5.5	5.5-6.0	6.0-7.0	7.0-8.0	8.0-9.0	9.0-10.0
0.0-0.5	0.000	0.000	0.209	1.501	1.116	0.291	0.195	0.018	0.076	0.000	0.000	0.000	0.000	0.000	0.000	0.000
0.5-1.0	0.000	0.000	1.067	9.682	7.721	3.363	1.083	0.474	0.265	0.147	0.126	0.018	0.056	0.037	0.009	0.000
1.0-1.5	0.000	0.000	2.280	24.380	27.695	12.654	4.902	1.713	0.851	0.698	0.343	0.162	0.065	0.056	0.009	0.000
1.5-2.0	0.000	0.000	5.250	41.311	54.168	35.216	13.870	5.830	2.592	1.781	1.156	0.575	0.185	0.065	0.019	0.045
2.0-2.5	0.000	0.000	2.615	40.890	79.721	64.141	35.164	15.649	6.469	3.286	1.861	1.329	0.408	0.176	0.104	0.027
2.5-3.0	0.000	0.000	0.795	20.170	77.631	92.448	64.396	36.181	16.155	6.664	3.216	2.119	0.787	0.333	0.075	0.100
3.0-3.5	0.000	0.000	0.251	7.944	45.314	98.247	96.807	62.871	33.198	15.842	7.389	4.274	1.630	0.601	0.254	0.100
3.5-4.0	0.000	0.000	0.251	2.929	18.310	64.632	104.124	96.593	61.214	33.759	15.592	7.740	3.048	0.971	0.264	0.145
4.0-4.5	0.000	0.000	0.126	1.830	7.083	29.598	78.213	110.858	94.544	61.020	31.979	17.149	6.076	1.360	0.537	0.254
4.5-5.0	0.000	0.000	0.063	1.226	2.886	11.526	42.303	85.680	107.654	90.153	58.483	33.131	13.274	2.859	1.102	0.354
5.0-5.5	0.000	0.000	0.084	0.787	1.788	5.145	17.600	48.752	95.944	106.932	87.210	57.176	24.593	6.476	1.798	0.554
5.5-6.0	0.000	0.000	0.105	0.659	1.222	1.636	7.654	23.483	59.587	95.073	103.959	82.010	43.045	14.035	3.964	1.226
6.0-7.0	0.000	0.000	0.105	0.842	1.647	2.254	4.298	14.064	44.700	102.911	172.632	200.438	155.580	66.688	21.949	6.131
7.0-8.0	0.000	0.000	0.084	0.512	0.708	1.036	1.740	2.988	8.323	25.315	65.494	125.413	184.722	142.157	66.260	24.980
8.0-9.0	0.000	0.000	0.084	0.458	0.514	0.854	0.728	1.130	1.967	5.434	14.905	38.985	113.138	178.720	135.354	66.719
9.0-10.0	0.000	0.000	0.084	0.220	0.443	0.400	0.533	0.528	0.946	1.524	3.487	9.463	39.608	124.171	171.897	126.316
10.0-11.0	0.000	0.000	0.105	1.757	1.718	1.654	1.776	1.731	2.081	2.735	3.505	5.243	14.969	75.949	225.408	414.546

Table 60: Probability of observing $\bar{\nu}_\mu$ NC Background in units of 10^{-3} , as a function of energy in GeV, for a stored μ^+ with a μ^- focusing detector field.

	0.0-0.5	0.5-1.0	1.0-1.5	1.5-2.0	2.0-2.5	2.5-3.0	3.0-3.5	3.5-4.0	4.0-4.5	4.5-5.0	5.0-5.5	5.5-6.0	6.0-7.0	7.0-8.0	8.0-9.0	9.0-10.0
0.0-0.5	0.000	0.000	0.000	0.000	0.000	0.000	0.000	0.000	0.000	0.004	0.000	0.000	0.000	0.000	0.001	0.000
0.5-1.0	0.000	0.000	0.000	0.000	0.013	0.000	0.000	0.000	0.000	0.000	0.000	0.000	0.004	0.003	0.001	0.003
1.0-1.5	0.000	0.000	0.000	0.000	0.000	0.000	0.000	0.006	0.000	0.004	0.004	0.010	0.012	0.006	0.009	0.007
1.5-2.0	0.000	0.000	0.000	0.000	0.000	0.028	0.007	0.029	0.050	0.050	0.040	0.042	0.043	0.040	0.051	0.043
2.0-2.5	0.000	0.000	0.000	0.000	0.000	0.000	0.007	0.029	0.025	0.050	0.051	0.035	0.058	0.045	0.052	0.055
2.5-3.0	0.000	0.000	0.000	0.000	0.000	0.000	0.007	0.017	0.025	0.042	0.036	0.023	0.046	0.041	0.039	0.066
3.0-3.5	0.000	0.000	0.000	0.000	0.000	0.009	0.000	0.006	0.005	0.025	0.014	0.013	0.023	0.039	0.041	0.042
3.5-4.0	0.000	0.000	0.000	0.000	0.000	0.000	0.000	0.006	0.000	0.017	0.011	0.010	0.012	0.018	0.028	0.031
4.0-4.5	0.000	0.000	0.000	0.000	0.000	0.000	0.000	0.000	0.000	0.012	0.004	0.023	0.019	0.028	0.027	0.019
4.5-5.0	0.000	0.000	0.000	0.000	0.000	0.000	0.000	0.000	0.000	0.000	0.004	0.003	0.009	0.008	0.016	0.014
5.0-5.5	0.000	0.000	0.000	0.000	0.000	0.000	0.000	0.000	0.000	0.000	0.007	0.000	0.016	0.005	0.004	0.019
5.5-6.0	0.000	0.000	0.000	0.000	0.000	0.000	0.000	0.000	0.005	0.004	0.000	0.003	0.003	0.014	0.007	0.011
6.0-7.0	0.000	0.000	0.000	0.000	0.013	0.000	0.000	0.000	0.005	0.004	0.004	0.006	0.012	0.006	0.017	0.021
7.0-8.0	0.000	0.000	0.000	0.000	0.000	0.000	0.000	0.000	0.000	0.000	0.000	0.000	0.007	0.010	0.002	0.008
8.0-9.0	0.000	0.000	0.000	0.000	0.000	0.000	0.000	0.006	0.000	0.000	0.007	0.003	0.006	0.006	0.006	0.010
9.0-10.0	0.000	0.000	0.000	0.000	0.000	0.000	0.000	0.000	0.005	0.000	0.004	0.000	0.003	0.004	0.001	0.011
10.0-11.0	0.000	0.000	0.000	0.000	0.000	0.000	0.000	0.000	0.000	0.008	0.007	0.010	0.013	0.010	0.017	0.024

Table 62: Probability of observing ν_τ CC Contamination in units of 10^{-3} , as a function of energy in GeV, for a stored μ^+ with a μ^- focusing detector field.

	0.0-0.5	0.5-1.0	1.0-1.5	1.5-2.0	2.0-2.5	2.5-3.0	3.0-3.5	3.5-4.0	4.0-4.5	4.5-5.0	5.0-5.5	5.5-6.0	6.0-7.0	7.0-8.0	8.0-9.0	9.0-10.0
0.0-0.5	0.000	0.000	0.000	0.000	0.000	0.000	0.000	0.333	0.000	0.032	0.115	0.036	0.041	0.031	0.026	0.029
0.5-1.0	0.000	0.000	0.000	0.000	0.000	0.000	2.770	1.112	0.699	0.452	0.576	0.342	0.421	0.341	0.332	0.188
1.0-1.5	0.000	0.000	0.000	0.000	0.000	0.000	5.540	3.224	3.264	2.001	2.188	1.404	1.324	1.112	0.817	0.614
1.5-2.0	0.000	0.000	0.000	0.000	0.000	0.000	2.770	6.670	6.179	3.745	3.916	3.582	3.238	2.465	2.180	1.659
2.0-2.5	0.000	0.000	0.000	0.000	0.000	0.000	11.080	9.337	9.035	6.811	6.381	6.103	5.308	4.699	3.596	2.689
2.5-3.0	0.000	0.000	0.000	0.000	0.000	0.000	11.080	9.782	9.909	9.329	8.431	9.289	7.609	6.440	4.833	3.694
3.0-3.5	0.000	0.000	0.000	0.000	0.000	0.000	11.080	10.227	11.541	10.620	10.412	10.441	9.536	7.934	6.170	4.876
3.5-4.0	0.000	0.000	0.000	0.000	0.000	0.000	8.448	12.299	10.717	11.218	10.891	10.622	10.622	9.387	7.664	5.953
4.0-4.5	0.000	0.000	0.000	0.000	0.000	0.000	5.540	4.446	8.044	9.361	10.665	11.648	10.527	9.513	8.224	7.110
4.5-5.0	0.000	0.000	0.000	0.000	0.000	0.000	8.310	2.446	5.188	7.586	9.605	10.387	10.371	9.743	8.656	7.262
5.0-5.5	0.000	0.000	0.000	0.000	0.000	0.000	2.770	2.334	4.197	5.004	7.394	9.055	9.238	9.051	9.202	7.894
5.5-6.0	0.000	0.000	0.000	0.000	0.000	0.000	0.000	1.112	1.865	3.099	4.492	6.517	7.914	8.826	8.713	7.601
6.0-7.0	0.000	0.000	0.000	0.000	0.000	0.000	0.000	0.445	1.049	2.453	4.123	6.427	10.276	13.949	15.516	14.559
7.0-8.0	0.000	0.000	0.000	0.000	0.000	0.000	0.000	0.000	0.233	0.420	1.129	1.818	4.744	8.506	11.343	13.305
8.0-9.0	0.000	0.000	0.000	0.000	0.000	0.000	0.000	0.333	0.175	0.194	0.253	0.612	1.554	4.117	7.537	10.160
9.0-10.0	0.000	0.000	0.000	0.000	0.000	0.000	0.000	0.000	0.291	0.065	0.046	0.324	0.380	1.390	3.684	6.683
10.0-11.0	0.000	0.000	0.000	0.000	0.000	0.000	0.000	0.111	0.350	0.549	0.576	0.396	0.652	1.033	2.604	6.181

Table 64: Probability of observing $\bar{\nu}_\mu$ CC Signal in units of 10^{-3} , as a function of energy in GeV, for a stored μ^- with a μ^- focusing detector field.

	0.0-0.5	0.5-1.0	1.0-1.5	1.5-2.0	2.0-2.5	2.5-3.0	3.0-3.5	3.5-4.0	4.0-4.5	4.5-5.0	5.0-5.5	5.5-6.0	6.0-7.0	7.0-8.0	8.0-9.0	9.0-10.0
0.0-0.5	0.000	0.000	0.000	0.000	0.104	0.088	0.120	0.018	0.056	0.000	0.018	0.000	0.019	0.000	0.000	0.000
0.5-1.0	0.000	0.000	0.000	0.018	2.534	3.199	1.598	0.784	0.282	0.166	0.055	0.055	0.019	0.029	0.000	0.019
1.0-1.5	0.000	0.000	0.000	0.129	9.478	11.743	6.598	2.637	1.296	0.515	0.458	0.164	0.085	0.067	0.060	0.019
1.5-2.0	0.000	0.000	0.000	0.166	23.104	38.568	21.890	9.781	4.075	1.804	0.953	0.564	0.283	0.173	0.070	0.039
2.0-2.5	0.000	0.000	0.000	0.092	22.531	60.365	49.278	26.938	10.667	4.842	2.053	1.055	0.529	0.211	0.060	0.116
2.5-3.0	0.000	0.000	0.000	0.000	15.588	57.781	71.287	48.442	24.395	10.162	4.455	2.564	0.831	0.557	0.189	0.116
3.0-3.5	0.000	0.000	0.000	0.018	8.870	54.213	82.112	71.656	46.311	25.018	9.679	5.074	1.833	0.586	0.309	0.203
3.5-4.0	0.000	0.000	0.000	0.018	4.721	35.509	88.435	95.263	70.461	42.876	21.669	11.057	3.751	0.884	0.459	0.251
4.0-4.5	0.000	0.000	0.000	0.018	2.187	17.579	66.494	107.520	100.115	69.588	39.762	21.187	7.984	1.960	0.678	0.387
4.5-5.0	0.000	0.000	0.000	0.018	1.232	7.541	35.755	86.444	115.063	97.515	65.794	39.628	15.334	3.948	1.157	0.638
5.0-5.5	0.000	0.000	0.000	0.018	0.972	3.692	15.051	50.865	99.814	116.973	95.327	61.942	28.429	7.541	2.094	0.764
5.5-6.0	0.000	0.000	0.000	0.000	0.521	2.356	6.460	23.660	65.691	105.615	113.586	89.476	47.165	14.824	4.069	1.314
6.0-7.0	0.000	0.000	0.000	0.018	0.903	3.006	5.704	14.253	48.733	116.016	195.109	222.889	167.582	69.487	21.909	6.737
7.0-8.0	0.000	0.000	0.000	0.000	0.434	1.318	2.577	4.133	10.554	29.363	77.398	144.325	203.437	153.106	65.828	22.259
8.0-9.0	0.000	0.000	0.000	0.000	0.295	0.949	1.529	1.853	3.211	8.155	18.900	47.248	132.397	198.096	137.808	63.337
9.0-10.0	0.000	0.000	0.000	0.000	0.156	0.721	1.151	1.390	2.103	3.038	6.050	11.857	49.622	144.316	186.553	129.505
10.0-11.0	0.000	0.000	0.000	0.074	1.041	2.338	3.179	3.634	4.056	6.186	8.378	11.730	26.559	101.392	280.493	477.765

Table 66: Probability of observing ν_μ NC Background in units of 10^{-3} , as a function of energy in GeV, for a stored μ^- with a μ^- focusing detector field.

	0.0-0.5	0.5-1.0	1.0-1.5	1.5-2.0	2.0-2.5	2.5-3.0	3.0-3.5	3.5-4.0	4.0-4.5	4.5-5.0	5.0-5.5	5.5-6.0	6.0-7.0	7.0-8.0	8.0-9.0	9.0-10.0
0.0-0.5	0.000	0.000	0.000	0.000	0.000	0.000	0.000	0.000	0.000	0.000	0.000	0.000	0.000	0.000	0.000	0.000
0.5-1.0	0.000	0.000	0.000	0.000	0.000	0.000	0.000	0.000	0.000	0.000	0.000	0.000	0.000	0.000	0.001	0.000
1.0-1.5	0.000	0.000	0.000	0.000	0.000	0.000	0.000	0.000	0.000	0.000	0.000	0.000	0.000	0.000	0.000	0.000
1.5-2.0	0.000	0.000	0.000	0.000	0.000	0.000	0.000	0.005	0.000	0.004	0.003	0.000	0.000	0.000	0.000	0.003
2.0-2.5	0.000	0.000	0.000	0.000	0.000	0.000	0.000	0.000	0.004	0.000	0.003	0.006	0.006	0.007	0.005	0.011
2.5-3.0	0.000	0.000	0.000	0.000	0.000	0.000	0.000	0.010	0.009	0.000	0.007	0.016	0.007	0.017	0.029	0.019
3.0-3.5	0.000	0.000	0.000	0.000	0.000	0.000	0.000	0.000	0.004	0.004	0.014	0.016	0.010	0.021	0.017	0.019
3.5-4.0	0.000	0.000	0.000	0.000	0.000	0.000	0.000	0.000	0.004	0.004	0.007	0.006	0.012	0.016	0.016	0.022
4.0-4.5	0.000	0.000	0.000	0.000	0.000	0.000	0.000	0.000	0.000	0.000	0.010	0.000	0.007	0.011	0.016	0.022
4.5-5.0	0.000	0.000	0.000	0.000	0.000	0.000	0.000	0.000	0.000	0.000	0.000	0.000	0.006	0.004	0.008	0.014
5.0-5.5	0.000	0.000	0.000	0.000	0.000	0.000	0.000	0.000	0.000	0.000	0.003	0.003	0.004	0.004	0.008	0.004
5.5-6.0	0.000	0.000	0.000	0.000	0.000	0.000	0.000	0.000	0.000	0.004	0.000	0.000	0.004	0.004	0.005	0.008
6.0-7.0	0.000	0.000	0.000	0.000	0.000	0.000	0.000	0.000	0.000	0.004	0.000	0.000	0.003	0.003	0.006	0.008
7.0-8.0	0.000	0.000	0.000	0.000	0.000	0.000	0.000	0.000	0.004	0.004	0.000	0.000	0.000	0.004	0.002	0.001
8.0-9.0	0.000	0.000	0.000	0.000	0.000	0.000	0.000	0.000	0.000	0.000	0.000	0.003	0.000	0.004	0.002	0.008
9.0-10.0	0.000	0.000	0.000	0.000	0.000	0.000	0.000	0.000	0.000	0.000	0.000	0.003	0.003	0.000	0.002	0.000
10.0-11.0	0.000	0.000	0.000	0.000	0.000	0.000	0.000	0.000	0.000	0.000	0.000	0.000	0.003	0.013	0.008	0.014

Table 68: Probability of observing $\bar{\nu}_\tau$ CC Contamination in units of 10^{-3} , as a function of energy in GeV, for a stored μ^- with a μ^- focusing detector field.

	0.0-0.5	0.5-1.0	1.0-1.5	1.5-2.0	2.0-2.5	2.5-3.0	3.0-3.5	3.5-4.0	4.0-4.5	4.5-5.0	5.0-5.5	5.5-6.0	6.0-7.0	7.0-8.0	8.0-9.0	9.0-10.0
0.0-0.5	0.000	0.000	0.000	0.000	0.000	0.000	0.000	0.000	0.000	0.000	0.000	0.000	0.000	0.005	0.004	0.007
0.5-1.0	0.000	0.000	0.000	0.000	0.000	0.000	0.000	0.000	0.109	0.044	0.026	0.130	0.047	0.071	0.067	0.083
1.0-1.5	0.000	0.000	0.000	0.000	0.000	0.000	0.000	0.000	0.652	0.483	0.475	0.335	0.418	0.328	0.360	0.302
1.5-2.0	0.000	0.000	0.000	0.000	0.000	0.000	0.000	1.200	1.846	2.063	1.901	1.844	1.536	1.164	1.017	0.944
2.0-2.5	0.000	0.000	0.000	0.000	0.000	0.000	0.000	5.598	3.693	2.283	3.169	3.352	2.782	2.208	2.160	1.641
2.5-3.0	0.000	0.000	0.000	0.000	0.000	0.000	0.000	4.398	3.476	4.082	4.278	4.041	3.712	3.740	3.140	2.623
3.0-3.5	0.000	0.000	0.000	0.000	0.000	0.000	0.000	2.799	3.801	5.399	5.677	5.364	5.140	4.930	4.250	3.497
3.5-4.0	0.000	0.000	0.000	0.000	0.000	0.000	0.000	1.599	6.082	5.575	6.073	5.699	6.346	5.777	5.388	4.545
4.0-4.5	0.000	0.000	0.000	0.000	0.000	0.000	0.000	1.999	4.453	6.716	6.918	7.338	7.215	7.032	6.439	5.676
4.5-5.0	0.000	0.000	0.000	0.000	0.000	0.000	0.000	1.999	4.019	5.267	6.628	6.835	7.491	7.219	6.992	6.338
5.0-5.5	0.000	0.000	0.000	0.000	0.000	0.000	0.000	1.999	1.955	3.731	5.360	6.127	6.979	7.279	7.059	6.501
5.5-6.0	0.000	0.000	0.000	0.000	0.000	0.000	0.000	0.800	0.978	1.844	3.961	5.047	5.834	6.538	6.674	6.210
6.0-7.0	0.000	0.000	0.000	0.000	0.000	0.000	0.000	0.400	0.326	1.361	3.380	4.563	8.063	10.278	11.949	11.913
7.0-8.0	0.000	0.000	0.000	0.000	0.000	0.000	0.000	0.000	0.109	0.658	1.215	1.620	3.449	6.392	8.453	9.721
8.0-9.0	0.000	0.000	0.000	0.000	0.000	0.000	0.000	0.000	0.326	0.088	0.396	0.596	1.381	2.924	5.346	7.279
9.0-10.0	0.000	0.000	0.000	0.000	0.000	0.000	0.000	0.000	0.109	0.132	0.079	0.223	0.451	1.200	2.562	4.493
10.0-11.0	0.000	0.000	0.000	0.000	0.000	0.000	0.000	0.000	0.000	0.219	0.396	0.633	0.701	1.038	2.282	4.795

J.2 Near Detector Migration Matrices

Near detector flux migration matrices are presented in this appendix.

J.2.1 Introduction

A simulation of the ND was performed in the scenario of a 10 GeV Neutrino Factory. One of the means for the flux monitoring is by identifying elastic neutrino-electron scattering interactions in the detector. In the following, *signal* refers to neutrino-electron scattering events. The Neutrino Factory has two modes of operation:

- μ^- decay mode: the beam is a mixture of ν_μ and $\bar{\nu}_e$,
- μ^+ decay mode: the beam is a mixture of $\bar{\nu}_\mu$ and ν_e .

We label the signal candidate sample in the first (second) NF operation mode as ES^- (ES^+). Hereafter we discuss the first mode of operation. Extension to the second one is straightforward.

The final states of $\nu_\mu + e^-$ and $\bar{\nu}_e + e^-$ interactions are indistinguishable in the ND. Hence, the number of elastic neutrino-electron interactions in the ND will be:

$$\frac{dN_{sig}}{dE} = \frac{dN_{flux,\nu_\mu}}{dE} P(\nu_\mu e|E) + \frac{dN_{flux,\bar{\nu}_e}}{dE} P(\bar{\nu}_e e|E), \quad (50)$$

where $N_{flux,\cdot}$ is the number of neutrinos incident on the ND and $P(\cdot|E)$ is the probability of interaction in the ND given neutrino energy E . Let $\varepsilon(E)$ be the reconstruction and selection efficiency. Let $p_{res}(E_{rec}|E)$ be the detector *response matrix* - the conditional probability density of a candidate's reconstructed neutrino energy E_{rec} given a true neutrino energy E . Then, the number of candidates as a function of the reconstructed neutrino energy is given by:

$$\frac{dN_{cand}}{dE_{rec}} = \int \frac{dN_{sig}}{dE} \varepsilon(E) p_{res}(E_{rec}|E) dE. \quad (51)$$

The fluxes of the two neutrino species cannot be disentangled by measuring N_{cand} and knowing Ps , ε and p_{res} . However, the two flux energy spectra are closely coupled since they are product of the same muon beam decay. Thus, we propose to use the relation of the two energy spectra obtained from the Monte Carlo simulation of the beam:

$$\rho(E) = \frac{dN_{flux,\nu_\mu}/dE}{dN_{flux,\nu_\mu}/dE + dN_{flux,\bar{\nu}_e}/dE}. \quad (52)$$

Consequently, flux migration functions can be constructed for both neutrino species:

$$M_{\nu_\mu}(E_{rec}, E) = \left(P(\nu_\mu e|E) + \frac{1 - \rho(E)}{\rho(E)} P(\bar{\nu}_e e|E) \right) \varepsilon(E) p_{res}(E_{rec}|E) \quad (53)$$

and

$$M_{\bar{\nu}_e}(E_{rec}, E) = \left(\frac{\rho(E)}{1 - \rho(E)} P(\nu_\mu e|E) + P(\bar{\nu}_e e|E) \right) \varepsilon(E) p_{res}(E_{rec}|E). \quad (54)$$

Then, equation 51 can be written as:

$$\frac{dN_{cand}}{dE_{rec}} = \int \frac{dN_{flux,\nu_\mu}}{dE} M_{\nu_\mu}(E_{rec}, E) dE \quad (55)$$

and

$$\frac{dN_{cand}}{dE_{rec}} = \int \frac{dN_{flux,\bar{\nu}_e}}{dE} M_{\bar{\nu}_e}(E_{rec}, E) dE. \quad (56)$$

These are the relations between measured energy spectra in the ND and incident neutrino flux for both neutrino species. Ideally, one should provide approximations (called *migration matrices*) to the functions $M_{\nu_\mu}(E_{rec}, E)$ and $M_{\bar{\nu}_e}(E_{rec}, E)$. Due to the fact that the two neutrino species cannot be disentangled by their elastic scattering on electrons in the ND, we rather provide the detector *response matrix* for each mode of operation.

J.2.2 Discretisation of the energy functions

We denote the bins in true neutrino energy by the index $j = 1 \dots n$. The bin boundaries are a_j and b_j . Bins in reconstructed neutrino energy are denoted by $i = 0 \dots n+1$, where the $i = 0$ and $i = n+1$ bins are “overflow” bins (i.e. one may assume that $a_0 = -\infty$ and $b_{n+1} = +\infty$). Let $w(E)$ be a weighting function proportional to dN_{sig}/dE , the expected signal events with the current Monte Carlo simulation of the neutrino flux. We tabulate the functions mentioned above in the following manner:

$$N_{flux,\cdot}^j \equiv \int_{a_j}^{b_j} \frac{dN_{flux,\cdot}}{dE} dE, \quad (57)$$

$$\rho_j \equiv \frac{N_{flux,\nu_\mu}^j}{N_{flux,\nu_\mu}^j + N_{flux,\bar{\nu}_e}^j}, \quad (58)$$

$$W_j \equiv \int_{a_j}^{b_j} w(E) dE, \quad (59)$$

$$P_j(\cdot) \equiv \frac{1}{W_j} \int_{a_j}^{b_j} w(E) P(\cdot|E) dE, \quad (60)$$

$$\varepsilon_j \equiv \frac{1}{W_j} \int_{a_j}^{b_j} w(E) \varepsilon(E) dE, \quad (61)$$

$$p_{res}^j \equiv \frac{1}{W_j} \int_{a_j}^{b_j} w(E) p_{res}(E_{rec}|E) dE, \quad (62)$$

$$p_{res}^{ij} \equiv \int_{a_i}^{b_i} p_{res}^j(E_{rec}|E) dE_{rec}. \quad (63)$$

The values $P_j(\cdot)$, ρ_j , ε_j and p_{res}^{ij} are given in the tables below. The bins in the true neutrino energy E_{true} go up to 10.5 GeV because of the energy spread of the muon beam. The bins in the reconstructed energy E_{rec} go from -1 GeV up to 11.0 GeV due to the detector resolution.

Table 70: Probability of interaction, muon neutrino flux fraction ρ and efficiency of ND for both modes of operation.

E_{true}	ES ⁻ sample				ES ⁺ sample			
	$P_j(\nu_{\mu}e) \times 10^{15}$	$P_j(\bar{\nu}_e e) \times 10^{15}$	ρ_j	ϵ_j	$P_j(\bar{\nu}_{\mu}e) \times 10^{15}$	$P_j(\nu_e e) \times 10^{15}$	ρ_j	ϵ_j
0.0-0.5	0.0185	0.0611	.3313 ± .0149	.0000 ± .0000	0.0129	0.1182	.3312 ± 0.0098	.0000 ± .0000
0.5-1.0	0.0458	0.1191	.3394 ± .0059	.0639 ± .0141	0.0461	0.2675	.3335 ± 0.0037	.1233 ± .0132
1.0-1.5	0.0710	0.1821	.3415 ± .0036	.1229 ± .0095	0.0566	0.4472	.3473 ± 0.0023	.2011 ± .0079
1.5-2.0	0.1077	0.2644	.3515 ± .0027	.1451 ± .0062	0.0883	0.6180	.3523 ± 0.0017	.2413 ± .0053
2.0-2.5	0.1395	0.3312	.3611 ± .0022	.1860 ± .0049	0.1098	0.7803	.3570 ± 0.0014	.2673 ± .0039
2.5-3.0	0.1587	0.3990	.3645 ± .0018	.2207 ± .0041	0.1361	0.9590	.3659 ± 0.0012	.2872 ± .0030
3.0-3.5	0.1916	0.4813	.3778 ± .0016	.2250 ± .0033	0.1613	1.1366	.3767 ± 0.0010	.2981 ± .0025
3.5-4.0	0.2203	0.5495	.3858 ± .0015	.2359 ± .0028	0.1856	1.3053	.3864 ± 0.0009	.3032 ± .0021
4.0-4.5	0.2516	0.6243	.3964 ± .0014	.2471 ± .0025	0.2124	1.4998	.3998 ± 0.0009	.3106 ± .0018
4.5-5.0	0.2787	0.7055	.4150 ± .0013	.2542 ± .0022	0.2356	1.6762	.4142 ± 0.0008	.3180 ± .0017
5.0-5.5	0.3110	0.7816	.4333 ± .0012	.2590 ± .0021	0.2632	1.8617	.4326 ± 0.0008	.3003 ± .0015
5.5-6.0	0.3412	0.8478	.4566 ± .0012	.2492 ± .0019	0.2837	2.0513	.4557 ± 0.0008	.2719 ± .0014
6.0-6.5	0.3683	0.9341	.4817 ± .0012	.2389 ± .0018	0.3128	2.2339	.4819 ± 0.0007	.2458 ± .0013
6.5-7.0	0.4030	1.0176	.5109 ± .0012	.2323 ± .0017	0.3427	2.4296	.5135 ± 0.0007	.2266 ± .0012
7.0-7.5	0.4349	1.1002	.5485 ± .0012	.2220 ± .0017	0.3673	2.6287	.5499 ± 0.0008	.2061 ± .0012
7.5-8.0	0.4741	1.1870	.5934 ± .0013	.2097 ± .0017	0.3963	2.8198	.5918 ± 0.0008	.1900 ± .0012
8.0-8.5	0.5051	1.2643	.6450 ± .0013	.2012 ± .0018	0.4226	3.0145	.6477 ± 0.0008	.1758 ± .0013
8.5-9.0	0.5347	1.3446	.7130 ± .0014	.1857 ± .0020	0.4490	3.2181	.7160 ± 0.0009	.1648 ± .0015
9.0-9.5	0.5696	1.4215	.8040 ± .0015	.1720 ± .0024	0.4740	3.3980	.8008 ± 0.0010	.1546 ± .0019
9.5-10.0	0.6042	1.4867	.8920 ± .0020	.1530 ± .0039	0.5019	3.5981	.8952 ± 0.0012	.1411 ± .0035
10.0-10.5	0.6055	1.4491	.9580 ± .0058	.1355 ± .0178	0.5002	3.6802	.9523 ± 0.0039	.1383 ± .0176

Table 71: ND response matrix for the ES⁻ sample, i.e. the probability to reconstruct neutrino energy E_{rec} given true neutrino energy E_{true} .

E_{rec}	E_{true}	0.0-0.5	0.5-1.0	1.0-1.5	1.5-2.0	2.0-2.5	2.5-3.0	3.0-3.5	3.5-4.0	4.0-4.5	4.5-5.0	5.0-5.5	5.5-6.0	6.0-6.5	6.5-7.0	7.0-7.5	7.5-8.0	8.0-8.5	8.5-9.0	9.0-9.5	9.5-10.0	10.0-10.5	10.5-11.5	
-1.0-0.0	.00000	.00000	.00000	.00000	.00000	.00000	.00000	.00000	.00000	.00000	.00000	.00000	.00000	.00000	.00000	.00000	.00000	.00000	.00000	.00000	.00000	.00000	.00000	.00000
0.0-0.5	.00000	.00000	.00000	.00000	.00000	.00000	.00000	.00000	.00000	.00014	.00000	.00000	.00000	.00000	.00000	.00000	.00000	.00000	.00000	.00000	.00000	.00000	.00000	.00000
0.5-1.0	.00000	.52632	.17808	.05066	.03727	.03727	.02305	.01453	.01214	.01229	.00711	.00885	.00931	.00834	.00645	.00730	.00583	.00675	.00478	.00608	.00477	.00000	.00000	.00000
1.0-1.5	.00000	.36842	.49315	.19604	.09583	.05920	.04017	.04017	.02898	.02741	.01990	.01949	.01715	.01869	.01662	.01412	.01471	.01360	.01614	.01546	.01191	.01191	.02000	.02000
1.5-2.0	.00000	.05263	.19863	.38546	.18012	.10167	.06524	.04856	.03632	.02821	.02629	.02451	.02451	.02263	.02095	.02070	.01956	.02035	.02032	.02179	.01191	.02000	.02000	.02000
2.0-2.5	.00000	.00000	.06164	.14537	.07269	.30080	.15273	.09117	.06246	.04451	.03762	.03434	.02933	.02534	.02566	.02207	.02261	.02078	.02153	.02153	.02145	.02224	.00000	.00000
2.5-3.0	.00000	.00000	.00000	.02055	.03084	.14286	.24401	.14103	.08518	.06231	.04582	.04140	.03774	.02966	.02725	.02680	.02521	.02292	.02525	.02153	.02224	.00000	.00000	.00000
3.0-3.5	.00000	.00000	.00000	.01370	.03084	.06832	.16132	.21339	.14177	.09114	.05807	.04578	.04027	.03314	.03188	.02865	.02799	.02335	.02340	.02458	.03257	.00000	.00000	.00000
3.5-4.0	.00000	.00000	.00000	.00000	.01982	.03904	.06688	.14330	.11846	.11672	.08387	.05875	.04665	.03831	.03636	.02993	.03320	.03299	.02197	.02914	.02939	.04000	.04000	.04000
4.0-4.5	.00000	.00000	.00000	.02055	.01101	.03017	.03931	.07578	.07578	.17013	.11952	.07753	.06053	.04766	.04258	.03844	.03687	.03267	.03319	.03362	.03319	.02859	.02000	.02000
4.5-5.0	.00000	.05263	.00000	.00000	.02203	.01508	.02892	.05442	.07480	.12053	.15309	.11365	.08431	.06218	.05291	.04646	.04082	.04006	.03437	.03040	.02621	.08000	.08000	.08000
5.0-5.5	.00000	.00000	.00000	.00000	.00441	.01154	.01943	.02963	.04758	.07814	.11558	.14281	.11380	.08798	.06870	.05722	.05015	.04424	.03945	.03420	.03336	.04000	.04000	.04000
5.5-6.0	.00000	.00000	.00000	.00000	.01542	.01863	.02079	.02479	.03936	.05723	.08168	.11017	.12671	.12537	.09291	.07760	.06397	.05463	.04991	.04586	.04369	.02000	.02000	.02000
6.0-6.5	.00000	.00000	.00000	.00000	.01982	.02573	.02711	.03362	.03897	.05002	.06638	.08942	.11445	.12004	.11424	.10039	.08945	.08023	.06949	.05979	.05163	.08000	.08000	.08000
6.5-7.0	.00000	.00000	.00000	.00000	.00441	.01065	.01672	.02336	.03936	.05045	.06189	.07905	.09313	.11332	.12456	.12102	.11179	.09983	.09205	.07018	.06275	.04000	.04000	.04000
7.0-7.5	.00000	.00000	.00000	.00000	.00661	.00355	.01536	.01652	.02487	.02798	.04396	.05526	.07638	.10026	.10842	.11538	.12471	.12200	.11327	.10008	.09928	.08000	.08000	.08000
7.5-8.0	.00000	.00000	.00000	.00000	.00441	.00335	.00678	.00997	.01371	.01738	.02701	.03622	.05032	.06620	.08706	.10842	.11538	.11997	.11999	.11300	.11438	.04000	.04000	.04000
8.0-8.5	.00000	.00000	.00000	.00000	.00441	.00444	.00633	.00855	.00959	.01371	.01793	.02164	.02753	.03885	.05275	.06765	.08111	.08890	.10669	.10438	.10326	.10000	.10000	.10000
8.5-9.0	.00000	.00000	.00000	.00000	.00220	.00089	.00407	.00541	.00490	.00579	.01061	.01189	.01405	.01545	.02300	.02817	.03795	.04831	.05977	.07677	.08817	.14000	.14000	.14000
9.0-9.5	.00000	.00000	.00000	.00000	.00220	.00177	.00271	.00256	.00431	.00525	.00612	.00689	.00956	.01305	.01503	.01918	.02476	.03556	.03930	.05194	.05480	.10000	.10000	.10000
9.5-10.0	.00000	.00000	.00000	.00000	.00220	.00266	.00000	.00085	.00098	.00339	.00426	.00411	.00523	.00657	.00850	.01027	.01669	.01874	.02346	.03294	.04845	.02000	.02000	.02000
10.0-10.5	.00000	.00000	.00000	.00000	.00000	.00000	.00000	.00000	.00020	.00014	.00044	.00036	.00074	.00108	.00091	.00120	.00206	.00278	.00359	.00380	.01112	.00000	.00000	.00000

Table 72: ND response matrix for the ES^+ sample, i.e. the probability to reconstruct neutrino energy E_{rec} given true neutrino energy E_{true} .

E_{rec}	E_{true}	0.0-0.5	0.5-1.0	1.0-1.5	1.5-2.0	2.0-2.5	2.5-3.0	3.0-3.5	3.5-4.0	4.0-4.5	4.5-5.0	5.0-5.5	5.5-6.0	6.0-6.5	6.5-7.0	7.0-7.5	7.5-8.0	8.0-8.5	8.5-9.0	9.0-9.5	9.5-10.0	10.0-10.5	
-1.0-0.0		.00000	.00000	.00000	.00000	.00000	.00000	.00000	.00000	.00000	.00000	.00000	.00000	.00000	.00000	.00000	.00000	.00000	.00000	.00000	.00000	.00000	.00000
0.0-0.5		.00000	.00000	.00000	.00000	.00000	.00016	.00000	.00000	.00005	.00000	.00000	.00007	.00004	.00012	.00000	.00000	.00000	.00000	.00000	.00000	.00000	.00000
0.5-1.0		.00000	.72368	.10659	.02764	.01694	.00897	.00919	.00650	.00477	.00453	.00415	.00476	.00401	.00359	.00529	.00435	.00542	.00398	.00452	.00359	.01887	.01887
1.0-1.5		.00000	.21053	.56008	.16260	.06330	.03590	.02443	.01602	.01453	.01065	.00906	.00904	.01036	.00923	.00980	.00985	.00998	.00891	.01120	.01078	.01887	.01887
1.5-2.0		.00000	.03947	.17636	.44280	.16256	.07228	.04061	.02872	.02087	.01591	.01514	.01340	.01528	.01398	.01422	.01410	.01504	.01300	.01376	.01796	.01887	.01887
2.0-2.5		.00000	.00000	.04457	.18509	.35632	.15484	.06963	.04009	.02943	.02313	.01861	.01775	.01826	.01603	.01727	.01616	.01461	.01604	.02064	.01437	.01887	.01887
2.5-3.0		.00000	.00000	.02907	.05077	.17741	.32403	.14908	.06998	.03903	.03177	.02351	.02132	.02079	.01982	.01873	.01867	.01768	.01950	.02044	.01293	.00000	.00000
3.0-3.5		.00000	.00000	.02132	.02699	.06954	.16463	.28855	.14373	.07107	.04250	.03204	.02981	.02625	.02248	.02352	.02183	.02003	.02202	.02437	.02155	.01887	.01887
3.5-4.0		.00000	.00000	.00969	.02249	.03091	.06657	.15544	.25484	.13676	.06585	.04969	.03911	.03133	.02849	.02648	.02710	.02502	.02129	.02673	.03017	.00000	.00000
4.0-4.5		.00000	.00000	.00388	.01864	.02080	.03818	.07172	.16086	.23921	.13169	.07561	.05430	.03966	.03767	.02990	.03032	.02695	.02663	.02535	.02945	.01887	.01887
4.5-5.0		.00000	.00000	.00388	.01157	.01872	.02643	.04698	.07390	.15151	.21986	.14193	.08504	.06251	.05036	.04180	.03712	.03457	.02925	.03302	.03592	.01887	.01887
5.0-5.5		.00000	.00000	.00969	.00771	.01308	.02154	.03111	.05138	.08196	.15149	.19189	.13755	.09090	.06640	.05337	.05013	.04420	.04037	.03656	.03592	.01887	.01887
5.5-6.0		.00000	.00000	.00969	.00900	.01308	.01615	.02537	.03507	.05198	.08457	.13428	.15154	.12907	.10435	.07958	.05976	.04890	.04666	.04835	.04598	.03774	.03774
6.0-6.5		.00000	.01316	.00581	.01028	.01813	.02252	.02485	.03455	.04472	.06311	.09212	.12847	.14305	.12413	.10479	.08850	.07713	.06239	.05877	.05244	.09434	.09434
6.5-7.0		.00000	.01316	.00194	.00643	.01426	.01419	.02161	.02887	.03957	.05152	.06819	.10212	.12464	.13691	.13186	.11686	.10629	.08766	.07429	.07112	.07547	.07547
7.0-7.5		.00000	.00000	.00194	.00643	.00594	.01289	.01378	.02097	.02911	.04088	.05841	.08299	.10996	.13151	.13710	.13765	.12988	.12006	.10574	.08262	.07547	.07547
7.5-8.0		.00000	.00000	.00194	.00257	.00594	.00832	.00773	.01137	.01523	.02322	.03504	.05058	.07619	.09895	.11828	.12796	.13323	.13107	.12009	.11422	.03774	.03774
8.0-8.5		.00000	.00000	.00194	.00257	.00505	.00506	.00512	.00775	.00976	.01522	.01895	.02888	.03836	.05629	.07689	.09416	.10893	.11408	.10613	.10129	.15094	.15094
8.5-9.0		.00000	.00000	.00000	.00193	.00238	.00310	.00595	.00687	.00819	.00936	.01259	.01690	.02453	.03433	.04558	.06259	.07556	.09091	.10122	.09842	.07547	.07547
9.0-9.5		.00000	.00000	.00388	.00321	.00327	.00212	.00418	.00399	.00564	.00753	.00868	.01209	.01746	.02341	.03432	.04006	.05425	.06648	.07626	.08836	.18868	.18868
9.5-10.0		.00000	.00000	.00775	.00129	.00208	.00114	.00324	.00288	.00390	.00533	.00852	.01100	.01362	.01946	.02602	.03372	.04729	.05818	.07626	.08118	.03774	.03774
10.0-10.5		.00000	.00000	.00000	.00030	.00030	.00098	.00146	.00140	.00255	.00274	.00419	.00525	.00550	.00753	.01021	.01453	.01618	.02842	.03007	.04167	.05660	.05660
10.5-11.5		.00000	.00000	.00000	.00000	.00000	.00000	.00000	.00030	.00016	.00051	.00061	.00048	.00084	.00081	.00155	.00229	.00235	.00398	.00432	.01006	.01887	.01887

K Cost estimate

Lead authors: JPa, AK